Applications of passive microwave data to monitor inundated areas and model stream flow

Shang, Haolyu

DOI
10.4233/uuid:66da67a6-cf90-4a71-822e-3d27d0e7ec8d

Important note
To cite this publication, please use the final published version (if applicable).
Please check the document version above.

Applications of passive microwave data to monitor inundated areas and model stream flow

PhD Thesis

Haolyu Shang

Applications of passive microwave data to monitor inundated areas and model stream flow

Proefschrift

ter verkrijging van de graad van doctor
aan de Technische Universiteit Delft,
op gezag van de Rector Magnificus prof.ir. K. C. A. M. Luyben;
voorzitter van het College voor Promoties,
in het openbaar te verdedigen op
maandag 13 november 2017 om 12:30 uur

Door

Haolyu SHANG

Master of Science in Geo-Information Science
Wageningen Universiteit, Nederland

geboren te Shengzhou, China

This dissertation has been approved by the

promotor: Prof. dr. M. Menenti
promotor: Prof. dr. L. Jia
copromotor: Dr. S.C. Steele-Dunne

Composition of the doctoral committee:

Rector Magnificus	chairperson
Prof. dr. M. Menenti	CiTG, TU delft, promotor
Prof. dr. L. Jia	Chinese Academy of Science (China), promotor
Dr. S.C. Steele-Dunne	CiTG, TU delft, copromotor

Independent members:
Prof. dr. ir. N.C. van de Giesen	CiTG, TU Delft
Prof. dr. Y. Kerr	CESBIO (France)
Prof. dr. Z.B. Su	Twente University
Prof. dr. M. Mancini	Politecnico di Milano (Italy)
Prof. dr. W.G.M. Bastiaanssen	CiTG, TU Delft, reserve Lid

Abstract

The observation of surface water bodies in all weather conditions and better knowledge about inundation patterns are important for water resource management and flood early warning. Microwave radiometers at 37 GHz were applied to observe and study the inundation pattern in large subtropical floodplains in China, i.e. the Poyang Lake and Dongting Lake floodplains, due to the trade-off between the capability to penetrate hydrometeors and vegetation, revisiting time, and spatial coverage and resolution. Taking the shallow sensing depth at 37 GHz into account, open water, inundated area and water saturated soil surface all determine the surface emittance measured by the radiometer. Thus, Water Saturated Surface (WSS) is defined as the combination of these three land surface elements.

In subtropical regions, seasonal changes in vegetation cover and various surface roughness conditions are the major challenges for the observation of surface water bodies with microwave radiometers. Atmospheric attenuation, observation gaps and errors in the microwave observations reduce the quality of daily radiometric observations. To deal with the attenuation due to vegetation and surface roughness, a two-step model was developed: the first step is to retrieve the polarization difference emissivity from Polarization Difference Brightness Temperature (PDBT) at 37 GHz with the simplified radiative transfer model and the vegetation optical thickness at 37 GHz parameterized from Normalized Difference Vegetation Index (NDVI) ; the second step is to retrieve the fractional area of WSS from the emissivity difference with a linear model, which can be parameterized according to the Qp surface roughness model. To remove the noise and extract the surface signal (including surface emittance and vegetation attenuation) from the daily PDBT time series, the Time Series Analysis Procedure (TSAP) was developed to identify the spectral features of noisy components in the frequency domain and remove them with a proper filter. The overall method combined the TSAP and the two-step model to derive daily observation of WSS area. The retrieved WSS area in the Poyang Lake floodplain was in a good agreement with the lake area observed from MODerate-resolution Imaging Spectroradiometer (MODIS) and Advanced Synthetic Aperture Radar (ASAR). The observations and analysis of the inundation patterns in the Poyang Lake and Dongting Lake floodplains with this method illustrated the close relationship between inundated area, precipitation and stream flow.

Furthermore, a lumped hydrological model, named the discrete rainfall-runoff model, was developed to fully use the retrieved WSS area and to study the role of inundated area in stream flow production. This model simulates stream flow as the integration of contributions of antecedent precipitation in a certain period. Three implementations of the model were developed with the help of ground water table depth and the retrieved WSS area. The case study in the Xiangjiang River basin (upstream catchment of the Dongting Lake floodplain), China, illustrated that: 1) the longest duration of antecedent precipitation

is a key parameter to determine model performance; 2) long duration would increase the model uncertainty and lead to overfitting; 3) the application of the WSS area can reduce the duration required to achieve a reasonable accuracy. The model parameters indicated the interaction between stream flow and various water storages, and the calibration results of three implementations implied the recharge period of ground water.

Summary

Fresh water is one of the key elements required by human life. Among the various types of fresh water on Earth, surface water is the major resource that human can fully utilize but also risks human life and properties frequently. Thus, the observation of surface water propagation in time and space is one of the essential topics of Earth Observation. Remote sensing technologies have been used to monitor surface water bodies in large and remoted area, with spatial resolutions in a wide range, from less than 30 m to more than 25 km. Satellite data with high spatial resolutions, e.g. acquired by optical and thermal sensors and Synthetic Aperture Radar (SAR), is definitely preferred to monitor surface features. Surface observations with optical and thermal sensors, however, is frequently hampered by aerosol, clouds and precipitation. Before sentinel 1 and COSMO, surface water observation with SAR images was limited by the slow revisiting time and small spatial coverage. Even now, satellite data with both high spatial and temporal resolutions is seldom used to observe daily surface water propagation, especially in a large floodplain and for a long period of time, mainly due to the huge requirement on data storage and the large computational cost. On the other hand, passive microwave data at 37 GHz, though has coarse spatial resolution, is efficient and convenient to monitor the daily dynamics of large-size surface water bodies, due to the capability to penetrate clouds, the large spatial coverage and daily revisiting. In this thesis, we develop the two-step model to retrieve the fractional area of Water Saturated Surface (WSS) from Polarization Difference Brightness Temperature (PDBT) at 37GHz, the Time Series Analysis Procedure (TSAP) to remove the observation gaps, errors and atmosphere attenuation from the PDBT time series and a discrete rainfall-runoff model to fully use the retrieval of WSS to model stream flow.

To monitor surface water bodies with passive microwave data, a radiative transfer model or an empirical model is needed to retrieve surface wetness index from surface brightness temperature measured by microwave radiometers. The main challenge in the model development is to take seasonal changed vegetation and various surface roughness conditions into account. The two-step model, developed for those purposes, includes: 1) the model to retrieve Polarization Difference Effective Emissivity (PDEE) from PDBT;2) the model to retrieve fractional area of WSS from PDEE. The 1st sub-model is derived from the zero-order radiative transfer model by neglecting the radiation that is scattered by vegetation canopy. Vegetation attenuation is described by the vegetation optical thickness, which can be identified through regressing the vegetation transmission function with NDVI and PDBT pairs in the flooded paddy fields. The 2nd sub-model is developed from the numerical analysis for the PDEE and soil moisture, with two dielectric mixing models, i.e. Wang-Schumgger Model and Dobson Model, and one surface roughness model, i.e. Qp model. We found that no matter which dielectric model is applied and what the surface roughness condition is, the fractional area of WSS is linearly related to the PDEE at 37 GHz.

PDBT time series at 37 GHz needs to be pre-processed before any implementation on retrieving surface features, due to that atmosphere attenuation, observation gaps and errors frequently reduce the data quality. Atmosphere attenuation at 37 GHz is due to the absorption and scattering of radiation by various hydrometeors, e.g. water vapor, cloud drops, rain drops and ice crystals. Observation gaps and errors are due to the configuration of satellites, radiometer designs and the uncertainty in the registration method. The Time Series Analysis Procedure is developed to filter out these negative influences, which includes the method to identify the spectral features of noisy components in the frequency domain, a boxcar-filter to remove observation gaps and errors and the Harmonic ANalysis of Time Series (HANTS) algorithm to filter out atmospheric components. The overall procedure to retrieve WSS area is the combination of the TSAP and the two-step model. The WSS area retrieved from 37 GHz data using the overall procedure was in a good agreement with the area of Poyang Lake observed from MODerate-resolution Imaging Spectroradiometer (MODIS) and Advance Synthetic Aperture Radar (ASAR) data. We applied the overall procedure to the whole Poyang Lake flood plain and found that the lake area was strongly influenced by the upstream WSS area with a 3 – 5 day time lag. This relationship was strengthened when the Three George Dam stopped stream flow in the upstream of the Yangtze River.

Surface water propagation is the result of the complicated hydrological processes in a catchment and also reflects the regional water storage capacity. The discrete rainfall-runoff model is developed to fully utilize the satellite observation of surface water propagation, based on the conceptual water balance model. Hydrological processes are typical Markov chain process in other hydrological models. The discrete rainfall-runoff model, however, assumes that the stream flow production by a catchment is determined by antecedent precipitations in a certain period of time. The term "discrete" means that contribution of precipitation is associated with the time interval of several days and the duration of antecedent precipitation is equally spaced by the time interval. This model mainly considers the fact that precipitation is redistributed into different component flows and is collected by river channels with different time lags. According to the complexity in input data, the three implementations of the discrete rainfall-runoff model are developed: 1) precipitation and base flow; 2) overland flow, infiltrated flow and base flow; 3) overland flow, potential subsurface flow and base flow. The base flow is estimated from observed ground water table depth with a linear model, while overland and infiltrated flows are estimated from precipitation and the WSS according to the water balance at top surface.

The three model implementations are calibrated and validate with the gauge measurements of 10-day averaged river discharge in 2001, 2002 and 2005 respectively at Changsha station, downstream of Xiangjiang river basin, China. The duration of antecedent precipitation is the key model parameter varying between 10 and 150 days. The calibration and validation processes proved that using the retrievals of WSS area can significantly reduce the duration of antecedent precipitation required in the model and thus solve the overfitting problem in the model. The set of parameters driving each implementation is an indication of dominant hydrological processes, particularly water storage, in determining the catchment response to rainfall. Significant differences in the annual water yield have

been observed across the three implementations. The Relative Root Mean Squared Error (RRMSE) in each season demonstrates the possible recharge period of the ground water in Xiangjiang river basin. The model validation also shows that the parameters averaged between dry and wet years are good candidates for model prediction.

Above all, we developed a complicated method to derive surface signals from the microwave radiometer data and to retrieve surface water wetness condition from the processed data. The retrieved WSS area can be used to monitor surface water propagation, to study the relationship of water propagation between up and down streams, and to understand and model the stream flow production in a catchment.

Samenvatting

Zoetwater is een van de primaire menselijke levensbehoeftes. Onder de verschillende vormen van zoetwater op aarde, is oppervlaktewater een belangrijk bestaansmiddel dat echter ook menselijke levens en infrastructuur bedreigt. Hierom is observatie van veranderingen van oppervlaktewater in ruimte en tijd een essentieel onderdeel van aardobservatie. Remote sensing technieken worden al langere tijd gebruikt voor het observeren van waterlichamen in grote en afgelegen gebieden, met spatiële resoluties in een groot bereik van minder dan 30 meter tot meer dan 25 km.

Satellietdata met hoge spatiële resolutie, bijvoorbeeld van optische- en warmtesensoren en Synthetic Apeture Radar (SAR) verdient de voorkeur bij het observeren van oppervlaktekenmerken. Dit wordt vaak bemoeilijkt door de aanwezigheid van aerosols, wolken en neerslag. Voordat Sentinel 1 en COSMO beschikbaar waren, werd oppervlaktewaterobservatie met SAR afbeeldingen beperkt door de lange tijd tussen twee opnamen en het beperkte spatiële bereik. Zelfs nu wordt satellietdata met hoge spatiële en temporale resolutie weinig gebruikt voor dagelijkse observatie. Zeker voor grote overstromingsvlaktes over langere periodes zijn dataopslag en de grote computationele kosten een limiterende factor. Een alternatief is passieve 37GHz microgolf. Ook al heeft dit een grove spatiële resolutie, is het effectief voor het monitoren van de dagelijkse dynamica van grote oppervlaktewaterlichamen door de eigenschap dat het wolken penetreert en de dagelijkse metingen. In deze thesis, hebben we een 2-staps model ontwikkeld om het fractionele oppervlak van Water Saturated Surface (WSS) te bepalen met behulp van Polarization Difference Brightness Temperature (PDBT) op 37GHz. En vervolgens de Time Series Analysis Procedure (TSAP) om gaten in observatie, fouten en atmosferische demping uit de PDBT te halen. En een discreet oppervlakte-afvoermodel om het bepaalde WSS volledig te kunnen gebruiken om rivierstroom te kunnen simuleren.

Om oppervlaktewater met passieve microgolfdata te kunnen observeren is een radiative transfer model of een empirisch model nodig om de surface wetness index te kunnen bepalen uit de helderheidtemperatuur zoals gemeten door een microgolfradiometer. De grootste uitdaging in de ontwikkeling van het model is om de seizoensvariatie van vegetatie en verschillende oppervlakteruwheden te vatten. Het 2-staps model dat hiervoor ontwikkeld is bevat: 1) het model om de Polarization Difference Effective Emissivity (PDEE) te bepalen uit PDBT; 2) een model om het fractionele oppervlak van WSS te bepalen uit PDEE. Het eerste submodel is afgeleid van het nulde orde radiative transfer model door de verstrooiing van de vegetatie te verwaarlozen. Demping door vegetatie is beschreven door de optische dikte van de vegetatie, wat bepaald kan worden door regressie van de vegetatie-transmissiefunctie met NDVI en PDBT paren in de overstroomde rijstvelden. Het tweede submodel is ontwikkeld met behulp van numerieke analyse van de PDEE en bodemvochtigheid, met 2 diëlektrische constante modellen van het bodem-watermengsel, i.e. het Wang-Schumgger Model en het Dobson Model en één oppervlakteruwheidsmodel, i.e. het Qp model. Het bleek dat voor beide diëlektrische

modellen en alle oppervlakteruwheden, het fractionele oppervlak van WSS altijd lineair afhangt van de PDEE bij 37GHz.

PDBT tijdreeksen op 37GHz moeten voorbewerkt worden voordat ze geanalyseerd kunnen worden. Atmosferische demping, gaten in observatie en fouten verslechteren vaan de kwaliteit van de data. Atmosferische demping op 37GHz is door de absorptie en verstrooiing aan waterdamp, regendruppels en ijskristallen. Gaten in de observatie worden veroorzaakt door de configuratie van satellieten, ontwerp van radiometers en fouten in de registratie van pixels. De 'Time Series Analysis Procedure' (TSAP), is ontwikkeld om deze negatieve invloeden uit data te filteren. Hierbij wordt gebruik gemaakt van een spectraal filter om ruis te verwijderen en een boxcar filter om fouten en gaten in de observatie te verwijderen. Het 'Harmonic Analysis of Time Series' (HANTS) algoritme wordt gebruikt om atmosferische componenten uit te filteren. De uiteindelijke procedure om het WSS oppervlak te bepalen is de combinatie van TSAP en het 2-staps model. Het WSS oppervlak dat op deze manier bepaald was is in goede overeenstemming het oppervlak van de overstromingsvlakte van het Poy ang meer als geobserveerd met MODerate-resolution Imaging Spectroradiometer (MODIS) en Advance Synthetic Apeture Radar (ASAR). De uiteindelijke procedure is toegepast op de hele overstromingsvlakte van het Poyang meer. Hieruit bleek dat het gebied sterk beïnvloed wordt door het WSS gebied stroomopwaarts met een tijdverschil van 3 tot 5 dagen. Dit effect werd versterkt toen de Jangtsekiang stroomopwaarts werd afgesloten door de Drieklovendam.

Oppervlaktewaterpropagatie is het resultaat van ingewikkelde hydrologische processen in een stroomgebied en de regionale wateropslagcapaciteit. Het discrete oppervlakte-afvoermodel is ontwikkeld om de satellietobservaties van oppervlaktewater volledig te kunnen gebruiken en is gebaseerd op een conceptueel waterbalansmodel. Hydrologische processen zijn meestal Markovkettingprocessen in andere hydrologische modellen. Het discrete oppervlakte-afvoermodel neemt echter aan dat de rivierstroom in een stroomgebied bepaald wordt door antecedentneerslag van een bepaalde periode. De term "discreet" betekent dat de neerslag als constant beschouwd wordt binnen een vast tijdsinterval van een aantal dagen. Dit model beschouwt het feit dat neerslag herverdeeld wordt in verschillende stromen en met verschillende vertraging opgevangen wordt door rivieren. Aan de hand van de complexiteit van de input data zijn er drie verschillende implementaties van het oppervlakte-afvoermodel ontwikkeld. : 1) neerslag en base flow; 2) overland flow, infiltrated flow en base flow; 3) overland flow, potential subsurface flow en base flow. De base flow wordt bepaald aan de hand van het gemeten grondwaterpeil gecombineerd met een lineair model. Overland en infiltrated flow worden geschat aan de hand van neerslag en het WSS met de waterbalans aan het oppervlak.

De drie verschillende implementaties van het model zijn gekalibreerd en gevalideerd met over 10 dagen gemiddelde metingen van het rivierpeilmetingen van het debiet in 2001, 2002 en 2005 bij het Changsha station, stroomafwaarts van de Xiangjiang in China. De periode van de antecedentneerslag is de belangrijkste modelparameter en varieert tussen 10 en 150 dagen. De kalibratie- en validatieprocessen hebben bewezen dat met het gebruik van WSS gebied, bepaald aan de hand van de 37GHz data, de duur van de antecedentneerslag sterk verkort kan worden. En hiermee overfitting van het model kan verhelpen. De set van

parameters die in de verschillende implementaties gebruikt worden is een indicatie van de dominante hydrologische processen, in het bijzonder wateropslag bij het bepalen van de reactie van het stroomgebied op neerslag. Er zijn significante verschillen in jaarlijks debiet tussen de drie verschillende implementaties. De Relative Root Mean Squared Error (RRMSE) in elk seizoen laat de mogelijke oplaadperiode van het grondwater in het stroomgebied van de Xiangjiang zien. De validatie van het model laat ook zien dat de parameters gemiddeld over droge en natte jaren een goede kandidaten zijn voor modelvoorspelling.

Bovenal hebben we een complexe methode ontwikkeld om oppervlaktesignalen uit de microgolf radiometerdata te kunnen bepalen en om de surface water wetness conditie te kunnen achterhalen uit de verwerkte data. Het bepaalde WSS gebied kan gebruikt worden voor het monitoren van oppervlaktewaterpropagatie; het bestuderen van de relatie tussen waterpropagatie stroomopwaarts en afwaarts; en om het debiet van een stroomgebied te begrijpen en te modelleren.

Table of Contents

List of Figures

List of Tables

List of Symbols

$*$	Convolution operator	-
ΔT	Polarization Difference Brightness Temperature	K
Δt	Sampling interval	day
ΔT_s	Polarization Difference Brightness Temperature of surface	K
$\Delta\epsilon$	Difference of vertically and horizontally polarized emissivity	-
$\Delta\epsilon^*$	Polarization difference effective emissivity	-
$\Delta\epsilon_{dry}^*$	Polarization difference effective emissivity of totally dry soil	-
$\Delta\epsilon_{sat}^*$	Polarization difference effective emissivity of water saturated soil	-
A^0	Average of whole time series	K
A_g^0	Average of the time series $g(t_i)$	K
A_h^0	Average of the time series $h(t_i)$	K
a_1	Half of the average of the atmospheric signal	K
a_2	Half of the average of the surface signal	K
a_3	Half of the average of a square wave	-
a_4	Half of the average of the summation of PDBT time series and white noise function	K
A^0	Amplitude of a harmonic component	K
A_n^F	Amplitude after filtering	K

a_p	Coefficient to calculate roughness parameter at 10.65 GHz	-
B	Constant base flow	mm day^{-1}
b_p	Coefficient to calculate roughness parameter at 10.66 GHz	-
C	Percentage of clay	%
c_p	Coefficient to calculate roughness parameter at 10.67 GHz	-
e	User-prescribed errors of HANTS reconstruction	K
E_i	Model estimated stream flow	mm day^{-1}
f	Uniformly sampled time series	-
f_l	Time series of a noisy PDBT time series	K
$FE_{i,j}$	Parts of P_i that were used by evapotranspiration at jth time step	mm day^{-1}
$FQ_{i,j}$	Parts of P_i that were used as water discharge at jth time step	mm day^{-1}
f_s^l	Surface signal	K
f_{si}	Fractional area of a sub-pixel area	-
f_{ss}	Fractional area of Water Saturated Surface	-
f_v	Fractional area of vegetation,	-
$g(t_i)$	Uniformly sampled time series	K
g_n^l	Harmonic component of a gap-and-noise signal	K
g_n^2	Harmonic component of a filtered signal	K

G_{max}	Maximum ground water table depth in each year	mm
G_{min}	Minimum ground water table depth in each year	mm
g_n	Harmonic component of a noise-and-gap-free singal	K
G_t	Ground water table depth	mm
H	Horizontal polarization	-
$h(t_i)$	Uniformly sampled time series	K
i	Time step	day
$IE_{i,t}$	Parts of ith infiltrated flow used for evapotranspiration at t^{th} time step	mm day^{-1}
$IG_{i,t}$	Parts of ith infiltrated flow stored in ground water at t^{th} time step	mm day^{-1}
Im	Imaginary part	-
$IG_{i,t}$	Parts of ith infiltrated flow used as stream flow at t^{th} time step	mm day^{-1}
$IS_{i,t}$	Parts of ith infiltrated flow stored in soil layer at t^{th} time step	mm day^{-1}
$IW_{i,t}$	Parts of ith infiltrated flow stored at surface at t^{th} time step	mm day^{-1}
k_b	Releasing factor of ground water	-
k_i	Sampling time	day
L	Period of a square wave	day
L_l	Duration of one gap segment	day
M	Half of the filter length	day

m	Longest duration of antecedent precipitation	day
n	Cycle number	-
N	Total sample size	-
ND	Normalized difference between the gap-and-noise-free and filtered amplitude	%
$NDVI$	Normalized Difference Vegetation Index	-
$NDVI_{soil}$	NDVI value of bare soil	-
$NDVI_{veg}$	NDVI value of full vegetation cover	-
n_o	Odd cycle number	-
n_s	Number of total sub-pixel areas	-
$\bar{O}$	Average of measured stream flows	mm day^{-1}
$OE_{i,t}$	Parts of ith overland flow used for evapotranspiration at t^{th} time step	mm day^{-1}
$OG_{i,t}$	Parts of ith overland flow stored in ground water at t^{th} time step	mm day^{-1}
O_i	Observed stream flow at i^{th} time step	mm day^{-1}
$OG_{i,t}$	Parts of ith overland flow used as stream flow at t^{th} time step	mm day^{-1}
$OS_{i,t}$	Parts of ith overland flow stored in soil layer at t^{th} time step	mm day^{-1}
$OW_{i,t}$	Parts of ith overland flow stored at surface at t^{th} time step	mm day^{-1}
p	Polarization	-
P	Record length	day

P_i	Antecedent precipitation occurring at the ith time step	mm day^{-1}
$P_{i,t}$	P_i in a catchment at the tth time step	mm day^{-1}
PS	Porosity of dry soil	-
Q_i^I	Infiltrated flow at i^{th} time step	mm day^{-1}
Q_i^o	Overland flow at i^{th} time step	mm day^{-1}
Q_P	Roughness parameter	-
Q_s^i	potential subsurface flow at i^{th} time step	mm day^{-1}
Q_t	Stream flow observed at t^{th} time step	mm day^{-1}
Q_t^b	Base flow at t^{th} time step	mm day^{-1}
Re	Real part of a complex number	-
R^s	Spectral features of the surface signal	-
S	Percentage of sand	%
s/l	Ration of root mean square height to correlation length	-
S_1	Square wave with phase = 0	-
S_2	Square wave with phase = 0	-
$SG_{i,t}$	Parts of P_i stored in ground water at the tth time step	mm day^{-1}
$SS_{i,t}$	Parts of P_i stored in soil at the tth time step	mm day^{-1}
S_w	Square wave	-

t_a	Transmission function of atmosphere	-
T_B	Brightness temperature at top of atmosphere	K
$T_{B,37V}$	Vertically polarized brightness temperature at 37 GHz	K
T_{BS}	Brightness temperature at the top of vegetation canopy	K
T_d	Down-welling brightness temperature of atmosphere	K
t_i	Sampling time	day
T_s	Surface temperature	K
T_{sb}	Temperature of bare soil	K
T_{sv}	Temperature of the soil-vegetation system	K
T_u	Up-welling brightness temperature of atmosphere	K
T_v	Temperature of vegetation canopy	K
t_v	Transmission function of vegetation canopy	-
V	Vertical polarization	-
W_c	Volumetric soil moisture	$cm^3\ cm^{-3}$
W_i	Volumetric soil moisture of a sub-pixel area	$cm^3\ cm^{-3}$
w_i	Contribution weight of the ith precipitation to observed stream flow	-
W_{sat}	Volumetric soil moisture when it is totally water saturated	$cm^3\ cm^{-3}$
WS_i	Fraction of the WSS area at i^{th} time step	-

W_t	Transition soil moisture	cm^3 cm^{-3}
x	DFT of a time series	-
$\mathbf{X}$	Matrix of the observations of precipitation and ground water table depth	-
x_a	Discrete Fourier Transform of the atmosphere signal	-
x_{f1}	Discrete Fourier Transform of noisy PDBT time series	-
$x_{g \times h}$	Side lobes in Discrete Fourier Transform of a combined signal	-
x_s	Discrete Fourier Transform of the surface signal	-
$x_{s \times a}$	Side lobes in Discrete Fourier Transform of a combined signal	-
x_w	Discrete Fourier Transform of Square wave	-
x_α	Discrete Fourier Transform of observation error	-
$x_{\alpha \times w}$	Side lobes in Discrete Fourier Transform of a combined signal	-
$x_{\Delta T}$	Discrete Fourier Transform of a PDBT time series	-
$x_{\Delta T \times w}$	Side lobes in Discrete Fourier Transform of a combined signal	-
$\mathbf{Y}$	Matrix of observed stream flow	-
α	Shape factor of the Dobson Model	-
α_n	White noise function	K
α_p	Coefficient to calculate roughness parameter at 37 GHz	-
β	Coefficient of the Dobson Model	-

β_i^{21}	Weight of overland flow in the second implementation	-
β_i^{22}	Weight of infiltrated flow in the second implementation	-
β_i^{31}	Weight of overland flow in the third implementation	-
β_i^{32}	Weight of potential subsurface flow in the third implementation	-
β_p	Coefficient to calculate roughness parameter at 37 GHz	-
$\boldsymbol{\beta_w}$	Weight matrix	-
Γ	Surface reflectivity	-
γ	Experimental parameter in Wang-Schmugge model	-
Γ^*	Effective Reflectivity	-
γ_a	Absorption coefficient	-
γ_e	Extinction coefficient	-
γ_s	Scattering coefficient	-
$\Gamma_{s,s}$	Reflectivity at smooth surface	-
ϵ	Surface emissivity	-
ε	Dielectric constant of a soil-water mixture	-
ε_a	Dielectric constant of air	-
ε_i	Dielectric constant of ice	-
ε_r	Dielectric constant of rock	-

ε_s	Dielectric constant of soil	-
ε_w	Dielectric constant of fresh water	-
ε_υ	Dielectric constant of a soil-water mixture at frequency υ	-
θ	Incidence angle	Rad
σ	Coefficient of vegetation transmission function	-
τ_a	Optical depth of atmosphere	-
τ_v	Optical depth (also called optical thickness) of vegetation canopy	-
υ	Microwave frequency	Hz
ϕ_n	Phase of a harmonic component	Rad
ω_p	Single scattering albedo	-

List of Acronyms

ALOS	Advanced Land Observation Satellite
AMSR-E	Advanced Microwave Scanning Radiometer for EOS
ASAR	Advanced Synthetic Aperture Radar
AVHRR	Advanced Very High Resolution Radiometer
BT	Brightness Temperature
COSMO	COnstellation of small Satellites for the Mediterranean basin Observation
DFT	Discrete Fourier Transform
DMSP	Defense Meteorological Satellite Program
EASE	Equal-Area Scalable Earth
EnKF	Ensemple Kalman Filter
EnKS	Ensemple Kalman Smooth
ENVISAT	Environmental Satellite
ERS	European Remote Sensing satellites
FFT	Fast Fourier Transform
FWS	Fractional Water Surface
GRACE	Gravity Recovery and Climate Experiment
HANTS	Harmonic ANalysis of Time Series
HJ	HuanJing
IFOV	Instantaneous Field Of View
InSAR	Interferometric Synthetic Aperture Radar

ISCCP	International Satellite Cloud Climatology Project
ITP	Institute of Tibet Plateau
JERS	Japanese Earth Resources Satellite
LAI	Leaf Area Index
LT	Local Time
MODIS	MODerate-resolution Imaging Spectroradiometer
MVI	Microwave Vegetation Index
NSE	Nash-Sutcliffe Efficiency
NDVI	Normalized Difference Vegetation Index
OWL	Open Water Likelihood
PALSAR	Phased Array type L-band Synthetic Aperture Radar
PDBT	Polarization Difference Brightness Temperature
PDF	Probability Distribution Functions
PDE	Polarization Difference Emissivity
PDEE	Polarization Difference Effective Emissivity
PDM	Probability Distributed Model
RRMSE	Relative Root Mean Square Error
SAC	Sacramento
SAR	Synthetic Aperture Radar
SMMR	Scanning Multi-channel Microwave Radiometer
SSM/I	Special Sensor Microwave Imager
SSMIS	Special Sensor Microwave Imager/Sounder
SIR	Spaceborne Imaging Radar

SPOT	Satellite Pour l'Observation de la Terre
SWOT	Surface Water and Ocean Temperature
TSAP	Time Series Analysis Procedure
TOVS	TIROS Operational Vertical Sounder
TMPA	TRMM Multi-satellite Precipitation Analysis
TRMM	Tropical Rainfall Measuring Mission
VIC	Variable Infiltration Capacity
WSS	Water Saturated Surface

Chapter 1

Introduction

1.1   Background on remote sensing observations of surface water bodies

Surface water bodies only cover a small fraction of the land surface, but they play an important role in water resource management (e.g. Asdorf, 2003; Alsdorf et al., 2007; Frappart et al., 2005). The water level of lakes and reservoirs, river stage, and river discharge can be empirically related to the extension of surface water in a lake, reservoir or river (e.g. Alsdorf, 2007; Bates et al., 2014; Bjerklie et al., 2003; Brakenridge et al., 2005; Brakenridge et al., 2007; Hostache et al., 2009; Pan et al., 2013; Peng et al., 2006; Sippel et al., 1998; Smith et al., 1996; Smith and Pavelsky, 2008). Floods in a river basin damage properties and life. Inundated area caused by floods leads to soil erosion (e.g. Smith et al., 2000; Vinnikov et al., 1999), transports sediment (e.g. Goel et al., Goel et al., 2002; Jain et al., 2002), but also brings nutrition and creates habitats for wildlife (e.g. Sakamoto et al., 2007; Sippel et al., 1994; Sippel et al., 1998). Wetlands and paddy fields are important forms of inundated area, which influence climate as major sources of methane (Houweling et al., 1999; Matthews and Fung, 1987; Matthews et al., 1991; Mialon et al., 2005; Papa et al., 2006; Prigent et al., 2001b; Prigent et al., 2007; Walter et al., 2001). Thus, mapping and monitoring surface water bodies is also relevant for disaster management, ecosystem research, and climate change studies.

In mid- and large- size river basins, however, it is difficult to delineate the water area by ground survey (Smith, 1997; Usachev, 1983). There are many forms of surface water bodies, such as permeant water in lake, river and permanent ponds, ephemeral standing water in ponds, seasonal wetlands, inundated areas caused by floods, and flooded paddy fields. Moreover, the boundary of a surface water body changes due to precipitation and water recession, such as monsoon lakes and seasonal wetlands (Dronova et al., 2011). Thus, it is impossible to cover all of these remote areas in a large river basin through field surveys.

On the other hand, remote sensing provides many ways to delineate the boundary of surface water bodies and to study their evolution. Optical and thermal sensors, active and passive microwave systems have been used for this purpose. To monitor surface water bodies in a floodplain, remote sensing data with high temporal and spatial resolutions have a clear potential. On the other hand, the analysis of a large volume of high resolution data may come at significant computational cost, increasing rapidly with the floodplain size and the temporal coverage of the analysis. In this study, we are not only interested in the observation of surface water bodies, but also the role that they play in stream flow production. The latter requires extended time series of high temporal resolution data. We used coarse spatial resolution data (i.e. tens of kilometer) to study surface water bodies in a large floodplain, while ensuring high temporal resolution and lower computational costs.

In the following three sections, the physical principles and limitations of each type of observations will be reviewed. The techniques and methods used for detecting and delineating a surface water body are summarized for each sensor type. The challenges in the observation of surface water bodies with space-borne sensors, i.e. the influence of vegetation and various atmospheric conditions, spatial and temporal resolutions, and the spatial coverage, will be detailed. Through this short review, it can be concluded that passive microwave radiometers can provide the data required for the long-term observation of flooded areas in large floodplains with dense vegetation coverage and various atmospheric conditions.

1.1.1 Optical and thermal sensors

Open water can be clearly observed in the images acquired by optical and thermal sensors (Table 1.1, in page 8) (e.g. Rasid and Pramanik, 1990), due to its much lower reflectance and radiometric temperature than other land cover types. This visual interpretation of open water is always used as reference for surface water body observations with other remote sensing data (e.g. Tanaka et al., 2000; Tanaka et al., 2003; Temimi et al., 2005). Water surface may be mixed with other land cover types in image pixels (Sheng et al., 2001). For example, the boundary of a surface water body may be partially covered by vegetation. Spectral features of a shadowed water surface may be different from that of a sunlit water surface (Sheng et al., 1998). In order to delineate a water body notwithstanding these mixed pixels, several methods have been proposed: a) single band model (e.g. Barton and Bathols, 1989; Sheng et al., 1998; Verdin, 1996); b) multi-band linear model (Xiao and Chen, 1987); c) band ratio model (Sheng et al., 1998); d) water index model (e.g. McFeeters, 1996; Xu, 2006) and e) linear mixing model (Sheng et al., 2001) to fully use the spectral features of a water surface in visible and infra-red bands.

Supervised or un-supervised classification methods may be applied to derive the threshold values implemented in these models to delineate a surface water body. The accuracy of these models highly depends on the training data, the complexity of mixed pixels and the spectral contrast between the water surface and other land covers. The Open Water Likelihood (OWL) algorithm combines multiple indices to deal with the spatial complexity (Guerschman et al., 2011). It is found that the threshold value for the OWL

index is very region specific, due to various surface conditions in different regions (Chen et al., 2013). For images acquired in the same region but at different times, changes in the spectral features of the water surface may be due to variable atmospheric conditions, occurrence of emerging vegetation and changes in the inundation boundary after water recession (Feng et al., 2012a). Thus for the long-term observation of water bodies, multiple models are combined by the decision tree to deal with the variability in surface and atmospheric conditions (see e.g. Islam et al., 2010; Sakamoto et al., 2007). Optical and thermal sensors, however, cannot penetrate cloud and vegetation to observe a water body underneath. This major drawback led to observe surface water bodies using active and passive microwave instruments.

1.1.2 Active microwave systems

Active microwave remote sensing can image the Earth surface nearly in all weather conditions (Smith, 1997). At most frequencies used in space-borne Synthetic Aperture Radar (SAR) systems (Table 1.2, in page 9), open water surface, in the absence of waves, yields much lower back-scatter than other targets. However, turbulence, wind, building corners, emergent vegetation and trees can all cause significant increases in radar back-scatter, making it difficult to delineate the boundary of a water surface (Schumann and Moller, 2015; Smith, 1997). For example, flooded forest area will have higher echo than unflooded forest, due to the double-bounce reflection on water surface (Alsdorf et al., 2001; Wang et al., 1995). Several image processing techniques have been developed to map inundated area, such as visual interpretation (e.g. Biggin, 1996; Oberstadler et al., 1997), histogram threshold method (e.g. Deschmukh and Shinde, 2005; Otsu, 1975), texture method (e.g. Irons and Petersen, 1981; Podest and Saatchi, 2002), and active contour model (e.g. Horritt2001). Except the visual interpretation, few methods can reach a classification accuracy (i.e. the ratio of the observed inundated area to its actual total area) above 90%, due to backscattering from multiple objects, remaining speckle, geometric distortions, and errors in geocoding (Schumann et al., 2009). Besides these practical problems, back scattering of surface objects also depends on the incidence angle (Schumann and Moller, 2015), while the incidence angle of each pixel changes due to the scan geometry of SAR and water waves, in the case of a water surface. Thus, multiple algorithms are combined to improve the classification accuracy of the inundated area (Schumann et al., 2009). Moreover, multi-frequencies and multi-polarizations SAR images can be used by the decision tree model to solve the above problems in dense forest regions (Hess et al., 1995).

The backscattering of surface objects changes due to the temporal variability in surface conditions like the seasonality of vegetation and to the different incidence angles for different scans. To some extent, these effects can be corrected by processing each SAR image independently, but this makes the processing complex to monitor water bodies (e.g. Townsend, 2001). Alternatively, the Probability Distribution Function (PDF) of the back-scatter of the targets is derived from a training data set with various incidence angles and surface conditions. The confidence level of attributing observed back-scatter to a certain surface type can be obtained according to the PDFs. This method has been used for dual-

season observation of wetlands in Amazon (Hess et al., 2003) and global observation of inundated area (Westerhoff et al., 2013). Differential interferometry can be further used to detect both water depth changes and inundated area, even under dense forest (Alsdorf et al., 2007; Alsdorf et al., 2001). L-band Interferometric SAR (InSAR) is not sensitive to the seasonal changes of vegetation canopy (Schumann and Moller, 2015), thus vegetation influences can be mitigated. The long revisiting period of most SAR system (Table 1.2), however, still limits application of SAR image data for long-term observation of inundated areas, especially if daily or weekly observations are required to capture water extent dynamics. The COSMO-SkyMed SAR constellation (Table 1.2) can acquire images with both high spatial and temporal resolutions for flood monitoring (Pulvirenti et al., 2011), but the cost is unacceptable for research purpose in a large floodplain and for a long period of time, due to its small spatial coverage. Moreover, SAR images acquired on rainy days cannot be used for the observation of surface water body due to the noise introduced by the scattering of rain drops.

1.1.3 Microwave radiometers

Passive microwave remote sensing is very suitable for the long-term observation of surface water bodies in large floodplains (e.g. Choudhury, 1989, 1991; Choudhury et al., 1990; Giddings and Choudhury, 1989), due to the fast revisiting and large spatial coverage of microwave radiometers (Table 1.3, in page 10). Microwave radiometers measure the intensity of radiation emitted by the atmosphere and the surface (Choudhury, 1991; Giddings and Choudhury, 1989). The surface emittance is determined by the surface temperature and emissivity, of which the latter is controlled by surface wetness condition (Ulaby et al., 1981). Surface wetness conditions can be roughly assessed by observed polarization difference brightness temperature (PDBT) (e.g. Jin, 1999; Tanaka et al., 2000; Tanaka et al., 2003) or be retrieved from surface emissivity by various radiative transfer models (e.g. Prigent et al., 2001b; Prigent et al., 2007; Prigent et al., 1997). Spatial resolution of radiometers (Table 1.3) increases and the sensing depth decreases with increasing microwave frequencies, thus higher frequencies, e.g. 19 GHz, 37 GHz and 85 GHz, have been used to monitor the Water Saturated Surface (WSS), i.e. the sum of open water, inundated area and water saturated soil surface. For example, the fractional abundance of WSS can be retrieved from PDBT at 37 GHz by a linear un-mixture model (e.g. Sippel et al., 1994). In the pathway from the surface to a space-borne radiometer, besides the influence of atmosphere emittance, surface emittance is also absorbed and scattered by the vegetation cover (Choudhury et al., 1992; Ulaby et al., 1981). To derive surface emittance from radiometer measurements by a space-borne radiometer, atmospheric emittance and vegetation attenuation needs to be accounted for by ancillary data and a (simple) radiative transfer model(Choudhury, 1989). Scattering by hydrometeors will be significant at 85 GHz, thus microwave emittance at 37 GHz is mainly used to retrieve WSS area, as a trade-off between spatial resolution and atmospheric influence. Several methods have been developed to observe inundated area from passive microwave observations:

> ➤ Brightness temperature difference. Both the brightness temperature difference between various frequencies or the Polarization Difference Brightness Temperature (PDBT) at the same frequency, e.g. 37 GHz, may be applied. The brightness temperature difference increases with surface wetness, filters out the up-welling atmospheric emittance and reduces the vegetation influence. 37 GHz is the key frequency when applying this method. For example, the brightness temperature difference between 19 GHz and 37 GHz was linearly related to the fractional abundance of surface water as shown in China by Tanaka et al. (2000). Total flooded area was retrieved from the brightness temperature difference between 37 GHz and 85 GHz, i.e. the flood index of Jin (1999), which takes the scattering of precipitation at 85 GHz into account. In a densely vegetated area, such as tropical forests, the fraction of inundated area can be retrieved from the PDBT at 37 GHz by a linear un-mixing model (Sippel et al., 1994), since the vegetation influence on PDBT at 37 GHz can be assumed to be uniform (Choudhury, 1989; Choudhury and Tucker, 1987; Choudhury et al., 1990; Giddings and Choudhury, 1989). The inundated area retrieved from PDBT at 37 GHz in the Amazon River basin was in a good agreement with the observation from SAR data (Sippel et al., 1994) and in the Mekong Delta was in a good agreement with the observations from AVHRR images (Tanaka et al., 2003). This PDBT method has been extended for inundation pattern studies in the savanna flood plains of South America (Hamilton et al., 2002, 1996, 2004).

> ➤ Surface Emissivity. Surface emissivity declines and the polarization difference of surface emissivity increases with increasing surface wetness (Basist et al., 2001; Jin, 1999; Prigent et al., 2001b; Prigent et al., 2007). The fractional abundance of surface water bodies can be linearly related to both at e.g. 37 GHz. To derive surface emissivity or its polarization difference at 37 GHz, atmosphere emittance and vegetation attenuation needs to be estimated by a radiative transfer model. Atmospheric emittance can be empirically related to atmospheric water content (Choudhury, 1989, 1991; Choudhury et al., 1992; Fily et al., 2003; Prigent et al., 2001b) and thus can be removed with ancillary data. Vegetation influence on surface emittance is complicated, due to the different vegetation types and seasonal changes. An unsupervised clustering technique was developed to estimate the surface emittance under various vegetation conditions, which are observed from NDVI or backscattering of SAR (Prigent et al., 2001a; Prigent et al., 2001b; Prigent et al., 2007). The polarization difference of surface emissivity, i.e. the Basist index, can be retrieved from the weighted average of the brightness temperatures differences among 19 GHz, 37 GHz, and 85 GHz (Basist et al., 1998; Basist et al., 2001). The atmospheric and vegetation conditions were considered by calibrating the weight parameters in the Basist index.

Above all, the influence of dense vegetation, which produces many problems in the observation of inundated area with other remote sensing techniques, can be alleviated in passive microwave observations by the brightness temperature difference. The methods using surface emissivity can take the seasonal changes in vegetation conditions into account.

The atmospheric influence on microwave observations can be removed by ancillary data or be mitigated by the brightness temperature difference. Thus microwave radiometers are very suitable to observe surface water bodies covered by dense or seasonal changed vegetation in almost all weather conditions. The fast revisiting time of radiometers (Table 1.3) is very useful to observe inundation pattern in floodplains. The major limitation of microwave radiometers is their coarse spatial resolution (Table 1.3) and thus these observations are normally applied to observe inundated area in large river basin or globally (e.g. Basist et al., 2001; Choudhury, 1989; Hamilton et al., 2002, 2004; Prigent et al., 2001b; Prigent et al., 2007; Tanaka et al., 2003).

Table 1.1: Space-borne optical and thermal sensors commonly used to observe surface water bodies

Sensor type	Instrument	data period	Spectral band	spatial resolution (m)	swath width (km)	revisiting time (days)	data accessibility
Optical and thermal	Landsat series	1972 — today	Visible, infra-red and thermal	15 — 30	185	16	Free
	AVHRR series	1978 — today	Visible, infra-red and thermal	1090	2900	1	Free
	SPOT series	1986 — today	visible and infra-red	1.5 — 20	60	4	Commercial
	MODIS	2000 — today	Visible, infra-red and thermal	250 — 1000	2330	<1	Free
	Sentinel 2	2015 — today	visible and infra-red	≤ 20	290	5	Free

Table 1.2: Space-borne SAR systems commonly used to observe surface water bodies

Sensor type	Instrument	data acquisition period	frequency (polarization)	spatial resolution (m)	swath width (km)	revisiting time (days)	data accessibility
	ERS-1/2	1991 - 2000/ 1995 - 2011	C (VV)	30	100	35	Free
	JESR-1	1992-1998	L(HH)	18	75	44	Free
	SIR-C/X-SAR	April and October 1994	L & C (quad) and X (VV)	≤ 30	15 to 80 (L- and C-Band) 15 to 40 (X-Band)	173	Free
	Radarsat-1	1995 — 2013	C (HH)	8 — 100	45 — 500	24	Commercial
	Radarsat-2	2007 — today	C (quad)	8 — 100	50 — 500	24	Commercial
	ENVISAT/ASAR	2002 — 2012	C (dual)	30 — 1000	58 — 400	35	Free
Active microwave system	ALOS/PALSAR	2006 — 2011	L (quad)	10 — 100	70 — 350	46	Free
	ALOS-2/PALSAR-2	2014 — today	L (quad)	1 — 100	50 — 350	14	Free
	TerraSAR-X/ TanDEM-X	2007 — today/ 2010 — today	X (quad)	1 — 18.5	10×5 — 1500×100	11	Commercial
	COSMO-SkyMed-1/4	2007 ... 2010 — today	X (quad)	1 — 100	10×10 for spotlight mode/swath width of 40 - 200 for other modes	constellation ≤ 1/single 16	Commercial
	HJ -1C	2012 — today	S (VV)	5, 20	40, 100	31	Limited
	Sentinel -1 a/b	2014 — today	C (dual)	5, 20×40	80 — 400	6	Free

Table 1.3: Space-borne microwave radiometers commonly used for observation of surface water bodies

sensor type	Instrument	data acquisition period	frequency bands (GHz)/polarization	spatial resolution (km)	swath width (km)	revisiting time (days)	data accessibility
Microwave radiometers	SMMR	1978 — 1987	6.63 (dual)	148×95	780	6	free
			10.6 (dual)	91×59			
			18 (dual)	55×41			
			21 (dual)	46×30			
			37 (dual)	27×18			
	SSM/I	1987 — current	19.3 (dual)	69×43	1400	1	free
			22.3 (V)	50×40			
			36.5 (dual)	37×28			
			85.5 (dual)	15×13			
	AMSR-E	2001 — 2013	6.9 (dual)	74×43	1445	1	fee
			10.7(dual)	51×30			
			18.7 (dual)	27×16			
			23.8 (dual)	31×18			
			36.5 (dual)	14×8			
			89 (dual)	6×4			

1.2   Problems in space-borne microwave radiometer data

Besides the attenuation due to vegetation and atmosphere, there are other problems with passive microwave observations of surface water bodies, i.e. observation gaps and errors. Microwave radiometers are on-board sun-synchronous satellites, which are designed with constant viewing angle and to pass the same region twice each day (Hollinger et al., 1990). To monitor surface water bodies underneath vegetation canopies, observations during night or early morning are used, so that the canopy temperature is almost the same as surface temperature (Choudhury, 1989; Choudhury et al., 1990). This restriction on observation time implies that only ascending or descending orbit data (depending on the orbit configuration of satellites) can be used. Due to the limited swath of radiometers (for example around 1400km of SSM/I (Hollinger et al., 1990)), observations of one orbit data cannot cover the whole Earth within one day, which means gaps always occur in the time series of daily microwave observation, in particular for low latitude regions. Due to the orbit configuration of sun-synchronous satellites and earth rotation (Poe, 1990), consecutive gaps occur after each period of observations. Thus the time series of daily observation observed by space-borne radiometers with only one orbit direction is split into segments, i.e. gap segments and observation segments.

Due to the scan configuration of space-borne radiometers, the Instantaneous Field Of View (IFOV) of each scan cell does not cover exactly the same target during repeated scans, thus the orbit radiometer data needs to be registered into a grid system to make sure that the same target is consistently observed in the time series. The commonly used grid system for passive microwave data is the EASE-Grid (Brodzik and Knowles, 2002). During this registration, observation errors arise due to three factors: 1) geolocation uncertainty of the center of IFOV (around 6km according to Poe and Conway (1990)); 2) the spatial difference between IFOV of radiometers and grid cell, for example, the footprint of the SSM/I IFOV at 37 GHz is 37km×28km, while they are all registered into the 25km×25km EASE-Grid (Brodzik and Knowles, 2002) ; 3) resampling method, for example, weighted average for SSM/I orbit observations(Armstrong et al., 1998; Poe, 1990) and nearest neighbor method for AMSR-E orbit observations (Knowles et al., 2006). The first two factors are due to the configuration of space-borne radiometers and the last one is commonly defined as the registration and resampling error. Hereinafter, the errors from the three factors will be referred to as the observation error in daily pixel-wise radiometer observations. This error will be very large and cannot be neglected in inhomogeneous regions, such as coastal region and mountain area (Ferraro and Marks, 1995; Kummerow et al., 1996; Wentz, 2013).

So the raw time series of daily radiometer data is full of gaps and observation errors. In other cases (Hamilton et al., 2002, 1996, 2004; Sippel et al., 1994; Sippel et al., 1998), these two problems were solved by aggregating raw daily data over time and space: gap pieces can be filtered out by monthly compositing and observation errors can be mitigated by spatial averaging (Hamilton et al., 1996; Sippel et al., 1994). The detailed spatial and

temporal information about atmospheric and surface water content, however, is also filtered out by temporal compositing and spatial averaging

1.3   Relationship between inundated area and river discharge

Inundation patterns in space and time indicates changes in surface water storage, as a result of hydrological processes in a river basin. Long-term observations of surface water bodies derived from passive microwave observations can be used to study such patterns and understand better the hydrological processes in a river basin. For example, river stage is highly related to the total inundated area of the Amazon floodplain, thus it was possible to estimate the historical flooded area from river stage data since 1903 (Sippel et al., 1998). It has been shown that in the Mackenzie River basin, Canada, river discharge can be estimated from the fractional surface water area in the whole river basin by modifying the rating curve at the reference river section (Temimi et al., 2005).

Passive microwave observations are closely related to surface wetness conditions, thus they can be also directly used to estimate river discharge. For example, river discharge in Amazon floodplain was linearly estimated from the resampled and upstream-integrated PDBT at 37 GHz, which was obtained by calculating the weighted moving average of previous, current and lagged PDBT observations (Vörösmarty et al., 1996). After removing the influence of vegetation and the atmosphere by re-calibrating the 37 GHz brightness temperature of a river crossing pixel using a local land pixel away from the river as a reference (Brakenridge et al., 2007), the recalibrated pixels were used to estimate the river discharge with a certain rating curve.

The above studies clearly documented a time lag between inundated area and river discharge or stage-height, and this time lag changes in different catchments. The cross-correlation analysis between the 37 GHz PDBT and river stage-height in several catchments of the Amazon floodplain showed that the time lag between peaks of inundated area and river stages varied between 0 and 2 months, depending on the location of the catchment (Sippel et al., 1998). The modified PDBT by Vörösmarty et al. (1996) considers the temporal influence of inundated area on river discharge for the Amazon floodplain. In the study by Brakenridge et al. (2007), a time lag of 2 days occurred in the Wabash River, but no time lag was observed in the Red River. To take this time lag into account, a time factor was used to modify the rating curve and to estimate river discharge from inundated area retrieved from microwave observations in the Mackenzie River basin (Temimi et al., 2005).

These statistical analyses lead to the question how inundated area influences stream flow production in a river basin. As documented by Miller and Nudds (1996), changes of wetland area (i.e. the major form of inundated area in the studied floodplain) are closely related to changes of stream flow in the Mississippi River basin. It remains a challenge however, to relate quantitatively wetland changes, to stream flow variation, due to the

complicated processes involved in wetland hydrology and the difficulty to obtain detailed spatial data for whole river basin, such as soil properties. On the other hand, inundated area indicates water saturation conditions at top surface. In some conceptual hydrological models, such as the Xinganjiang model(Zhao, 1977, 1984), the Probability Distributed Model (PDM) rainfall-runoff model (Moore, 2007, 1985), the TOPMODEL (Beven and Kirkby, 1979; Beven et al., 1984), the Variable Infiltration Capacity (VIC) model (Liang et al., 1994; Wood et al., 1992) and the ARNO model (Todini, 1996), water saturated soil is the key parameter to estimate streamflow from precipitation. In a catchment, the depth of saturated soil varies with topography and water storage (Beven and Kirkby, 1979; Wood et al., 1992), while inundated area derived from passive microwave observation at 37 GHz is a surface feature. This difference implies that a new model needs to be developed to account for the role that inundated area plays in stream flow production, based on these current hydrological models. This new model (Chapter 5) aims at better understanding the influence of inundated area on the mechanism of stream flow in a river basin.

1.4   Problem statement

Our area of interest is large floodplains in the subtropical zone of China, i.e. the Poyang Lake floodplain and the Dongting Lake floodplain (Fig. 1.1), where dense population is threatened by frequent floods. The analysis articulated in the previous section leads to conclude that long-term daily or weekly observations of surface water body are very useful to study inundation patterns and to understand the hydrologic processes which determine such patterns. Observations of surface water bodies using optical and thermal sensors are limited by frequent clouds and precipitation and dense vegetation cover in our study area. Active microwave sensors, however, cannot supply daily or weekly observations covering such large floodplains. Microwave radiometers at 37 GHz are very suitable to observe inundation pattern in this subtropical zone, due to the capability to penetrate clouds and vegetation canopy, to the fast revisiting and to the large spatial coverage. Long-term data records at frequencies around 37 GHz and their free accessibility are also attractive (Table 1.3), especially to study the inundation pattern for a long period of time. Since microwave at 37 GHz senses a depth of roughly 0.8mm (Ulaby et al., 1981), it detects open water, inundated area and water saturated soil surface, i.e. the Water Saturated Surface (WSS).

The methods mentioned above for passive microwave observations of surface water bodies cannot be directly applied to observe daily inundated area in a subtropical zone, mainly due to the seasonality of vegetation and surface roughness. The method that uses the brightness temperature difference was developed by assuming that vegetation attenuation is constant in time and space at 37 GHz (Choudhury, 1989, 1991; Giddings and Choudhury, 1989). This assumption, however, does not hold for areas covered by seasonal vegetation. The clustering method used by Prigent et al. (2001b); and Prigent et al. (2007) can be only applied to a smooth surface. Within the same cluster of NDVI or backscatter values, surface emissivity and its polarization difference depend on both surface wetness and roughness. Variable surface roughness will change the emissivity and the polarization difference

emissivity of the water saturated and dry targets that are used to relate the retrieved emissivity to surface wetness, so this will enlarge the uncertainty in the clustering method (e.g. Prigent et al., 2001a; Prigent et al., 2001b; Prigent et al., 2007) and the linear models (e.g. Basist et al., 1998; Basist et al., 2001; Fily et al., 2003; Tanaka et al., 2003; Temimi et al., 2005). The effect of the variability in surface roughness on the linear relationship between surface wetness and emissivity has not been well studied in previous studies. Above all, a new method needs to be developed to retrieve surface emissivity underneath seasonal vegetation cover and to take variable surface roughness conditions into account for estimating surface wetness condition from the retrieved surface emissivity.
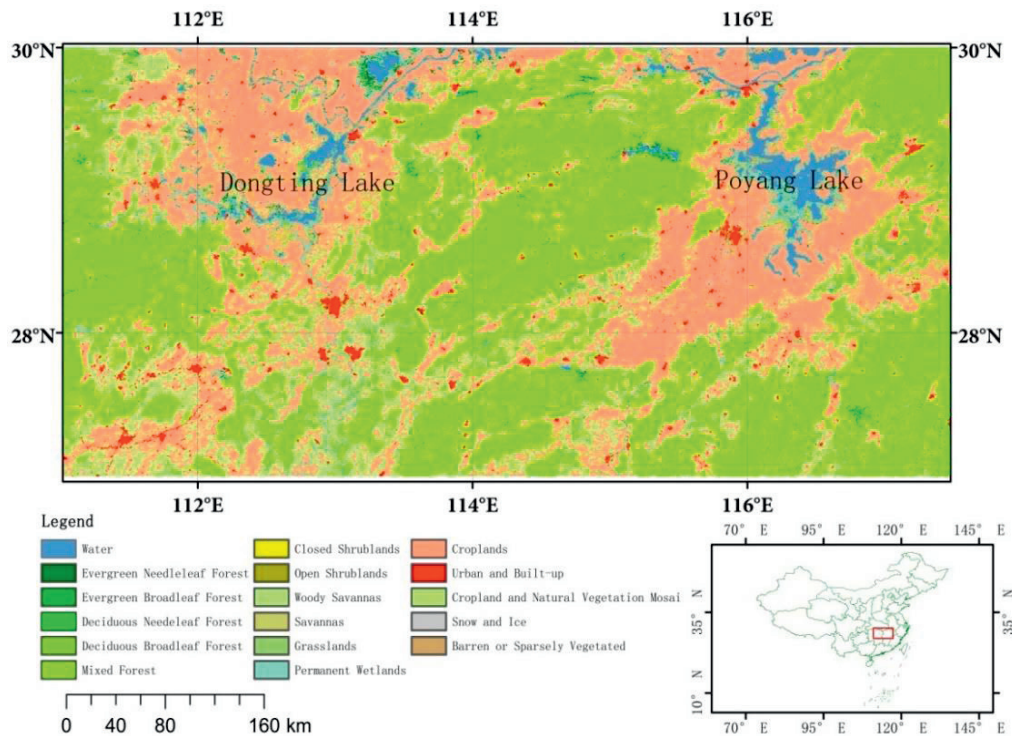
Figure 1.1: The land cover map of the Poyang Lake and Dongting Lake floodplains. The red rectangle in right-down map is the location of these two floodplains in China.

To observe surface water bodies with microwave radiometers, atmospheric influence, observation gaps and observation errors in passive microwave data need to be removed. Ancillary data on atmospheric water content, e.g. TIROS Operational Vertical Sounder (TOVS) products (Prigent et al., 1997; Rossow and Schiffer, 1999)), is needed to account for daily atmospheric water content, when to retrieve surface emissivity (e.g. Prigent, 2001b; Prigent et al., 2007). It is difficult, however, to obtain ancillary data simultaneously with the passing time of microwave radiometers (Prigent et al., 1997). Moreover, ancillary data has insufficient accuracy in the presence of clouds or rain (e.g. Behrangi et al., 2016;

Boukabara et al., 2010; Prigent et al., 1997; Reale et al., 2003). Besides the influence from atmospheric water content, observation gaps and geolocation errors are additional difficulties when analyzing consistent changes in surface conditions from microwave radiometer observations. The methods mentioned above, i.e. temporal compositing and space averaging, however, filter out detailed information on space and time variability captured by the original observations, and are not suitable to process daily observations. Thus a new method needs to be developed to solve these problems with less dependence on ancillary data and retaining the spatial and temporal resolution of the original microwave radiometer data.

The inundation pattern in the subtropical zones of this study, i.e. the evolution of WSS area in space and time, is closely related to monsoon and irrigation plans. Human impacts on inundation pattern are much more significant in the Poyang Lake and Donging Lake floodplains than those in the tropical forest regions. The rating curve or regression method between inundated area and river discharge that were applied in previous studies in the Amazon River basin (Sippel et al., 1998) and the Mackenzie river Basin (Temimi et al., 2005) may not be appropriate for the floodplains in our study area with extensive irrigation. Moreover, the WSS area cannot be directly used by the current hydrological models to study the relationship between WSS area and streamflow, due to the difference in the very shallow depth associated with WSS and the depth of water saturated soil as applied in hydrological models. To understand how inundation pattern influences stream flow production, a new model needs to be developed based on the mechanisms that are used in current conceptual hydrological models.

1.5   Research questions and objectives

To solve the problems outlined above, the research questions leading to this thesis are detailed as follow:

1.   *Is there a method to retrieve Water Saturated Surface from PDBT at 37 GHz taking the seasonality of vegetation cover and surface roughness into account?*

In the studies by Hamilton et al. (2002, 1996, 2004); Sippel et al. (1994); Sippel et al. (1998); Tanaka et al. (2003), PDBT at 37 GHz filtered out the up-welling atmospheric emittance but did not take seasonal vegetation, e.g. in a subtropical zone, into account. A radiative transfer model that includes a scatter model to simulate vegetation attenuation can be applied to retrieve Polarization Difference Effective Emissivity (PDEE) from the PDBT at 37 GHz. For example, in the zero-order radiative transfer model of (Choudhury, 1989, 1991), vegetation attenuation is quantified by vegetation optical thickness. There has been a lot of work on the parameterization of this optical thickness from satellite observations, such as Microwave Vegetation Index (MVI) (Shi et al., 2008), Leaf Area Index (LAI) (Wen et al., 2003) and Normalized Difference Vegetation Index (NDVI) (Gao et al., 2004). Previous work assumed that the observed area is fully covered by vegetation. Vegetation fractional cover, however, is variable in our study area, but can be

estimated from NDVI using a linear function. This parameter needs to be accounted for in the radiative transfer model. The relationship between monthly NDVI and PDBT at 37 GHz has been studied extensively for semi-arid vegetation, forest and grasslands (Choudhury, 1989, 1991; Choudhury and Tucker, 1987; Choudhury et al., 1990; Giddings and Choudhury, 1989). In semi-arid areas, the PDBT is negatively correlated with NDVI. This suggests that when soil moisture is rather stable, attenuation by vegetation can be obtained from NDVI. This idea will be extended in Chapter 2.

The relationship between PDEE and degree of soil water saturation at the sensed depth of microwave radiometers is the bridge connecting satellite observations with the regional soil water saturation condition at that depth. Taking the shallow sensed depth at 37 GHz and the spatial heterogeneity of soil water saturation conditions into account, the regional soil water saturation condition can be expressed as the fractional area of WSS (see section 2.3.4). The PDEE measured by a microwave radiometer is determined by the dielectric constant of a soil-water mixture and the surface roughness. The quasi-linear relationship between degree of soil water saturation and PDEE was first studied by De Ridder (2000) at 19 GHz by simulating soil emissivity of a smooth surface with a dielectric mixture model, i.e. Wang-Schmugge model (Wang and Schmugge, 1980). The dielectric constant of a soil-water mixture is, however, frequency dependent. Two types of dielectric mixture models, i.e. physical (e.g. Dobson model (Dobson et al., 1985)) and empirical (e.g. Wang-Schmugge model (Wang and Schmugge, 1980)) models, have been developed to relate the dielectric constant of soil-water mixture to soil properties. But their parameters are calibrated against the measurements at various frequencies, i.e. Wang-Schmugge model at 1.4 GHz and 5 GHz and Dobson model from 1.4 GHz to 19 GHz. At 37 GHz, the uncertainty in simulated PDEE by both Wang-Schmugge model and Dobson model is large, according to the measurements by Calvet et al. (1995). There is, however, no other study about the soil-water mixture model at 37 GHz, currently. Thus both Wang-Schmugge model and Dobson model will be applied to evaluate whether the linear relationship between PDEE and soil moisture still holds at 37 GHz. The influence of surface roughness on this linear relationship can be analyzed by introducing various surface roughness models, e.g. the Qh roughness model (Choudhury et al., 1979; Mo and Schmugge, 1987; Wang and Choudhury, 1981) or the Qp roughness model (Shi et al., 2005). Thus the possible linear relationship at 37 GHz for various rough surface can be evaluated by combining a soil-water mixture model and a surface roughness model.

2.   Is it possible to design a method to remove the atmospheric influence, observation gaps and errors in time series of microwave observations?

As mentioned above, a time series of microwave observations includes four component signals: the surface signal including surface emittance and vegetation attenuation, the atmospheric signal including the emittance and attenuation of atmospheric water content, observation gaps and observation errors (Shang et al., 2016). To derive the surface signal from the time series of microwave observations,

the Discrete Fourier Transform (DFT) (Agrawal et al., 1993; Keogh et al., 2001; Lin et al., 1995; Mörchen, 2003; Wu et al., 2000) can be used to identify the spectral features of component signals. Given its linear and multiplicative properties, the DFT of a time series of gappy-and-noisy microwave observations can be modeled as a weighted linear combination of the DFT of its component signals. Taking the PDBT observations at 37 GHz as an example, the spectral features of observation gaps and errors can be identified in the power spectrum of the PDBT time series, by properly modelling the time series of observation gaps and errors.

It is often assumed that the changes in atmospheric conditions are much faster than in surface conditions (see e.g. Prigent et al. (1997)), which gives the opportunity to separate the spectral features of atmospheric and surface signals. The spectral features of the atmospheric signal can be revealed by the time series of rain-gauge data, since the emittance and scattering of atmospheric water content at 37 GHz is mainly due to the hydrometeors (Choudhury et al., 1992). The surface emittance, however, is also influenced by precipitation. Studies on field-measured soil moisture show that the soil moisture signal is dominated by seasonal changes (see e.g. Entin et al. (2000); Skøien et al. (2003); Vachaud et al. (1985); Vinnikov et al. (1996); Wilson et al. (2004)), i.e. the characteristic time scale of soil moisture in top 10 cm is 1 to 2.4 months. On the other hand, ground-measured precipitation time series do show an annual component but no significant seasonal changes (Skøien et al., 2003), with much larger short-term periodic variations than soil moisture (D'Odorico and Rodríguez-Iturbe, 2000), i.e. closer to a random process. Thus, the power spectrum of precipitation time series can be used to identify the frequency range associated with the large but short-term periodic variations in the atmospheric signal.

According to the spectral range of each component signal, various filter designs, e.g. boxcar filter (Lee et al., 1998; Nerem et al., 1999), can be applied to remove the spectral features in a specific frequency range. The spectral features of some component signals may be located in a similar frequency range. For example, the spectral features of the atmospheric signal may be located in a frequency range that also includes spectral features of the surface signal. If the spectral features of these two signals overlap (i.e. have same frequencies), we cannot separate the amplitude contribution of these signals. Thus, we assume that in the frequency rang where the atmospheric and surface signals overlap, the spectral features derived from the rain-gauge time series are all associated to the atmospheric signal and the remaining spectral features to the surface signal. The Harmonic ANalysis of Time Series (HANTS) algorithm (Menenti et al., 1993; Verhoef, 1996) can model the time series according to the user-defined harmonic components. Thus, the identified spectral features of the surface signal can be used by HANTS algorithm to reconstruct the surface signal from PDBT time series and remove the influence of the atmospheric signal in the PDBT time series. Above all, with a new hybrid method, named as Time Series Analysis Procedure (TSAP), the noisy component signals in the PDBT time series can be removed and the surface signal can be extracted.

3.   ***Is it possible to build up a new rainfall-runoff model that applies the retrieved WSS to model the surface water balance?***

The WSS area is the result of processes at the surface including precipitation, evapotranspiration, regional water storage and drainage. It determines the partition of precipitation into overland and infiltrated flows at the surface (Beven and Kirkby, 1979; Liang et al., 1994; Sivapalan et al., 1987; Wood et al., 1992). Overland flow reaches directly channels and rivers, while infiltrated flow is stored by soil layers and gradually released into channels and rivers. The VIC model simulates stream flow as the sum of direct runoff (i.e. overland and fast subsurface flow) and base flow (i.e. slow water flow released by soil layers and ground water) (Wood et al., 1992). The infiltration capacity parameter and regional water storage, which are used by the VIC model to identify the fast and slow water flows, are difficult to be estimated or calibrated. On the other hand, the daily WSS retrieved from PDBT at 37 GHz is an indicator of the changes of regional water storage and evapotranspiration and determines the partition of each antecedent precipitation at the surface. It is possible to modify the structure of VIC model to use the WSS area.

The catchment response to rainfall includes the partition of precipitation into different water flows and the drainage of precipitation into rivers and channel. Conceptual hydrological models, e.g. VIC, simplified the quantification of precipitation contribution to stream flow. Some statistical models, e.g. the two component linear model by Jakeman and Hornberger (1993); Jakeman et al. (1990), show that this quantification can also be estimated by a time series method, e.g. a recursive linear regression, according to the relationship between the time series of stream flow and precipitation. To fully use the high frequency and long-term observations of WSS, the physical basis of the VIC model is combined with the time series method, to simulate stream flow and understand the role that the WSS plays in the catchment response to rainfall.

Accordingly, the research objectives of this thesis are:

1.   ***To retrieve the daily fractional area of Water Saturated Surface in large floodplains from PDBT at 37 GHz***

2.   ***To extract the surface signal from PDBT time series by removing the atmospheric influence, observation errors and gaps***

3.   ***To develop a new rainfall-runoff model to simulate stream flow with the retrieved WSS***

1.6   Thesis outline

There are other six chapters besides Chapter 1 Introduction. Their contents are summarized below.

Chapter 2 introduces the two-step model to retrieve the fractional WSS area from PDBT at 37 GHz: 1) the radiative transfer model to retrieve the PDEE from PDBT at 37 GHz; 2) the linear model to derive the fractional WSS area from the retrieved PDEE. The 1st research question will be addressed through the development of the simplified radiative transfer model that takes the fractional vegetation cover into account and is used to parameterize vegetation optical thickness based on the studies on PDBT and NDVI in flooded paddy fields. The relationship between WSS and PDEE is determined by numerical analysis combining soil-water-mixture models and a surface roughness model. Both physical and empirical models, i.e. the Dobson model (Dobson et al., 1985) and the Wang-Schmugge model (Wang and Schmugge, 1980), will be applied to evaluate the impact of model uncertainty on estimated dielectric constant of a soil-water mixture at 1.4 GHz, 19 GHz and 37 GHz (Calvet et al., 1995) and more specifically whether the linear relationship between soil moisture and PDEE depends on different models and frequencies. A surface-roughness model, i.e. Qp model (Shi et al., 2005), is used to analysis the influence of surface roughness on the linear relationship. The linear model to retrieve the fractional WSS area from PDEE is then derived based on the above analyses.

Chapter 3 addresses the 2nd research question by using Discrete Fourier Transform (DFT) and harmonic analysis. A numerical model is developed to mimic a time series of gappy-and-noisy PDBT observations. The spectral features of the PDBT time series are analyzed for each component signal, given the linear and multiplicative properties of DFT. Based on that, a hybrid method, the Time Series Analysis Procedure (TSAP), was developed and includes two steps: 1) identify the spectral ranges of observation gaps and errors according to the spectral analysis of the numerical model and filter them out by a modified boxcar filter; 2) identify the spectral features of the atmospheric signal according to the spectral analysis of rain-gauge time series and remove them by the Harmonic ANalysis of Time Series (HANTS) algorithm. The spectral features of the surface signal can be identified by excluding the spectral features of the atmospheric signal in the power spectrum of PDBT time series. We then applied the HANTS algorithm to reconstruct the surface signal, using these spectral features to remove the atmospheric signal. The statistical evaluation of this hybrid method is also demonstrated.

Chapter 4 presents a case study on inundation patterns in the Poyang Lake and Dongting Lake floodplains using the methods described above. The overall method to retrieve WSS from PDBT combines the TSAP and the two-step model and is evaluated by comparing the retrieved WSS area in Poyang Lake with the lake area observed by MODerate-resolution Imaging Spectroradiometer (MODIS) and Advanced Synthetic Aperture Radar (ASAR). This overall method will be applied to the whole Poyang Lake floodplain to study the relationship between the lake extension and WSS area in upstream. The evolution of WSS area in the Poyang Lake and Dingting Lake floodplains will be demonstrated in a dry and wet year respectively, in order to study the relationship between WSS area, precipitation and stream flow and the possibility of using WSS area for flood early warning.

Chapter 5 addresses the 3rd research question. A discrete rainfall-runoff model was developed to fully use the retrievals of WSS from 37 GHz PDBT. This model is based on

the redistribution of antecedent precipitation in a certain period and the water balance equation. Three implementations of the model are developed with increasing complexity, using the retrievals and the observed ground water table depth to reduce the duration required to achieve a reasonable performance. The three levels are defined by the key-variables as: 1) precipitation and base flow; 2) overland, infiltrated and base flows; 3) overland, potential subsurface and base flows. The set of model parameters can be calibrated with a linear regression method and metrics for model performance are illustrated.

Chapter 6 introduces a case study on modelling stream flow with the three implementations of the discrete rainfall-runoff model and the retrieved WSS in Xiangjiang River basin. The three implementations of the discrete rainfall-runoff are calibrated for dry (2005) and wet (2002) years and validate in a relative wet year (2001). Cross validation method is applied in the calibration period to evaluate whether over-fitting occurs when the duration is increased step-wisely. The application of this model is also aimed to study how WSS influences the catchment response to precipitation.

Chapter 7 summarizes the major developments and results in the thesis and outlines the perspectives.

Chapter 2

The two-step model

2.1 Introduction

The brightness temperature measured by microwave radiometers can be modeled as a linear combination of emittance and scattering from surface, vegetation, and atmosphere on the basis of radiative transfer theory (Mätzler, 2006). Surface emittance is determined by surface effective emissivity and temperature, of which the former is related to soil moisture and surface roughness. In wet areas the surface emittance is dominated by the, Water Saturated Surface (WSS), i.e. the sum of open water, inundated area and water saturated soil surface, due to the shallow detected depth at 37 GHz (0.08mm - 8mm). To retrieve the WSS fractional area from microwave observation, vegetation and atmospheric influence needs to be estimated or removed. The influence from atmospheric water content will be dealt with in Chapter 3, thus this chapter focuses on quantifying vegetation scattering and attenuation, especially for a water surface under seasonal vegetation cover. The relationship between soil moisture and surface emissivity can be expressed by a linear model (see e.g. Basist et al., 1998; Choudhury, 1991; Fily et al., 2003; Prigent et al., 2001b; Prigent et al., 2007; Sippel et al., 1994; Temimi et al., 2005). The linear relationship at 37 GHz and at rough surface, however, has not been well studied yet. This chapter will evaluate the linear relationship at 37 GHz under various surface roughness conditions.

The influence of vegetation canopy on the radiation emitted or reflected by the surface may be simulated with various scattering models, such as the zero-order scattering model (Kirdiashev et al., 1979; Wigneron et al., 1993), the single-scattering model (Tsang et al., 1982) and the multi-scattering model (Wiesmann and Mätzler, 1999).The differences among these models lie in the complexity in the radiation scattering by vegetation canopy. In many studies on the observation of inundated area with microwave radiometers, a zero-order scattering model was applied (e.g. Basist et al., 1998; Choudhury, 1989). In this

chapter, the zero-order radiative transfer model is simplified to retrieve the Polarization Difference Effective Emissivity (PDEE) from microwave observations at 37 GHz. In areas partially covered by vegetation, it is difficult to quantify the absorption and scattering of vegetation layers, which may change seasonally in subtropical zones. The Polarization Difference Brightness Temperature (PDBT) at 37 GHz shows an opposite trend to the Normalized Difference Vegetation Index (NDVI) on surface wetness and vegetation conditions in semi-arid regions (Choudhury, 1989, 1991). This implies that the vegetation influence, i.e. vegetation coverage and optical thickness, on PDBT at 37 GHz can be related to NDVI. If vegetation would be the only factor to determine changes in PDBT, paired observations of PDBT and NDVI could be used with a zero-order radiative transfer model to estimate the vegetation influence.

The retrieved surface effective emissivity or its polarization difference is assumed to be linearly related to the wetness or water saturated soil surface (see e.g. Basist et al., 1998; Choudhury, 1991; Fily et al., 2003; Prigent et al., 2001b; Prigent et al., 2007; Sippel et al., 1994; Temimi et al., 2005). Polarization Difference Emissivity (PDE), i.e. the difference between horizontally and vertically polarized emissivity, was preferred in many cases (e.g. Choudhury (1991); Fily et al. (2003); Prigent et al. (2001b); Prigent et al. (2007); Tanaka et al. (2003); Temimi et al. (2005)), since it filters out the up-welling atmosphere emittance. Owe et al. (2001) proved that the PDE at 19 GHz is quasi-linearly related to degree of soil water saturation, using the Wang-Schmugge model (Wang and Schmugge, 1980) to simulate the dielectric constant of a soil-water mixture. The dielectric constant of a soil-water mixture, however, depends on frequency, while there is no numerical model developed for 37 GHz yet. The Wang-Schmugge model is an empirical dielectric mixture model developed for L and C bands. On the other hand, the Dobson model (Dobson et al., 1985), as a semi-physical model, developed and validated for 1.4 GHz – 18 GHz, thus possibly applicable at higher frequencies, e.g. 19 GHz. The experiment by Calvet et al. (1995), however, shows that the uncertainty of both the Dobson model and the recalibrated Wang-Schmugge model is large at 37 GHz. It needs to be evaluated whether the linear relationship between degree of soil water saturation and PDE still holds at 37 GHz or at least whether is model dependent. To mitigate the impact of these uncertainties in the soil-water mixture models at 37 GHz, we applied both the Wang-Schmugge model and the Dobson model at 1.4 GHz, 19 GHz and 37 GHz. The trend in the simulated PDE vs. soil water saturation at these frequencies, may help us determine which model may be applied at 37 GHz and whether the linear relationship still holds at 37 GHz.

In previous studies (see e.g. Owe et al. (2001); Prigent et al. (1997)), the surface was assumed to be smooth. In reality, at the same surface water content, the emissivity of a rough surface is lower than the one of a smooth surface. The surface property retrieved from microwave radiometric data is the effective emissivity, i.e. the emissivity attenuated by surface roughness. It is not clear yet whether the linear relationship between degree of soil water saturation and surface emissivity still holds when surface roughness is taken into account. There are many surface roughness models developed, such as Qh model (Choudhury et al., 1979; Mo and Schmugge, 1987; Wang and Choudhury, 1981), Qp model (Shi et al., 2005) and so on. Among them, the Qp roughness model can simulate the

effective emissivity at 37 GHz (Shi et al., 2005) and is applied to evaluate the influence of surface roughness on the linear relationship in this chapter. Based on this relationship, a linear model to retrieve fractional area of WSS from the Polarization Difference Effective Emissivity (PDEE) will be derived, which takes the shallow sensed depth at 37 GHz and the spatial heterogeneity of soil water saturation conditions into account.

A two-step model is developed in this chapter, to retrieve the fractional area of WSS from PDBT at 37 GHz in a region covered by seasonal vegetation and with various surface roughness conditions. The model includes two steps: the 1st step to retrieve PDEE from PDBT using a simplified radiative transfer model; the 2nd step to retrieve the fractional area of WSS from the PDEE with a linear model. In section 2.2, the zero-order radiative transfer model was simplified to apply to PDBT observations at 37 GHz. The methods to determine model parameters, especially those related to the vegetation influence, are also described. In section 2.3, the linear model is derived from the numerical analysis of the relationship between soil moisture and surface emissivity. The Dobson model and Wang-Schumgge model were applied to a smooth surface to study the relationship between the PDEE at 1.4 GHz, 19 GHz and 37 GHz, and degree of soil water saturation. PDEE at 37 GHz was calculated with the Qp roughness model to evaluate the relationship for a rough surface. In section 2.4, the parametrization of the two-step model for the area with seasonal vegetation and given surface roughness conditions is explained and a case study on the Poyang Lake floodplain is developed. Vegetation types, the irrigation schedule applied to paddy fields and surface roughness of the study area are illustrated. The data set, i.e. microwave brightness temperature and NDVI, are described, including the procedure to bin each set of observations into the same grid system to parameterize the vegetation influence. The conclusions are summarized in section 2.5

2.2 Retrieving the Polarization Difference Effective Emissivity

2.2.1 The zero-order radiative transfer model

The zero-order radiative transfer model assumes that the total polarized scattered radiation through a vegetation canopy is zero along the direction of wave propagation, and only single interactions between vegetation and the soil surface are taken into account. This model was first derived by Kirdiashev et al. (1979), and was also called the 'ω-τ' model by Wigneron et al. (1995). According to the Rayleigh-Jeans approximation, radiation measured by a microwave radiometer can be linearly related to the brightness temperature. Neglecting the atmospheric radiation scattered by vegetation in the zero-order model, Choudhury (1989) modeled the brightness temperature at the top of vegetation canopy, i.e. T_{BS}, as:

$$T_{BS}(p,\theta) = \epsilon(p,\theta) \times t_v \times T_s + \left[1 + t_v \times \Gamma(p,\theta)\right] \times \left[1 - \omega_p\right] \times (1 - t_v) \times T_v + \Gamma(p,\theta) \times t_v^2 \times T_d \qquad (2.1)$$

where p is the polarization, θ is the incidence angle, T_s and T_v are the temperature of the soil surface and vegetation respectively, T_d is the down-welling brightness temperature of atmosphere; $\epsilon(p,\theta)$ is the surface emissivity at polarization p and with incidence angle θ, $\Gamma(p,\theta)$ is the surface reflectivity at polarization p with incidence angel θ, according to the Kirchhoff's law:

$$\epsilon(p,\theta) + \Gamma(p,\theta) = 1 \qquad (2.2)$$

ω_p is the single scattering albedo at polarization p

$$\omega_p = \frac{\gamma_s}{\gamma_e} \ , \quad \gamma_e = \gamma_a + \gamma_s \qquad (2.3)$$

where γ_a is the absorption, γ_s the scattering and γ_e the extinction coefficient of the layer between the soil surface and vegetation respectively, and t_v is the transmission function of the vegetation canopy

$$t_v = \exp\left(\frac{-\tau_v}{\cos\theta}\right) \qquad (2.4)$$

where τ_v is the optical depth (also called optical thickness) of the vegetation canopy.

The measured brightness temperature by space-borne microwave radiometers at the top of atmosphere, i.e. T_B, is

$$T_B(p,\theta) = T_{BS}(p,\theta) \times t_a + T_u \qquad (2.5)$$

where T_u is the up-welling brightness temperature of atmosphere and t_a is the transmission function of atmosphere

$$t_a = \exp\left(\frac{-\tau_a}{\cos\theta}\right) \qquad (2.6)$$

where τ_a is the optical depth of atmosphere. The influence of the atmosphere will be explained in Chapter 3. In the following text, atmosphere is assumed to be transparent, i.e. $t_a=1$.

2.2.2 The simplified radiative transfer model

The brightness temperature for horizontal or vertical polarization measured by microwave radiometers includes the emittance from vegetation canopy and atmosphere, besides the surface emittance. The zero-order radiative transfer model can be simplified for observations at 37 GHz. Atmospheric emittance is not the signal we are targeting for land

surface studies and we assumed is un-polarized, i.e. the same magnitude for horizontal and vertical polarization. Under this assumption, the up-welling atmospheric brightness temperature is filtered out by using the difference between the vertically and horizontally polarized brightness temperature, i.e. PDBT. In the night or early morning it can be assumed that surface temperature is the same as vegetation temperature, i.e. $T_v = T_s$, and the reflected fraction of vegetation brightness temperature (emittance) scattered by the surface is very small, i.e. $\Gamma(p,\theta) \times \omega_p \ll 0$ (Choudhury, 1989). Thus, according to Eq. (2.1), Eq. (2.2) and Eq. (2.5), PDBT, i.e. ΔT, at 37 GHz can be written as:

$$\Delta T = T_B(V,\theta) - T_B(H,\theta)$$
$$= (\omega_H - \omega_V) \times (1 - t_v^2) \times T_{sv} + [\Gamma(H,\theta) - \Gamma(V,\theta)] \times (t_v \times T_{sv} - t_v^2 \times T_d) \tag{2.7}$$

where T_{sv} is the temperature of the soil-vegetation system. The above equation expresses the PDBT from an area fully covered by vegetation. For areas with partial vegetation cover, the PDBT can be expressed as:

$$\Delta T = (1 - f_v) \times [\Gamma(H,\theta) - \Gamma(V,\theta)] \times T_{sb}$$
$$+ f_v \times \left[(\omega_H - \omega_V) \times (1 - t_v^2) \times T_{sv} + [\Gamma(H,\theta) - \Gamma(V,\theta)] \times (t_v \times T_{sv} - t_v^2 \times T_d) \right] \tag{2.8}$$

where f_v is the fractional area of vegetation and T_{sb} is the temperature of bare soil. If only the microwave observation during night or early morning is used, it can be assumed that $T_{sb} = T_{sv}$. According to the field measurements by Pampaloni and Paloscia (1985), the difference of vertically and horizontally polarized single scattering albedos is very small. Thus $\omega_H - \omega_V$ can be neglected in Eq. (2.8). The down-welling atmospheric emittance, i.e. Td, can be removed through the methods described in Chapter 3. Eq. (2.8) can then be simplified as:

$$\Delta T = [f_v \times t_v + (1 - f_v)] \times \Delta\epsilon \times T_s \tag{2.9}$$

where T_s is the surface temperature, $\Delta\epsilon$ is the difference of vertical and horizontally polarized emissivity

$$\Delta\epsilon = \epsilon(V,\theta) - \epsilon(H,\theta) = \Gamma(H,\theta) - \Gamma(V,\theta) \tag{2.10}$$

If the surface is smooth, $\Delta\epsilon$ is the PDE; if the surface is rough, $\Delta\epsilon$ is the PDEE. Equation (2.10) is derived according to Eq. (2.2).

2.2.3 Parameter derivation

To calculate PDEE from PDBT at 37 GHz with Eq. (2.9), surface temperature, fractional area of vegetation and vegetation transmission function need to be estimated. T_s can be obtained from the vertically polarized brightness temperature $T_{B,37V}$ at 37 GHz (Holmes et al., 2009):

$$T_s = 1.11 \times T_{B,37V} - 15.2 \qquad (2.11)$$

According to Gutman and Ignatov (1998), the fractional area of vegetation, i.e. f_v, can be estimated from the observed *NDVI*:

$$f_v = \left(NDVI - NDVI_{soil} \right) \big/ \left(NDVI_{veg} - NDVI_{soil} \right) \qquad (2.12)$$

where $NDVI_{soil}$ is the NDVI value of bare soil, and $NDVI_{veg}$ is the value of full vegetation cover. We assumed $NDVI_{soil} = 0$, since water saturated surface is observed. The $NDVI_{veg}$ is set as 0.60, the same as that of shrub land (Montandon and Small, 2008).

The vegetation transmission function, i.e. t_v, is determined by the vegetation optical thickness τ_v in Eq. (2.4). τ_v may be a linear function of NDVI (Vandegriend and Owe, 1993). Thus, Eq. (2.4) can be modified as:

$$t_v = \exp\left(-\sigma \times NDVI \right) \qquad (2.13)$$

where σ is the coefficient to relate vegetation optical thickness to NDVI at incidence angle θ.

The opposite fluctuations of the time series of NDVI and PDBT in arid areas (Choudhury and Tucker, 1987) suggest that when surface temperature and wetness are constant, the ΔT changes only due to vegetation influences, i.e. fractional vegetation cover and optical thickness. To derive vegetation optical thickness, Eq. (2.9) is modified as:

$$\Delta T = \Delta T_S \times \left[\left(1 - f_v \right) + f_v \times \exp\left(-\sigma \times NDVI \right) \right] \qquad (2.14)$$

where $\Delta T_s = T_s \times \Delta \epsilon$, which is the PDBT of surface. The coefficient "σ" in Eq. (2.14) can be determined with a set of observations where ΔTs is constant and ΔT changes only with f_v. Because fv can be estimated from NDVI by Eq. (2.12), the only undetermined parameters in Eq. (2.14) are two constants: ΔT_s, and coefficient "σ". Thus by regressing the variable NDVI with its dependent variable ΔT using Eq. (2.14), the coefficient "σ" can be estimated. Paddy fields in flooding periods fit our assumptions and are used to determine this coefficient (see Sect. 2.4.2).

2.3   Relationship between WSS and surface emissivity

2.3.1 Dielectric constant of a soil-water mixture

Surface emissivity is determined by the dielectric constant of a soil-water mixture, i.e. ε, which depends on soil moisture and frequency. Both empirical and physical models, e.g. Wang-Schmugge model (Wang and Schmugge, 1980) and the Dobson model (Dobson et al., 1985), have been developed to simulate the dielectric constant of a soil-water mixture, but for frequencies not higher than 18 GHz. Currently, there is no soil-water mixture model

developed at 37 GHz yet, and both physical and empirical models lead to large uncertainty in the simulation of soil emissivity at 37 GHz (Calvet et al., 1995). To mitigate the impact of model uncertainty, in this study, both the Wang-Schmugge model (Wang and Schmugge, 1980) and the Dobson model (Dobson et al., 1985) were used to estimate the PDE at 1.4 GHz, 19 GHz and 37 GHz.

2.3.1.1   Wang-Schmugge model

In the Wang-Schmugge model, the dielectric constant of a soil-water mixture, i.e. ε, is parameterized as:

$$\begin{cases} W_c \leq W_t, \varepsilon = W_c \left(\varepsilon_i + \left(\varepsilon_w - \varepsilon_i \right) \frac{W_c}{W_t} \gamma \right) + \left(PS - W_c \right) \varepsilon_a + \left(1 - PS \right) \varepsilon_r \\ W_c > W_t, \varepsilon = W_t \left(\varepsilon_i + \left(\varepsilon_w - \varepsilon_i \right) \gamma \right) + \left(W_c - W_t \right) \varepsilon_w + \left(PS - W_c \right) \varepsilon_a + \left(1 - PS \right) \varepsilon_r \end{cases} \quad (2.15)$$

where PS is porosity of dry soil, ε_a, ε_w, ε_r, and ε_i, are the dielectric constants of air, fresh water, rock and ice respectively. γ is the parameter used to fit the equation with experimental data; W_c is the soil moisture content (cm³ cm⁻³); W_t is the transition moisture (cm³ cm⁻³), before and after which, the dielectric constants of a soil-water mixture is increasing.

Table 2.1: The dielectric constant of ice, air and rock used by the Wang-Schmugge model

	ε'	ε''
ice	3.2	0.1
air	1	0
rock	5.5	0.2

Table 2.2: The dielectric constant of fresh water at three frequencies

Frequency	1.4 GHz	19 GHz	37 GHz
$\varepsilon'_w=$	79.3	39.2	18.8
$\varepsilon''_w=$	6.0	37.1	28.7

According to the measurements by Calvet et al. (1995), $\gamma = 0.81$, and $W_t = 0.17$ at 36.5 GHz, which are used at 37 GHz. PS of dry soil was assumed to be 0.5. The dielectric constants of ice, air and rock are given in Table 2.1. The dielectric constant of fresh water, i.e. ε_w, changes with frequency (Table 2.2), and is determined by the model developed by Liebe et al. (1991); Manabe et al. (1987).

2.3.1.2   Dobson model

In Dobson model, the dielectric constant of a soil-water mixture is parameterized as:

$$\varepsilon^{\alpha} = 1 + \left(1 - PS\right)\left(\varepsilon_s^{\alpha} - 1\right) + W_c^{\beta}\varepsilon_w^{\alpha} - W_c \tag{2.16}$$

where W_c is the soil moisture content (cm³ cm⁻³); $\alpha = 0.65$ is the shape factor; β is a coefficient depending on the soil-texture

$$\beta_{\varepsilon'} = \frac{\left(127.48 - 0.519S - 0.152C\right)}{100} \tag{2.17}$$

$$\beta_{\varepsilon''} = \frac{\left(133.797 - 0.603S - 0.166C\right)}{100} \tag{2.18}$$

where S and C is the percentage of sand and clay respectively; ε_w is the dielectric constant of fresh water calculated from a modified Debye equation (Lane and Saxton, 1952) under different frequencies (also applicable at 37 GHz), which can be referred to Dobson et al. (1985); ε_s is the dielectric constant of dry soil and is set as 4.5 at frequencies between 1.4 GHz and 18 GHz, according to Dobson et al. (1985), which does not change with frequency and thus can be used at 37 GHz. A silt loam soil is used in this numerical analysis with 13.5% clay and 30.6% sand, thus β can be determined through Eq. (2.17) and Eq. (2.18). The major uncertainty in the Dobson model at 37 GHz lies in the parameters α and β according to Calvet et al. (1995). In this case, we need to verify whether α and β calibrated against the measurements from 1.4 GHz to 18 GHz can be applicable to estimate the PDE at 37 GHz. Thus, PDE at 1.4 GHz and 19 GHz, which is assumed to be reliable with Dobson model, is also calculated and helps us interpret the model performance at 37 GHz.

The difference between the Wang-Schmugge and the Dobson model lies in the theoretical basis. The Wang-Schmugge model is a linear mixture of the soil components' dielectric constants. It uses the wilting point to describe maximum bound water fraction, while the Dobson model used the double-layer model (Dobson et al., 1985) to describe the Debye type relaxation of a soil-water mixture. The Dobson model, however, is a linear mixture of the components' dielectric constants to the power α, which is obtained from field measurements. From a theoretical point of view, the Dobson model describes better the dielectric constant at higher frequencies, e.g. 19 GHz, because it accounts for the imaginary loss of microwave radiance at higher frequencies.

2.3.2 The linear relationship at a smooth surface

The difference of vertical and horizontal polarized emissivity (i.e. PDE) can be calculated from surface reflectivity (Eq. (2.10)). Reflectivity of a smooth surface is derived from the Fresnel Equation:

$$\Gamma_{s,s}(H,\theta,\upsilon) = \left| \frac{\cos\theta - \sqrt{\varepsilon_\upsilon - \sin^2\theta}}{\cos\theta + \sqrt{\varepsilon_\upsilon - \sin^2\theta}} \right|^2 \tag{2.19}$$

$$\Gamma_{s,s}(V,\theta,\upsilon) = \left| \frac{\varepsilon_\upsilon \times \cos\theta - \sqrt{\varepsilon_\upsilon - \sin^2\theta}}{\varepsilon_\upsilon \times \cos\theta + \sqrt{\varepsilon_\upsilon - \sin^2\theta}} \right|^2 \tag{2.20}$$

where ε_υ is the dielectric constant of a soil-water mixture at frequency υ; $\Gamma_{s,s}(H,\theta,\upsilon)$ and $\Gamma_{s,s}(V,\theta,\upsilon)$ is horizontally (*H*) and vertically (*V*) polarized reflectivity respectively at smooth surface, with the incidence angel θ at frequency υ.

PDE at 1.4 GHz, 19 GHz and 37 GHz is modelled with Eq. (2.10) where the polarized reflectivity is calculated with Eq. (2.19) and Eq. (2.20). The dielectric constant at the corresponding frequency is calculated from the Wang-Schmugge model (Eq. (2.15)) and the Dobson model (Eq. (2.16)) respectively. A silt loam soil is used in this numerical analysis with 13.5% clay and 30.6% sand, since it is the major soil type in the middle stream of the Yangtze River basin. Simulations by both models show (Fig. 2.1) that a quasi-linear relationship exits at all frequencies, but with different slopes and intercepts. The Wang-Schmugge model gave a very similar slope at different frequencies: the PDE increased from 0.17 with volumetric soil moisture, reaching a plateau at $\Delta\epsilon = 0.3$, when the volumetric soil moisture was close to 0.255 cm^3 cm^{-3} (Fig. 2.1a), which is the field capacity of the silt loam soil according to De Ridder (2000). The simulations with the Dobson model show that the parameters of the quasi-linear relationship depend on frequency: The plateau $\Delta\epsilon$ had a very similar value around 0.3, at all three frequencies (Fig. 2.1b); at 1.4 GHz $\Delta\epsilon$ increased from 0.16 and reached the plateau $\Delta\epsilon$ when soil volumetric moisture close to 0.14 cm^3 cm^{-3}. At 19 GHz $\Delta\epsilon$ starts to increase from 0.15 and reaches the same plateau when soil volumetric moisture is around 0.26 cm^3 cm^{-3}, wetter than that at 1.4 GHz; At 37 GHz, $\Delta\epsilon$ around 0.14, lower than other two frequencies, and reaches the plateau when soil moisture is close to 0.5 cm^3 cm^{-3}, i.e. totally water saturated.

(a)   (b)
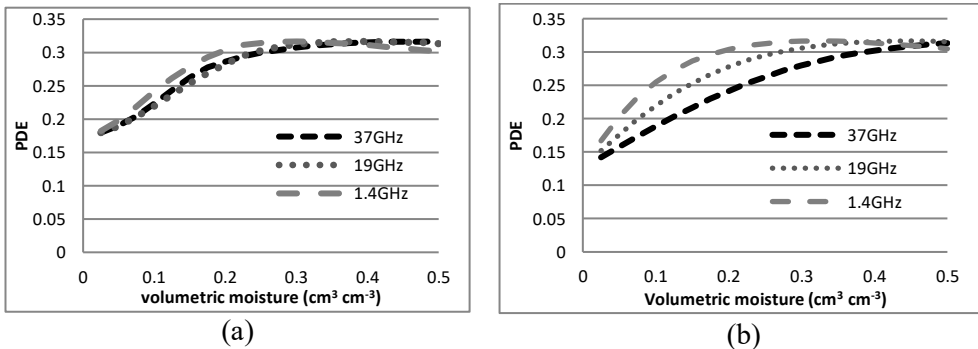
Figure 2.1: The simulated Polarization Difference Emissivity (PDE) vs. volumetric soil moisture for silt loam soil. Simulations by Wang-Schmugge model (a) and by Dobson model (b)

The Dobson model suggests that only at higher frequencies the relationship is close to a linear model, while Wang-Schmugge model gives similar quasi-linear relationships at all frequencies. It is interesting that linear or quasi-linear relationships occur at all frequencies in both model simulations and the plateau $\Delta\epsilon$ is almost constant for different frequencies, though Dobson model gives a frequency dependent slope and intercept $\Delta\epsilon$.

The difference between the Wang-Schmugge model and Dobson model is due not only to their physics basis, as explained in the previous section, but also to different calibration schemes. The parameters in the Wang-Schmugge model were calibrated against measurements of soil-water mixtures at 1.4 GHz, 5 GHz and at 36.5 GHz by (Calvet et al., 1995), while the parameters in the Dobson model were calibrated against measurements at frequencies from 1.4 GHz to 18 GHz. The Dobson model overestimated the surface emissivity for both polarizations at 37 GHz, which leads to a maximum bias of 0.09 in the PDE, while, the maximum bias in the PDE at 37 GHz using the Wang-Schmugge model is around 0.05 (Calvet et al., 1995). The experiment done by Sippel et al. (1994), however, illustrates that the PDBT at 37 GHz is sensitive to the area of water saturated surface (i.e. volumetric soil moisture ≥ 0.5 cm^3 cm^{-3}), not to the area of soil surface with moisture beyond the field capacity (i.e. volumetric soil moisture ≥ 0.26 cm^3 cm^{-3}). This indicates that the linear relationship in the Dobson model is closer to reality than the Wang-Schmugge model. Besides that, the simulation with Dobson model at 1.4 GHz and 19 GHz, of which the parameters are calibrated from measurements and thus are assumed to be reliable, strongly indicates that the slope of the linear relationship decreases with increasing frequencies. At 37 GHz, only the simulation with Dobson model fit this trend. Thus, in the next section, we used the Dobson model to estimate the PDEE of a rough surface.

2.3.3 The linear relationship at a rough surface

PDEE is calculated from PDE by taking the surface roughness into account. The Qp roughness model calculates the effective reflectivity as:

$$\Gamma^*\left(p,\theta,\upsilon\right)=Q_p\left(\upsilon\right)\times\Gamma_{s,s}\left(q,\theta,\upsilon\right)+\left[1-Q_p\left(\upsilon\right)\right]\times\Gamma_{s,s}\left(p,\theta,\upsilon\right) \tag{2.21}$$

where $\Gamma^*(p,\theta,\upsilon)$ is the effective reflectivity at frequency υ at p polarization and incidence angle θ; $Q_p(\upsilon)$ is a roughness parameter. According to (Shi et al., 2005), for υ=37 GHz, $Q_p(37\ GHz)$ is calculated from $Q_p(10.65\ GHz)$ as

$$Q_p\left(37GHz\right)=\alpha_p+\beta_p\times Q_p\left(10.65\ GHz\right) \tag{2.22}$$

where α_p and β_p are the coefficients obtained by applying the Advanced Integral Equation Model (AIEM). The surface roughness parameter at 10.65 GHz, i.e. $Q_p(10.65\ GHz)$, is calculated as:

$$\ln\left[Q_p\left(10.65\ GHz\right)\right]=a_p+b_p\times\ln\left(s/l\right)+c_p\times\left(s/l\right) \tag{2.23}$$

where a_p, b_p and c_p are coefficients estimated from AIEM simulations at 10.65 GHz (Shi et al., 2005) and s/l is the ratio of r.m.s.[1] height to correlation length, which is the roughness property of surface.

According to Eq. (2.10) and Eq. (2.21), PDEE, i.e. $\Delta\epsilon^*$, is then calculated:

$$\Delta\epsilon^* = \left[1 - \left(Q_H + Q_V\right)\right] \times \Delta\epsilon \tag{2.24}$$

The $\Delta\epsilon$ given by Dobson model should be reliable at higher frequencies, because the model parameters are derived from field measurements at 19 GHz. Thus, the Dobson model is used to calculate $\Delta\epsilon$ in Eq. (2.24). The linear relationship between $\Delta\epsilon^*$ and soil moisture still occurs as shown in Fig. 2.2, though the intercept $\Delta\epsilon^*$ and the plateau $\Delta\epsilon^*$ are roughness dependent. The s/l value represents the surface roughness: smaller s/l value means a smoother surface. The slope decreases with increasing roughness. This suggests that the linear model to retrieve WSS from PDEE needs to take surface roughness into account.
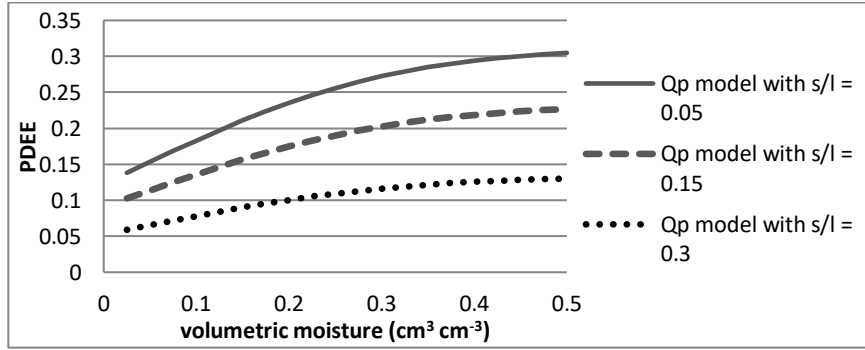
Figure 2.2: Polarization Difference Effective Emissivity (PDEE) vs. volumetric soil moisture at 37 GHz

2.3.4 The linear model to retrieve fractional area of WSS

Through the numerical analysis in the above subsections, it can be concluded that soil moisture, i.e. W_c, is quasi-linearly related to PDEE at 37 GHz. According to the linear relationship shown in Fig. 2.2, the water saturation condition at surface can be linearly related to PDEE as:

$$\frac{W_c}{W_{sat}} = \frac{\Delta\epsilon^* - \Delta\epsilon_{dry}^*}{\Delta\epsilon_{sat}^* - \Delta\epsilon_{dry}^*} \tag{2.25}$$

---

[1] r.m.s: root mean square

where W_{sat} (cm^3 cm^{-3}) is the volumetric soil moisture when it is totally water saturated, normally as 0.5 cm^3 cm^{-3}; $\Delta\epsilon_{dry}{}^*$ and $\Delta\epsilon_{sat}{}^*$ are the PDEE of a completely dry and water saturated soils respectively.

Water Saturated Surface (WSS) is the area where the soil moisture exceeds the field capacity. Taking the spatial heterogeneity into account, the fractional abundance of WSS in the whole pixel, i.e. f_{ss}, can be expressed as:

$$f_{ss} = \sum_{i=1}^{i=ns} f_{si} \times \frac{W_i}{W_{sat}} = \frac{W_c}{W_{sat}} \tag{2.26}$$

where f_{si} is the fractional area of a sub-pixel with a volumetric soil moisture W_i (cm^3 cm^{-3}); ns is the number of sub-pixel areas.

In Eq. (2.26), spatial heterogeneity of soil water saturation condition in one pixel region is represented by the various soil moistures in the subpixels. The regional water saturation condition is calculated as the sum of the saturation conditions in each sub-pixel fraction with the same soil moisture (Eq. (2.26)). The fractional area and the degree of soil water saturation of each sub-pixel in Eq. (2.26) can be exchanged with each other, since both can be taken as a weight factor of the other (both range from 0 to 1). Thus in Eq. (2.26), the fractional area of WSS has the same meaning as the regional water saturation condition. Inserting Eq. (2.25) into Eq. (2.26), the fractional area of WSS can be derived from PDEE as:

$$f_{ss} = \frac{\Delta\epsilon^* - \Delta\epsilon_{dry}^*}{\Delta\epsilon_{sat}^* - \Delta\epsilon_{dry}^*} \tag{2.27}$$

This linear model also holds when lower frequencies are used to retrieve PDEE, such as at 19 GHz.

2.4   Parameterization of the two-step model

To apply the two-step model to retrieve the fractional area of WSS, the vegetation transmission function (Eq. (2.13) and in Eq. (2.14)) and the PDEE of a completely dry and water saturated soils in Eq. (2.27) needs to be estimated first. Our study area in this thesis is the Dongting Lake and the Poyang Lake floodplains, located in the middle reach of the Yangtze River basin. These two floodplains are in the subtropical zone and influenced by the same monsoon system, thus the vegetation types and their phenology in these two floodplains are similar. The Poyang Lake floodplain is used as an example to explain the parameterization of the two-step model in this section. The results will be used for further applications of the two-step model in both floodplains, as shown in Chapter 4 and Chapter 6.

2.4.1 Vegetation and roughness conditions

2.4.1.1   Vegetation condition

The *Poaceae* are the major vegetation type in the Dongting Lake and Poyang Lake floodplains, including rice, *Phragmites* and other grasses. It can be assumed that the vegetation influence in these two floodplains can be derived from the flooded paddy fields, due to the similar structure of the *Poaceae*. Rice is the major crop in the region and paddy fields are planted with double-cycle rice in these two flood plains. About 73% of annual water consumption is used for irrigation (Ye et al., 2013). Paddy fields are flooded in specific periods of the rice growing season (Table 2.3 and Li et al. (2012)). Normally, between two subsequent flooding periods, there is a long dry period. Thus, the irrigated paddy fields can be taken as flooded or water-saturated area and the un-irrigated paddy fields can be taken as dry soil. The fractional area of paddy fields does not change year by year due to the control of rice production according to local statistical records[2], and rice growth demands for a precise irrigation schedule. This implies that PDEE will be approximately constant during the flooding periods. The land surface temperature T_s will change in a small range in the early morning or night of the flooding periods (since only early morning and night observations are used), because of the relative high thermal capacity of water. Thus we assume that ΔT_s averaged over flooding periods of paddy fields does not change in Eq. (2.16), and the only factor that change PDBT is the vegetation influence, i.e. the fractional vegetation abundance and vegetation optical thickness.

---

[2] Statistical yearbook of Jiangxi Province, China

Table 2.3: Duration of each stage (days) of rice growth cycle and their flooding conditions

	Period of seeding establishment	early period of tillering	late period of tillering	booting stage	earing stage	milk stage	yellow ripening stage
early rice	18	18	13	15	12	9	15
late rice	6	18	14	21	11	12	26
flooding condition	flooded or early period is flooded, later period is drying	flooded	flooded or drying	flooded	Flooded	wet	drying

2.4.1.2 Roughness condition in the Poyang Lake

The PDEE of dry and water saturated surface is influenced by surface roughness. This roughness may be due to topography, human activities (e.g. cultivation and land management), and wind. The first two factors are assumed to yield time-invariant surface roughness. The geomorphy of the Poyang Lake floodplain (Fig. 2.3) is introduced first to understand the historical records of wind speeds around the lake area. Poyang Lake and its flood plain are surrounded by mountains. The shape of the Poyang Lake floodplain looks like a quadrangle, with its northern edge facing to the North-West and southern edge facing to the South-East. The east and west edges are almost parallel (Fig. 2.3). The mean north-south distance is about 140 km and mean east-west distance is about 120 km. The lake has an irregular shape — it is located in the central floodplain and its East boundary is elongated in the same way as the East edge of the floodplain, with an N–S distance of about 100 km and E – W distance of about 80 km. The lake connects to the Yangtze River to the North through a funnel shape area, with wide mouth to the South and narrow head to the North. Thus, in lake area, a North – South wind blows on most days. Only in July and August, the monsoon from the Indian Ocean forces a South – North wind. The connecting funnel area yields a higher wind speed in the narrow head to the North and the wind speed will decrease from North to South over the floodplain, after passing through this connecting area.

Thus, the highest mean wind speed occurs in the northern Poyang Lake, with annual mean wind speed between 3.0 m s^{-1} and 4.0 m s^{-1} from 1998 to 2007. In the center of lake area, the mean wind speed is reduced to 2.0 – 3.0 m s^{-1}. In the southern Poyang Lake 58% of the wind speeds measured at the Boyang weather station is less than 2.0 m s^{-1} and 97% is less than 4.0 m s^{-1}. According to the polarimetric sea surface emissivity model developed by Wentz (1992), the difference between PDDE retrieved from flat open water surface and from open water surface with the wind speed $\leq$ 4.0 m s^{-1} is $\leq$ 0.017, much less than the reduction in PDEE induced by the roughness in soil (Fig. 2.2). Thus, we assume that in the driest condition of a pixel area including open water surface and land surface, the roughness of open water surface in Poyang Lake is almost constant and the overall roughness of the pixel area is due to the roughness of land surface. At the Nanchang meteorology station, in the South of the lake, the mean wind speed is only 1.7 m s^{-1}. So, in this study, the impact of wind on land surface roughness has been assumed negligible, and the major determinants of surface roughness are topography and human activities.
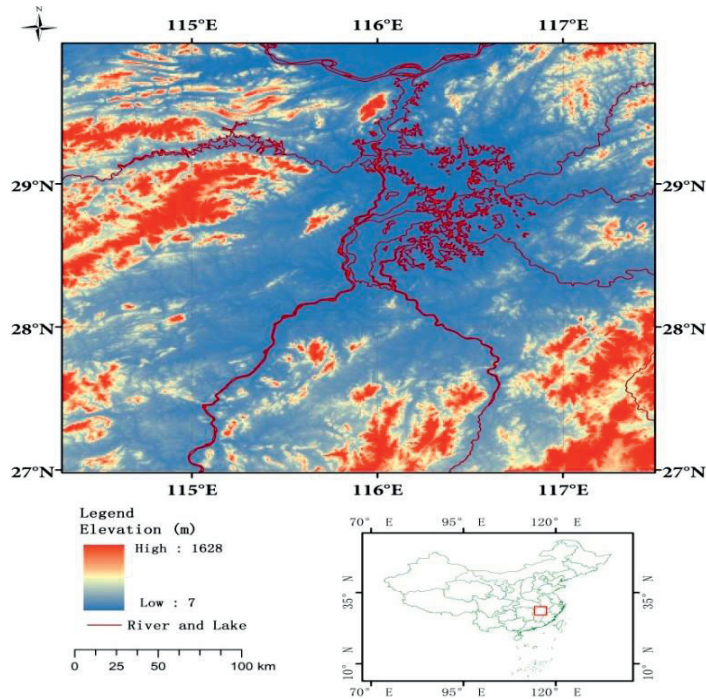
Figure 2.3: DEM map of the Poyang Lake floodplain. The red rectangle in the right-down map is the location of the Poyang Lake floodplain in China.

2.4.2 Data set

To parameterize the vegetation transmission function with Eq. (2.14), PDBT observations at 37 GHz are needed and both fractional vegetation abundance and vegetation optical thickness are estimated from NDVI in Eq. (2.14). Currently, there are two sensors providing measurements around 37 GHz with dual polarization: the Special Sensor Microwave Imager (SSM/I) and The Advanced Microwave Scanning Radiometer for EOS (AMSR-E). In this case the SSM/I on board the Defence Meteorological Satellite Program (DMSP) F13 satellites was used. Detailed information about the sensor is given in Chapter 4. The SSM/I brightness temperature has been inter-calibrated with that of AMSR-E and both are registered into the EASE-Grid system. NDVI was aggregated from MODIS data. In order to choose a reliable data set, two MODIS datasets were compared first: the MOD09A1 8-day composite surface reflectance data of bands $1 - 7$, and the MOD13A2 16-day composite NDVI data. The spatial resolution of the reflectance dataset is 500 m, while the NDVI dataset is 1 km. Because of the non-linear dependence of NDVI on red and near-infrared reflectance, the surface reflectance was averaged first over a 25 km×25 km EASE-Grid (a common grid system used for microwave radiometer data) and then used to calculate the NDVI. On the other hand, MOD13A2 was directly aggregated to the 25

km×25 km NDVI. The aggregation from NDVI (i.e. MOD13A2) and from the aggregated reflectance (i.e. MOD09A1 with the spatial resolution of 500 m) does not show large difference for the paddy fields, when cloud influence is small (Fig. 2.4). This only applies to crop land. For other land types with large spatial heterogeneity, the NDVI for the EASE-Grid needs to be aggregated from MOD09A1. The data quality of MOD13A2 is much better than MOD09A1, i.e. without sudden low values (cloud contaminated samples) in Fig. 2.4. MOD13A2 data has been corrected for differences in the satellite view angle based on MOD09A1, thus large off-nadir and forward-scattering view angle and large solar zenith angles are avoided in MOD13A2. To guarantee the observation quality, MOD13A2 is used to parameterize the vegetation transmission function.
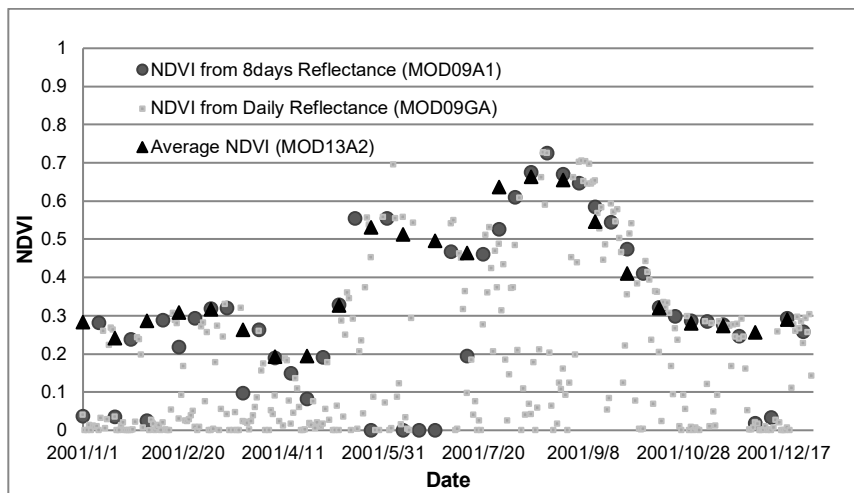
Figure 2.4: Time series of spatially aggregated NDVI of paddy fields from MOD09A1, MOD09GA and MOD13A2, respectively, in 2001. The paddy fields are located within the pixel numbered as 1 in Fig. 3.2

2.4.3 Parameterization of the vegetation transmission function

Large paddy fields are located downstream of the Ganjiang River basin near the Poyang Lake (Li et al., 2012; Torbick et al., 2011). Pixels with a large fraction of flooded paddy fields fit the assumptions to derive the coefficient of vegetation transmission function using NDVI and PDBT observations. During each rice cropping season in 2001 (one from March to July and the other from July to October according to the NDVI time series of Fig. 2.5), there was a large peak in the PDBT time series in the early stage. This indicates the sowing time and the start of irrigation of the paddy fields, since the PDBT increase with WSS. The flood duration is about 50 days according to the irrigation schedule in Table 2.3. It covers several stages of rice phenology and includes 3 or 4 observations of the 16-day composites NDVI data. Since the irrigation schedule is similar across fields, the surface temperature and PDEE can be taken as constant during these 50 days at the observation time (early morning). Thus, the measured PDBT is only affected by the

vegetation fractional abundance and the optical thickness. The vegetation fractional area can be calculated from NDVI by Eq. (2.12). The vegetation optical thickness, which determines the scattering and absorption of the surface emittance by vegetation, can be parameterized by NDVI using the vegetation transmission function Eq. (2.13). The simplified radiative transfer model Eq. (2.14) was developed to account for this.
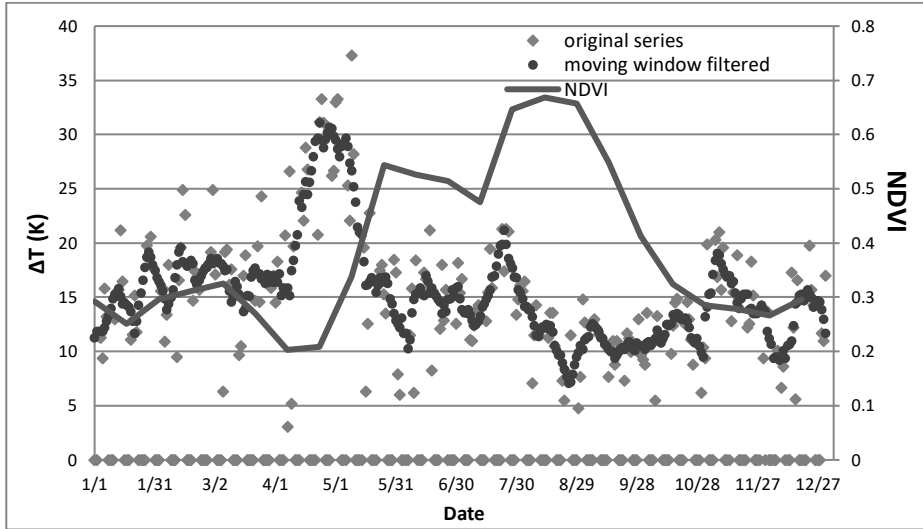
Figure 2.5: Time series of original PDBT, boxcar filtered PDBT and NDVI at paddy fields in 2001. The paddy fields are located within the pixel numbered as 1 in Fig. 3.2

To get sufficient observations to estimate the coefficients in Eq. (2.14), NDVI data and the corresponding boxcar-filtered PDBT data (see Chapter 3) of one EASE-Grid pixel area (25km×25km, with the center located at 28.3807° N and 115.8351° E) were chosen during the rice flooding periods from 2001 to 2003 (Fig. 2.6), since most of this area is covered by paddy fields and the total rice area in this region shows little variability during these three years. By fitting the data points with Eq. (2.14), a regression equation was derived as shown in Fig. 2.5: the ΔT_s in Eq. (2.14) is 26.9 K and the coefficient σ is 1.23179. Thus, the vegetation transmission function, i.e. Eq. (2.13), is:

$$t_V = \exp\left(-1.23179 \times NDVI\right) \tag{2.28}$$

In this regression, Eq. (2.11) was not used to calculate the land surface temperature, because the model uncertainty of Eq. (2.11) might be introduced into the derivation of the vegetation transmission function. The uncertainty of this regression is highly dependent on the model to identify vegetation fractional area from NDVI. The linear and quadratic models (Carlson and Ripley, 1997; Gutman and Ignatov, 1998) were compared. When the same setting of $NDVI_{veg}$ and $NDVI_{soil}$ as described in section 2.2.3 was used, the Root Mean Square Error (RMSE) of our regression obtained with the quadratic model was 3.2 K, higher than the RMSE of linear model, i.e. 2.8 K in Fig. 2.6.

The uncertainty of vegetation fractional cover model in Eq. (2.12) has little influence on this regression. Different settings of $NDVI_{soil}$ = -0.05, 0, and 0.05 were applied, which is the major uncertainty in Eq. (2.12) according to Montandon and Small (2008). The RMSE of the regression model varied only from 2.7 K to 2.8 K. Because there is no field measurement of NDVI for flooded soil, which could have negative values close to water, $NDVI_{soil}$ is set equal to 0. Different settings of NDVI value of full vegetation coverage, i.e. $NDVI_{veg}$ around 0.6, lead to negligible variation in RMSE of the regression model. We can find that when NDVI>0.6, ΔT in the regression model (Fig. 2.6) changes much smoother than when NDVI<0.6. This indicates that under dense vegetation coverage when NDVI is saturated (e.g. NDVI>0.7), vegetation attenuation can be taken as homogeneous at 37 GHz. This finding agrees with the previous studies of 37 GHz PDBT observations in tropical forest area (e.g. Choudhury, 1989, 1991).
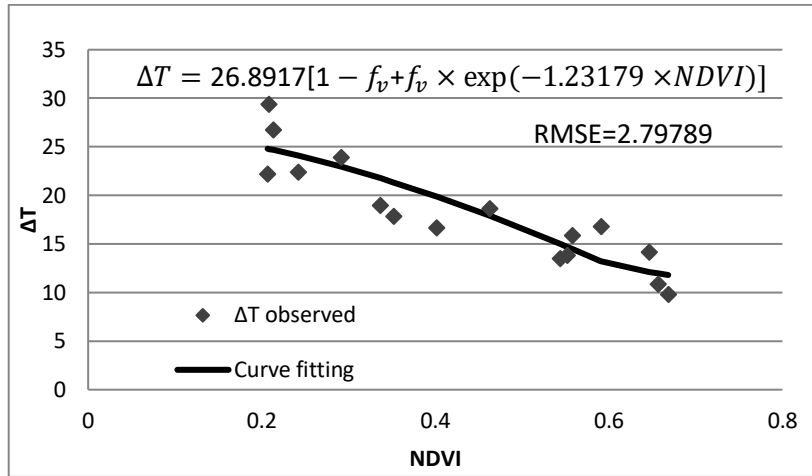
Figure 2.6: Scatter plots of ΔT and corresponding NDVI observations and the result of curve fitting

2.4.4 Parameterization of the linear model

To derive the linear model expressed by Eq. (2.27), the PDEE of dry and water-saturated surface needs to be identified. A common method is to assume that the maximum value in the time series of PDEE retrieved from PDBT with Eq. (2.9) represents the total water-saturated surface (e.g. De Ridder, 2000). The roughness parameter, i.e. s/l, can be identified by optimizing Eq. (2.24) with the PDEE and PDE of a totally water-saturated surface. This method, however, may not be applicable to all the pixels in a floodplain, since large spatial heterogeneity of surface moisture in each pixel may not fit the assumption. Thus the PDEE of dry and water-saturated surface was estimated in the Poyang Lake area to derive the global optimized values for the Dongting and Poyang Lake flood plains. According to Choudhury (1989) the PDEE of dry soil was calculated as 0.091. Its surface roughness was calculated from an open water area by Choudhury (1989) with

corresponding $s/l = 0.175$. The PDEE of the flooded paddy fields in Fig. 2.6, however, was close to 0.1 (the land surface temperature is assumed to 270 K). This suggests that the land surface is much rougher than open water, thus s/l was set as 0.25, with corresponding $\Delta\epsilon_{dry}^*$ = 0.068. For water totally-saturated soil, it can be assumed that $\Delta\epsilon_{sat}^*$ is the same as standing water — 0.21 given by Choudhury (1989). The pixels in the floodplain contain both land surface and water surface, thus Eq. (2.27) is expressed as:

$$f_{ss} = \left(\Delta\epsilon^* - 0.068\right)\big/\left(0.21 - 0.068\right) \tag{2.29}$$

2.5   Conclusions

This chapter introduced the two-step model to retrieve the fractional area of WSS from PDBT at 37 GHz for an area with seasonal vegetation cover and corresponding surface roughness. It includes two sub models: 1) the simplified radiative transfer model to retrieve PDEE from PDBT at 37 GHz; 2) the linear model to retrieve fractional abundance of WSS from PDEE. The zero-order radiative transfer model was simplified with the assumption that the scattering between vegetation and surface can be neglected. The fractional vegetation cover was introduced into the simplified model. The derivation of parameters for this model was explained in detail. For the vegetation transmission function of the vegetation canopy, paired observations of PDBT at 37 GHz and NDVI at the flooded paddy fields were used to estimate the coefficient in the function.

The linear model to derive WSS from PDEE was built according to the numerical analysis of the relationship between soil moisture and PDEE. In this numerical analysis, two soil-water mixture models, i.e. Wang-Schmugge model and Dobson model, were used first to calculate PDE of a smooth surface. It is found that soil moisture was quasi-linearly related to PDE at frequencies between 1.4 GHz and 37 GHz, whatever soil-water mixture model were used. Increasing surface roughness would smooth but not change the quasi-linear relationship between soil moisture and PDEE. Taking the spatial heterogeneity into account, the fractional area of WSS was derived from PDEE with the linear model. The PDEE of the dry and water-saturated surfaces was estimated for Poyang Lake floodplain. The two-step model will be evaluated as one component model in the overall method as shown in Chapter 4.

Chapter 3

Time Series Analysis Procedure

3.1 Introduction

Microwave radiometers, e.g. Special Sensor Microwave Imager (SSM/I) and Advanced Microwave Scanning Radiometer for EOS (AMSR-E), are typically on-board sun-synchronous satellites and conically scan the surface with a swath less than 1500 km and a constant incidence angle (see e.g. Hollinger et al. (1990); Kawanishi et al. (2003)). The configuration of satellite orbit and scanning leads to observation gaps in a time series of daily microwave observation. Especially when daily observations in only one-orbit direction are used, regularly spaced gaps split the time series into segments. A continuous time series of daily microwave observations in a region is derived by resampling orbit data into a grid system (e.g. Armstrong et al. (1998); Knowles et al. (2006); Prigent et al. (1997)), since the Instantaneous Field Of View (IFOV) of each scan cell does not cover exactly the same region during subsequent scans (Poe, 1990). Observation errors will be introduced after resampling by the geo-location uncertainty in the center of IFOV (e.g. around 6km for SSM/I in Poe and Conway (1990)), by spatial difference between IFOV and grid cell, and by various resampling methods (e.g. Armstrong et al. (1998); Knowles et al. (2006)). These types of errors can have a very large impact when observing coastal regions, lake-land boundaries and mountain areas (Ferraro and Marks, 1995; Kummerow et al., 1996; Wentz, 2013). Besides these two kinds of systematic noise, a time series of microwave radiometer observations carries the information about surface emittance, vegetation attenuation, atmosphere emittance and atmospheric attenuation. The surface signal includes the former two items and the atmospheric signal includes the latter two.

Surface emittance at microwave frequencies is positively related to surface wetness condition (Ulaby et al., 1981), e.g. the fractional area of Water Saturated Surface (WSS), i.e. water saturated soil and inundated area. Thus, in order to retrieve WSS from microwave observations, influences of vegetation and atmosphere need to be removed. Vegetation influence can be removed by combining data acquired by multiple satellite instruments – microwave radiometers, and optical and IR sensors (see e.g. Prigent et al. (2001a); Prigent et al. (2001b); Prigent et al. (2007); Shang et al. (2015)), as shown in Chapter 2. In this chapter, a hybrid method is developed to extract the surface signal, after removal of the atmosphere influence, observation errors and gaps from a time series of daily microwave observations.

The capability in penetrating clouds and the spatial resolution of a microwave radiometer both depend on the frequency (Ulaby et al., 1981), but in an opposite way, i.e. lower frequencies have higher penetrating capability but lower spatial resolution, while higher frequencies have higher spatial resolution but influenced more by atmosphere and vegetation. Thus microwave frequencies not higher than Ka band (26.5 GHz – 40 GHz) are normally used to monitor surface wetness conditions (e.g. Kerr et al. (2001); Njoku et al. (2003); O'Neill et al. (1993); Paloscia et al. (2001); Wang and Choudhury (1981)). Observation at 37 GHz, is preferred to observe inundated area (e.g. Choudhury (1989); Giddings and Choudhury (1989); Hamilton et al. (2002, 1996, 2004); Sippel et al. (1994); Sippel et al. (1998); Tanaka et al. (2003)), due to its higher spatial resolution than lower frequencies, while retaining sufficient sensitivity to surface wetness. In our previous study (Shang et al., 2015) and chapter 2, the fractional area of WSS was retrieved using the Polarization Difference Brightness Temperature (PDBT) observations at 37 GHz, taking the vegetation influence and surface roughness into account. Atmosphere influence on observations at 37 GHz is significant, especially during rainy days (Choudhury et al., 1992; Shang et al., 2015). Observation errors cause a larger variability in daily PDBT at 37 GHz at lake-land boundaries (e.g. above 40 K in Fig. 3.1b) than that of monthly averages on inundated areas (e.g. 20 K in the Pantanal by Choudhury (1991)). To eliminate the temperature difference between surface and vegetation canopy, only night or early-morning data at 37 GHz, i.e. in one-orbit direction, are used to retrieve WSS, which leads to large amount of observation gaps (Fig. 3.1). Thus noise due to the combination of atmosphere influence, observation gaps and errors must be removed prior to apply 37 GHz PDBT time series to retrieve inundated area.
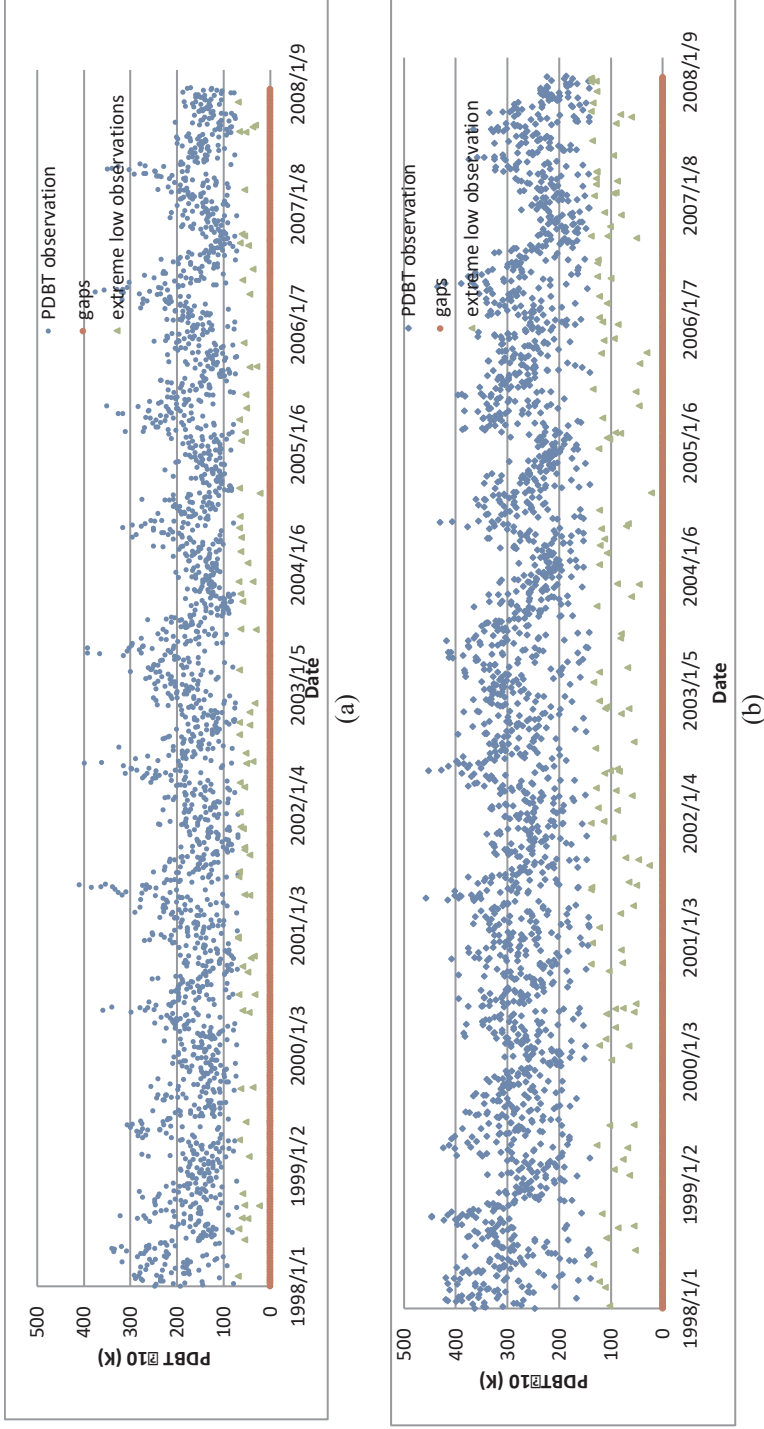
Figure 3.1: The Raw space-borne Polarization Difference Brightness Temperature (PDBT) time series at the 1st (a) and 2nd (b) sample pixels from 1998 to 2007. The dominant land cover of the 1st sample pixel is farm land, centered at 28.603°N and 115.835°E. The dominant land cover of the 2nd sample pixel is open water and wetland, centered at 29.049°N and 116.356°E. Their locations are shown in Fig. 3.2

In other studies (Giddings and Choudhury, 1989; Hamilton et al., 2002, 1996, 2004; Sippel et al., 1994; Sippel et al., 1998), systematic noise was removed by aggregating raw daily data over time and space: gaps can be filled by monthly compositing and observation errors can be mitigated by spatial averaging. The detailed spatial and temporal information about atmospheric and surface water content, however, is also filtered out by temporal compositing and spatial averaging. Atmosphere influence on monthly data can be reduced by two different approaches. The first one is a statistical composition method, i.e. to select the second lowest value in each month as an indicator of the monthly surface wetness condition, e.g. Hamilton et al. (2002, 1996, 2004); Sippel et al. (1994). The second approach is to use ancillary data about atmospheric and land surface properties from other satellites (e.g. cloud fraction and Land Surface Temperature (LST) from International Satellite Cloud Climatology Project (ISCCP), and atmospheric temperature and total precipitable water from TIROS Operational Vertical Sounder (TOVS) products (Prigent et al., 1997; Rossow and Schiffer, 1999)) to parameterize the atmosphere influence on emittance at 37 GHz with a radiative transfer model (Prigent et al., 1997) or to apply a neural network inversion method (Aires et al., 2000). For daily time series, the first method is not applicable and the second one gives estimates of surface emittance of insufficient accuracy in the presence of clouds or rain (e.g. Behrangi et al. (2016); Boukabara et al. (2010); Prigent et al. (1997); Reale et al. (2003)).

This chapter develops a hybrid method, named "Time Series Analysis Procedure (TSAP)", to extract the surface signal from a noisy time series of daily pixel-wise PDBT observations at 37 GHz by filtering out atmosphere signal, observation gaps and errors. TSAP includes two stages: 1) to identify the spectral range related to observation errors and gaps and filter them out with a boxcar filter; 2) to identify the spectral features of the atmospheric signal by applying Discrete Fourier Transform (DFT) analysis of precipitation time series and filter them out with the Harmonic ANalysis of Time Series (HANTS) algorithm. TSAP is based on the feature extraction from time series with DFT (Agrawal et al., 1993; Keogh et al., 2001; Lin et al., 1995; Mörchen, 2003; Wu et al., 2000), commonly used in data mining. EASE-Grid SSM/I 37 GHz brightness temperature data (Armstrong et al., 1998) acquired in the early morning pass was used in this chapter to illustrate the problems, to explain the proposed method and to validate it. Section 3.2 introduced the theory of DFT and its properties. Section 3.3 described the study area and data set used in this study. Section 3.4 illustrated the implementation of TSAP in detail and analyzes the mitigation of the noise present in the raw (unfiltered) time series. In Section 3.5 a case study on Poyang Lake was presented to evaluate TSAP by analyzing the accuracy in the retrieval of the WSS area before and after applying TSAP. Discussion about TSAP and its performances was articulated in Section 3.6. Conclusions were summarized in Section 3.7.

3.2 Theoretical background of the Time Series Analysis Procedure

3.2.1 General

A time series of daily 37 GHz PDBT consists of observation gaps and errors, atmospheric and surface signals. More precisely the atmospheric signal includes atmosphere emittance and attenuation, while the surface signal includes surface emittance and vegetation attenuation. According to the linear and multiplicative properties of DFT, the spectral properties of component signals can be revealed in the power spectrum of the mixed signal, i.e. the PDBT time series. Once the spectral features of each component signal are identified, a proper filter method can be designed to extract the surface signal.

The frequency range associated with observation gaps can be easily identified in the power spectrum of a time series of daily 37 GHz PDBT observations obtained in one-orbit direction. Observation errors are commonly assumed to yield a white noise (see e.g. Harris (1978)), while a high frequency periodic component in the DFT of the PDBT time series can be noted (Fig. 3.3). To evaluate these findings, a numerical model was developed (see sect. 3.2.4) to mimic observation gaps and errors. By analyzing the synthetic signal generated with the model and the PDBT time series, it was found that the signal components associated with observation gaps and errors are in the higher frequency region. Thus, A boxcar filter is applied to remove the high frequency components (see e.g. Nerem et al. (1999)), mainly due to its high coherent gain and narrow equivalent noise bandwidth, compared with other window –based filters (Harris, 1978). The high scallop loss of a boxcar filter is mitigated by using long-term time series of daily observations. The boxcar filter was modified according to the number of gaps in the PDBT time series (see Sect. 3.4.2). The transfer function of the modified boxcar filter will be evaluated later on.

It is often assumed that the changes in atmospheric conditions are much faster than in surface conditions (see e.g. Prigent et al. (1997)). This gives an opportunity to separate the atmospheric and surface signals by means of an appropriate filter, provided the associated spectral features can be identified. In our previous study (Shang et al., 2015), it is noted that atmosphere attenuation on PDBT time series at 37 GHz is almost synchronous with precipitation observed on ground, which agree with the findings in Choudhury et al. (1992), where it was noted that the precipitation rate is positively related to the water depth of hydrometeors that mainly contributes to atmosphere emittance and attenuation at 37 GH. This led to the idea of estimating the frequency range associated with the atmospheric signal by analyzing a time series of rain-gauge data. The risk of this approach is that precipitation also causes changes in soil moisture, which is the major factor controlling the surface signal (Choudhury, 1989, 1991). Studies on field-measured soil moisture in the extratropics, however, show that the moisture variations in top 1 meter have high auto-correlation within a time lag between 1 to 2.5 month, which is the characteristics time scale of soil moisture (see e.g. Entin et al. (2000); Skøien et al. (2003); Vachaud et al. (1985);

Vinnikov et al. (1996); Wilson et al. (2004)). The characteristic time scale of soil moisture in top 10 cm is 1 to 2.4 months, slightly less than that in 1 meter (Entin et al., 2000). This long-memory of soil moisture is defined as time stability by Vachaud et al. (1985), which is determined by the field capacity of soil and evapotranspiration. Though the detected depth of 37 GHz (around 8.2mm) is much shallower than the depth of field measurements mentioned, the small difference in the characteristic time scale of soil moisture between 10 cm and 1m indicates the time scale of soil moisture in such shallow surface layer would be comparable, albeit slightly shorter, with the characteristic time scale in deeper layers, due to the strong evapotranspiration at top surface. Based on the characteristic time scale, Wilson et al. (2004) found that the seasonal changes is dominant in the time series of field-measured soil moisture. On the other hand, ground-measured precipitation time series do show an annual component but no significant seasonal changes (Skøien et al., 2003), with much larger short-term periodic variations than soil moisture (D'Odorico and Rodríguez-Iturbe, 2000), i.e. closer to a random process. Thus, the power spectrum of precipitation time series can be used to identify the frequency range associated with the large but short-term periodic variations of atmospheric influence and to design a filter to extract the surface signal in 37 GHz PDBT time series.

The surface signal was extract by applying HANTS algorithm, first developed by Menenti et al. (1993) and used to reconstruct cloud-free time series of Normalized Difference Vegetation Index (NDVI) and LST (Jia et al., 2011; Roerink et al., 2003; Roerink et al., 2000; Verhoef, 1996). This algorithm applies user-selected harmonic components to model a signal and algorithm parameters can be set to reconstruct the upper-envelope of a time series of samples. The latter feature removes the atmosphere-affected samples as outliers, since atmospheric influence always attenuates surface PDBT (see Sect. 3.4.3).

3.2.2 Discrete Fourier Transform of a time series

An uniformly sampled time series, i.e. $f(t_i)$, with sampling interval Δt and record length P, can be expressed with a Fourier series as:

$$f\left(t_i\right) = \frac{A_0}{2} + \sum_{n=1}^{N} A_n \sin\left(\frac{2\pi n t_i}{P} + \phi_n\right), \text{ for integer } N \geq 1, t_i = 0, \Delta t, 2\Delta t, ..., N\Delta t \quad (3.1)$$

where A_0 is the average of whole time series, A_n and ϕ_n is the amplitude and phase respectively of the harmonic component with cycle number n, N is the largest cycle number involved and also the total sample size, i.e. N=integer of $P/\Delta T$, and t_i is the sampling time. The amplitude and phase of harmonic components in Eq. (3.1) are obtained by calculating the Discrete Fourier Transform (DFT) of $f(t_i)$. According to (Keogh et al., 2001), The DFT of $f(t_i)$ is denoted as $x(n)$ and is defined as:

$$x\left(n\right) = \sum_{t_i=0}^{N \times \Delta t} f\left(t_i\right) \exp\left(\frac{-i 2\pi n t_i}{P}\right), \text{ for integer } n \in \left[-\frac{N}{2}, \frac{N}{2}\right] \quad (3.2)$$

where n is the cycle number involved in Eq. (3.1), t_i is sampling time. The amplitude and phase of each harmonic component in Eq. (3.1) can be calculated as follows:

$$A_n = |x(n)| = \sqrt{\text{Re}(x_n)^2 + \text{Im}(x_n)^2}, \text{ for integer } n \in \left[-\frac{N}{2}, \frac{N}{2}\right]$$

$$\phi_n = \arctan\left(\frac{\text{Re}(x_n)}{\text{Im}(x_n)}\right), \text{ for integer } n \in \left[-\frac{N}{2}, \frac{N}{2}\right] \quad (3.3)$$

where $\text{Re}(x_n)$ and $\text{Im}(x_n)$ is the real and imaginary part of $x(n)$ respectively. The DFT can be calculated using many Fast Fourier Transform algorithms. More detailed information about FFT can be found in (Cooley et al., 1967; Cooley and Tukey, 1965; Singleton, 1969). In this chapter, the FFT algorithm in IDL is used. The power spectrum of a time series is the plot of the squared amplitude against the frequency, cycle number or period.

3.2.3 The two properties of the Discrete Fourier Transform

Two important properties of Fourier Transform are needed to analyze the power spectrum of a mixed signal and its component signals, e.g. a time series of daily PDBT space-borne observations:

1) **Linearity**: If $f(t_i)$ is the weighted sum of two component time series, then the DFT of $f(t_i)$, i.e. $x(n)$, is also the weighted sum of the DFTs of two component time series.

2) **Multiplicative**: If $f(t_i)$ is the product of two time series, i.e. $g(t_i)$ and $h(t_i)$, then the DFT of $f(t_i)$, i.e. $x(n)$, is the convolution of the DFTs of two component time series as:

$$x(n) = x_g(n) * x_h(n) = \frac{A_0^h}{2} \times x_g(n) + \frac{A_0^g}{2} \times x_h(n) + x_{g \times h}(n), \text{for integer } n \in \left[-\frac{N}{2}, \frac{N}{2}\right] \quad (3.4)$$

where $*$ is the convolution operator; A_0^g and A_0^h is the average of $g(t_i)$ and $h(t_i)$ respectively; $x_{g \times h}(n)$ is the side lobes introduced by the convolution operator. This property was analyzed by (Project et al., 1954).

The two properties can be easily proven by expressing both component time series with Fourier series. These properties are very useful to understand the contribution of each component signal in the DFT of PDBT time series, since both the radiative transfer model in Eq. (3.5), used to describe surface and atmospheric signals, and the numerical model in Eq. (3.7), used to describe the observation errors and gaps, only include the linear and product operators.

3.2.4 Numerical model of a PDBT time series

This section describes a simple model used to simulate how observation gaps and errors, atmospheric and surface signals concur to yield a time series of 37 GHz PDBT

observations. This model was used to explain how each component can be identified in actual time series and how the filters can be designed to apply in stage 1 and 2 of TSAP to extract the surface signal.

A space-borne radiometer measures surface and atmospheric emittance, which are attenuated by atmosphere (Choudhury et al., 1992). Thus a time series of gap-and-noise-free daily PDBT observations at bare soil includes the surface and atmospheric signals, of which the former is the polarization difference of surface emittance and the later includes the down-welling atmospheric emittance reflected and polarized by the surface and atmosphere attenuation (Choudhury, 1989). According to the Rayleigh-Jeans approximation, emittance measured by microwave radiometry can be linearly related to the brightness temperature. Thus, the PDBT time series at 37 GHz, i.e. $\Delta T(t_i)$, can be described by the following radiative transfer model:

$$\Delta T\left(t_i\right) = \Delta\epsilon^*\left(t_i\right) \times T_s\left(t_i\right) \times t_a\left(t_i\right) - \Delta\epsilon^*\left(t_i\right) \times T_d\left(t_i\right) \times t_a\left(t_i\right), \; t_i = 0, \; \Delta t, \; 2\Delta t, ..., N\Delta t \qquad (3.5)$$

Where t_i is the sampling time with constant sample interval Δt; $\Delta\epsilon^*(t_i)$ is the Polarization Difference Effective Emissivity (PDEE), $T_s(t_i)$ is the surface temperature, $T_d(t_i)$ is the down-welling apparent brightness temperature of the atmosphere, and $t_a(t_i)$ is the atmospheric transmission function, at t_i. Surface wetness determines the PDEE. Thus, the surface signal carries information on surface temperature and soil wetness, while the atmospheric signal carries information on down-welling atmospheric emittance and atmospheric attenuation. In the two-step model to retrieve the fractional area of WSS in Chapter 2, the attenuation by vegetation has been taken into account, while here is neglected since it is intended to illustrate how the signal components can be identified by time series analysis and filtered to extract the surface signal.

Taking into account the two properties of DFT (Section 3.2.3), the DFT of the time series of gap-and-noise-free daily PDBT, i.e. $x_{\Delta T}(n)$, can be expressed as:

$$x_{\Delta T}\left(n\right) = a_1 \times x_s\left(n\right) + a_2 \times x_a\left(n\right) + x_{s\times a}\left(n\right), \text{ for integer } n \in \left[-\frac{N}{2}, \frac{N}{2}\right] \qquad (3.6)$$

where $x_s(n)$ and $x_a(n)$ is the DFT of the surface and atmospheric signals respectively, $x_{s\times a}(n)$ is the DFT of side lobes introduced by the product of surface and atmospheric signals (see Eq. (3.5)), a_1 and a_2 is half of the average of the atmospheric signal and the surface signal respectively.

The radiometers on board sun-synchronous satellites introduce observation gaps and errors in the time series of daily PDBT space-borne observations. All gaps are set as 0 and occur periodically in the time series. Thus, this item can be expressed in the time series of daily PDBT space-borne observations, i.e. $f_1(t_i)$, by adding a noise function to $\Delta T(t_i)$ and multiplying it with a square wave as:

$$f_1\left(t_i\right) = S_w\left(t_i\right) \times \left[\Delta T\left(t_i\right) + \alpha_n\left(t_i\right)\right], \qquad (3.7)$$

$$S_w\left(t_i\right) = \begin{cases} 1 & L_1 < t_i \le L \\ 0 & 0 \le t_i \le L_1 \end{cases} \text{ and } S_w\left(t_i + L\right) = S_w\left(t_i\right), \, t_i = 0, \, \Delta t, \, 2\Delta t, ..., N\Delta t$$

where $S_w(t_i)$ is the square wave, $\alpha_n(t_i)$ is the noise function, all gaps are set to 0, L_1 is the duration of one gap segment and L is the period of the square wave. Since $S_w(t_i)$ is a piece-wise continuous function, according to the two properties of DFT, the DFT of $f_1(t_i)$, i.e. $x_{f1}(n)$, can be calculated as:

$$x_{f1}\left(n\right) = a_3 \times x_{\Delta T}\left(n\right) + a_3 \times x_a\left(n\right) + a_4 \times x_w(n) + x_{\Delta T \times w}\left(n\right) + x_{a \times w}\left(n\right), \text{ for integer } n \in \left[-\frac{N}{2}, \frac{N}{2}\right] \quad (3.8)$$

where $x_a(n)$ and $x_w(n)$ is the DFT of observation error and the square wave respectively, $x_{\Delta T \times w}(n)$ and $x_{a \times w}(n)$ is the side lobes introduced by multiplying the square wave with $\Delta T(t_i)$ and $\alpha_n(t_i)$ respectively, a_3 is half of the average of the square wave and a_4 is half of the average of the summation of $\Delta T(t_i)$ and $\alpha_n(t_i)$.

Inserting the DFT of $\Delta T(t_i)$ (Eq. (3.6)) into Eq. (3.8), the DFT of $f_1(t_i)$ can be calculated from its component signals as:

$$x_{f1}\left(n\right) = a_3 \times a_1 \times x_s\left(n\right) + a_3 \times a_2 \times x_a\left(n\right) + a_3 \times x_a\left(n\right)$$
$$+ a_4 \times x_w(n) + a_3 \times x_{s \times a}\left(n\right) + x_{\Delta T \times w}\left(n\right) + x_{a \times w}\left(n\right), \text{ for integer } n \in \left[-\frac{N}{2}, \frac{N}{2}\right] \quad (3.9)$$

Eq. (3.9) shows that the spectral features of component signals also will appear in the power spectrum of the time series of daily PDBT space-borne time series, i.e. $f_1(t_i)$, although the power values will be different from the power spectrum of component signals alone, because the harmonic components in $f_1(t_i)$ also include contributions from other component signals as shown in Eq. (3.9). This important property helps us to identify which spectral features are due to which component signals.

3.3   Data set and study area

To demonstrate and validate the TSAP, a case study on the Poyang Lake floodplain, located between 27.50° N to 29.38° N, and from 115.10° E to 117.25° E, was carried out. The two sample pixels in Figure 3.1 are within the Poyang Lake floodplain (Fig. 3.2). Poyang Lake is the largest lake in the Yangtze River basin, located between 28.05° N to 29.38° N, and from 115.44° E to 117.00° E. There is a clear dry season from October to March and the flooding season is from April to September. Ten EASE-Grid pixels are needed to cover the whole Poyang lake area, including the 2nd sample pixel in Figure1. The SSM/I early morning data will be used in Chapter 4 to retrieve the WSS area of Poyang Lake, with the ancillary data of MOD09A1 to model the vegetation influence on microwave observation and the two-step model introduced in Chapter 2. Considering the large footprint of SSM/I (25 km × 25 km), the spatial heterogeneity is very large at the lake-land boundary area, i.e. a mixture of dry land surface, wetland and lake area. The

length of the observation period is ten years, from 1998 to 2007. The rain-gauge data at the two sample pixels was used to estimate the spectral features associated with the atmospheric signal. The Lake areas observed by (Yésou et al., 2011) from MODerate-resolution Imaging Spectroradiometer (MODIS) and Advanced Synthetic Aperture Radar (ASAR) will used to validate the application of the TSAP described in this study to the PDBT time series in Chapter 4.
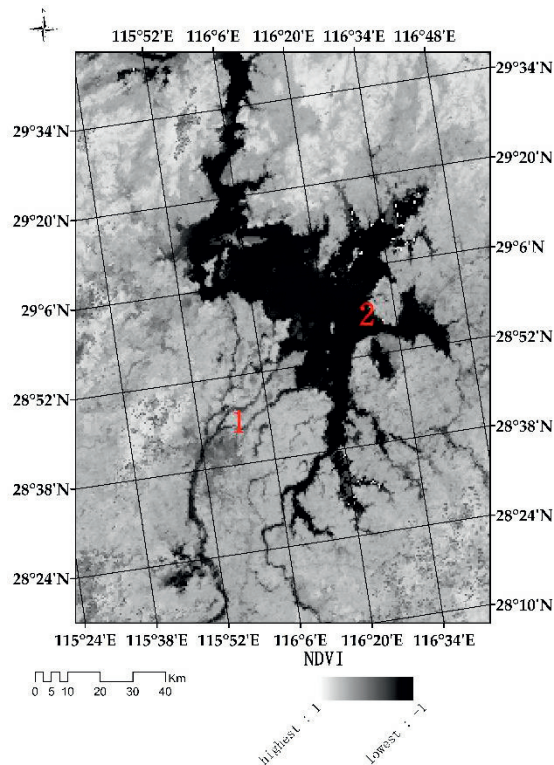
Figure 3.2: Location of the first (numbered with 1) and the second (numbered with 2) sample pixel in the Poyang Lake floodplain, China. The EASE-Grid is plotted.

3.4   Implementation of the Time Series Analysis Procedure

The application of Time series Analysis Procedure (TSAP) includes the following steps:

1. Identify the frequency range of observation gaps and errors

2. Remove the observation gaps and errors with a boxcar filter

3. Identify the harmonic components associated with the surface signal

4. Extract the surface signal from the filtered PDBT time series with the HANTS algorithm.

In this section, the two sample pixels (their PDBT time series shown in Figure 1) are used to demonstrate and analyze each step of the method. Observation gaps and errors in PDBT time series can be identified by comparing the power spectrum of PDBT and of square waves (Section 3.4.1). They can be removed by a boxcar filter, designed as described in Section 3.4.2. The atmospheric signal is difficult to identify directly, thus the power spectrum of a precipitation time series is used estimate the characteristic frequency range (spectral features) of atmospheric signal (Section 3.4.3). The atmospheric signal is removed by reconstructing the surface signal in the PDBT time series by applying the HANTS algorithm (Section 3.4.4). Statistics are analyzed to evaluate the performance of the boxcar filter and of the HANTS algorithm.

3.4.1 The frequency range of observation gaps and errors

Almost 50% of samples in the time series of daily PDBT observations are gaps, i.e. $L_1 = L/2$ in Eq. (3.7). Thus a square wave $S_1(t)$ with phase = 0 and an unit amplitude can be expressed with a Fourier series (Thompson et al., 2008) as:

$$S_1\left(t_i\right) = \frac{1}{2} + \frac{2}{\pi} \sum_{n_o=1,3,5,\cdots}^{\infty} \frac{1}{n_o} \sin\left(\frac{2\pi t_i}{P} \times \frac{n_o P}{L}\right), \, t_i = 0, \, \varDelta t, \, 2\varDelta t, \ldots, N\varDelta t \qquad (3.10)$$

where $n_o P/L$ is the cycle numbers of harmonic components applied to represent $S_1(t_i)$. The length of the observation period, i.e. P, is 10 years for the two sample pixels in Figure 3.1, while L is normally of the order of a few days, thus $n_o P/L$ is very large, i.e. the harmonic components of $S_1(t_i)$ lie in the high frequency range. In the power spectrum of these two examples (Fig. 3.3), there are two extreme high peaks in the high frequency range (i.e. short periods): one with a period of 7 days, and the other with a period of 8 days. When $L = 8$ *days*, the power spectrum of Eq. (3.10) is shown in Figure 3.4a. The largest peak of this square wave equals to 8 days and the second largest peak equals to 8/3 days (Fig. 3.4a). This means that the other extreme high peak in the power spectrum of $f_1(t_i)$ (Fig. 3.3) does not come from the square wave with $L = 8$ *days*, but comes from another square wave, i.e. $S_2(t_i)$ with $L = 7$ *days* as Figure 3.4b shows.

These two square waves split the whole time series into three types (Fig. 3.1): 1) gaps with value of 0; 2) observations with values averaging around 5 K in Figure 3.1a and 10 K in Figure 3.1b, i.e. extreme low observations; 3) observations with values around 15 K in Figure 3.1a and 25 K in Figure 3.1b. When the rain rate is around 25 mm/h, the modeled up-welling PDBT at 37 GHz has been shown to be around 5 K for various land cover types (Czekala et al., 1999). This strong attenuation by heavy precipitation leads to many observations with values around 5 K in Figure 3.1a and values around 10 K in Figure 3.1b.

These attenuated observations periodically occur in the time series of PDBT observations according to its DFT in Figure 3.3, but such evidence is not found in the DFT of time series of ground-measured precipitation. This implies that the periodic influence of precipitation on PDBT observations is probably due to a periodic component in the observation errors, e.g. the periodic scan configuration in SSM/I (Poe, 1990) may lead to these periodic sampling errors. Thus, it can be assumed that the observation errors consist of one non-periodic component, i.e. white noise, and one periodic component, i.e. the square wave with $L=$ 7 days or $L=$ 8 day*s*.
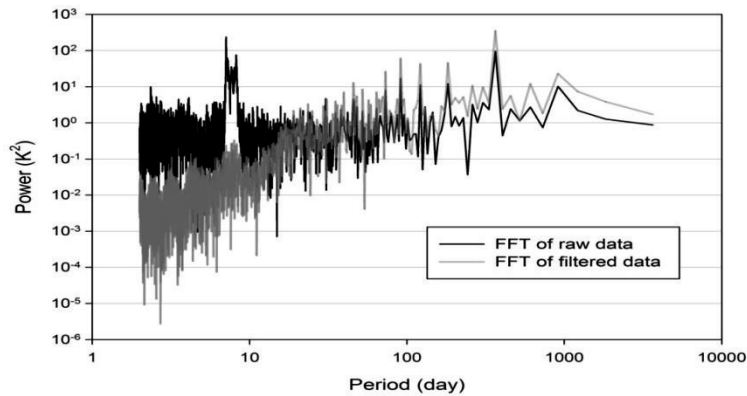
(a)
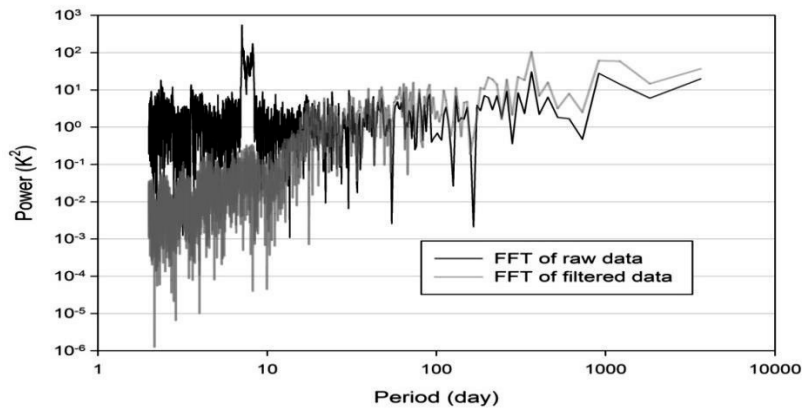
(b)

Figure 3.3: Power spectrum of the space-borne Polarization Difference Brightness Temperature (PDBT) time series at the 1st (a) and 2nd (b) sample pixels from 1998 to 2007. The dominant land cover of the 1st sample pixel is farm land, centered at 28.603° N and 115.835° E. The dominant land cover of the 2nd sample pixel is open water and wetland, centered at 29.049° N and 116.356° E.
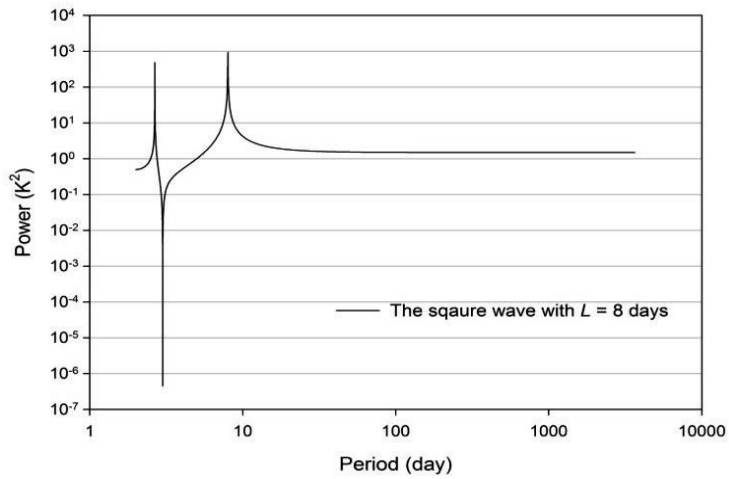
(a)
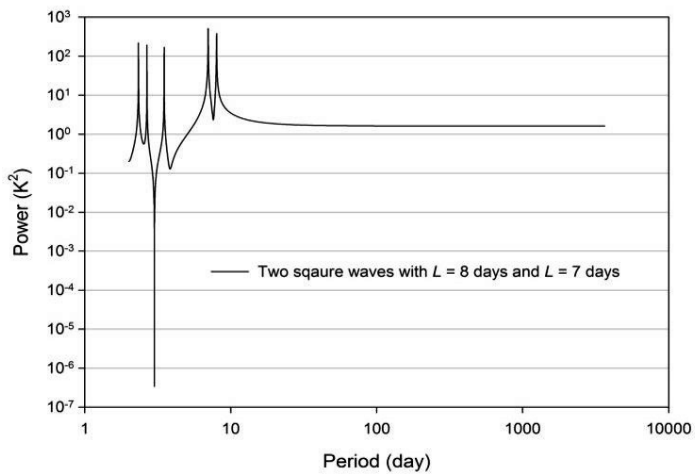
(b)

Figure 3.4: Power spectrum of the square wave in Eq. (3.10) with L= 8 days (a), and power spectrum of the sum of two square waves with L= 7 days and L= 8 days with unit amplitude (b)

3.4.2 The modified boxcar filter and its transfer function

3.4.2.1 The modified boxcar filter

The power spectrum of the PDBT time series of both sample pixels 1 and 2 (Fig. 3.3) shows two clear peaks with periods of 7 and 8 days. Using Eq. (3.8), a time series with two square-wave components with periods of 7 and 8 days was generated: the power spectrum of this time series (Fig. 3.4) shows that the two peaks at 7 and 8 days in Fig. 3.3 can indeed be explained by two square-wave components, i.e. one due to gaps and the other due to observation errors. To filter out the harmonic components due to observation gaps and errors in the raw PDBT time series, a boxcar filter is modified, by adapting the filter length to the gap size and location:

$$f_2(t_i) = \frac{\sum_{k=t_i-M}^{k=t_i+M}\left[\begin{array}{l}f_1(k)-\min[f_1(t_i-M),\cdots,f_1(t_i+M)]_{unzero}\\-\max[f_1(t_i-M),\cdots,f_1(t_i+M)]_{unzero}\end{array}\right]}{S_M-2} \tag{3.11}$$

where $f_1(k) \in [f_1(t_i-M), f_1(t_i-M+1), \cdots, f_1(t_i+M-1), f_1(t_i+M)]$, which is a subset symmetric with center at t_i, $2{\times}M$ is the filter length. $[f_1(t_i-M), f_1(t_i-M+1), \cdots, f_1(t_i+M-1), f_1(t_i+M)]_{unzero}$ means non-zero elements. In each subset, S_M is the number of non-zero elements. S_M varies through the time series, i.e. $t_i \in [0,1,\cdots,N]$. The minimum non-zero value in each subset is filtered out in Eq. (3.11), to reduce the impacts of the strong attenuation due to heavy rainfall or clouds. The maximum value is also filtered out, as suggested by Prigent et al. (1997).

The minimum length of a boxcar filter depends on the lowest frequency of square wave components in PDBT , see e.g. Gerek and Yardimci (1997). There must be at least 1 non-zero observation available, i.e. $S_M > 2$ in Eq. (3.11), within the interval $2{\times}M$. The maximum length of gaps, i.e. numbers of samples with value of 0 in the interval $2{\times}M$, occurs at the beginning and end of the time series. To guarantee $S_M > 2$, the minimum filter length can be calculated as:

$$[2 \times M]_{\min} = L + 2 \tag{3.12}$$

where L is the period of the square wave. With this minimum length = 10 days, the modified boxcar filter in Eq. (3.11) can filter out all frequencies higher than the lowest frequency associated with observation gaps and errors, i.e. with shorter periods than the maximum period of the two square waves, i.e. $L = 8$ days in Fig. 3.3.

3.4.2.2 On the transfer function of the modified boxcar filter

The modified boxcar filter is a low pass filter, thus it can filter out the frequencies with periods shorter than the maximum period of the observation gaps and errors

components and retain the frequencies with longer periods. The question is whether the modified boxcar filter modifies the lower frequency components. If the noise-and-gap-free PDBT time series is represented with harmonic components in Eq. (3.1), the transfer function of the boxcar filter can be evaluated in the frequency domain. It is assumed that the power due to observation errors is half of the total power in the PDBT time series according to the Parseval's theorem. In this way, the processing loss of the modified boxcar filter can be calculated as follows.

$g_n(t_i)$ is a harmonic component in the noise-and-gap-free PDBT time series with cycle number n:

$$g_n\left(t_i\right) = A_n \sin\left(\frac{2\pi n t_i}{P}\right), \; t_i = 0, \, \Delta t, \, 2\Delta t, ..., N\Delta t \tag{3.13}$$

where A_n is the amplitude of the harmonic component in $f(t_i)$ and P is the length of observation period. In our experiment, $P=10\times365$ days. Adding the white noise to $g_n(t_i)$ and multiplying it with $S_l(t_i)$ (Eq. (3.10)), a gappy-and-noisy time series can be expressed as:

$$g_n^1\left(t_i\right) = A_n \left[\sin\left(\frac{2\pi n t_i}{P}\right) + \alpha_n\left(t_i\right) \right] \times S_1\left(t_i\right), \; t_i = 0, \, \Delta t, \, 2\Delta t, ..., N\Delta t \tag{3.14}$$

where $\alpha_n(t_i)$ is the white noise due to the observation errors with the same amplitude as the amplitude of this component. The noise floor level in the PDBT time series is around 0.2 K due to calibration errors according to (Wentz, 2013), much less than the possible variation due to observation errors, thus it is negligible in this study. After applying the modified boxcar filter in Eq. (3.11), the filtered time series is expressed as:

$$g_n^2\left(t_i\right) = A_n^F \sin\left(\frac{2\pi n t_i}{P}\right), \; t_i = 0, \, \Delta t, \, 2\Delta t, ..., N\Delta t \tag{3.15}$$

where A_n^F is the amplitude after filtering. The normalized difference between the gap-and-noise-free amplitude and filtered amplitude for each harmonic component, i.e. ND_n, is used to represent the processing loss of the filter and is defined as:

$$ND_n = \left| \frac{A_n^F}{A_n} - 1 \right| \times 100\% \tag{3.16}$$

ND_n does not depend on A_n. To simplify our analysis, $A_n=1.0$ is set for all tested n belonging to $[1,2,3,...,N]$. Smaller ND values mean less processing loss after applying the modified boxcar filter.

According to the power spectrum of PDBT observations in Fig. 3.3, the maximum period of the two square waves is 8 days, thus the minimum filter length (according to Eq. (3.11)) is 10 days and the period of the square wave introduced in this experiment is 8 days. The white noise is generated using the RONDOMU function in IDL. Since the FFT algorithm calculates frequencies with cycle number in the range $[-N/2, N/2]$, only $n \in$

$[1,2,3, \cdots, N/2]$ was analyzed, with $N=3650$. When frequency ≥ 0.05, i.e. period ≥ 20 days , the *ND* values are all above 40% (Fig. 3.5), which indicates that the components with higher frequency have been filtered out by the modified boxcar filter.
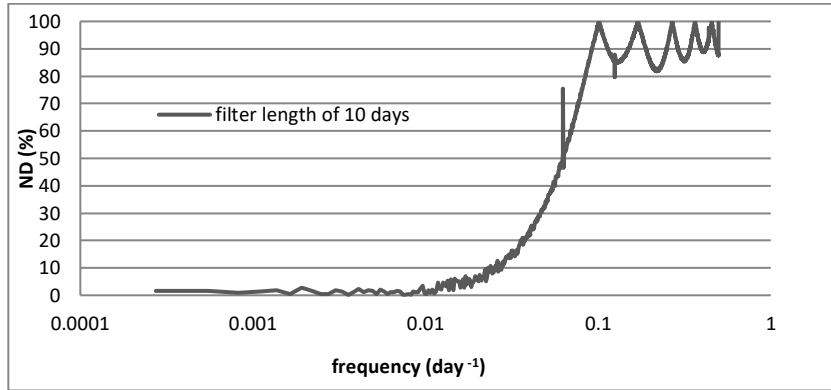
Figure 3.5: The Normalized Difference (ND) between amplitudes of harmonic components in Eq. (3.13) and their filtered amplitudes for 10-year time series.

3.4.3 Identify the spectral features of the surface signal

3.4.3.1   Identify frequency range of the atmospheric signal from precipitation time series

The atmospheric attenuation and the down-welling atmospheric emittance are both primarily controlled by precipitable water hydrometeors (Choudhury, 1989; Choudhury et al., 1992). Satellite retrievals of both daily total precipitable water content and precipitation have large uncertainties over land (see e.g. (Behrangi et al., 2016; Boukabara et al., 2010)), hence it is difficult to identify spectral features related to the atmospheric signal by analyzing satellite data. The occurrence of precipitation correlates with large clouds (Richards and Arkin, 1981) and it was observed (see Fig. 3.6) that large drops in the filtered PDBT time series during precipitation events. Accordingly, the time series of rain-gauge data was used to identify the spectral features associated with the atmospheric signal.

The cumulated power spectrum of the rain-gauge time series at two locations (Fig. 3.7) shows that most of the variability is associated with harmonic components at frequency > 0.00274 day^{-1}, i.e. periods < 73 days. Moreover, there is a jump in the cumulated power spectrum at a frequency of 0.0137 day^{-1}, i.e. period = 365 days. Since components with periods <20 days have been filtered out by applying the boxcar filter (see Fig. 3.5), It may be concluded that the spectral features associated with the atmospheric signal have periods range of [20 days, 73 days].
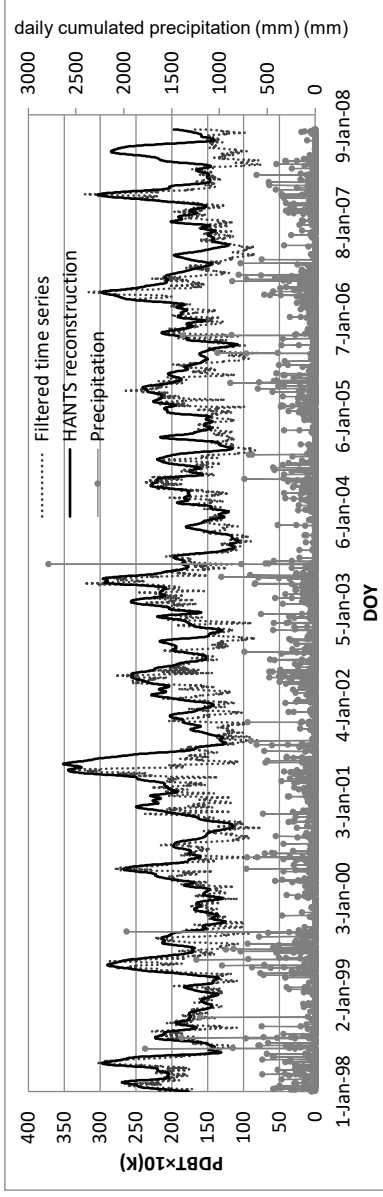
(a)
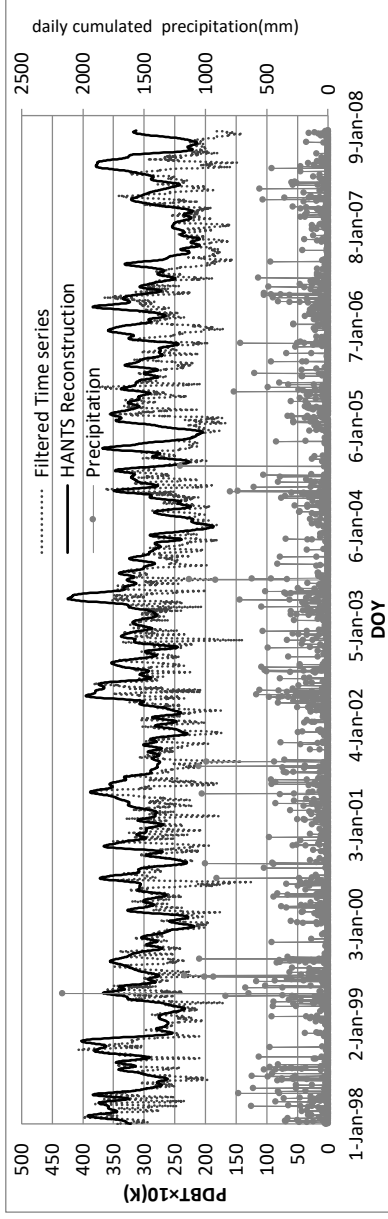
(b)

Figure 3.6: The Polarization Difference Brightness Temperature (PDBT) time series after applying the boxcar filter, its HANTS reconstruction and the daily cumulated precipitation from 1998 to 2007 at the 1st sample pixel (a) and the 2nd sample pixel (b)
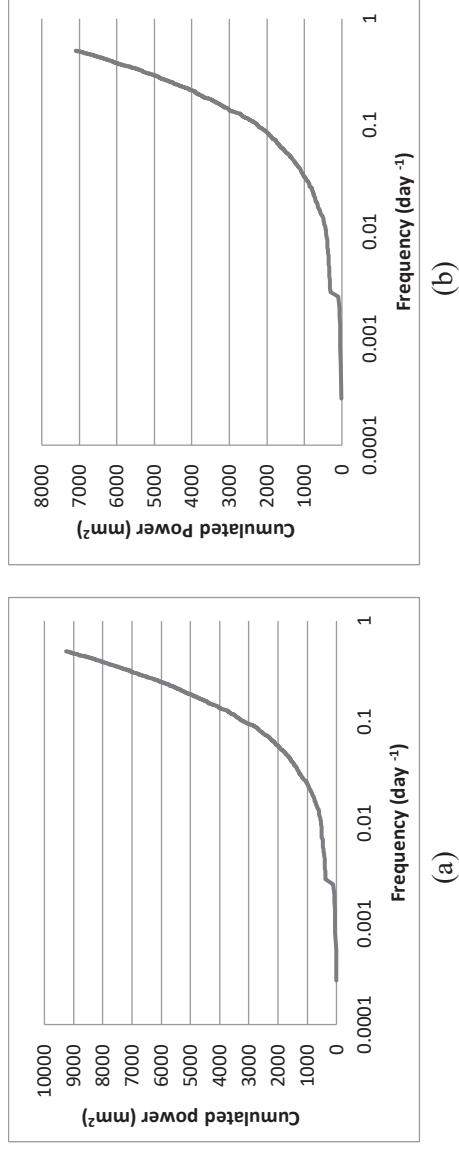
Figure 3.7: The cumulated power spectrum of 10-year precipitation time series at the 1st sample pixel (a) and the 2nd sample pixel (b)

3.4.3.2   Identify the spectral features of the surface signal

To identify more precisely the surface signal, the power spectrum of the rain-gauge time series at higher frequencies (Fig. 3.8) has been compared with the power spectrum of the boxcar-filtered PDBT time series (Fig. 3.9). Most of the variability in rain-gauge time series is accounted for by high frequency component, more precisely the ones having periods between say 20 and 73 days (Fig. 3.8). On the other hand, most of the variability in the PDBT time series is accounted for by components at lower frequencies, namely the components with periods > 73 days (Fig. 3.9). This confirms the conclusion that atmospheric signal in the PDBT time series is accounted for by components with periods in the range [20 days, 73 days], while the surface signal is associated with components having periods >73 days.

In the main lobe peaks of the PDBT time series (Fig. 3.9), it is also noticed that several components are not associated with the atmospheric signals in the range [20days, 73 days] (Table 3.1). These components may represent the short-term variations in the surface signal.

Table 3.1: Surface components, i.e. the spectral features associated with the surface signal, with period (higher frequency) shorter than the threshold component = 73 days in the 10-year time series.

pixel location	period of surface components (days)
Pixel 1	64, 57, 46, 34, 31, 25, 23, 20
Pixel 2	47, 42, 40, 31, 29, 26, 25, 23
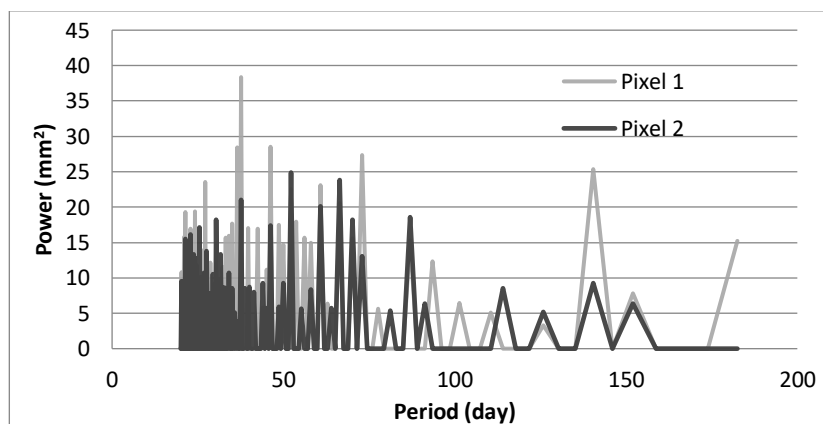
Figure 3.8: Harmonic components with peak power in the power spectrum of rain-gauge time series in the period range [20 days, 182 days] for both the 1st and the 2nd sample pixels
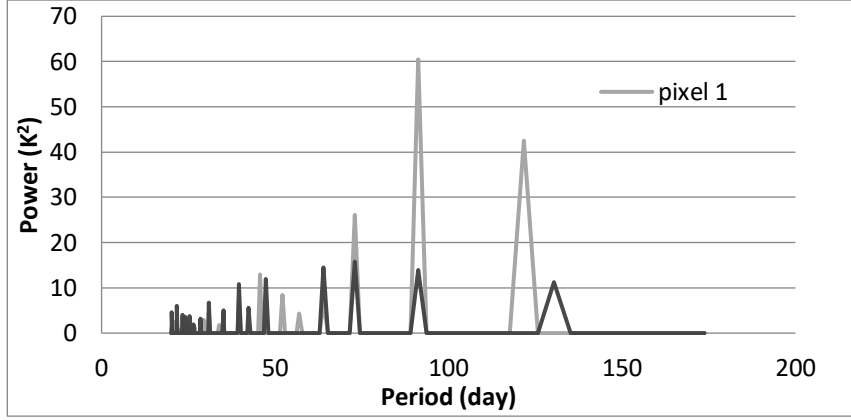
Figure 3.9: Harmonic components with main lobe peak in the power spectrum of the PDBT time series in the period range [20 days, 182 days] for both the 1st and the 2nd sample pixels. The main lobe peaks are defined as the peak values in the upper envelope of the power spectrum.

3.4.4 Extract the surface signal by HANTS

Having identified the spectral range associated with the surface signal, the PDBT time series can be expressed as:

$$f_s^1(t_i) = A_0^s + \sum_{j \in R^s} A_j^s \times \sin\left(\frac{2\pi j}{N} t_i + \phi_j^s\right), \; t_i = 0, \, \Delta t, \, 2\Delta t, ..., N\Delta t \qquad (3.17)$$

where $f_s^1(t_i)$ is the surface signal and (j/N) gives periods > 20 days, i.e. it is expressed by the harmonic components due to the surface signal — $j \in R^s$; R^s is the spectral features of the surface signal. The threshold period, i.e. 20 days, is identified according to the transfer function of the modified boxcar filter in section 3.4.2. After boxcar filtering, the power of harmonic components with period < 20 days is very small in Fig. 3.3, i.e. the amplitude contributions of these components can be neglected in the filtered PDBT time series, which is due to the high attenuation of the modified boxcar filter (see the transfer function in Fig. 3.5). It is reasonable to assume that the upper envelope of the filtered PDBT time series (Fig. 3.6) consists only of the samples without or with less atmospheric attenuations. The HANTS algorithm estimates the amplitudes and phases in Eq. (3.17) through an iterative procedure that ends when the following constraint is met:

$$\min\left|f_s^1(k_i) - f_1(k_i)\right| \le e \qquad (3.18)$$

where k_i is sampling time, $f_s^1(k_i)$ is the modeled value using HANTS algorithm with Eq. (3.17), e is the user-prescribed errors of reconstruction; See (Roerink et al., 2000) for a detailed explanation of HANTS parameter setting. If values much lower than the

reconstructed time series are regarded at outliers, HANTS gives a reconstruction close to the upper envelope as the example shown in Fig 3.6.

3.4.5 Statistical evaluation of TSAP

A statistical summary (Table 3.2) about raw, boxcar filtered and HANTS reconstructed PDBT time series shows that the averaged and non-zero minimum values of time series both increase after each step of TSAP. This indicates that after each step of TSAP, lower values, which are due to observation errors or due to atmosphere attenuation, have been replaced by higher values in the time series. The maximum value is assumed to be a correct observation in the raw data. The maximum values after HANTS reconstruction were closer to the raw data than those after boxcar filtering, in both samples. It means that HANTS improved the representation of the time series, compared with the boxcar filtering. After the reconstruction, the range over open water area is reduced from 43.6 K (raw data) to 24.8 K that is close to the expected range of PDBT over inundated areas observed by (Choudhury, 1991). The Root Mean Square Deviation (RMSD) was calculated between two time series after each step of TSAP (Table 3.3). The large decrease in standard deviations (Table 3.2) from the raw data to the boxcar-filtered time series comes together with large RMSD between them, mainly related to the power reduction in the frequency range associated with observation gaps and errors after filtering in Fig. 3.3. This means most of noise in the raw data was removed by the modified boxcar filtering. The standard deviations of boxcar filtered and HANTS reconstructed time series were similar, but the RMSD between them was not negligible, although smaller than the RMSD between the raw and filtered time series. The improvements in HANTS reconstructed time series were mainly the representation of the upper envelope and the mitigation of the impact of atmospheric attenuation, as shown by higher values of mean, minimum, and maximum compared with the boxcar filtered time series (Table 3.2).

Table 3.2: Statistical summary on original, boxcar filtered, and reconstructed PDBT time series.

	1st example at crop land			2nd example at lake area		
	raw data	boxcar filter	HANTS	raw data	boxcar filter	HANTS
non-zero Minimum (K)	2.2	7.4	10.6	2.2	12.6	18.7
Maximum (K)	41	34.3	35.1	45.8	40.8	42.5
Mean (K)	16.1	16.2	18.9	25.9	26.4	29.8
Std[3] (K)	9.2	4.3	4.5	14	4.6	4.3

[3] Standard Deviation

Table 3.3: Root Mean Square Deviation (RMSD) at each step in TSAP.

	1st example at crop land		2nd example at lake area	
	raw - boxcar filter	boxcar filter - HANTS	raw - boxcar filter	boxcar filter - HANTS
RMSD (K)	11.7	4.4	18.1	5.5

3.5   Discussion

TSAP requires two important assumptions. One is the physical assumption that is the characteristic time scales of soil moisture, hydrometeors (precipitation as an indicator in this case), observation gaps and errors are different and distinguishable. The other is the mathematical assumption that if a signal consists of component signals and can be represented by linear and product operations, the characteristic frequency range of component signals can be identified in the power spectrum of the mixed signal. Based on these assumptions, the component signals can be revealed in the power spectrum of 37 GHz PDBT time series. For example, the large peaks with periods between 6 and 9 days in the power spectrum at two sample pixels (Fig. 3.3) are definitely not due to atmospheric or surface signal. By analyzing the power spectrum of a synthetic signal (Fig. 3.4) generated with the numerical model (Eq. 3.9) and the square wave (Eq. 3.10), it was concluded that the extreme peak values are due to a linear combination of two square waves, which lead to these extreme-low but non-zero values in the PDBT time series (Fig. 3.1). The estimated duration of consecutive gaps from power spectrum analysis also agrees with the orbit and scanning configuration of SSM/I (Hollinger et al., 1990). This analysis clearly supports the mathematical assumption and helps interpret the spectral range of atmospheric signal in Fig. 3.9. In the power spectrum at both sample pixels (Fig. 3.3), it was also noticed that many side lobe peaks present around the harmonic components associated with the two squares waves, due to the mixture of the component signals (i.e. two square waves, atmospheric and surface signals). Thus, to identify the spectral features of the surface signal, only the main lobe peaks in the power spectrum of PDBT time series were used (Fig. 3.9).

Time series of rain-gauge data were used to reveal the characteristic frequency range of the atmospheric signal, since the occurrence of precipitation is related to large scale clouds and high water depth of hydrometeor (Richards and Arkin, 1981). It is found that clear spectral features in the power spectrum of a PDBT time series, which can be related to surface and atmospheric signals in the PDBT time series (Fig. 3.9). The seasonal changes in soil moisture can be clearly observed in the power spectrum of PDBT time series, especially for crop land (Fig. 3.3 and Fig 3.9). The shortest seasonal changes have a period

of 73 days, which is comparable with the time scale of field-measured soil moisture according to Vinnikov et al. (1996). This indicates that the long-term memory of soil moisture, which is determined by the field capacity and potential evapotranspiration, probably smooths the influence of precipitation, thus identifies the shortest seasonal changes in PDBT time series. The slower longer seasonal changes in soil moisture, which can be observed in PDBT time series, may be associated with the seasonal climate (Wilson et al., 2004), e.g. monsoons and solar radiation. The amplitudes of components in the spectral range of the atmospheric signal are much smaller than those of components representing the seasonal changes in soil moisture (Fig. 3.9). This means that surface signal mainly controls the variations in the PDBT time series, while the atmosphere signal causes perturbations. Soil moisture is one of the major factors that determine the surface signal, since the fastest seasonal changes in PDBT time series are probably due to its time scale. This conclusion agrees with the physical characteristics of 37 GHz microwave, which is sensitive to surface wetness and influenced mainly by the absorption of hydrometeors. Although the spatial resolution at frequencies higher than 37 GHz can be better, e.g. at 85 GHz, the scattering of hydrometeors will be more significant (Ulaby et al., 1981), which causes much larger variation in the atmospheric signal. So PDBT at 37 GHz is the trade-off between spatial resolution and atmosphere influence to detect surface wetness. It was also noticed that some short-term periodic variations in Fig. 3.9 (as shown in Table 3.1), whose harmonic components have very small variations in the power spectrum of precipitation time series (Fig. 3.8). Since the PDBT time series is mainly controlled by soil moisture, these short-term periodic variations are classed into the surface signal. The analysis on the spectral features of component signals in the PDBT time series supports our physical assumption.

The performance of the modified boxcar filter (Fig. 3.5) shows that the filter transfer function at higher frequencies is rather smooth, which may retain part of surface and atmospheric signal, i.e. the components in the lower frequency range. The short-term components are filtered out with periods less than 20 days, as shown by the transfer function of the modified boxcar filter. The performance of the HANTS algorithm is controlled by the quality of input data, i.e. the number of reliable observations in clear days. Gaps lead to smaller number of observations and increase the difficulty of reconstructing the surface signal in the presence of extensive and persistent cloud cover. As discussed in Shang et al. (2015), long-term high cloud cover in winter does not lead to precipitations but does attenuate the PDBT values. This may have an impact on the identification of atmospheric signal using rain-gauge data as done in our study. Thus, in the future it will be explored that how to reduce the gap size by merging multi-sources data, e.g. AMSR-E and SSM/I and to combine satellite data products on precipitable water and cloud cover. In this case the application of TSAP reduced the range in daily PDBT in the lake-land boundary region from 42 K to 25 K as expected in inundated areas according to Choudhury (1991).

3.6   Conclusions

In this Chapter, a new method, named Time Series Analysis Procedure (TSAP), was developed to remove the daily atmospheric influence on daily 37 GHz PDBT time series and the occurrence of observation gaps and errors in this time series. Other than traditional methods, this method is based on the power spectrum analysis of daily PDBT time series with Discrete Fourier Transform (DFT), since the spectral features of component signals can be revealed in the power spectrum of a mixed time series. The daily 37 GHz PDBT time series consists of the surface signal (including surface emittance and vegetation attenuation), the atmospheric signal (including atmosphere emittance and attenuation, mainly from hydrometeors), observation gaps and errors. The DFT of the PDBT time series is the linear combination of the weighted DFT of component signals and side lobes introduced by mixing signals. According to the power spectrum analysis of PDBT time series, TSAP included two stages. In the first stage, it was found that the consecutive gaps and periodic components in observation errors introduced extreme peaks in the very high frequency spectral range. Both of them can be removed by the modified boxcar filter. The minimum filter length was determined by the longest period of peak harmonic components associated with the observation gaps and errors. In the second stage, the spectral features of the atmospheric signal can be revealed by the power spectrum of precipitation time series, due to that atmosphere emittance and attenuation at 37 GHz is mainly from hydrometeors. The harmonic components associated with the surface signal were mainly in the lower frequency domain, i.e. representing the seasonal changes of soil moisture, and have larger amplitudes than those associated with the atmospheric signal, due to that the microwave sensitivity to surface wetness is larger than to atmospheric water content at 37 GHz. Thus the spectral features of the surface signal can be identified and be used by the Harmonic ANalysis of Time Series (HANTS) algorithm to reconstruct the surface signal from the filtered PDBT time series. The performance of the modified boxcar filter was mainly controlled by the gap size according to the Nyquist theorem. Overall, the modified boxcar filter reduced the noise level in raw PDBT time series significantly and the HANTS algorithm mitigated the impact on sample largely attenuated by the atmosphere. After TSAP, the PDBT range of the lake-land boundary region was closer to the observed range in other large flooded area, i.e. Pantanal.

Chapter 4

Inundation patterns in the Poyang Lake floodplain

4.1 Introduction

Poyang Lake and its floodplain is a hotspot of hydrological studies in past decades (Guo et al., 2008; Guo et al., 2011; Guo et al., 2012; Shankman et al., 2006; Ye et al., 2011; Ye et al., 2013; Zhang et al., 2012; Zhang et al., 2006; Zhang et al., 2011; Zhao et al., 2010), mainly due to that large floods in 1998 lead to extreme damages on life and properties in this area (Zong and Chen, 2000). The floodplain is located in the middle reach of the Yangtze River basin and on the south side of the Yangtze River. Poyang Lake, i.e. the largest freshwater body in China, is located at the north-eastern part of the floodplain and connects to the Yangtze River through the outlet area on lake's north side. The lake receives water flow from five rivers in the floodplain: Ganjiang, Fuhe, Xinjiang, Raohe and Xiushui Rivers. The floodplain has a typical subtropical and monsoon climate, with the annual mean precipitation around 1680mm. 59% of annual discharge of this floodplain arrives in the rainy season, normally from March to June, and most runs into Poyang Lake; while only 14% arrives in the dry season, from October to next January (Ye et al., 2013). Besides receiving water from upstream, the lake area also interacts with the Yangtze River (Guo et al., 2011; Hu et al., 2007). So, Poyang Lake is a very important natural reservoir for both the floodplain and the Yangtze River basin. In the floodplain, wide alluvial plains and broad alluvial valleys are one of the largest rice growing regions in China. The largest wetland in China is also located around the lake and supplies habitat for water fowls. Water resource management becomes more and more important to balance the water competition between human activities (e.g. agriculture) and ecosystem (e.g wetland) in the Poyang Lake

floodplain, especially under changed climate. The closer of the Three Gorges Dam significantly modifies stream flow in the Yangtze River basin, and thus also influences the lake area and wetlands in Poyang Lake, which aggravates the water competition in the floodplain.

For flood early warning and water resource management in such subtropical floodplain, it is necessary to monitor lake area, observe inundated area in upstream and study the relationship between them. Remote sensing technologies can be used to observe surface water bodies. There were many studies to identify the surface water body and wetlands in Poyang Lake with optical and thermal sensors (e.g. Dronova et al., 2011; Feng et al., 2012a; Feng et al., 2012b; Li et al., 2012; Zhang et al., 1998). Using optical and thermal sensors, however, is largely hampered by frequent clouds and precipitation. Rice, aquatic vegetation, and emergent vegetation complicate the spectral features of surface water bodies in visible and thermal bands (Dronova et al., 2011). Synthetic Aperture Radar (SAR) can observe surface water bodies underneath clouds and vegetation canopy, but its low temporal resolution and small spatial coverage makes it difficult to observe the evolution of a monsoon lake or the inundation pattern of a large floodplain. Yésou et al. (2011) combines the surface water body observations from MODerate-resolution Imaging Spectroradiometer (MODIS) and Advanced Synthetic Aperture Radar (ASAR), in order to delineate the seasonal changes of Poyang Lake.

Microwave observations at 37 GHz have been used to observe inundated area under dense vegetation coverage in many tropical floodplains (e.g., Hamilton et al., 2002; Hamilton et al., 1996, 2004; Sippel et al., 1994; Sippel et al., 1998), thus are applied in this thesis to observe surface water bodies. The previous methods, however, cannot be directly used in the subtropical floodplains, mainly due to the seasonal changed vegetation and various surface roughness conditions. In Chapter 2, the two-step model has been developed to retrieve the fractional area of Water Saturated Surface (WSS), i.e. open water, inundated area and water saturated soil surface, from Polarization Difference Brightness Temperature (PDBT) at 37 GHz, which takes the seasonal changed vegetation and various surface roughness conditions into account. Time series Analysis Procedure (TSAP described in Chapter 3) can extract the surface signal in the time series of daily PDBT observations, so that remove the atmospheric influence, i.e. clouds and precipitation. With combining these two methods, it is possible to delineate the daily changes of surface water body in Poyang Lake and the floodplain, regardless of the variable conditions in vegetation and atmosphere.

Two problems still remain in the implementation of the combined method. The first one is how to evaluate or validate the retrieved WSS area. Since WSS includes water saturated soil and inundated, it is difficult to use field measurement to validate it. The second problem is that there is no rain-gauge data for all pixels covering the whole Poyang lake floodplain, i.e. pixels numbered from 1 to 36 in Fig. 4.1. Rain-gauge data is needed by TSAP to identify the spectral features of the atmospheric signal in the PDBT time series.

During clear days, optical and thermal sensor and SAR can observe open water with very high accuracy. Thus open water observed by these two types of sensors were used to validate the inundated area retrieved from microwave radiometer data (e.g. Sippel et al.,

1994; Tanaka et al., 2003). The lake area observed from MODIS and SAR by Yésou et al. (2011) can be the reference data to validate the retrieved WSS area in this case. Rain-gauge time series has very small correlation in space (Skøien et al., 2003), i.e. small space scale. Thus, precipitation time series could be taken as a random process and may reveal large variations in the spectral features of the atmospheric signals between pixels. The spectral features of the atmospheric signal are used to identify the spectral features of the surface signal that is dominated by soil moisture and vegetation. The correlation of soil moisture time series is large in space and the space scale of field measured soil moisture could be as large as 500 km (Skøien et al., 2003; Vinnikov et al., 1996). Vegetation phenology is dominated by the climate types. Thus, in a subtropical floodplain, as the Poyang Lake floodplain, the spatial variation in the surface signal is much less than that in the atmospheric signal, i.e. uniform spectral features of the surface signal may be derived and applied to the whole floodplain.

This chapter is aimed to study inundation patters in the Poyang Lake floodplain with the method combining the two-step model and TSAP developed in the previous chapter. To solve the two problems in the implementation, the lake area observed from MODIS and ASAR by Yésou et al. (2011) is used as reference data and rain-gauge data in Chapter 3 is used to derive the uniform spectral features of the surface signal in the Poyang Lake floodplain. Section 4.2 described data set and the study area. Section 4.3 introduced the overall method and evaluates the retrieved WSS area in Poyang Lake with the observations from MODIS and ASAR. Section 4.4 illustrated the study on the inundation pattern in the Poyang Lake floodplain. The uniform spectral features of the surface signal were derived from rain-gauge data at two stations and were evaluated by comparing the retrieved WSS area and lake area observed by MODIS and ASAR. The comparison between different microwave radiometers was also analyzed, in order to evaluate the consistency, observation bias and possible noise of these two sensors, which may also lead to the model uncertainty of the overall method. Section 4.5 showed the inundation patterns of the Dongting Lake and Poyang Lake floodplains in a flooded and a normal year, in order to evaluate the possibility to use WSS area as an indicator of flood early warning. Section 4.6 summarized the conclusions.
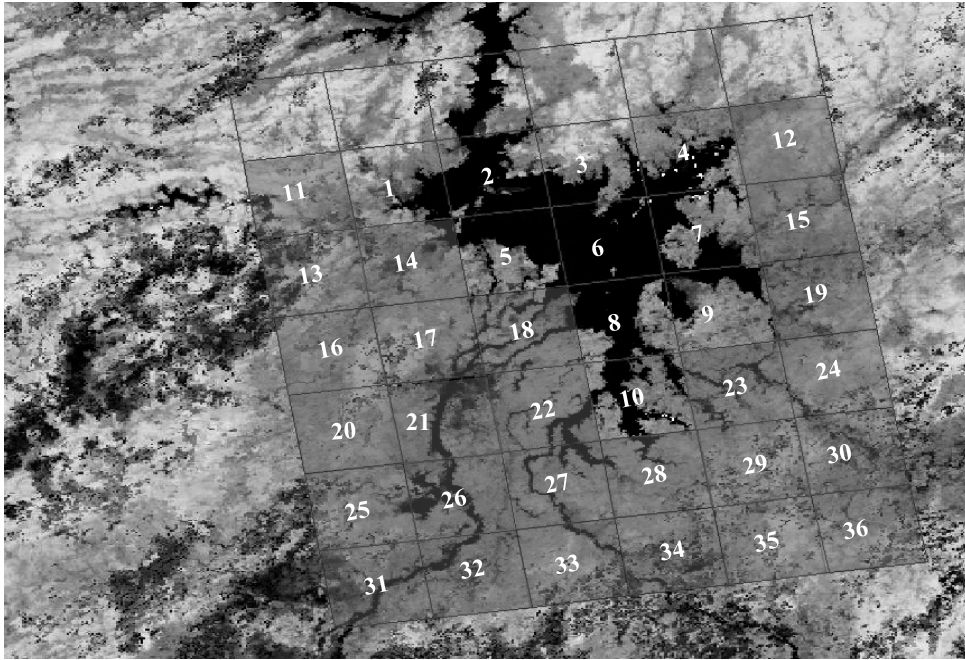
Figure 4.1: The study area of Poyang Lake and its floodplain. Pixels numbered from 1 to 10 covers the whole Poyang Lake area and those from 11 to 36 covers the floodplain.

4.2   Data set and the study area

The study area is the Poyang Lake floodplain (see the rectangles in Fig. 4.1, the rectangle area is the Equal-Area Scalable Earth Grid (EASE-Grid) with spatial resolution of 25km (Brodzik and Knowles, 2002)), located between 28.048° N to 29.384° N, and from 115.444° E to 117.007° E. There is a clear dry season from October to next January and the flooding season is from March to June.

Currently, there are two sensors providing brightness temperature measurements around 37 GHz with dual polarization: the Special Sensor Microwave Imager (SSM/I) and The Advanced Microwave Scanning Radiometer for EOS (AMSR-E). In this case the SSM/I on board the Defence Meteorological Satellite Program (DMSP) F13 satellites was used. It is a seven channel four-frequencies radiometric system providing global observations at a constant incidence angle of 51.2° since July 1987 (Hollinger et al., 1990). The period covered by our case-study is from 2001 to 2008, mainly concerning the start observation by the Moderate Resolution Imaging Spectroradiometer (MODIS) (in June 2000) and the enclosure of the Three Gorge Dam (in November 2002). The footprint of the 37 GHz observations is about 28 km by 37 km, with geo-location uncertainty of about 6 km. The data acquired at 05:58:00 LT was used in this case. The AMSR-E on board the Aqua

satellite measures radiation since May 2001 at six frequencies in the range 6.9 – 89 GHz, all at dual polarization, with a constant incident angle of 55˚. The 36.5 GHz data has a footprint of 14km by 8km and is acquired by AMSR-E at local solar time of 1:30:00 LT. SSM/I brightness temperature has been inter-calibrated with that of AMSR-E and both are registered into the EASE-Grid system. Thus, for the same pixel area, the time series of PDBT at similar frequencies (37 GHz for SSM/I while 36.5 GHz for AMSR-E) should have similar fluctuations. The PDBT time series at the same pixels are compared to validate the consistency, observation bias and possible noise of these two sensors. The daily SSM/I and AMSR-E data gridded into the EASE-Grid (Brodzik and Knowles, 2002) were downloaded from the National Snow & Ice Data Centre (NSIDC) (Armstrong et al., 1998). Poyang lake area covers 10 pixels of EASE-Grid data as indicated in Fig. 4.1 by the white numbered rectangles. The upstream area of Poyang Lake covers the four major tributary river systems coming from west, south-west, south-east and east directions, indicated in Fig. 4.1 by the gray shading rectangles numbered with white color.

Normalized Difference Vegetation Index (NDVI) is needed to estimate the fractional area of vegetation and vegetation transmission function as Chapter 2 shows. It was derived from the MODIS data: the MOD09A1 8-day composite surface reflectance data of bands 1 – 7. Because of the non-linear dependence of NDVI on red and near-infrared reflectance, the surface reflectance will be averaged first over each EASE-Grid and then used to calculate its NDVI.

4.3   The overall method and the evaluation

4.3.1 The overall method

To retrieve daily fractional area of WSS with the two-step model, daily noise-free NDVI, PDBT and vertical Brightness Temperature (BT) need to be obtained at first. Thus the overall method includes three steps as:

1. *Gap fill and noise removal*: TSAP was applied to both PDBT and vertical BT at 37 GHz, in order to derive daily noise-free data as described in Chapter 3. The parameters of TSAP were identified in section 4.2.2. HANTS algorithm was applied to NDVI aggregated from MOD09A1, in order to derive daily cloud-free NDVI. HANTS parameters used to reconstruct NDVI was described by Shang et al. (2015).

2. *Retrieve the Polarized Difference Effective Emissivity*: After identifying the land surface temperature using vertical BT at 37 GHz with Eq. (2.11), the vegetation fractional area and the vegetation transmission function using NDVI data with Eq. (2.12) and Eq. (2.28) respectively, daily Polarization Difference Effective Emissivity (PDEE) can be retrieved using the simplified radiative transfer model (Eq. 2.9).

3. *Retrieve the fractional area of the WSS from PDEE*: The fractional area of WSS can be derived from PDEE with linear model (Eq. 2.29).

The parameterization of the two-step model for the Poyang Lake floodplain had been illustrated in Chapter 2. According to Chapter 3, there are two stages in the TSAP: 1) boxcar filtering; 2) HANTS reconstructing. The parameters in TSAP were derived at first (Sect. 4.3.2). The overall method was used to retrieve the WSS area within the Poyang Lake and evaluated by comparing the retrieval with the lake area observed from MODIS and ASAR, after each step of TSAP applied to PDBT data (Sect. 4.3.3). The vertical BT used in this evaluation was the noise-free data processed by TSAP, so that to reduce the influences of atmosphere on the estimation of surface temperature.

4.3.2 Implementation of TSAP

The TASP method uses two filters to remove the atmosphere signal, observation gaps and errors in each pixel: 1) the modified boxcar filter; 2) the HANTS algorithm as Chapter 3 shown. In the first stage of TSAP, the DFT of 37 GHz PDBT time series was used to identify the spectral range associated with gaps, i.e. $L = 8days$ in our case. This value was rather uniform in the Poyang Lake area, which gave a minimal filter length of 10days, according to Eq. (3.10). In the second stage of TSAP, the DFT of the time series of rain-gauge data was used to identify the frequency range associated with the atmospheric signal. It is assumed that the rain-gauge data observed in the pixel numbered with 6 in Fig. 4.1 could represent precipitation over the whole Poyang Lake area, i.e. pixels numbered from 1 to 10 in Fig. 4.1, so that the spectral features of PDBT time series can be identified for each pixel. The threshold frequency separating the surface and atmospheric signals can be estimated by analyzing the difference between the power spectrum of precipitation time series and the filtered PDBT time series. It was found that this threshold value was almost constant in the Poyang Lake area and it gave a period equal to 73 days. All the harmonic components at frequencies lower than this threshold were due to the surface signal. The harmonic components listed in the 2nd sample pixel (Table 3.1) were also due to the surface signal, but with periods < 73days. These harmonic components (Table 3.1) were also found in the spectral features of the surface signal in other pixels covering the lake area. It is reasonable, since the lake area and the vegetation types change in a similar way for these pixels. Thus, the harmonic components with periods > 73 days and those associated with the surface signal of the 2nd sample pixel in Table 3.1 were used to extract the surface signal with HANTS for each pixel in the lake area.

4.3.3 Evaluation of the overall Method

It is difficult to validate the retrieved WSS area, since no ground measurements are available for an area as large as 25km ×25km. Yésou et al. (2011) combined the water body observation from MODIS and ASAR data to delineate the seasonal changes of Poyang Lake area, which can be a ruler to evaluate our retrieval. In the overall method, two aspects need to be evaluated: 1) the performance of TSAP; 2) the performance of the two-step model. To evaluate the performance, the overall method was applied to the ten pixels

covering the Poyang Lake to retrieve its WSS area using the PDBT observations at each stage of TSAP.

The WSS area retrieved with three PDBT data sets, i.e. original PDBT observations, boxcar-filtered PDBT data and HANTS-reconstructed PDBT data, was compared with the lake area estimated with MODIS and ASAR images by (Yésou et al., 2011) (Figure 4.2). Though the R^2 is higher when using the original PDBT, its Relative Root Mean Squared Error (RRMSE) is also larger (Table 4.1) and the retrieved WSS area is much less than the observed lake area, while WSS area is the sum of lake area, wetland and water saturated soil, i.e. it should be WSS > lake area. The retrieved WSS areas with the HANTS reconstructed surface signal has the lowest R^2 value but the best RRMSE, and samples are located around the 1:1 line (Figure 4.2). This indicates that TSAP gives a more accurate estimate of WSS area than the raw 37 GHz PDBT observations. R^2 of three stages was all above 0.77. This proves that the two-step model can be used to retrieve the WSS area from PDBT observations at 37 GHz.
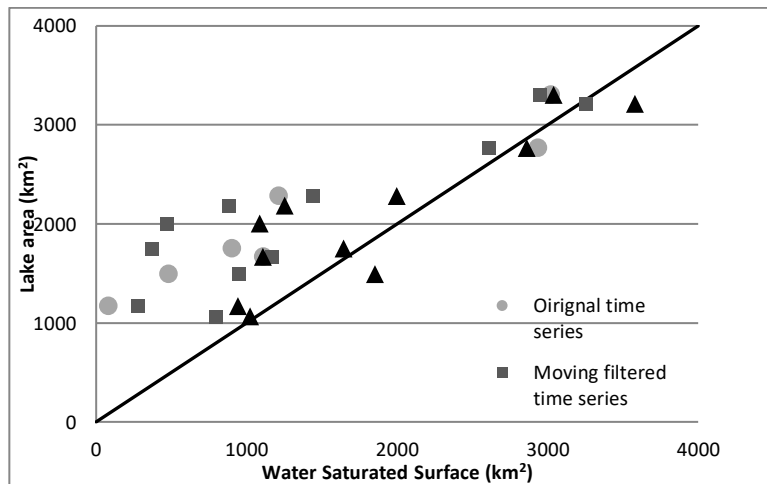
Figure 4.2: Retrieved Water Saturates Surface at Poyang Lake from original PDBT data, filtered PDBT and HANTS reconstructed PDBT, compared with lake area observed from the MODIS and ASAR by Yésou et al. (2011).

Table 4.1: Correlation of retrieved Water Saturated Surface at Poyang lake with PDBT in different stages of TSAP and lake area observed by Yésou et al. (2011), and their relative RMSE.

	R^2	RMSE	Relative RMSE
Original Time series	0.9195	802.14	38.48%
Moving filtered	0.7845	866.93	41.59%
HANTS Reconstruction	0.7747	479.33	22.99%

4.4   Inundation pattern of the Poyang Lake floodplain

Through the evaluation in the above section, it can be concluded that the overall method can be used to retrieve WSS. Another implementation problem is that the rain-gauge data cannot cover all pixels in a floodplain. The used assumption that rain-gauge data at limited locations can represent precipitation over the whole study area may not be proper to identify the spectra features of the surface signal in the whole Poyang Lake floodplain, due to the large spatial variability in atmosphere conditions. On the other hand, the spectral features of the surface signal may be uniform over the whole floodplain, since the wetness in the floodplain is dominated by the same monsoon system. Under the same climate zone, the vegetation phenology may also be similar. In this section, the uniform spectral features of the surface signal were identified (Sect. 4.4.1) and were evaluated by comparing the retrieved WSS area with the lake area observed from MODIS and SAR (Sect. 4.4.2). The observations between SSM/I and AMSR-E were compared, in order to validate the possible errors in the microwave radiometers (Sect. 4.4.3), which may also lead to the uncertainty in the overall method. After the evaluation, the overall method can be applied to retrieve daily WSS area in whole floodplain (Sect. 4.4.4) and to study the inundation pattern.

4.4.1 The uniform spectral features of the surface signal

In many floodplains, rain-gauge data cannot cover each 25km×25km pixel within the whole floodplain. Thus, uniform spectral features of the surface signal need to be identified from samples with rain-gauge data, e.g. the two sample pixels in Chapter 3 for the Poyang Lake floodplain. In the implementations of TSAP at crop land and lake area (Chapter 3), the threshold periods for the spectral features of the surface signal in the lower frequency are the same at these two samples, i.e. 73 days. Thus, harmonic components with period ≥ 73 days were the uniform spectral features of the surface signal in the lower frequency domain. The variability in the spectral features of the surface signal lies in higher frequency domain, mainly due to the different spectral features of the atmosphere signal, according to the implementations of TSAP in Chapter 3. The significant differences in the spectral features of the atmospheric signal between two samples were observed in period range of [20 days, 30 days] (Fig. 3.8), and these spectral features of the atmosphere signal had large powers. This indicates that the spatial variations in the atmospheric signals are mainly in high frequency domain. On the other hand, the spectral features of the surface signal in this high frequency range had very small powers (Fig. 3.9). Thus, to eliminate the spatial variation due to the atmospheric signals, only the spectral features of the surface signals within the range of [30 days, 73days] (Table 3.1) are used to identify the uniform spectral features. The intersection of the spectral features of their surface signals in this range, i.e. period = 46 days and 31 days, was chosen as the uniform spectral features. The harmonic component with period of 64 days was also a member of the uniform spectral features in this area, since it is a very important component for crop land as Fig. 3.9 shown. Above all, the uniform spectral features of the surface signal in the floodplain have periods ≥73days, and periods = 64days, 46days, and 31days.

4.4.2 Evaluate the uniform spectral features

The uniform spectral features of the surface signal had been identified in the above section, according to the DFT of PDBT time series at two sample pixels, i.e. lake area and the crop land. In the implementation of the TSAP in Chapter 3 and section 4.3.2, the spectral range of observation gaps was constant for the studied samples, i.e. *L=8day*, thus the length of the modified boxcar filter was 10 days for all pixels. Using the filter length and the uniform spectral features, TSAP can be applied to the whole floodplain. To evaluate the uniform spectral features, the WSS area enclosing the Poyang Lake (rectangles numbered from 1 to 10 in Fig. 4.1) was retrieved from 2001 to 2003 using the overall method, and was compared with the Poyang Lake area observed from MODIS and ASAR data (Huber et al., 2012; Yésou et al., 2011; Yesou et al., 2013). The trend of our retrieved WSS area was close to the observed Poyang Lake area as shown in Fig. 4.3. The RMSE of the retrieved WSS area is 361.22 Km^2 or RRMSE 17.74%. The RRMSE using the uniform spectral features is better than that using the derived spectral features of the surface signal for the lake area as shown in section 4.3.3. The uniform spectral features of the surface signal include longer periods than the spectral features derived from the lake area. When using the uniform spectral features, the overall method smooths the short-term variations in the retrieved WSS area. Meanwhile, most of the reference lake area is observed from 8-day composition of MODIS reflectance data, which also smooth the short-term variation in time. Thus, using the uniform spectral features has the better RRMSE.

A wet case and dry case of the pixel region centered at 29.0485° N and 116.0954°E was shown in Fig. 4.4. In the 'wet case' of July 4th, 2002, the fractional area of WSS, which is calculated from SSM/I (65.28%), was close to the fractional area of open water (58.81%) observed from MODIS NDVI image. However, in the dry case of October 24th 2002, the fractional area of WSS (46.24%) was much larger than that of open water (21.85%) observed from NDVI. That's because, the degraded lake area become wetland and is occupied by aquatic vegetation, mainly *Phragmites*. An optical sensor, like MODIS, cannot observe the standing water beneath the vegetation canopy, while a microwave radiometer can penetrate it. Thus, the WSS area is close to the total area of open water and the wetland vegetation.
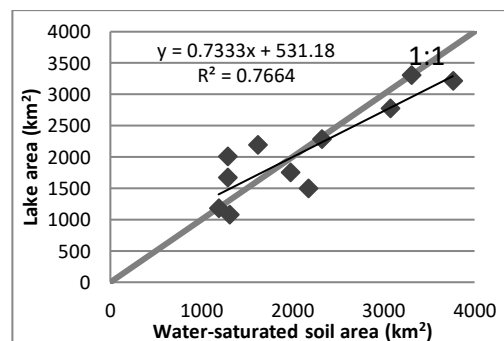
Figure 4.3: Scatter plot of lake area estimated with MODIS and ASAR data by Yesou et al. (2011) and water-saturated surface calculated from SSMI 37 GHz
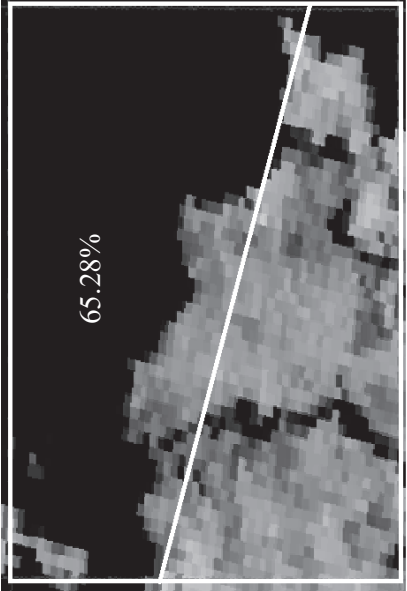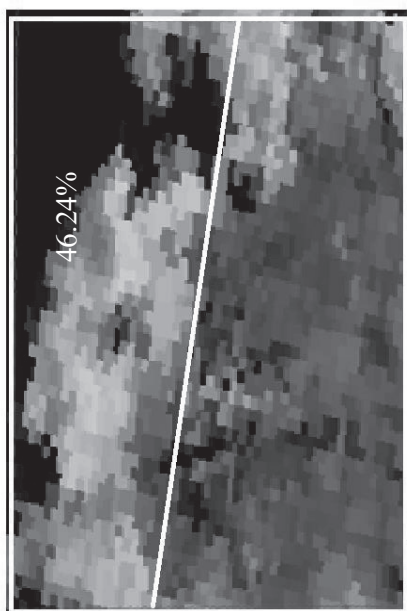
DOY	July 4th 2002	October 24th 2002
Image	65.28%	46.24%
label	Green vegetation	Vegetation soil mixture	Open water

Figure 4.4: The wet and dry cases of the pixel numbered with 5 at Poyang lake (Fig. 4.1) with corresponding NDVI image. The White rectangle is the pixel area of SSM/I 25KM EASE-Grid in Poyang Lake area (Fig. 4.1) at July 4th and October 24th, 2002. The upper part of the red rectangle represents the percentage (the numbers outside the parenthesis) of the water saturated soil and standing water area, which is calculated from SSM/I. The NDVI image is obtained from MOD09A1 with spatial resolution of 500m. The fractional open water area calculated from NDVI is shown in the parenthesis.

4.4.3 Comparison between SSM/I and AMSR-E

The difference between our retrieved WSS area and the lake area observed from MODIS and ASAR data is mainly caused by three factors: 1. The study area is different: Yesou et al. (2011) focus on the Poyang Lake area, while our study area does not only cover the Poyang Lake, but also the wetland and cropland adjacent to Poyang Lake as Fig. 4.1 show; 2. The observed features are different: the MODIS and ASAR capture the open water, while the total area of water saturated soil at surface and inundated area is retrieved, i.e. open water, flooded vegetation and the water saturated soil cannot be discriminated using our model; 3. The temporal resolution is different: SSM/I data supplies daily brightness temperature data, while the MODIS data used by Yesou et al. (2011) is 8 day composite and ASAR has 35 days repeat orbit. Thus, near daily monitoring is one of the advantages of using 37 GHz microwave radiometer data. Another very important factor is the different impact vegetation on the three types of observation. The MODIS observations cannot penetrate under vegetation. In principle ASAR can capture the backscatter from the water surface underneath the vegetation, but the scattering by vegetation is very strong. Our model takes the emittance of the WSS under vegetation cover into account.

Besides the difference between microwave radiometers and other sensor types, the difference between various microwave radiometers is also interesting. After inter-sensor calibration, the retrieved sea surface temperature from SSM/I and AMSR-E has difference less than 0.5 K (Wentz, 2013), i.e. the difference in radiometers is very small. Though the brightness temperature data of the two radiometers have been both registered into the EASE-Grid system, the IFOV of original data is rather different: 37km×28km for SSM/I while 14km×8km for AMSR-E. Thus AMSR-E observes detailed changes of lake area especially during the dry season. The PDBT of the SSM/I seemed to be saturated earlier than that of the AMSR-E as shown by e.g. the peaks during May to October in Fig. 4.5, probably due to that the AMSR-E observed a higher fractional WSS area in its small IFOV than SSM/I. Taking the peaks in March and November in Fig. 4.5 as an example, the PDBT of SSM/I did not increase simultaneously with the AMSR-E, but 10 days later. In the period of 4/11//2203 – 24/11/2003 (rectangle period in Fig. 4.5), the SSM/I PDBT was about 5 K lower than AMSR-E, with the retrieved WSS area 345 km^2 lower than that from AMSR-E. The time series trend should be almost the same since two sensors both measures before sun rise. Over all comparison samples, our retrieved WSS from of SSM/I was closer to the Poyang lake area observed from MODIS and SAR than that from AMSR-E, except that samples in November 2003. Thus, there is need of future work on the analysis of these two data sets.
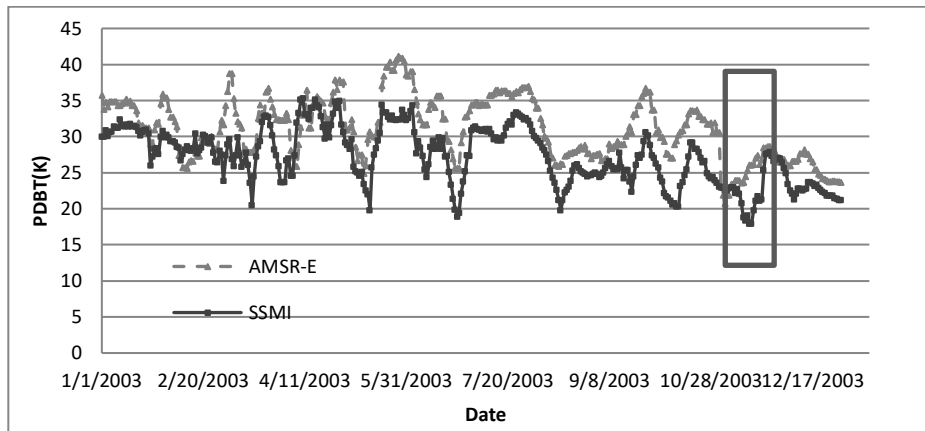
Figure 4.5: Boxcar filtered PDBT time series: comparison of AMSR-E and SSM/I measurements

4.4.4 The inundation pattern in the Poyang lake floodplain

Through the comparison between WSS area and the Poyang Lake area observed from higher spatial resolution data, it can be concluded that the uniform spectral features can be applied to the Poyang Lake floodplain. The retrievals of WSS area from SSM/I PDBT data had better performance than from AMSR-E data, except one samples, thus SSM/I data was preferred in our study. To observe the inundation pattern in the floodplain, the WSS area in pixles of the upstream floodplain, which were indicated in Fig. 4.1 by the EASE grid-cells numbered from 11 to 36, was retrieved with the overall method. This upstream area includes the major tributary river systems from West, South-West, South-East and East directions. The downstream area is the lake area indicated by the EASE grid-cells numbered from 1 to 10.

The time series of the Poyang Lake area from 2001 to 2008 had similar fluctuations with the upstream WSS area (Fig. 4.6). For most periods, the Poyang lake area increased with the upstream WSS area. This is proved by the cross correlation analysis between these two time series (Fig. 4.7): the maximum cross correlation values from 2001 to 2008 were all higher than 0.5 and the time lag was no more than 5 days. The time lag indicates that the two time series are better correlated if shifted by this time lag relatively to the other. In this case, it means that the increase of WSS area at upstream catchment will come earlier than that of Poyang lake area.
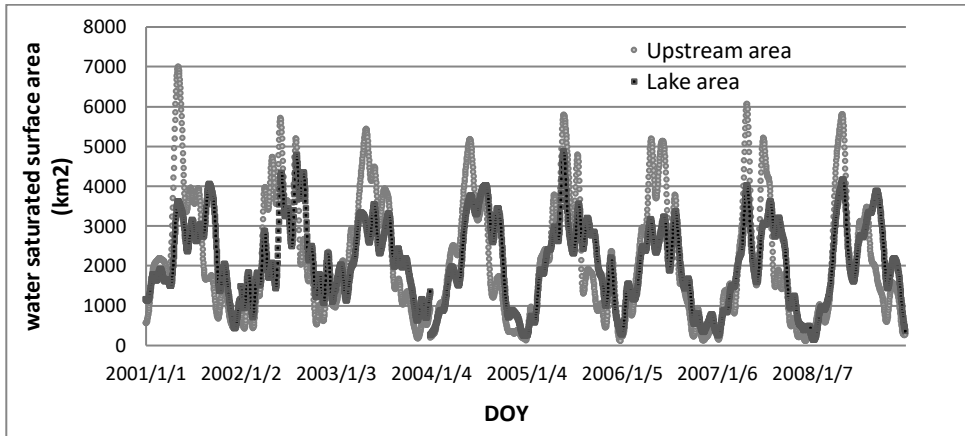
Figure 4.6: Comparison in Water Saturated Surface between in upstream and at Poyang Lake.
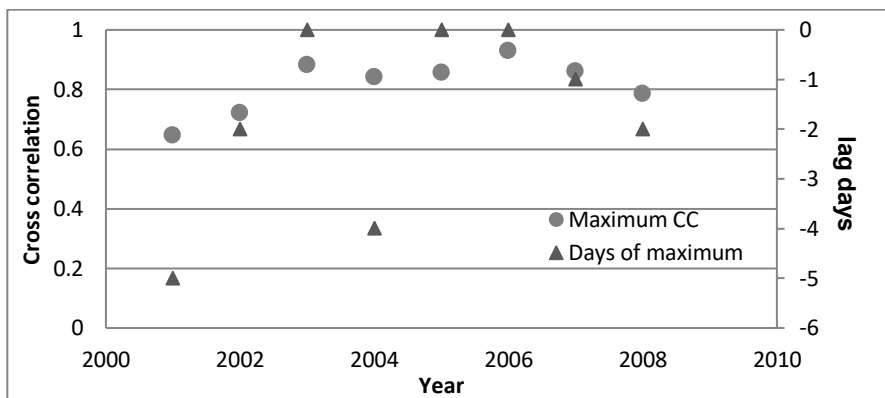
Figure 4.7: Maximum cross correlation values between time series of Water Saturated Surface in upstream and at Poyang Lake from 2001 to 2008, and the time-lag days of maximum value occurs.

There were some peaks of the upstream WSS area that did not lead to the simultaneous increasing of lake area in Fig. 4.6. The reason is that the water source changes for the lake area. According to the long-term hydrological data in the Poyang Lake, before July of each year, the water from upstream of the Poyang Lake flood plain (it is the sub basin of the Yangtze River basin) is the major source of lake. During this time, the lake area fluctuation was close related to the upstream WSS area in most years. There were some spikes in upstream not leading to same response in the Poyang Lake, for example in the end of April of 2002 and 2003. That is because the surface runoff and stream flow had been consumed by irrigation and other human activities, before reaching the lake. Since August in each year, the Poyang lake area was supplied by water flow from both the upstream and the Yangtze River. Thus, the asynchronism between upstream WSS area and the lake area

becomes larger. For example, the spikes of lake area in September of 2001 and 2008 are probably caused by the water flow from the Yangtze River.

It is also interesting to observe that since 2003, the maximum cross correlation value increased significantly. The major reason why the correlation coefficient changed after 2002 is that the water supplied by the Yangtze River changed due to the building of the three George dam. The Three Georges dam was closed to store water from November 2002 to 2006. Water flow from the Yangtze River to the Poyang Lake was limited in the period from August to September, i.e. the flooding season of the Yangtze River. Thus, the water source of the Poyang Lake was mainly from the upstream catchment of the Poyang Lake floodplain and the correlation coefficients increase from 2003 to 2006. Since 2007, the dam stopped storing water and released stream flow as usual. Then an obvious decrease occurs in the coefficients of Fig. 4.7. This again proved that the water supplement from the Yangtze River will significantly influence the lake changes.

4.5   A case study of observing flood propagation

The temporal evolution of inundated area between up and down stream in the Poyang Lake floodplain had been studied in the above section, using the retrievals of the WSS area from PDBT at 37 GHz. The spatial evolution of WSS area over the whole floodplain is also interesting to study the propagation of flood waves and for flood early warning. Considering the coarse spatial resolution of the SSM/I data, the WSS area in the Dongting Lake and Poyang Lake floodplains were shown in this case. The Poyang Lake and Dongting Lake floodplains are in subtropical climate zone and influenced by the same monsoon systems, thus the uniform spectral features of the surface signal that were identified for the Poyang Lake floodplain can be directly applied in the Dongting Lake floodplain. According to the local hydrologic records, During April and May 2010, heavy rainfall in these two floodplains led to river stages in these two floodplains higher than the warning level, while in normal years, there is no flooding during this period. The WSS area of these two floodplains in this period of 2010 (Figure 4.8) was calculated and compared with that in a normal year, e.g. 2011 (Figure 4.9). The extension of WSS area in these two floodplains shows clear difference in 2010 and 2011. Large flooded area, i.e. large WSS area, can be observed in 2010, which lasts almost one month from 23rd April to 25th May. In 2011, however, large WSS area was primarily observed in the upstream of these two floodplains (i.e. south part of the southern floodplains) and the mountain area between these two floodplains, because rainy season starts in April and monsoon system brings rainfall from south to north. This difference agrees very well with the local hydrologic and meteorological records. Thus it can be concluded that the WSS area follows well with the propagation of flood and can be used for flood early warning
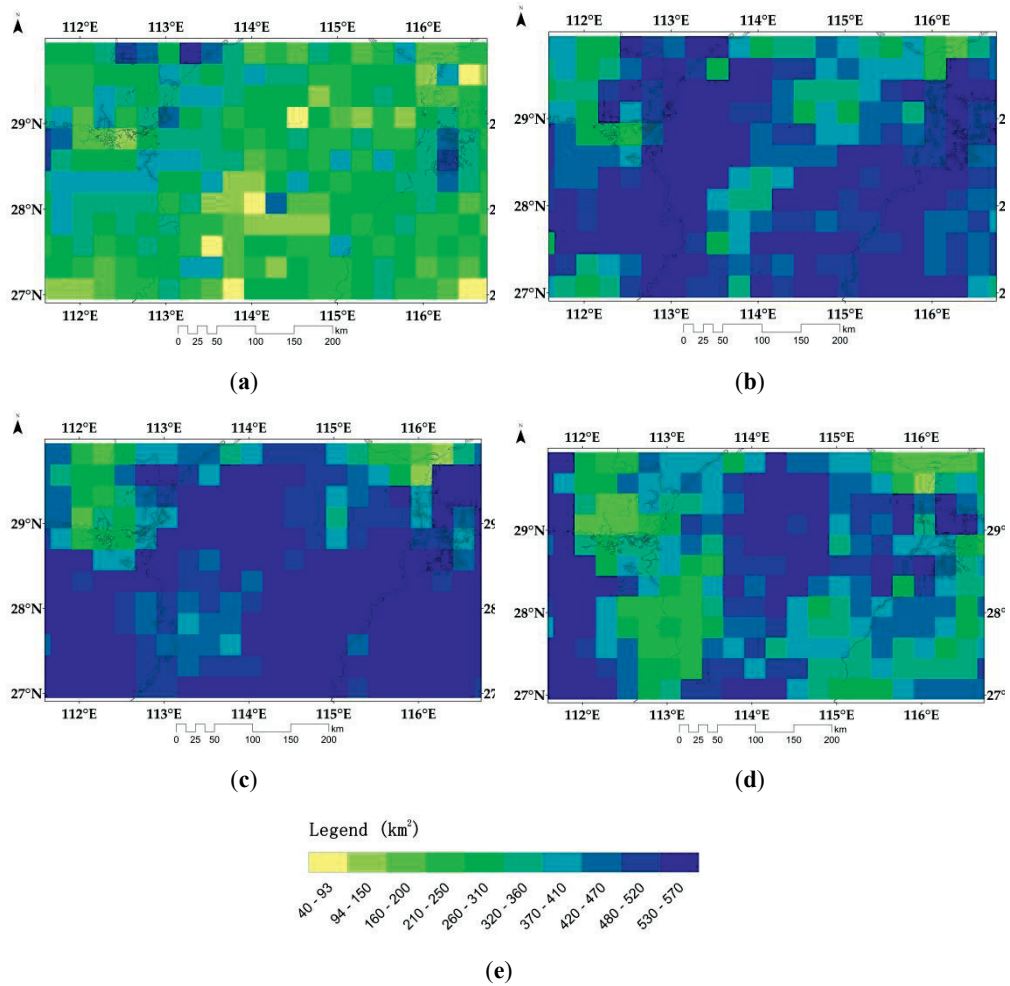
Figure 4.8: The Water Saturated Surface (WSS) area within each 25km × 25km pixel on: 7 April (a); 23 April (b); 9 May (c); and 25 May (d) of 2010 in the Dongting Lake and Poyang Lake floodplains; (e) the legend of images from (a) to (d). Dongting Lake is located on the left side and Poyang Lake is located on the right side, with their boundary lines shown in each image.
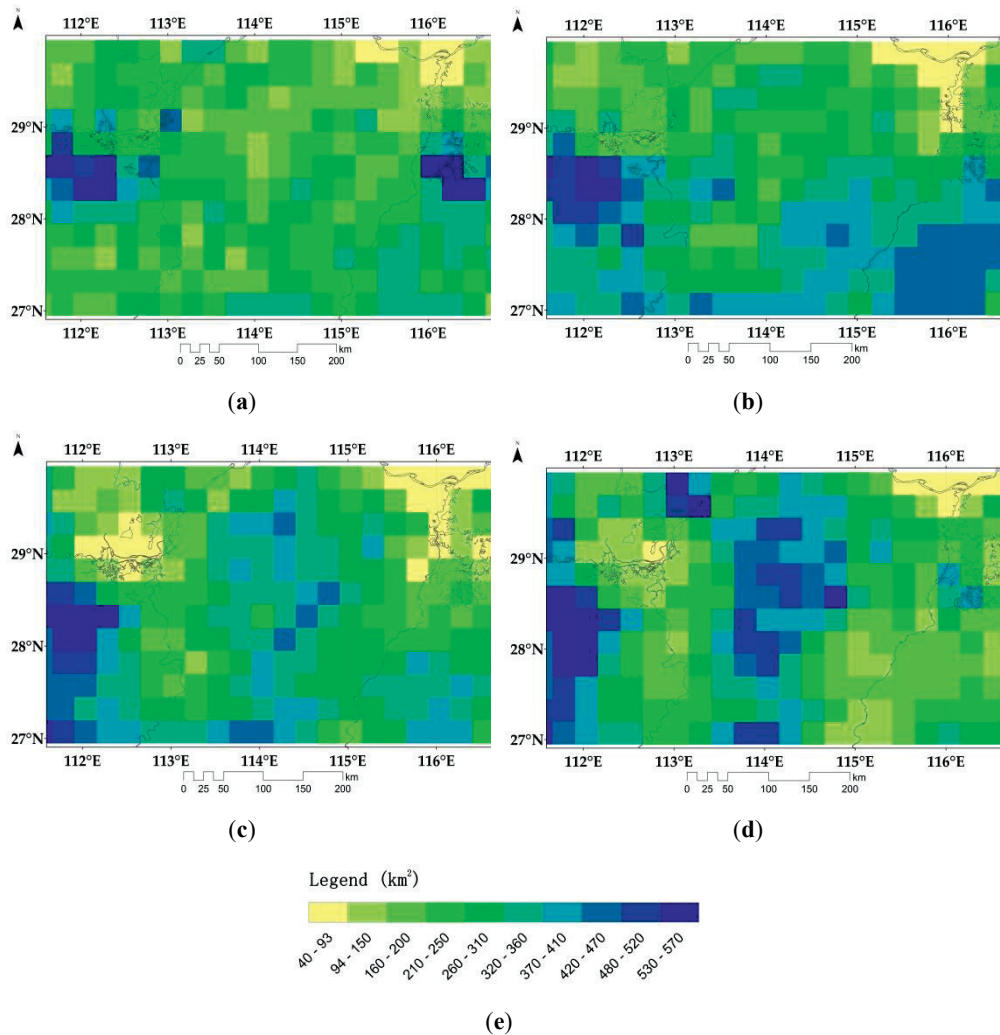
Figure 4.9: The Water Saturated Surface area within each 25km × 25km pixel on: 7 April (a); 23 April (b); 9 May (c); and 25 May (d) of 2011 in the Dongting Lake and Poyang Lake floodplains; (e) the legend of images from (a) to (d). Dongting Lake is located on the left side and Poyang Lake is located on the right side, with their boundary lines shown in each image.

4.6   Conclusions

In this chapter, the overall method combining the TSAP and the two-step model that have been developed in the previous chapter was used to retrieve daily WSS area from

PDBT at 37 GHz, so that to study the inundation pattern in the Poyang Lake floodplain. To evaluate the overall method, the WSS area covering Poyang Lake was retrieved with the PDBT in three stages of TSAP — original PDBT, boxcar-filtered PDBT and HANTS reconstructed PDBT, and was compared with the lake area observed from MODIS and ASAR data respectively. The rain-gauge data at Boyang meteorological station was used to identify the spectral features of the surface signal in the lake area. R^2 between the retrievals and observed lake area was higher than 0.77 and RRMSE was reduced from 38.5% to 23.0%, when using the PDBT processed by each step of the TSAP. The accuracy of the overall method is acceptable, taking the difference in the surface objects observed by microwave radiometers and other sensor types into account.

Rain-gauge data is needed by TSAP to identify the spectral features of the surface signal in PDBT time series at each pixel. To solve the problems of limited rain-gauge data available in a large floodplain, e.g. the Poyang Lake floodplain, the uniform spectral features of the surface signal was identified as the intersection of the spectral features of the surface signal at pixels having rain-gauge data. The overall method using the uniform spectral features was evaluated again by comparing the retrievals of the WSS area covering Poyang Lake with the lake area observed by higher spatial resolution data, with R^2 of 0.76 and RRMSE of 17.7%. This method was then applied to retrieve the daily WSS area at upstream Poyang Lake floodplain. The WSS area at upstream catchment and the lake area were highly correlated with a time lag of 3 – 5 days. The correlation level was influenced by the water flow in the Yangtze River. The spatial evolution of the retrievals of the WSS area in the Dongting Lake and Poyang Lake floodplains agreed with the propagation of flooding in the spring of 2011. The retrieved WSS area can be an indicator of surface water bodies and be used for flood early warning in large floodplains.

Chapter 5

The Discrete Rainfall-runoff Model

5.1 Introduction

In many conceptual hydrological models, such as Xinganjiang model (Zhao, 1977, 1984), Probability Distributed Model (PDM) (Moore, 2007, 1985), TOPMODEL (Beven and Kirkby, 1979; Beven et al., 1984), Variable Infiltration Capacity (VIC) (Liang et al., 1994; Wood et al., 1992) and ARNO (Todini, 1996) , water saturated soil is a conceptual parameter that determines the fast runoff produced after a storm, i.e. overland flow and fast subsurface flow. Fractional area of water saturated soil can be derived from regional water storage with some physically parameters, such as the topography-soil index in TOPMODEL (Sivapalan et al., 1987) or the infiltration factor in VIC (Liang et al., 1994; Wood et al., 1992). It is, however, difficult to measure regional water storage precisely (Eagleson, 1978) and to optimize these physical parameters for various catchments. In the Chapter 4, it has been shown that the fraction area of Water Saturated Surface (WSS) can be retrieved from the Polarization Difference Brightness Temperature (PDBT) observed by space-borne microwave radiometers at 37 GHz, after taking the influence of the vegetation and the atmosphere into account (Shang et al., 2015). The WSS area is where inundated area or water-saturated top soil occurs, such as wetlands, ponds, lakes and rivers. WSS area normally occurs in the lower reach of a catchment, which may be directly connected to rivers by channels or on the pathway of surface runoff close to rivers. Precipitation cannot percolate in the WSS area, similar to water saturated soil, thus precipitation falling on WSS area will be drained into rivers directly or became surface runoff quickly. Meanwhile, WSS area also stores water flow produced upstream and by itself, leading to an increase in the

WSS area and modifies peaks of river discharge (e.g. Winter and Valk, 1989). So the WSS area indicates the regional water storage capacity and has a close relationship with stream flow production. The observation, e.g. the retrieval with 37 GHz PDBT, could be a potential input to these conceptual hydrological models towards mitigation of data requirement and model calibration.

The difference between the WSS area and the conceptual water saturated soil is significant. The WSS area only represents the water saturation condition at top surface, while the depth of the conceptual water saturated soil is variable, depending on water storage, soil porosity and the topography (Beven and Kirkby, 1979; Wood et al., 1992). A possible method to bridge this difference is to model regional soil moisture using a soil-canopy-atmosphere model and the observations from Special Sensor Microwave Imager (SSM/I) as shown by Lakshmi et al. (1997a, 1997b). In their studies, microwave at lower frequencies (e.g. 19 GHz), however, were preferred, rather than 37 GHz, because the penetration depth at 37 GHz is too shallow (i.e. 0.08cm – 0.8 cm). The parameterization of the soil-canopy-atmosphere model adds to the difficulty and uncertainty in this approach (see, e.g. Lakshmi et al. (1997a)). Crow and Ryu (2009) used Ensemple Kalman Filter/Smoother (EnKF/EnKS) to correct the prediction of soil water states with soil moisture retrieved from 1.4 GHz radiometer (i.e. Soil Moisture and Ocean Salinity (SMOS)), which together with the correction of precipitation (i.e. a data assimilation system with dual rainfall/state correction procedure) improves the Sacramento (SAC) hydrologic model. This data assimilation system mitigates the difficulty in model calibration, however, its accuracy heavily depends on the retrievals of soil moistures. Hydrological models provide reasonable accurate estimates of soil water content, while model estimates of spatial patterns, like the delineation of inundated areas and wetlands are rather challenging, because of the required hydrological processes require spatially detailed data on soil texture, soil porosity, vegetation and ground water table depth, according to the studies of wetlands in the prairies of North America (Hayashi et al., 1998; Kazezyılmaz-Alhan et al., 2007; Shjeflo, 1968; Su et al., 2000; Winter and Rosenberry, 1995; Winter and Valk, 1989; Woo and Rowsell, 1993). On the other hand, many studies show a straightforward but lagged relationship between the WSS area and the river discharge or stage. The brightness temperature observed by 37 GHz can be directly used to estimate river discharge with a local correction on vegetation and atmospheric influence and a certain time lag (Brakenridge et al., 2007). In chapter 4, the upstream WSS areas were highly correlated with the downstream Poyang Lake area, with a time lag between 3 and 5 days. Many other findings suggested that the inundated area retrieved from microwave observation at 37 GHz might be used directly to estimate river discharge or stage with a certain rating curve and a modification on time lags (e.g. Sippel et al., 1998; Temimi et al., 2005; Vörösmarty et al., 1996). These results suggest also that conceptual hydrological models might be simplified significantly by using the retrievals of WSS area.

The WSS area is the result of comprehensive processes at surface including precipitation, evapotranspiration, regional water storage and drainage. It determines the partition of precipitation into overland and infiltrated flows (Beven and Kirkby, 1979; Liang et al., 1994; Sivapalan et al., 1987; Wood et al., 1992), and modifies stream flow by

storing and gradually releasing water flows (e.g. Winter and Valk, 1989). One advantage of the retrievals with PDBT at 37 GHz is that it provides daily observation. To fully use such high frequency observations of surface wetness condition, a lumped hydrological model, i.e. the discrete rainfall-runoff model, is developed, based on the redistribution of antecedent precipitation. Many hydrological processes result in this redistribution. For example, in a storm event, a fraction of precipitation produces fast flow, i.e. over land flow and fast subsurface flow, while the remaining precipitation is stored in subsurface and ground water and produces subsurface and base flows, during a recession period (Beven and Kirkby, 1979; Moore, 1985; Sivapalan et al., 1987; Sophocleous, 2002; Todini, 1996; Wood et al., 1992; Xu and Singh, 2004). Antecedent precipitation reaches rivers and channels at different times. During the period when overland flow is drained by channels and rivers, a fraction of overland flow may percolate into the subsurface, be stored into lakes, wetlands and reservoirs, i.e. extends WSS area, or be used by human activities (e.g. irrigation). The stored or consumed overland flow will be released to stream flow with a time lag (see e.g. Vörösmarty et al. (1996)). The water stored in soil and ground water interacts with surface water and stream flow through percolation and seepage (e.g. Mertes, 1997; Sophocleous, 2002). These processes redistribute antecedent precipitation within a catchment into its components over different periods of time, which results in the time lag between precipitation and stream flow (Gleick, 1987). The lagged release of overland flow and the interactions between surface and soil layers complicate the redistribution of precipitation in time. On the other hand, observation of WSS area reflects the redistribution of surface water and indicates the interaction of water flow between surface and soil layers (e.g. seepage of subsurface flow and infiltration of surface flow both contribute to the changes of WSS area).

In VIC model, precipitation is partitioned into direct runoff (e.g. overland flow and fast subsurface flow) and slow runoff released from soil layers, according to the regional water storage and the infiltration capacity parameter (Wood et al., 1992). These two parameters are difficult to estimate or calibrate, however, the catchment response to rainfall can also be modelled by some simpler statistical approaches. For example, Jakeman and Hornberger (1993); Jakeman et al. (1990) developed the two component linear model, i.e. quick and slow flows, to simulate the time series of stream flow from the precipitation time series, according to their statistical relationship. The VIC model can take the interaction between water flows and various water storages into account by estimating the regional water storage from satellite observations (e.g. Lakshmi et al. (1997a)) or directly using the retrieved soil moisture with two-layer VIC model (e.g. Liang et al., 1994), while the two component linear model did not take that into account.

The time series of daily or weekly WSS area indicates the changes of regional water storage and evapotranspiration and determines the production of fast and slow flow at surface. Our discrete rainfall-runoff model combines the physical basis of the VIC model with the time series method used by the statistical models, so that to reduce the complication in the calibration for the conceptual models and take the interaction between water flows and various water storages into account. Our model assumes that stream flow integrates the contributions of precipitation or specific component flows within a certain

period. The weight of each contribution to stream flow at a given time constitutes the core of our model and depends on the duration of antecedent precipitation. This duration can vary from days to months. Long duration means a large number of model parameters, which may lead to the problem of overfitting (see Chapter 6). Thus, a relatively short duration is preferred in the model implementation.

Observed ground water table depth and the retrieved WSS area are used to develop the three implementations with increasing complexity. It will be evaluated whether the increasing complexity in the model implementations can reduce the duration of antecedent precipitation required to achieve a reasonable performance in Chapter 6. One advantage of using the retrieved WSS area is that fewer data are required for calibration, compared with other conceptual models, since some complicated hydrological processes, e.g. evapotranspiration and interaction between storage elements, are not described explicitly in our model, but accounted for by the retrievals and by the weights assigned to antecedent precipitation. Moreover, most of the data required in the three implementations can be derived from satellite observations, e.g. precipitation from Tropical Rainfall Measuring Mission (TRMM) (Huffman et al., 2007), the WSS area from SSM/I (Shang et al., 2015) and in the future even stream flow by the Surface Water and Ocean Topography (SWOT) mission (Bates et al., 2014; Gleason and Smith, 2014; Paiva et al., 2015) .

Overall, this chapter is aimed at developing the discrete rainfall-runoff model with the help of the retrievals of WSS area from 37 GHz microwave observations. The discrete rainfall-runoff model is a lumped hydrological model, developed according to the water balance equation and the redistribution of antecedent precipitation in time. The term "discrete" means the contributions of precipitation in a certain period are assigned to time intervals of 10 days or longer. The method applied to retrieve the WSS from 37 GHz PDBT has been described in Chapter 4 and Shang et al. (2015). In this chapter, the discrete rainfall-runoff model was developed based on the water balance equation and the redistribution of precipitation in time, as descriptions in section 5.2. It was explained how to derive the three implementation forms of the discrete rainfall-runoff model in sequence in section 5.3. The calibration and validation of these three implementation forms was demonstrated in the next Chapter.

5.2   The discrete rainfall-runoff model

In the Budyko framework, the change in the regional soil water storage is the difference between precipitation and outflows, i.e. stream flow and evapotranspiration, during a certain period. The period needs to be longer than the time scale of fluctuations in soil water storage, thus the model describes the quasi-steady-state conditions as in Donohue et al. (2007); Eagleson (1978). This requirement on the duration of antecedent precipitation implies that only precipitations in a certain period influence stream flow. It is assumed that this duration is constant for observed stream flows. Taking the redistribution of precipitation in a catchment into account, the water balance equation of each antecedent precipitation can be expressed as:

$$P_i = P_{i,t} = SS_{i,t} + SG_{i,t} + \sum_{j=i}^{j=t} FE_{i,j} + \sum_{j=i}^{j=t} FQ_{i,j} \, ,$$

(5.1)

for integers t, i and j, $t \geq j \geq i \in [t-m, t]$

where P_i is antecedent precipitation occurring at the ith time step; t is the observation time step and m is the longest duration of antecedent precipitation; $P_{i,t}$ is the P_i in a catchment at the tth time step; $SS_{i,t}$ and $SG_{i,t}$ are parts of P_i stored in soil and ground water respectively at the tth time step; $FE_{i,j}$ and $FQ_{i,j}$ are parts of P_i that were used by evapotranspiration and as water discharge respectively at the jth time step; $\sum_{j=i}^{j=t} FE_{i,j}$ and $\sum_{j=i}^{j=t} FQ_{i,j}$ are the cumulated evapotranspiration and cumulated water discharge to rivers due to P_i during the period $[i, t]$.

The VIC model simulates stream flow as the summation of direct runoff from precipitation and base flow from soil layers (Wood et al., 1992). The former one is the contribution of precipitation occurring at the observation time step and the later one integrates the contribution of precipitation in a certain antecedent period. Thus, the stream flow observed at t^{th} time step, i.e. Q_t, can be calculated as the integration of released water flow at this time step due to precipitations in a given antecedent period, i.e. $FQ_{i,t}$, as follow:

$$Q_t = \sum_{i=t-m}^{i=t} FQ_{i,t}$$

(5.2)

Using Eq. (5.1), Eq. (5.2) can be expressed as

$$Q_t = \sum_{i=0}^{i=t} \left[P_i - SS_{i,t} - SG_{i,t} - \sum_{j=i}^{j=t} FE_{i,t} - \sum_{j=i}^{j=t-1} FQ_{i,t} \right],$$

(5.3)

for integers t, i and j, $t \geq j \geq i \in [t-m, t]$

where $i = t$, $\sum_{j=i}^{j=t-1} FQ_{i,j} = 0$. Since $SS_{i,t}$, $SG_{i,N}$, $\sum_{j=i}^{j=t} FE_{i,j}$, and $\sum_{j=i}^{j=t-1} FQ_{i,j}$ are difficult to estimate, the discrete rainfall-runoff model is developed to implement Eq. (5.3) with precipitation as the only input:

$$Q_t = \sum_{i=t-m}^{i=t} w_i \times P_i \, , \text{ for integers } t \text{ and } i, \; t \geq i \in [t-m, t]$$

(5.4)

where

$$w_i = \frac{P_i - SS_{i,t} - SG_{i,t} - \sum_{j=i}^{j=t} FE_{i,t} - \sum_{j=i}^{j=t-1} FQ_{i,t}}{P_i}$$

(5.5)

and w_i is the weight accounting for the contributions of the ith precipitation to observed stream flow at the tth time step, taking into account the other terms of the catchment water

balance. Eq. (5.4) means that the stream flow at t^{th} time step is due to the contributions of antecedent precipitations during a certain constant period, i.e. $i \in [t - m, t]$. The evapotranspiration and interactions between storage elements are not represented explicitly by the weights, but contribute to determine the weight value. The weights as Eq. (5.5) shows can have positive or negative values, which indicate either water discharge (positive value) or recharge (negative value) to stream flow within the whole catchment. The negative values in Eq. (5.5) indicate the interaction between stream flow and the water storage in a catchment. Stream flow, which is immediately produced by P_i (e.g. overland flow) and slowly produced by P_i stored in soil and ground water (e.g. subsurface and base flows), may recharge soil layers and ground water in the lower reach of a catchment under consideration (Mertes, 1997; Sophocleous, 2002), or be stored in lakes and reservoirs and released later on (Vörösmarty et al., 1996). For example, in the spring, the water table depth is higher than river water level in the upper catchment, i.e. groundwater is released to river, while in the lower catchment, groundwater table depth is lower than the river water level, i.e. stream flow recharges soil and ground water. Human activities intensify the interaction between surface water and subsurface. Irrigation system allocates surface water from rivers and channels to crop land in the lower catchment, so that water flow released from upper catchment is used for evapotranspiration and recharged subsurface and ground water in the lower catchment. Thus, negative weight values are one of the important factors in our model.

5.3   The three implementations

5.3.1 First implementation of the discrete rainfall-runoff model

The weights in Eq. (5.4) can be estimated by calibrating this conceptual model with observed stream flow and precipitation using the linear recursive regression method (Young, 1984), if the influence period of antecedent precipitation, i.e. m, is known. In the studies of water balance in a catchment (see e.g. Donohue et al. (2007); Eagleson (1978)), m was normally set as one year. When m is so large, it might lead to the problem of overfitting in our model. To avoid this problem, the duration of antecedent precipitation is reduced by introducing the base flow released by ground water. It is assumed that precipitation in a long antecedent period influences stream flow through ground water. Based on that, the first implementation of the discrete rainfall-runoff model is developed from Eq. (5.4) as:

$$Q_t = \sum_{i=t-m}^{i=t} w_i \times P_i + Q_t^b \text{ , for integer } t \in [t_1, t_2] \qquad (5.6)$$

where

$$Q_t^b = k_b \times G_t + B$$

Q_t^b is the base flow produced from the ground water and estimated using observed ground water table depth G_t at t^{th} time step as a linear reservoir with a releasing factor, i.e. k_b, plus a constant flow, i.e. B; m is a constant value that represents the longest duration of antecedent precipitation; t_1 and t_2 are the start and end time of annual time series; w_i has the same meaning as in Eq. (5.5). For each t, the antecedent precipitation is in the time interval [t-m, t]. Thus, m, i.e. the duration of antecedent precipitation, is an inherent parameter of the model in Eq. (5.6) and needs to set before running the model. The weights set, i.e. $[w_{t-m}, w_{t-m+1}, \cdots, w_t]$, is constant for all t, once the duration of antecedent precipitation, i.e. m, is defined, so that Eq. (5.6) can be calibrated with an annual time series.

As Eq. (5.6) shows, the ground water reservoir is described by using observed ground water table depth and is only due to precipitations older than the $(t$-$m)^{th}$ time step. In the case that our first assumption in the first implementation is not satisfied, the releasing factor and constant flow, i.e. k and B, in Eq. (5.6) needs to be calibrated to balance the proportion of base flow related to the precipitation events in the time interval [t-m, t] with that related to older precipitation events. This indicates that this model describes the fluctuations of the regional ground water table depth, rather than its spatial pattern. The ground water table depth used by Eq. (5.6) may not be an accurate spatial average over the whole catchment, since a limited number of field measurements of ground water table is used to estimate k and B in Eq. (5.6).

5.3.2 Second implementation of the discrete rainfall-runoff model

The first implementation was developed by taking the component flow with the slowest response to precipitation, i.e. base flow, into account. The WSS area describes the water saturation condition at the surface, which determines the partitioning of precipitation into overland and infiltrated flow (Beven and Kirkby, 1979; Liang et al., 1994; Moore, 1985; Sivapalan et al., 1987; Todini, 1996). The overland flow and the infiltrated flow are drained by rivers and channels with a different time lag, because the water flow velocity at the surface is faster than that in the soil (Sophocleous, 2002). The overland flow provides a fast way for precipitation to reach river, while the infiltrated flow provides a slow way. The first implementation may be improved, when these component flows are specified, instead of precipitation in Eq. (5.6). Thus, in the second implementation, precipitation in Eq. (5.6) was replaced with the tow component flows using the fraction of WSS area as:

$$Q_t = \sum_{i=t-m}^{i=t} \beta_i^{21} \times Q_i^O + \sum_{i=t-m}^{i=t} \beta_i^{22} \times Q_i^I + Q_t^b \text{ , for integer } t \in [t_1, t_2] \tag{5.7}$$

where

$$Q_i^O = WS_i \times P_i$$

$$Q_i^I = (1 - WS_i) \times P_i$$

Q_i^O and Q_i^I are parts of precipitation (i.e. P_i), determined by the fraction of the WSS area (i.e. WS_i); β_i^{21} and β_i^{22} are the weights of overland (i.e. Q_i^O) and infiltrated flow (i.e. Q_i^I))

at the ith time step, respectively. In Eq. (5.7), all precipitation falling on WSS area is transformed into overland flow, which will be drained into rivers quickly or be stored in WSS area, similar to lakes and wetlands. The stored overland flow will extend the WSS area observed in the next time step, i.e. reduce the water storage capacity of a river basin. Precipitation falling outside WSS area percolates into soil layers, which produces both fast and slow subsurface flow from soil layers. The interception by the vegetation canopy is not taken into account in Eq. (5.7).

Q_i^O and Q_i^I are also redistributed in time by a catchment after they are produced. The contribution of produced overland and infiltrated flow to stream flow is a function of time, which is demonstrated by the weight set, i.e. $[\beta_{t-m}^{21}, \beta_{t-m+1}^{21}, \cdots, \beta_t^{21}]$ and $[\beta_{t-m}^{22}, \beta_{t-m+1}^{22}, \cdots, \beta_t^{22}]$. These weight sets reflect that the storing and releasing of component flows from surface (i.e. lakes, wetlands and reservoirs) and soil layers. Thus, similar with the redistribution of precipitation in Eq. (5.1), the redistribution of overland flow, i.e. $Q_{i,t}^O$, over the whole catchment after a certain period of time, can be expressed as:

$$Q_i^O = Q_{i,t}^O = OW_{i,t} + OS_{i,t} + OG_{i,t} + \sum_{j=i}^{j=t} OE_{i,j} + \sum_{j=i}^{j=t} OQ_{i,j} \, ,$$

$$(5.8)$$

for integers t, i and j $t \geq j \geq i \in [t-m, t]$

where $OW_{i,t}$, $OS_{i,t}$, and $OG_{i,t}$ are parts of Q_i^O stored at surface (e.g. lake and reservoir), in soil layers and in ground water respectively at the tth time step; $\sum_{j=i}^{j=t} OE_{i,j}$ and $\sum_{j=i}^{j=t} OQ_{i,j}$ are the cumulated evapotranspiration and cumulated stream flow from Q_i^O during the period $[i, t]$. The redistribution of infiltrated flow, i.e.$Q_{i,t}^I$, over the whole catchment after a certain period of time can be expressed as:

$$Q_i^I = Q_{i,t}^I = IW_{i,t} + IS_{i,t} + IG_{i,t} + \sum_{j=i}^{j=t} IE_{i,j} + \sum_{j=i}^{j=t} IQ_{i,j} \, ,$$

$$(5.9)$$

for integers t, i and j $t \geq j \geq i \in [t-m, t]$

where $IW_{i,t}$, $IS_{i,t}$, and $IG_{i,t}$ are parts of Q_i^I stored at surface (e.g. lake and reservoir), in soil layers and ground water respectively at the tth time step; $\sum_{j=i}^{j=t} IE_{i,j}$ and $\sum_{j=i}^{j=t} IQ_{i,j}$ are the cumulated evapotranspiration and cumulated stream flow from Q_i^I during the period $[i, t]$.

According to Eq. (5.5), the weights of the overland and infiltrated flows can be expressed as:

$$\beta_i^{21} = \frac{\left(Q_i^O - OW_{i,t} - OS_{i,t} - OG_{i,t} - \sum_{j=i}^{j=t} OE_{i,j} - \sum_{j=i}^{j=t-1} OQ_{i,j} \right)}{Q_i^O}$$

$$(5.10)$$

$$\beta_i^{22} = \frac{\left(Q_i^I - IW_{i,t} - IS_{i,t} - IG_{i,t} - \sum_{j=i}^{j=t} IE_{i,j} - \sum_{j=i}^{j=t-1} IQ_{i,j} \right)}{Q_i^I} \tag{5.11}$$

In Eq. (5.8) and Eq. (5.9), evapotranspiration consumes water from both Q_i^O and Q_i^I. Positive weights in Eq. (5.10) and Eq. (5.11) means the component flows contribute to stream flow, while the negative values mean that stream flow recharges water storage.

A very important reason to apply the WSS area in Eq. (5.7) is that overland and infiltrated flows, which are produced from the same precipitation event, are collected into stream flow with different time lag, i.e. $\beta_i^{21} \neq \beta_i^{22}$. The role that WSS area plays in stream flow production is similar to a natural reservoir, e.g. lakes and wetlands, which store water and release it gradually to rivers. Precipitation falling outside the WSS area, i.e. above unsaturated soil layers, percolates and is assumed to be released at a different rate from that in WSS area, due to that water velocity at the surface is faster than that in soil layers. The resident time of water flow stored by artificial reservoirs may be longer than that in natural ones, which complicates the estimation and meaning of the weight set of overland flow. Accordingly, in the second implementation, the weights of precipitation, i.e. w_i in Eq. (5.6), can be calculated as:

$$w_i = \beta_i^{21} \times WS_i + \beta_i^{22} \times \left(1 - WS_i \right) \tag{5.12}$$

Our second assumption is that it can be better to estimate the w_i with the retrieved WS_i and a relatively shorter duration of antecedent precipitation.

5.3.3 Third implementation of the discrete rainfall-runoff model

The second implementation partitions precipitation into overland and infiltrated flows. A fraction of the infiltrated flow will result in subsurface flow when it encounters deeper saturated soil layers (Beven and Kirkby, 1979; Beven et al., 1984; Sivapalan et al., 1987), which is define as potential subsurface flow. The rest of infiltrated flow is stored into soil and ground water and mainly used for evapotranspiration. Model performance might be improved by specifying the potential subsurface flow, instead of the infiltrated flow in the second implementation. It is assumed that the fraction associated with potential subsurface flow can be scaled linearly with ground water table depth. This assumption implies that the depth of the water saturated soil is linearly related to the ground water table depth, Thus, the upper and lower boundary wetness conditions of the whole soil layer, i.e. the WSS and inundated area and the ground water table depth, can be used to model the outflow produced from the soil layer (i.e. overland flow and subsurface flow). Based on this assumption, the third implementation replaces the infiltrated flow in the second implementation (Eq. (5.12)) with potential subsurface flow as follows:

$$Q_t = \sum_{i=t-m}^{i=t} \beta_i^{31} \times Q_i^O + \sum_{i=t-m}^{i=t} \beta_i^{32} \times Q_i^S + Q_t^b \qquad (5.13)$$

where

$$Q_i^S = Q_i^I \times \frac{G_i - G_{min}}{G_{max} - G_{min}}$$

i.e. Q_i^S is the potential subsurface flow; β_i^{31} and β_i^{32} are the weights of overland flow and potential subsurface flow (i.e. Q_i^S) at i^{th} time step respectively, which have similar meaning as in Eq. (5.10) and Eq. (5.11). Q_i^S is estimated using observations of the ground water table depth (i.e. G_i) scaled by the range between maximum and minimum ground water table depth in each year (i.e. G_{max} and G_{min}).

β_i^{31} will be compared with β_i^{31}, and β_i^{32} with β_i^{22} respectively in chapter 6 to evaluate the fourth assumption. The precipitation weights can then be calculated from the weight spaces in the third implementation as:

$$w_i = \beta_i^{31} \times WS_i + \beta_i^{32} \times (1 - WS_i) \times \frac{G_i - G_{min}}{G_{max} - G_{min}} \qquad (5.14)$$

In Eq. (5.14), the surface wetness conditions (i.e. WS_i) and the ground water table depth (i.e. G_i) are the boundary conditions of water flow in the soil. In the third implementation, the description of complicated flow processes, such as water flow in the vadose zone and evapotranspiration, is not required to simulating stream flow.

5.4   Conclusions

To understand the role that inundated area plays in stream flow production, a discrete rainfall-runoff model was developed to fully use the retrievals of Water Saturated Surface (WSS). Based on the water balance equation and the redistribution of precipitation at a catchment, this model estimated the stream flow as the weighted sum of precipitations in certain antecedent period of time. Three implementations of this model were developed with increasing complexity, in order to evaluate whether the implementation of WSS area would reduce the required duration or not (see Chapter 7). The first implementation used the ground water table depth to simulate base flow. The second implementation was developed based on the first implementation. Considering the water balance at surface, retrievals of WSS area were used by the second implementation to partition precipitation into overland and infiltrated flows. Thus, stream flow in the second implementation is the sum of three components: the accumulated weighted sum of overland flows, the accumulated weighted sum of infiltrated flows and the base flow. The potential subsurface flow is water flow produced when the infiltrated flow encounters saturated soil layers underneath surface. It can be estimated from the infiltrated flow as a function of the ground water table depth. The third implementation was developed by replacing the infiltrated flow

in the second implementation with the potential subsurface flow. The calibration and validation of the three implementations will be illustrated in Chapter 6.

Chapter 6

Calibration and validation of the discrete rainfall-runoff model: a case study in the Xiangjiang River basin

6.1 Introduction

The Xiangjiang River basin is the largest watershed in the Hunan Province, China (Fig. 6.1), and discharges to Dongting Lake, which is the second largest fresh water body in China. It connects to the Dongting Lake floodplain through Changsha, the capital of Huanan Province. The river basin is located at the subtropical and monsoon climate zone, with mean annual precipitation 1900 mm and the rainy season from April to September. Abundant water resources make the Xiangjiang River basin as one of the best irrigated floodplains in China. Paddy fields consume the largest share of water resources. Due to the development of industry, heavy metal in sediments is transported through the river basin and to the Dongting Lake floodplain(Chunguo and Zihui, 1988; Li et al., 2013). Heavy metal also largely hampered the quality of ground water and risked children's lives in this region (Chai et al., 2010; Wang et al., 2011). Thus, it is very important to simulate the river

discharge from the Xiangjiang river basin and to understand discharge and recharge scheme of ground water in this region.

The discrete rainfall-runoff model developed in the previous chapter is very suitable for this purpose, since this model simulates the stream flow by taking the redistribution of precipitation among surface, subsurface and underground into account. The ground water table depth is an essential variable in its three implementations as described in Chapter 5. The three implementation forms need data of precipitation, Water Saturated Surface (WSS) and ground water table depth. TRMM Multi-satellite Precipitation Analysis (TMPA) supplies the daily precipitation data over the range from 50°N to 50°S (Huffman et al., 2007). Area of WSS can be retrieved from PDBT at 37 GHz as shown in Chapter 4 and by Shang et al. (2015). To monitor the heavy metal, Changsha city has many wells to measure the heavy metal concentrations and also the ground water table depth. The vegetation types and climate type are very similar with that in the Poyang Lake floodplain, Thus, the parameters derived in Chapter 4 can be directly used to retrieve the WSS area in the Xiangjiang River basin.
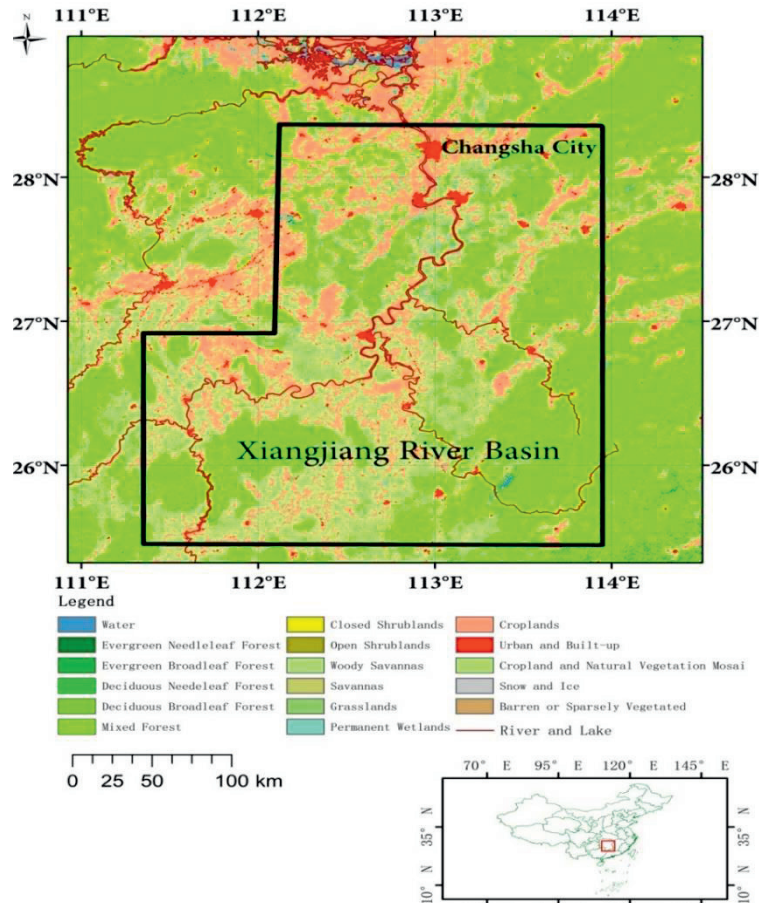
Figure 6.1: The land cover map of the Xiangjiang river basin, China. The black polygon in the upper map is the study area (blue polygon in Fig. 6.2). The red rectangle in the right lower map is the location of the Xiangjiang river basin in China

Besides that most of the required data can be derived from satellite observation, another advantage of the three implementations is that they can be calibrated with a linear regression method, much easier than the calibration methods used by other conceptual hydrological models, e.g. automatic calibration (Gupta et al., 1999; Madsen, 2000). This linear regression method may lead to the problem of overfitting, i.e. model reproduces the calibration data set just because of the number of model parameters being comparable with the number of observations (Babyak, 2004; Hawkins, 2004). Thus, relative short-term period of antecedent precipitation is preferred. The three implementations were developed with increasing complexity by using the ground water table depth and the retrievals of WSS area. It was assumed that increasing complexity would reduce the duration. This assumption will be evaluated in this chapter.

In this chapter, the three implementations of the discrete rainfall-runoff model were applied to the middle and upstream reach of Xiangjiang River basin. A short description of the river basin and of model input data was provided in section 6.2, including the retrieval of the WSS area. Section 6.3 introduced the calibration method, validation and cross validation methods, and the metrics to evaluate model performance. In section 6.4, the calibration and validation results were illustrated for each implementation to evaluate the performance. In section 6.5, the relationship between the model complexity and the duration of antecedent precipitation was discussed by comparing the model performances among three implementations. The stability of the three implementations was also evaluated, using the parameters derived from their validation results. The weight spaces of three implementations were analyzed to explain the difference in the model performance between implementations and to understand the relationship between the first implementation and the rest two. The cause that increasing durations improved the model performances in the calibration period was interpreted. Major conclusions were summarized in section 6.6.

6.2   Data set and Study Area

The study area is the Changsha upstream catchment in the Xiangjiang River basin (blue polygon in Fig. 6.2), covering 88,125 km^2 and located at 25°12'32.29" N - 28°29'30.11" N and 111°01'10.29" E - 113°52'58.29" E. Abundant water resources make the Xiangjiang River basin as one of the best irrigated floodplains in China. Paddy fields consume the largest share of water resources. Many small lakes, wetlands and fish ponds are the natural reservoirs of the river basin. There are also many artificial reservoirs distributed along the tributaries and the main stream of the Xiangjian River, in order to meet increasing requirements for electrical power from industry and cities.

The observations of the ground water table depth at 9 wells in Changsha (at the pixel numbered with 1 in Fig. 6.2) were used. Only mean values over 10 days were freely

available and were used to calculate the spatially averaged values over this pixel, without knowing the precise location of each observation site, due to the data policy in China. The spatially averaged 10-day mean values in the pixel numbered 1 were used to represent the ground water table depth in the whole study area, since the spatial representation is not so important in our model. The WSS area, precipitation and stream flow data were also averaged over 10-day. The input data was then 10-day averages of the WSS area (Fig. 6.3) over the whole study area, as retrieved with daily 37 GHz PDBT observations as Chapter 4 shows. In our previous study, the atmosphere influence on PDBT at 37 GHz was removed by a time series analysis method as Chapter 3 shows, which extracts surface signals from the PDBT time series. The vegetation attenuation was quantified by combining the PDBT observations and Normalized Difference Vegetation Index (NDVI) derived from MODerate-resolution Imaging Spectroradiometer (MODIS). Then, the surface Polarization Difference Effective Emissivity (PDEE) was estimated using a simple radiative transfer model. The fraction of the area was derived using a linear model, which uses the PDEE at dry and totally-water-saturated soil to scale the retrieved PDEE. Considering surface roughness in the Xiangjiang River basin, the PDEE of dry and total-water-saturated soil is set as 0.022 and 0.122 respectively. The PDBT data at 37 GHz from SSM/I was used, which is registered in the EASE-Grid with the spatial resolution of 25 km × 25 km (Armstrong et al., 1998). SSM/I is on board Defense Meteorological Satellite Program (DMSP) satellites, which are sun-synchronous and scans earth surface with a constant incidence angle of 53°. Only the early morning overpass data are used to retrieve the fraction of the WSS area, so that the temperature difference between vegetation canopy and surface could be neglected. Since the discrete rainfall-runoff model is lumped, the fractional area of the WSS was calculated over the whole catchment (Fig. 6.3). The 10-day averages of precipitation data (Fig. 6.3) was extracted from ITP-atmosphere forcing data set (Chen et al., 2011; Yang et al., 2010) over the whole study area. This data set is based on the calibration of TRMM precipitation retrievals against rain-gauge data in China. The daily stream flow at the Changsha hydrology station is not affected by water consumed for irrigation and by water storage in the reservoir. The daily stream flow was also averaged over 10-day (Fig. 6.3). The 10-day averaged data was used to calibrate and validate the three implementations of the discrete rainfall-runoff model. Three annual time series of gauged stream flow and ground water table depth were available, in 2001, 2002, and 2005. 2002 is the wettest year and 2005 the driest year from 2000 to 2006, according to the precipitation data. The calibration period was in 2002 (wet year) and 2005 (dry year), and the validation period was 2001.
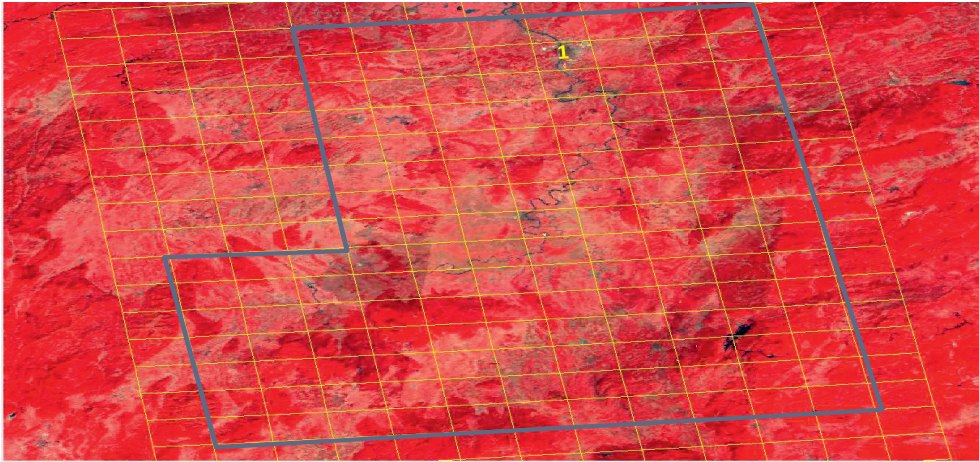
Figure 6.2: The study area in the middle and upstream of Xiangjiang river basin, China. The blue polygon covers the whole study area. The yellow grid is the 25km×25km EASE-Grid. Background image: RGB composite of MOIDS near-infrared, red and green spectral bands. The wells that measure ground water table depths are located within the yellow pixel numbered with 1.

(a)   (b)
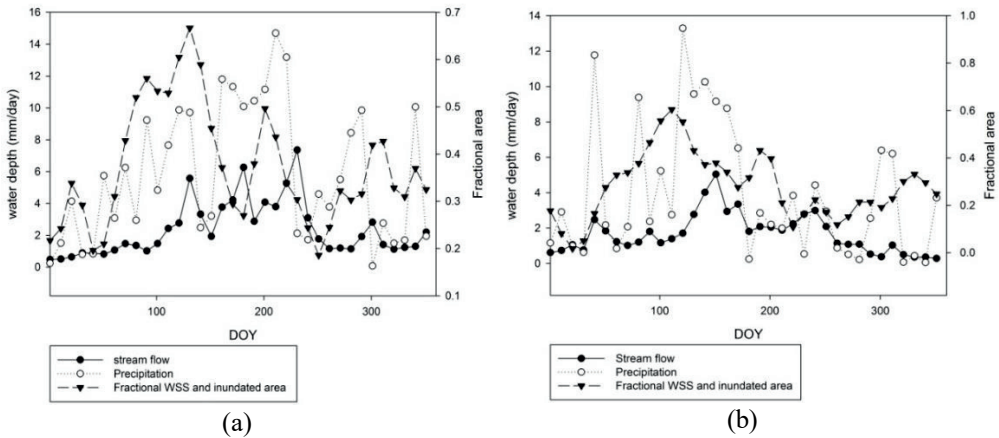
Figure 6.3: Major input data for the discrete rainfall-runoff model. 10-day averaged Precipitation was extracted from ITP forcing data set (Chen et al., 2011; Yang et al., 2010), 10-day averaged fractional WSS area was retrieved from SSM/I 37 GHz PDBT data, and the 10-day averaged stream flow was observed at Changsha station, in 2002 (a) and 2005 (b), respectively.

6.3   Method

6.3.1 Application of the discrete rainfall-runoff model

The three implementations of the discrete rainfall-runoff model were developed with increasing complexity: The first implementation with precipitation and base flow; the second one with overland flow, infiltrated flow and base flow; the third one with overland flow, potential subsurface flow and base flow. They were applied to estimate the 10-day averaged stream flow at Changsha station in 2002 (wet year) and 2005 (dry year) respectively. All the inputs are 10-day averages and at the same time step, i.e. 10 days. The duration of precipitation was increased stepwise from 1 to 15 antecedent time steps, in order to simulate stream flow and demonstrate how the model performance changes with increased durations.

6.3.2 Model calibration

Once the duration of antecedent precipitation is estimated by setting the parameter "m", the number of required weight in Eq. (5.6), (5.7) and (5.13) are determined and their values can be estimated by calibration against stream flow. The total number of weights needs to be less than the total number of samples in the annual time series, i.e. $n+1$. The linear least squares method is used to solve such over-determined linear equation, so that the model parameters minimize the difference between observed and modelled stream flows. Taking Eq. (5.6) as an example, the optimal model parameter values are determined by solving the equation:

$$\left(X^T X\right)\beta_w = X^T Y \tag{6.1}$$

where

$$X = \begin{bmatrix} P_0 & P_{-1} & \cdots & P_{-m} & G_0 & 1 \\ P_1 & P_0 & \cdots & P_{1-m} & G_1 & 1 \\ \vdots & \vdots & \ddots & \vdots & \vdots & \vdots \\ P_n & P_{n-1} & \cdots & P_{n-m} & G_n & 1 \end{bmatrix} \quad \beta_w = \begin{vmatrix} w_t \\ w_{t-1} \\ \vdots \\ w_{t-m} \\ k_b \\ B \end{vmatrix} \quad Y = \begin{vmatrix} Q_0 \\ Q_1 \\ \vdots \\ Q_n \end{vmatrix}$$

where matrix **X** includes the observations of precipitation, P_i, ground water table depth G_i, and a constant water flow valued as 1; the matrix β_w is the weights vector including the weights of precipitation contributions, w_i, ground water releasing parameter k_b, and the constant water release factor B; the matrix **Y** includes the observations of stream flow Q_i. In Eq. (6.1), the precipitation in **X** includes the observations in the antecedent year, i.e. [P_{-1}, P_-

$_2$, ..., P_{-m}]. The derivation of Equation (6.1) and more detailed information on the linear least squares method can be found in many handbooks, such as Björck (1996); Lawson and Hanson (1974). The same method can be applied to the second and third implementation forms by replacing the precipitations in the matrix **X** with component flows and extending the matrix $\boldsymbol{\beta_w}$.

In Eq. (6.1), the weights in $\boldsymbol{\beta_w}$ are constant for all stream flow observations, but applied to observed precipitations at different times, i.e. the P_i in each row of matrix **X** are different. This means that the volumetric contribution of precipitation to stream flow varies at each time step, although the ratio remains constant. On the other hand, in the matrix **X**, the observation P_i is in the rows from s from i^{th} to $(i+m)^{th}$ and the column position of observation P_i changes from 0th to m^{th} according to the row position of the contribution weights of precipitation from w_t to w_{t-m}, in the vector $\boldsymbol{\beta_w}$. This means the contribution weights of precipitation in $\boldsymbol{\beta_w}$ also indicates the evolution of the contributions of the ith precipitation from 0 to $–m$ (negative value means antecedent) time steps, with corresponding stream flows at time steps from i to $i+m$. In section 6.5, the pattern of weights will be interpreted by relating it to the evolution of contributions of precipitation and component flows to various stream flows during a certain period.

6.3.3 Metrics to evaluate model performance

To evaluate the model performance, two metrics were used in this study: 1. the Nash-Sutcliffe Efficiency (Nash and Sutcliffe, 1970) , i.e. NSE:

$$NSE = 1 - \frac{\sum_{i=1}^{N}\left(E_i - O_i\right)^2}{\sum_{i=1}^{N}\left(O_i - \overline{O}\right)^2} \tag{6.2}$$

where E_i and O_i is the model estimated and observed stream flow at i^{th} time step respectively, $\overline{O}$ is the average of measured stream flows, N is the total number of observations;

and 2. Relative RMSE (RRMSE):

$$RRMSE = \frac{\sqrt{\dfrac{\sum_{i=1}^{N}\left(E_i - O_i\right)^2}{N}}}{\overline{O}} \times 100\% \tag{6.3}$$

NSE indicates how well the model estimates replicate the observations, while RRMSE is a measure of the bias in the model estimates.

6.3.4 Model validation

6.3.4.1   Calibration/Validation Process

In calibration/validation process, the time series of stream flow observations are partitioned into calibration and validation periods, respectively. The model parameters, i.e. weight space of β_w in Eq. (6.1), are identified first in the calibration period. The calibrated parameters are used to predict the stream flow in the validation period. The model performance needs to be evaluated in both periods. The weight space in Eq. (6.1), however, is determined by not only the duration of antecedent precipitation, but also the annual time series of stream flow observations. To illustrate the difference in model parameters between dry and wet years, the weight space will be calibrated in both years, respectively.   The model parameters used to predict stream flows are derived from three experiments: 1) calibrated parameters in the wet year: 2) calibrated parameters in the dry ear; 3) parameters averages over wet and dry years.

6.3.4.2   Cross-validation process

The linear regression method as Eq. (6.1) shown may lead to the problem of overfitting in calibration period, when the number of unknown parameters in matrix β_w is close to the number of total observations in an annual time series, i.e. in matrix $\mathbf{Y}$. To evaluate the overfitting, the Leave-One-Out (LOO) method is used. LOO method removes one sample in stream flow observations, e.g. Q_i in the matrix $\mathbf{Y}$, and its involved precipitation observations, e.g. i^{th} row in the matrix $\mathbf{X}$, from the one-year time series. The model parameters are calibrated from the rest observations and then used to predict the specific stream flow that has been removed. Thus, for an annual time series with constant 10 days interval, there are 36 cross-validation results. The RRMSE of each prediction is calculated to evaluate the performance in the cross-validation.

6.4   Results of model simulation

6.4.1 General

The three implementation forms were calibrated with 10-day averaged stream flow at Changsha station in 2002 (wet year) and 2005 (dry year) respectively. The wettest and driest conditions would help us to identify globally optimal parameters. The longest duration of antecedent precipitation was increased step-wise from 1 to 15 time steps, i.e. 10 days to 150 days, in order to evaluate how the model performance would change with the duration of antecedent precipitation. Cross validation was applied to evaluate whether the changes in model performance were due to overfitting. The LOO method was applied to

each implementation with various durations of antecedent precipitation for 2002 and 2005 respectively. For annual time series (sampled at 10 days intervals), there were 36 data points useful for cross-validation results for each applied duration.

In addition, the three implementations were used to estimate stream flow in 2001 to validate the performance. The annual precipitation of 2001 was close to 2002, i.e. a relatively wet year. In the validation process, the model parameters were derived from three experiments: 1) calibration with stream flow in 2002: 2) calibration with stream flow in 2005; 3) parameter averages over 2002 and 2005.

6.4.2 Simulation with the first implementation

6.4.2.1   Calibration of the first implementation

The first implementation was developed by adding the base flow to the discrete rainfall runoff model and assuming that the weights are constant and only depend on the duration of antecedent precipitation (Eq. 5.6). The calibration was done against the stream flow in 2002 (wet year) and 2005 (dry year), with the longest duration of antecedent precipitation increasing from 1 to 15 time steps (i.e. from 10 days to 150 days). As the three examples of the simulated stream flows show (Fig. 6.4), over-estimation occurred after September in 2002 and before September in 2005, and under-estimation occurred in the other months, when the longest duration of antecedent precipitation was 1 time step. In both years, the duration of antecedent precipitation between 8 or 15 time steps reduced the bias (Fig. 6.4).
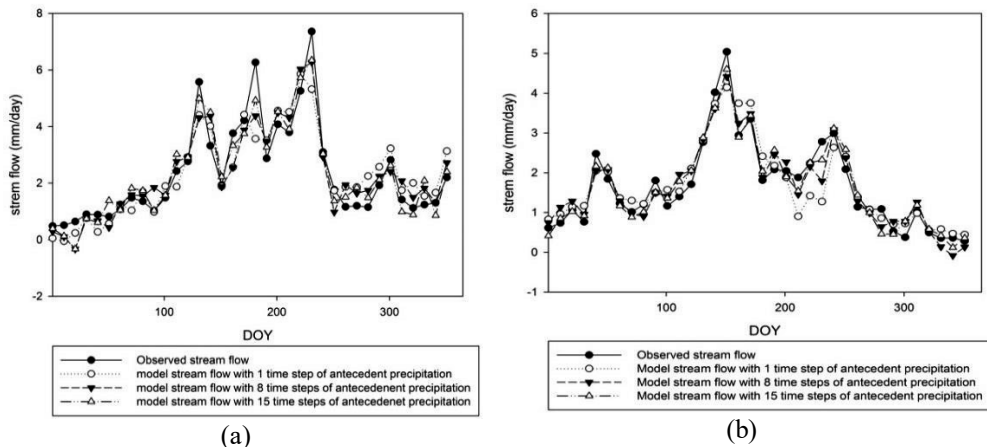
Figure 6.4: Observed and modelled 10-day averaged stream flow in the calibration period using the first implementation of the discrete rainfall-runoff model. The applied durations of antecedent precipitation are 1, 8 and 15 time steps with the time interval of 10 days in 2002 (a) and 2005 (b) respectively.

Model performance was improved in calibration when increasing the longest durations of antecedent precipitation from 1 to 15 time step (Fig. 6.5 and Fig. 6.6): the NSE of the first implementation increased from 0.78 to 0.91 in 2002 (Fig. 6.5a) and from 0.82 to 0.94 in 2005 (Fig. 6.6a), while the RRMSE decreased from 34 % to 22 % in 2002 (Fig. 6.5b) and from 28 % to 17 % in 2005 (Fig. 6.6b). The improvement rate, however, was different at various stages: in 2002, the improvement was larger when the duration was increased from 1 to 3 time steps and from 7 to 8 time steps than in the other stages (Fig. 6.5); in 2005, the largest improvement occurred when the duration was increased from 6 to 7 steps (Fig. 6.6). These findings suggest that there is some specific duration of antecedent precipitation that has a large impact on model performance. The first implementation integrates the contribution of antecedent precipitation to stream flow in a certain period of time and assumes that antecedent precipitation beyond a certain duration is transformed into base flow released by ground water. Thus, the model performance changes with different durations and indicates how the catchment partitions precipitation at surface and in the soil layers (i.e. above ground water table depth) and produces stream flow from precipitation stored there (i.e. through fast and slow runoff). The large improvement in model performance, when the duration of antecedent precipitation is 3 time steps (30 days) in 2002, probably indicates the duration that the catchment takes to produce fast runoff (i.e. overland flow and fast subsurface flow). When the duration of antecedent precipitation is 8 time steps (80 days) in 2002 and 7 time steps (70 days) in 2005, the large model performance improvements indicate the duration that the catchment takes to produce slow runoff (i.e. slow subsurface flow and the lately-released overland flow). The contribution of component flows can be further interpreted by the weight sets of the second and third implementations (see Sect. 6.5.3). The model performance was slightly degraded when increasing the duration from 2 to 7 time steps in 2002 (Fig. 6.5), while in 2005, the model performance was improved gradually with increasing the duration of antecedent precipitation. This difference in model performance changes relates to inter-annual differences in the catchment response to rainfall, which will be further discussed in Sect. 6.5.3. It needs to be mentioned that the model performances in 2002 and 2005 do not show a large difference when the same duration is used by the first implementation, thus the assumption, i.e. a constant duration of antecedent precipitation contributes to stream flow production, can be applied to various years with different wetness condition. The duration that the catchment takes to produce the slow runoff seems similar between wet and dry years, i.e. 80 days in 2002 and 70 days in 2005, which further proves that the assumption of a constant duration is reasonable.

(a)   (b)
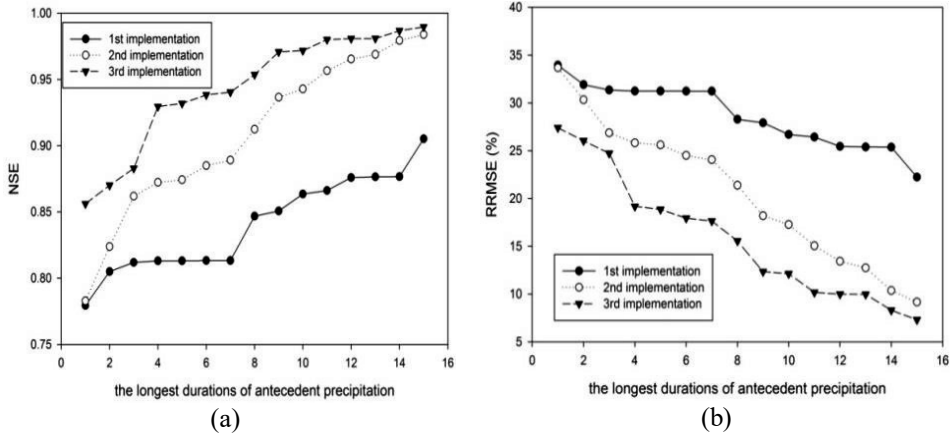
Figure 6.5: The Nash--Sutcliffe Efficiency (NSE) (a) and Relative Root Mean Square Error (RRMSE) (b) of the three implementations of the discrete rainfall-runoff model in the calibration for 2002. The duration of antecedent precipitation were increased from 1 to 15 time steps with time interval of 10 days. The input of the first implementation is precipitation and base flow; the input of the second implementation is overland flow, infiltrated flow and base flow; the input of the third implementation is overland flow, potential subsurface flow and base flow.

(a)   (b)
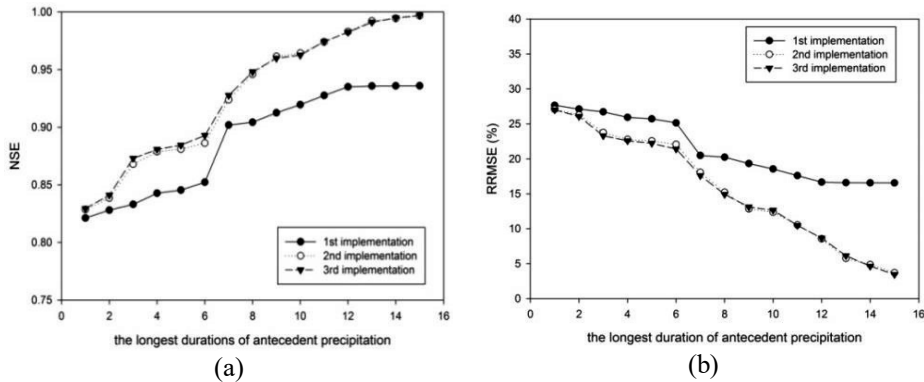
Figure 6.6: The Nash--Sutcliffe Efficiency (NSE) (a) and Relative Root Mean Square Error (RRMSE) (b) of the three implementations of the discrete rainfall-runoff model in the calibration for 2005. The duration of antecedent precipitation were increased from 1 to 15 time steps with time interval of 10 days. The input of the first implementation is precipitation and base flow; the input of the second implementation is overland flow, infiltrated flow and base flow; the input of the third implementation is overland flow, potential subsurface flow and base flow.

6.4.2.2   Cross validation of the first implementation

When the duration is increased step-wisely, the number of model parameters also increases. The improvement in model performance may also be related to the overfitting of the linear regression in Eq. (5.15). To evaluate that, it was summarized that the RRMSE of all LOO tests for each duration of antecedent precipitation applied in the evaluation of the first implementation (Fig. 6.7). The RRMSEs clearly varied in a similar range when the duration was increased step-wisely (Fig. 6.7): the median values in 2002 and 2005 fluctuated between 20 % to 30 % with various durations, i.e. with a different number of weights (model parameters). The mean value slowly increased in 2002, while in 2005 the mean value varied in a similar range as the median values. This means that the overfitting is not the cause of the model improvement in the first implementation when increasing durations, i.e. the model improvement is due to the different period of time that the catchment takes to produce fast and slow runoff.

(a)   (b)
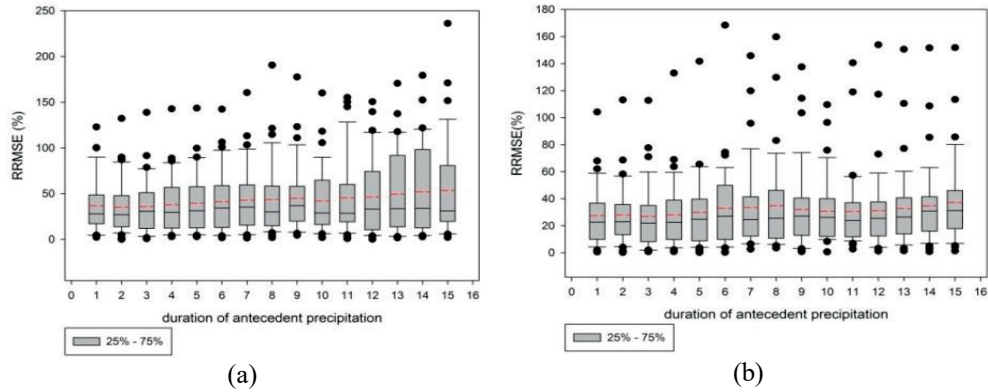
Figure 6.7: The box plot of the Relative Root Mean Square Error (RRMSE) of the Leave-One-Out cross validation for the first implementation in 2002 (a) and 2005 (b). The duration of antecedent precipitation was increased step-wisely from 1 to 15 time steps with time interval of 10 days. The red dash line in each box is the mean value, the black line is the media value, and dot points are outliers.

6.4.2.3   Validation of the first implementation

The calibrated model parameters were applied in three validation experiments. In these experiments (Fig. 6.8a), increasing duration of antecedent precipitation did not improve the model performance as significantly as in the calibration experiments. The model performance was improved only when the duration was increased from 60 to 80 days (from 6 to 8 time steps in Fig. 6.8a) with parameter from 2002 (i.e. the experiment 1) and the averaged parameter (i.e. the experiment 3), in the similar time steps as when the model performance was improved in the calibration period (Fig. 6.5 and Fig. 6.6), which strongly indicates the duration (i.e. 70 — 80 days) that the catchment takes to produce slow runoff. Through analyzing the RRMSE in each season (see Sect. 6.5.4), we find that precipitation

falling on the catchment takes 80 — 90 days to be transformed into base flow, i.e. the recharge duration of ground water. Since the first implementation uses base flow to estimate the contribution of precipitation at time steps longer than the applied duration, the NSE stopes improving after the duration is longer than the recharge duration of ground water, i.e. 90 days. With the same duration, the experiment 3 (i.e. using parameters averaged over 2002 and 2005) gave the highest NSE ($0.69 \leq$ NSE ≤ 0.82) and lowest RRMSE ($35.0 \% \leq$ RRMSE $\leq 58.5 \%$) than the other two experiments. Both the highest NSE and lowest RRMSE did occur in the experiment 3 (Table 6.1), but the former with duration = 9 time steps (90 days) and the latter with duration = 2 time steps (20 days). When using the parameters and the durations in Table 1, the stream flow predicted by the first implementation follows the seasonal changes of stream flow very well but overestimates the peaks, especially in the rainy season (Fig. 6.9a). The predicted stream flow with the duration =2 time steps (20 days) lagged the peak of the observed stream flow at DOY 121, Thus, the duration = 9 time steps (90 days) gives the best performance in the study area with the first implementation. Through the calibration and validation processes, it can be concluded that a constant weight set with a constant duration of precipitation can be applied to estimate stream flow with the first implementation.

Table 6.1: The best model performances, their experiment types and the used duration in the validation period in 2001 for each implementation of the discrete rainfall-runoff model.

|		NSE	RRMSE	Used Parameter	Duration
The first Implementation	Highest NSE	0.83	35.40%	average	9 time steps
	Lowest RRMSE	0.82	34.10%	average	2 time steps
The second Implementation	Highest NSE	0.84	32.89%	2002	1 time step
	Lowest RRMSE	0.83	32.83%	average	1 time steps
The third Implementation	Highest NSE	0.82	40.05%	average	1 time step
	Lowest RRMSE	0.82	40.05%	average	1 time step

(a)

(b)

(c)
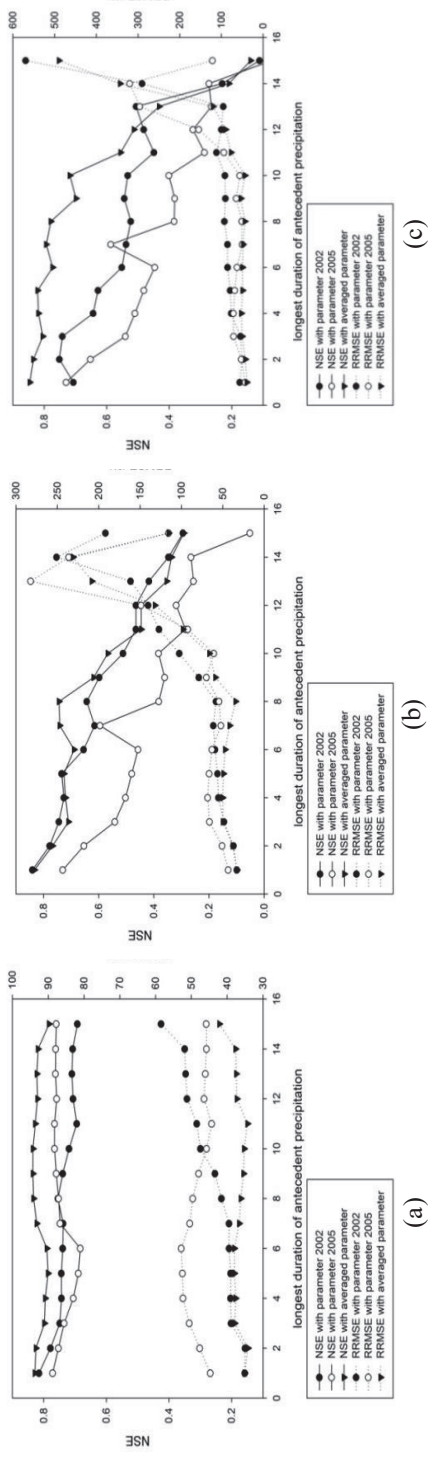
Figure 6.8: The Nash–Sutcliffe Efficiency (NSE) and Relative Root Mean Square Error (RRMSE) of the three implementations in the 2001 validation. a) parameters from calibration of 2002; b) the second implementation; c) the third implementation. Three experiments are designed as: 1) parameters from calibration of 2002; 2) parameters from calibration of 2005; 3) parameters averaged over 2002 and 2005. The duration of antecedent precipitation were increased step-wisely from 1 to 15 time steps with time interval of 10 days.
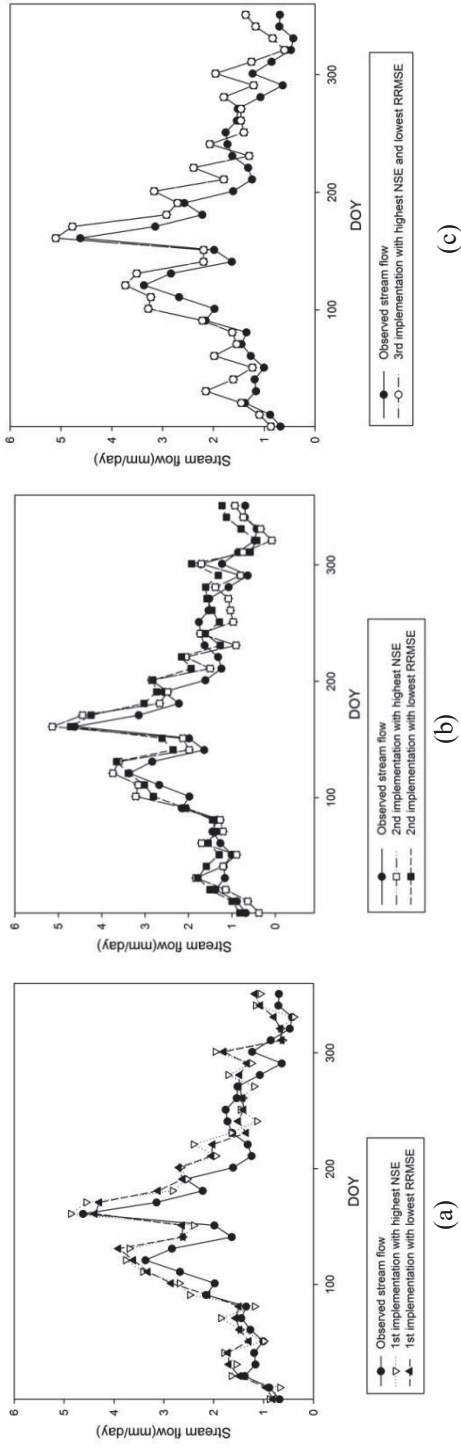
Figure 6.9: Observed and predicted stream flow in 2001 using the three implementations with the parameters in Table 1. a) the first implementation; b) the second implementation; c) the third implementation.

6.4.3 Simulation with the second implementation

6.4.3.1   Calibration of the second implementation

The second implementation applies two paths for precipitation to reach rivers and channels with the WSS area (Eq. 5.7). One is fast overland flow and the other one is slow infiltrated flow. In the calibration of the second implementation, the bias in the stream flow simulated with a duration of 1 time step (10 days) in Fig. 6.10 was similar to the bias obtained with the first implementation when using the same duration (Fig. 6.4). When the duration = 8 time steps (80 days), however, the second implementation simulated the stream flow (Fig. 6.10) as well as the first implementation with the duration = 15 time steps (150 days) in Fig. 6.3. This could also be observed from their NSE and RRMSE (Fig. 6.5 and 6.6): NSE and RRMSE of the second implementation with the duration = 8 time steps (80 days) were similar to the first implementation with the duration = 15 time steps (150 days). In the calibration experiments, the NSE and RRMSE of the second implementation were better than the first implementation with the same duration (Fig. 6.5 and Fig. 6.6). When the duration of antecedent precipitation was increased from 1 to 10 time steps, NSE increased from 0.78 to 0.94 in 2002, from 0. 83 to 0.96 in 2005, and RRMSE decreased from 34 % to 17 % in 2002, from 27 % to 12 % in 2005. The better model performance with the second implementation than the first one is probably due to the application of WSS area, which memories the intensity of antecedent precipitation, indicates regional water storage capacity by the changes in WSS area (i.e. storing and gradually releasing water flow that is produced by the catchment from antecedent precipitation), and helps to identify the component flows.

The improvement rate in model performance was slightly different in various stages: in 2002, large improvements occurred when the duration was increased from 1 to 3 time steps and from 7 to 9 time steps; in 2005, the large improvements occurred when the duration was increased from 2 to 3 time steps and from 6 to 9 time steps. In the calibration of the first implementation, model performance changes in 2002 reflect the influence of fast runoff, but did not in 2005. Compared with the first implementation, model performance changes of the second implementation in both 2002 and 2005 indicate the duration that the catchment takes to produce fast runoff (i.e. 30 days) and slow runoff (i.e. around 90 days). That is probably due to that the component flows, estimated with the WSS area by the second implementation, can better describes the catchment response to rainfall, i.e. how precipitation is allocated and transformed into component flows with different velocity. We will further discuss that through interpretation on the weight sets of the three implementations in Sect. 6.5.3. It is also notice that the improvement rate of model performance in the second implementation is higher than that in the first implementation in most cases. This indicates that the second implementation is more sensitive to the duration of antecedent precipitation than the first one. When the duration = 10 time steps, the model performance of the second implementation was better than 90% of current hydrological

models in the calibration process, according to the statistical assessment by Ritter and Muñoz-Carpena (2013). The performance improvement when the duration > 10 time steps is probably due to the overfitting, as shown next.
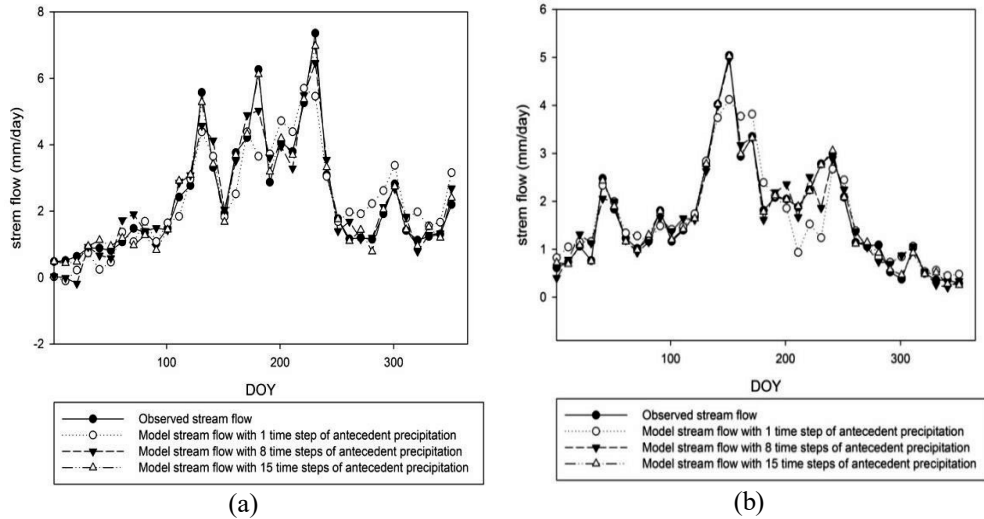
Figure 6.10: Observed and modelled 10-day averaged stream flow in the calibration period using the second implementation of the discrete rainfall-runoff model. The applied durations of antecedent precipitation are 1, 8 and 15 time steps with the time interval of 10 days in 2002 (a) and 2005 (b) respectively.

6.4.3.2   Cross validation of the second implementation

The calibration of the second implementation gave very high model performance with duration = 15 time steps. In this case the number of model parameters was close to the total number of stream flow observations. This leads to the problem of overfitting that was evaluated by applying the LOO method to the second implementation. The box plot of LOO results shows that (Fig. 6.11): in 2002 with a duration ≤10 time steps, both median and mean RRMSE values fluctuated between 20% to 30%; with a duration > 10 time steps, median and mean values increased and the 25% — 75% variation range was enlarged significantly. In 2005, a similar condition was observed, but the transition duration was longer, i.e. up to time step = 13. This indicates that the overfitting problem occurred when the duration of antecedent precipitation > 10 time steps in the second implementation. Thus, only when the duration ≤ 10, the improved performance is related to involve the duration that the catchment takes to produce slow and fast runoff and the application of the retrieved WSS area (e.g. to partition component flows and as an indicator of regional water storage capacity) in the second implementation.
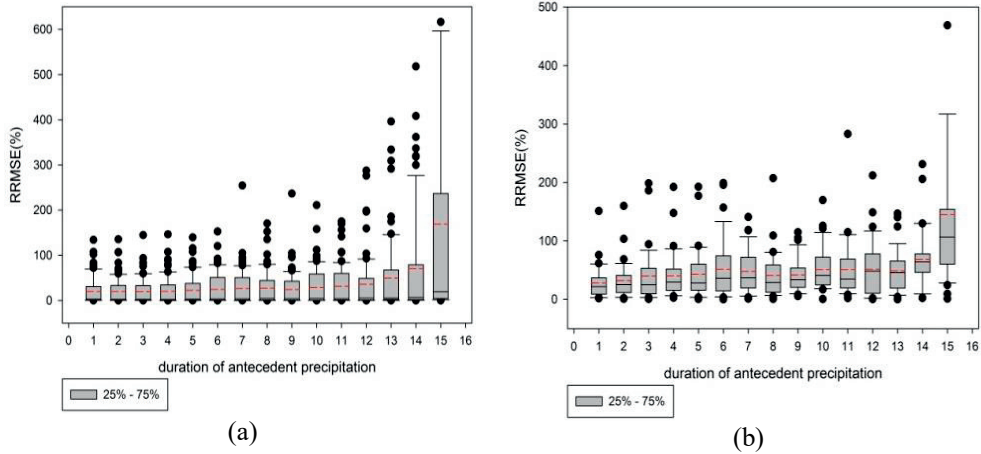
Figure 6.11: The box plot of the Relative Root Mean Square Error (RRMSE) of the Leave-One-Out cross validation for the second implementation in 2002 (a) and 2005 (b). The duration of antecedent precipitation was increased step-wisely from 1 to 15 time steps with time interval of 10 days. The red dash line in each box is the mean value, the black line is the media value, and dot points are outliers.

6.4.3.3 Validation of the second implementation

The validation of the second implementation required more complex experiments. There were three stages in the evolution of NSE with the duration of antecedent precipitation (Fig. 6.8b): 1) when the duration $\leq$ 3 time steps, the experiment 1 (i.e. parameters calibrated for 2002) gave the best NSE ($0.73 \leq$ NSE ≤ 0.84); 2) when $5 <$ duration $\leq$ 10 time steps, the experiment 3 (i.e. parameters averaged over 2002 and 2005) had the highest NSE ($0.58 \leq$ NSE ≤ 0.74); 3) when the duration > 10 time steps, NSE for all experiments was lower than 0.5. Changes in RRMSE were similar, but with different duration ranges (Fig. 6.8b): 1) when the duration $\leq$ 10 time steps, experiment 3 had better RRMSE than the other two, with $32.8\% \leq$ RRMSE $\leq 66.2\%$;; 2) when the duration > 10, RRMSE for all experiments was higher than 70 %.

Overall, the model performance decreased when the duration increased in the validation experiments, expect when the duration was increased from 6 to 7 time steps in the experiment 3 and the experiment 2. In the second implementation, the calibrated weight sets of overland and infiltrated flows illustrated the catchment response to rainfall in wet (the experiment 1) and dry (the experiment 2) years. The improved model performance when the duration was increased from 6 to 7 time steps in the validation period (i.e. in 2001) indicates the duration that the catchment takes to produce slow runoff, which is similar with that in the calibration period (i.e. in 2002 and 2005). In the second implementation (also the third implementation), the observed WSS area were used to reflects the inter-annual difference in regional water storage changes and partition precipitation into overland and infiltrated flows. The decayed model performance in the validation experiments of the

second implementation, however, indicates that the catchment response to longer antecedent precipitation (i.e. weight sets of component flows) highly depends on the regional water storage conditions indicated by the WSS area. According to Eq. (5.12), the difference in WSS area between different years is one of model error sources in the estimation of precipitation contributions with the second implementation. The large variation in the weight sets of component flows using different durations enlarges the model uncertainty of the second implementation (see Sect. 6.5.3). Besides that, the model error is cumulated with increasing the duration, since when the second (also the third) implementation integrates the contributions of component flows in each time step, the model error is also cumulated.

The highest NSE occurred in the experiment 1 with duration = 1 time step, while the lowest RRMSE occurred in the experiment 3 with duration = 1 time steps (Table 6.1). The stream flows that were predicted by the second implementation using the parameters having the best model performances (Table 6.1) overestimated the peaks in the rainy season (Fig. 6.9b), but performed better than the first implementation (Fig. 6.9a). Thus, the second model implementation, the duration = 1 time step gives better results than the first implementation with duration = 9 time steps. This proves that a reasonable model performance can be achieved with a shorter duration of antecedent precipitation when using the retrievals of WSS area.

6.4.4 Simulation with the third implementation

6.4.4.1   Calibration of the third implementation

The third implementation estimates the potential subsurface flow from the infiltrated flow derived in the second implementation to specify the path of precipitation through soil layers to rivers and channels. In-situ measurements of the ground water table depth were used to estimate the fraction of infiltrated flow that produces the potential subsurface flow (Eq. 5.13). In the calibration experiments, with duration of antecedent precipitation = 1 time step, the error of estimate was (Fig. 6.12) similar to the other two implementations (Fig. 6.4 and 6.10). With duration = 8 and 15 time steps, the accuracy of simulated stream flow in 2002 was better (Fig. 6.12a) than with the other two implementations (Fig. 6.4a and Fig. 6.10a). In 2005, the accuracy of simulated stream flow was comparable with the second implementation. The comparison of NSE and RRMSE (Fig. 6.5 and Fig. 6.6) leads to similar conclusions: when the duration was increased from 1 to 10 time steps, the third implementation gave the best performance among the three implementations with NSE increasing from 0.86 to 0.97 in 2002 and from 0. 83 to 0.96 in 2005, while RRMSE decreased from 27 % to 12 % in 2002 and from 27 % to 12 % in 2005. In 2005 the performance of the third and the second implementation was almost the same (Fig. 6.6). This implies that in dry year, the depth of water saturated soil is close to the ground water table depth, Thus, the water storage capacity of soil layers can be reflected by the ground water table depth. Above all, it is reasonable to estimate the potential subsurface flow from

the infiltration flow using the ground water table depth. In both 2002 and 2005, the model performance changes in the third implementation are similar with those in the second implementation. This indicates that the application of WSS area improves the model performance by reflecting the changes in water storage capacity and helps to identify the component flows. The performance improvement also indicates that the weight set of the third implementation is sensitive to the duration of antecedent precipitation.
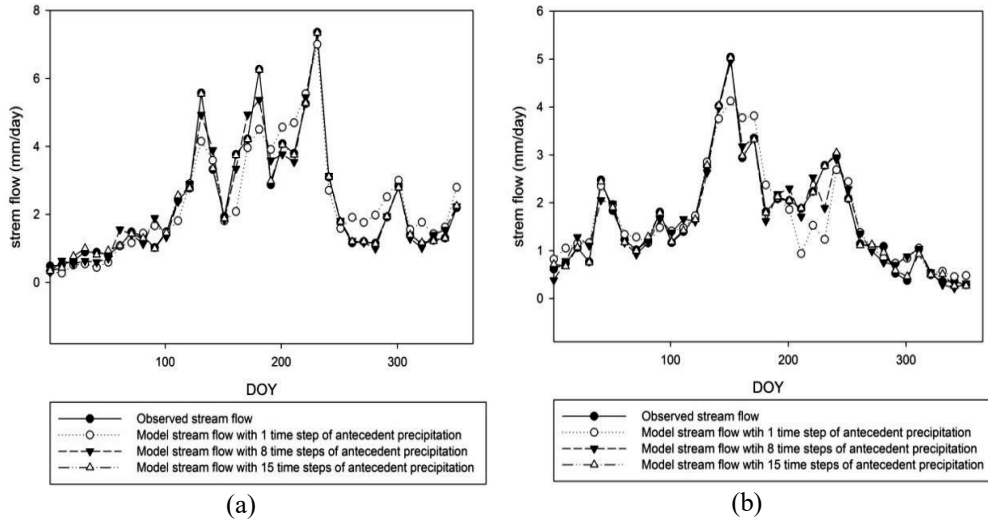
Figure 6.12: Observed and modelled 10-day averaged stream flow in the calibration period using the third implementation of the discrete rainfall-runoff model. The applied durations of antecedent precipitation are 1, 8 and 15 time steps with the time interval of 10 days in 2002 (a) and 2005 (b) respectively.

6.4.4.2   Cross validation of the third implementation

Similar to the second implementation form, the overfitting problem needs to be evaluated for the third implementation. The box plot of LOO results for the third implementation forms (Fig. 6.13) show that: in 2002, when the longest duration <10 time steps, both median and mean values fluctuated between 20% to 40%, while when the duration ≥ 10 time steps, median and mean values were increased and the box is enlarged; in 2005, a similar condition was observed, but the transition duration was longer, i.e. at the time step = 14. The condition of overfitting in the third implementation is very similar to the second implementation. Thus, only when the duration ≤ 10, the improved performance is related to involving the duration that the catchment takes to produce slow and fast runoff and the application of the retrieved WSS area (e.g. to partition component flows and as an indicator of regional water storage capacity) in the third implementation.

(a)   (b)
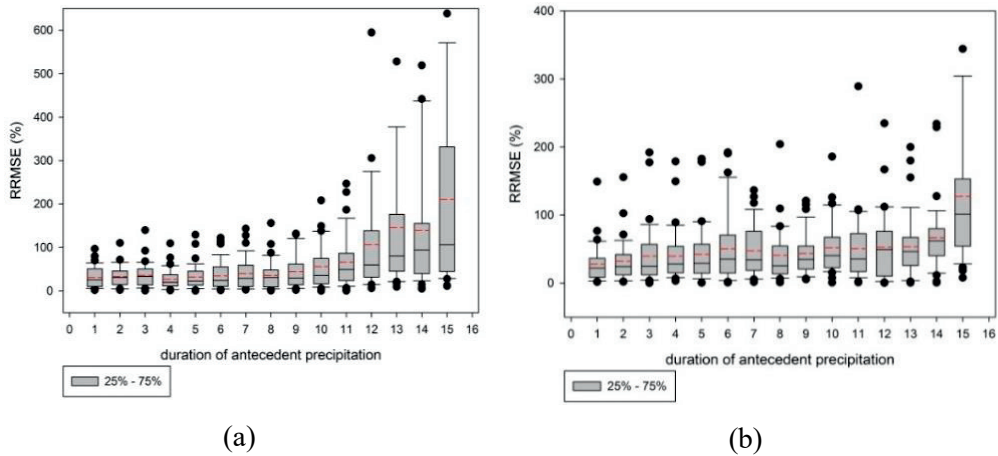
Figure 6.13: The box plot of the Relative Root Mean Square Error (RRMSE) of the Leave-One-Out cross validation for the second implementation in 2002 (a) and 2005 (b). The duration of antecedent precipitation was increased step-wisely from 1 to 15 time steps with time interval of 10 days. The red dash line in each box is the mean value, the black line is the media value, and dot points are outliers.

6.4.4.3   Validation of the third implementation

The validation experiments showed that the model performance was acceptable only when the duration $\leq$ 10 time steps (Fig. 6.8c). The experiment 3 (parameters averaged over 2002 and 2005) had higher NSE ($0.65 \leq$ NSE ≤ 0.82) and lower RRMSE ($40.1\% \leq$ RRMSE $\leq 50.4\%$). Overall the influence of the duration of antecedent precipitation in the third implementation was similar to the second implementation, i.e. leading to decreasing model performance with increasing the duration. There are, however, some exceptions when the model performance was improved with increasing durations: in the experiment 1 (with parameters from 2002), when the duration was increased from 1 to 2 time steps; in the experiment 2 (with parameters from 2005), when the duration was increased from 6 to 7 time steps; in the experiment 3 (parameters averaged over 2002 and 2005), when the duration was increase from 3 to 4 time steps and from 6 to 7 time steps. These model improvements again indicate the duration that the catchment takes to produce fast and slow runoff, similar to the results derived from the second implementation. We will further discuss that through the weight sets of the third implementation in Sect 6.5.3.

The highest NSE and lowest RRMSE occurred in the experiment 3 (parameters averaged over 2002 and 2005) with the duration = 1 time step (Table 6.1). In this experiment the third implementation captured the time of major streamflow peaks correctly, but with larger errors than the second implementation (Fig. 6.9b and Fig. 6.9c). In the experiment 3, however, when the duration is 2 and 3 time steps, the model performance of the third implementation is better than the second implementation. Overall, the calibration and validation results show that the potential subsurface flow can be estimated with the

retrieved WSS area and in-situ observations of ground water table depth. The calibration of weight sets in the third implementation highly depend on the observation of WSS area and ground water table depths (Eq. (5.14)), and are also sensitive to the duration. Similar to the second implementation, the large model uncertainty in the weight sets (see Sect. 6.5.3) and the cumulated model error with longer durations both enlarge the model errors in the validation experiments when the duration of antecedent precipitation was increased.

6.5   Discussion

6.5.1 Calibration and validation results

The results presented in Sect.6.4 document the feasibility of calibrating the three model implementations and to achieve a satisfactory performance by using the mean values of parameters calibrated for a wet and a dry year. The three implementations were designed with increasing complexity by specifying the slow and fast component flows produced from precipitation. The aim of this chapter was to evaluate whether the increasing complexity with the retrieval of WSS area could reduce the duration of antecedent precipitation required to achieve a reasonable accuracy. The calibration experiments showed that a short duration of antecedent precipitation gave a model performance with the second and third implementation similar to the first one with a long duration (Fig. 6.5 and Fig. 6.6). For example, when the duration of antecedent precipitation = 8 time steps, the simulated stream flow using the second (Fig. 6.10) and third implementation (Fig. 6.12) was close to or better than those using the first one with the duration = 15 time steps (Fig. 6.4). In the calibration experiments the third implementation gave a slightly better model performance than the second one, but the difference was small (Fig. 6.5 and Fig. 6.6). The results of cross validation for the three implementations showed when the duration ≤ 100 days, overfitting did not occur in the all three implementations. Thus, within this duration range, the model improvement from the first to the second and third implementations was due to the application of the WSS area. In the validation experiments (Table 6.1), the first implementation required the duration of 9 time steps to achieve a similar performance as the second and third implementations, which only used the duration of 1 time step. This analysis supports that increasing complexity and applying the retrievals of WSS area in the discrete rainfall runoff model reduces the required duration of antecedent precipitation, without degradation of model performance. The second implementation achieved better performance than the other two implementations (Table 6.1). This indicates that the complexity of the second implementation is enough to simulate and predict stream flow. The application of WSS area in the second and third implementations determines the partitioning of precipitation into overland and infiltrated flow and indicates the regional water storage capacity. The changes of WSS area are mainly associated with the balance between the inflow (e.g. storage of water flow produced in the previous time step) and outflow (i.e. gradual releasing water flow to rivers). Thus, WSS area also includes the information of antecedent precipitation and its application in the discrete rainfall-runoff

model reduces the duration of antecedent precipitation required to achieve a reasonable model accurate.

The longest duration of antecedent precipitation determines the number of unknown parameters in the matrix $\boldsymbol{\beta_w}$ in Eq. (5.15). For a given duration, the second and third implementations require the same number of unknown parameters, while the first implementation requires fewer parameters. Besides the duration of antecedent precipitation, the influence of the number of unknown parameters on the model performance needs to be evaluated. The model performances were compared among the three implementations with the same number of unknown parameters. In the calibration experiments for 2002 (Fig. 6.14a), the second and third implementations gave better NSE than the first one, except when the number of unknown parameter = 4. In 2005 (Fig. 6.14b), the situation is opposite: the first implementation gave better NSE than the other two, except when the number of unknown parameter = 8. This large difference between 2002 and 2005 indicates that the WSS and inundated area will be more important in the wet year than in the dry year. The mean parameter values were used to analyze the influence of the number of model parameters in the 2001 validation experiments (Fig. 6.15), since this set of model parameters gave the best accuracy for all three implementations, compared with the other two experiment sets (Fig. 6.8). The second implementation had better NSE than the other two when the number of unknown parameters = 4 and the third one had better NSE than the other two when the number of unknown parameters = 6. When the parameter number ≥ 8, the first implementation had the best NSE. With parameter number ≤ 6, the NSEs of the second and third implementations were similar to the NSE of the first implementation with parameter number ≥ 8 (Fig. 6.14). In other words, comparable accuracy was achieved when using the retrievals of WSS area and fewer model parameters. The reduced model parameters will benefit the calibration and application of the discrete rainfall-runoff model in different regions.

(a)   (b)
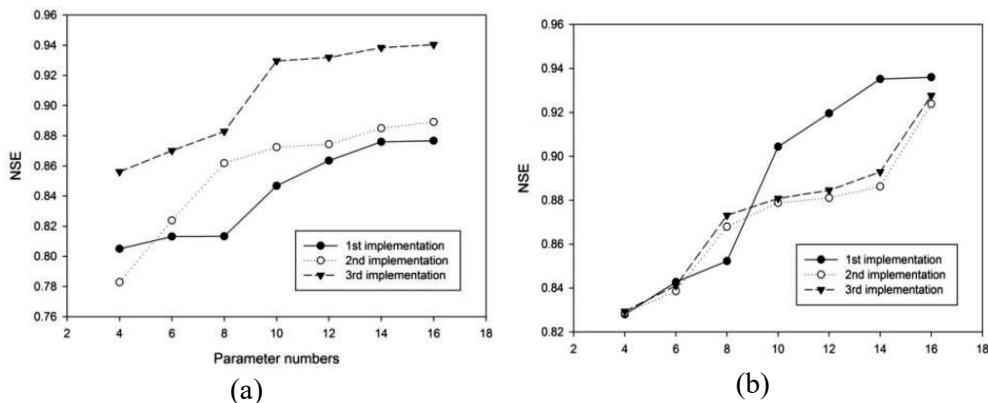
Figure 6.14: The Nash-Sutcliffe Efficiency (NSE) of three implementations with the same number of model parameters in calibration for 2002 (a) and 2005 (b).
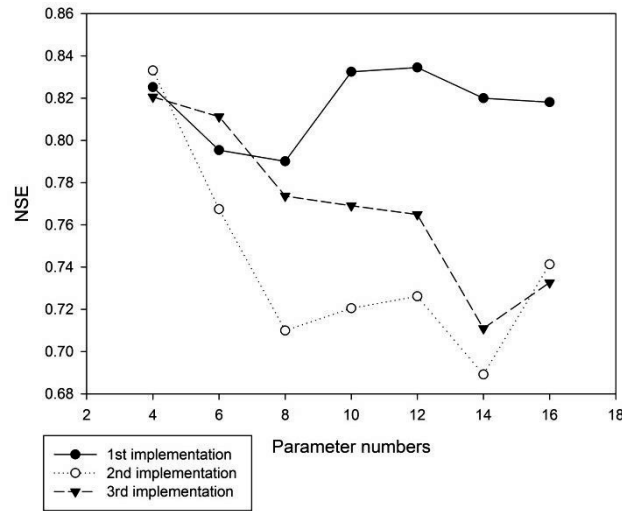
Figure 6.15: The Nash-Sutcliffe Efficiency (NSE) of three implementations with the same number of averaged model parameters in the validation for 2001.

6.5.2 Model performance with the mean model parameters

In the validation experiments, the best performance for all three implementations was obtained when using the parameter values averaged over the wet (2002) and dry (2005) (Fig. 6.8 and Table 6.1). In Table 6.1, it was also listed that the longest durations of antecedent precipitation applied to achieve the best performance with each implementation. The averaged parameters and the corresponding durations in Table 6.1 can also be used to predict the stream flow in 2002 and 2005 to evaluate the performance of the three implementations, since they are different from the ones obtained by calibration for each year. For the first implementation, the averaged parameters and the duration of 9 time steps were applied, while for the second and third implementation, the averaged parameters and a duration of 1 time step were applied. The first and second implementations gave similar estimates of stream flow (Fig. 6.16). Streamflow was underestimated between DOY 100 and 240 in 2002, and between DOY 200 and 260 days in 2005, while it was overestimated between DOY 240 and 365 in 2002, and between DOY 160 and 180 in 2005. The performance metrics for the first and second implementations using averaged parameters and the chosen durations were also similar, with $0.77 \leq NSE \leq 0.80$ and $34\% \leq RRMSE \leq 36\%$ in 2002 and $0.78 \leq NSE \leq 0.79$ and RRMSE=33% in 2005 (Table 6.2). The third implementation had the best performance in 2002 (with NSE = 0.83 and RRMSE = 31 %) but worst in 2005 (with NSE = 0.67 and RRMSE = 43%). These results suggest that the first and second implementations have a relative stable performance with the averaged parameters and the chosen durations, while the performance of the third implementation was very different in the dry and wet year. This is probable due to the difference in ground water table depth, which also determines the weight sets in the third implementation (Eq. (5.13)).

Table 6.2: Model performance in predicting stream flow in 2002 and 2005 with the three implementations and the mean parameters.

	2002		2005	
	NSE	RRMSE	NSE	RRMSE
1st implementation	0.80	34%	0.78	33%
2nd implementation	0.77	36%	0.79	33%
3rd implementation	0.83	31%	0.67	43%
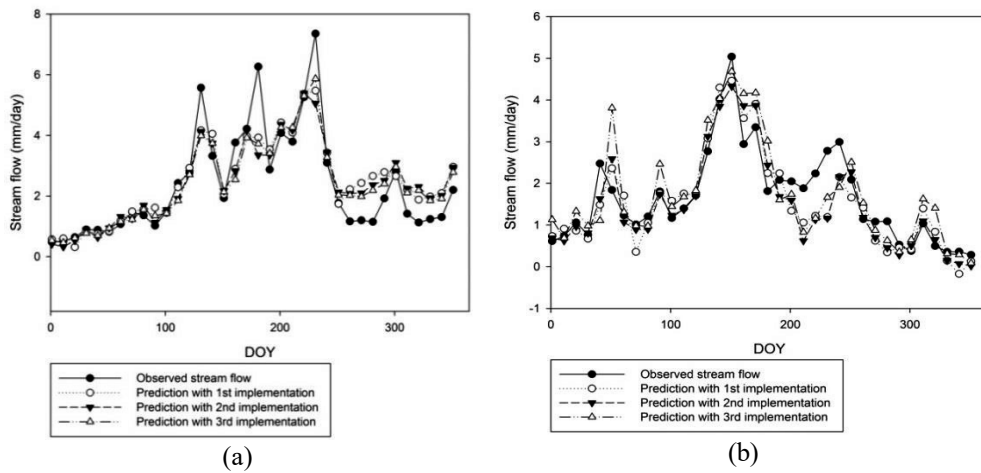
Figure 6.16: The observed and predicted stream flow in 2002 (a) and 2005 (b) with the three implementations using mean parameters and the chosen durations in Table 6.1.

6.5.3 Interpretation of the weight set

In the calibration periods of the three implementations, there are some key durations that largely improved model performance. In the validation experiments of the three implementations, there is also some duration that changed the overall-decayed-trend of model performance when the duration of antecedent precipitation was increased step-wisely. These clear performance improvements in calibration and validation periods probably indicate the duration that the catchment takes to produce fast and slow runoff, which can be interpreted by the weight sets of each implementation. The weight set illustrates the evolution of the contributions of precipitation or the component flow to stream flows at various time steps. The model performance changes when the duration of antecedent precipitation was increased, e.g. from 6 to 7 time steps, is related to the integrated contributions of precipitations from current to the increased longest duration (i.e. 0 to 7

time steps). It needs to mention again that the weight can have negative or positive values. The positive value means that a certain amount of precipitation (or component flow in the second and third implementations) is transformed into stream flow. The negative value indicates the catchment stores part of produced water flow (i.e. base flow from ground water and water flow from other antecedent precipitations). The stored water may be in surface storage elements, e.g. lakes, reservoirs, and wetlands (i.e. WSS area), or be in subsurface storage elements, e.g. soil layer and aquifer, which will be released gradually later on. Thus, through interpreting the weight set within a certain duration, we can understand the catchment response to rainfall, i.e. storing and releasing water flows in time. Since the second and third implementations partition precipitation into component flows (e.g. overland and infiltrated flows in the second implementation and overland and potential subsurface flows in the third implementation), their weight sets can be used to better interpret the catchment response analyzed from the weight sets of precipitation with the first implementation.

Two kinds of catchment response lead to the performance changes in all three implementations. The first one is associated with the duration to release fast or slow water flows. For example, in the calibration period of 2002, the catchment takes 20 days to produce fast water flow, due to that the large model performance improvement from 1 to 2 time steps in the first implementation (Fig. 6.5) are associated with the largest positive weights of precipitation at time step 1 and 2 in 2002 (Fig. 6.17a). Both overland flow and fast subsurface flow contributes to the fast flow in 2002, since at the time step 1 and 2, the weights of both overland and infiltrated flows in the second implementation (Fig. 6.18a and 6.18b) have positive values, while fast subsurface flow is the major pathway, since the weights of the potential subsurface flow is larger than overland flow at time step 1 and 2 in 2002 (Fig. 6.19a and 6.19b). This finding agrees with the results derived from model analysis about the contributions of component flows in wet tropical catchments (see e.g. Chappell et al., 2017), where fast subsurface flow is the dominant pathway for precipitation. In the rainy season of the Xiangjiang river basin, monsoon brings intensive precipitation and the water storage capacity is low, similar to the condition in wet tropical catchments, Thus, fast surface flow is easily produced, due to shallow depth of water saturated soil in such kind of catchments.

The duration that the catchment takes to produce slow water flow seems similar in dry and wet year, i.e. about 70 – 80 days. In the calibration period of 2002, the large performance improvement in the first implementation occurs when the duration was increased from 7 to 8 time steps, while in 2005, performance improvement occurs when the duration was increased from 6 to 7 time steps. Slow subsurface flow is the major path of precipitation within such long duration, due to that both infiltrated and potential subsurface flow have continuous positive weights from time step around 5 to 8 in Fig. 6.18 and Fig. 6.19. The large model improvement in the second and third implementations when the duration was increased from time step 7 to 9 in 2002 (Fig. 6.5) and 2005 (Fig. 6.6) is probably due to the largely releasing of overland flow (i.e. large positive weights of overland flows at time step 8 and 9 in the second and third implementations in Fig. 6.18 and Fig. 6.19) and large storage of infiltrated flow and potential subsurface flow (i.e. large

negative weights of infiltrated flow and potential subsurface flow at the same time step in Fig. 6.18 and Fig. 6.19. This long term releasing of overland flow may be associated with the release of the stored water in WSS area, like wetlands, lakes and reservoirs. For example, the stream flow mechanism in South America (Vörösmarty et al., 1989; Vörösmarty et al., 1996) shows that the large inundated forest area stores stream flow from upstream and releases surface runoff gradually later on. In the Xiangjiang river basin, large paddy area and hundreds of small lakes plays the similar role as the inundated forest area. After time step 9, the performance improvement was very slow in the second and third implementations, mainly due to that antecedent precipitation after time step 9 is used to recharge ground water and has been released by base flow.

The second kind of catchment response that significantly influence model performance is the storage of over-produced water flow in surface (i.e. enlarging the WSS area) and subsurface (i.e. increasing soil moisture). For example, the mode improvement from 2 to 3 time steps in 2002 is probably due to the storage of water flow by the catchment at time step 3, i.e. the negative weight of precipitation at time step 3 in the first implementation (Fig. 6.17a). According to the weights of component flows at the same time step in the second and third implementations (Fig. 6.18a,b and Fig. 6.19a,b), the storage probably occurred in fast subsurface flow, i.e. negative weights in infiltrated flow (Fig. 6.18b) and potential subsurface flow (Fig. 6.19b). This storage is reasonable. It indicates that the produced water flow in past 20 days is too much for the catchment to release, thus antecedent precipitation within the duration of 20 – 30 days was not transformed to stream flow and part of produced water flow in past 20 days was stored by the catchment, e.g. in WSS area (e.g. lakes, wetlands, reservoirs) and un-saturated soil surface and aquifers. The stored water flow by WSS area will be released gradually in later periods of time. In fact, at time step 4 in the third implementation in 2002, we can find strong releasing in overland flow (i.e. the peak weight in Fig. 6.19a) and also a high amount of stored potential subsurface flow (i.e. the high negative weight in Fig. 6.19b). This catchment response at time step 4 leads to the large model improvement in calibration periods of the third implementation, when the duration was increased from 3 to 4 time steps in 2002 (Fig. 6.5).

There are several interesting differences in the weights sets between 2002 and 2005. The first one is that the overland flow takes different time to reach river and channels between wet and dry years. In a wet year (Fig. 6.17a), overland flow is continuously released for 50 days after rainfall, which is close to 1.5 month time lag between precipitation and stream flow in a large catchment as observed by Gleick (1987). The shorter period of continuously releasing overland flow in 2005, i.e. 30 days after rainfall, is probably due to the relative dry condition in the catchment. The produced water flow after 30 days in 2005 may be stored by soil layers through percolating (i.e. the negative weights after time step 3 in Fig. 6.18c and Fig. 6.19c) and leads to the release of subsurface flow (i.e. the positive weights after time step 4 in Fig. 6.18d and Fig. 6.19d). This interaction between surface and subsurface runoff complicated the simulation of stream flow, which, in fact, is seldom taken into account by current conceptual or statistical hydrological models. It needs further studies about this interaction in other catchments, however, in the Xiangjiang river basin, the interaction of water flow between surface and subsurface is very significant.

Another interesting difference between 2002 and 2005 is the precipitation contribution at 0 time step, i.e. when it falls on the catchment. When rain falls in 2002, precipitation contributed to stream flow mainly through overland flow, since the overland flow at 0 time step had large positive weights in the second (Fig. 6.18a) and third (Fig. 6.19a) implementations, while the produced infiltrated flow, had been used to recharge soil layers, since the infiltrated and potential subsurface flow both had negative weights (Fig. 6.18b and Fig. 6.19b). In 2005, an opposite situation occurs: the overland flow was used to recharge soil layers, i.e. negative mean and median weights in overland flow at 0 time step (Fig. 6.18c and Fig. 6.19c), while fast subsurface flow reached rivers, i.e. positive mean and median weights in infiltrated ((Fig. 6.18d)) and potential subsurface flow (Fig. 6.19d). This difference is mainly related to the different soil wetness condition in wet and dry years. In 2002, water saturation condition in the top soil layer was high, thus a large fraction of precipitation was used to produce overland flow. In 2005, top soil layer was dry, thus a large fraction of precipitation percolated into deep soil and produced fast subsurface flow.

In 2005, the weights of overland flow in the third implementation form (Fig. 6.19c) were almost the same as in the second implementation form (Fig. 6.18c), and the weights of potential subsurface flow in the third implementation (Fig. 6.19d) were very similar to the ones of infiltrated flow in the second implementation (Fig. 6.18d). This means that the potential subsurface flow in combination with observed groundwater table is an effective schematization of hydrological processes in the study area.

Through above analysis on the weight sets of three implementations, we can find that the inter-annual difference in the catchment response is very significant and when different duration of antecedent precipitation is involved by the model, the weight sets are also changed. This means that the weight sets are sensitive to both regional water storage conditions and the duration, which can be used to explain the different model performance in calibration and validation periods.

The weight set indicates the evolution of the contributions of precipitation or the component flow to stream flows at various time steps during a certain period. The variability in the model performance of three implementations can be explained by analyzing the estimated weights. It was found that when the duration of antecedent precipitation was increased, the weights in the first implementation (Fig. 6.17) varied in a smaller range than the weights in the second and third implementations (Fig. 6.18 and Fig. 6.19). In the first implementation, the 25% — 75% range of precipitation weights varies between 0.01 to 0.1 in 2002 and 0.005 to 0.05 in 2005 (Fig. 6.17). Due to that the overfitting problems occurred in the second and third implementations when the duration > 10 time steps, the weights applying to duration $\leq$ 10 time steps were analyzed. In the second implementation, the 25% — 75% range of weights in overland flow was 0. 1 to 0.4 in 2002 and 0.05 to 0.35 in 2005, while the 25% —75% range of weights in infiltrated flow was 0.05 to 0.3 in 2002 and 0.02 to 0.18 in 2005. In the third implementation form, the range of weights in component flows was similar to that in the second implementation. The small range in the first implementation means that the weights are not so sensitive to the duration of antecedent precipitation as in the second and third implementations. This may explain why in the calibration and validation experiments the performance of the first

implementation fluctuated in a small range. The large weight ranges in the second and third implementations yielded faster model improvement than in the first implementation in the calibration experiments (Fig. 6.5 and Fig 6.6). But the high sensitivity of the weights to the duration of precipitation and the significant inter-annual variability in the weights (see the analysis below) resulted in the degraded performance of the second and third implementations in the validation experiments. In fact, the model error is accumulated when the duration is longer, since the discrete rainfall runoff model integrates errors at each time step involved in the model duration.

(a)   (b)
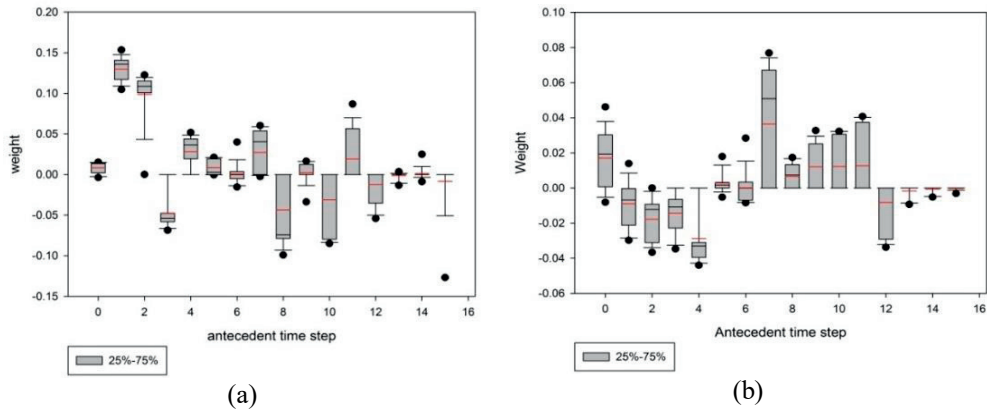
Figure 6.17: The box plot of precipitation weight at each antecedent time step in calibration of the first implementation. (a) weights in calibration for 2002; (b) weights in calibration for 2005.The duration of antecedent precipitation were increased step-wisely from 1 to 15 time steps in the calibration. The red dash line in each box is the mean value, the black line is the media value, and dot points are outliers.
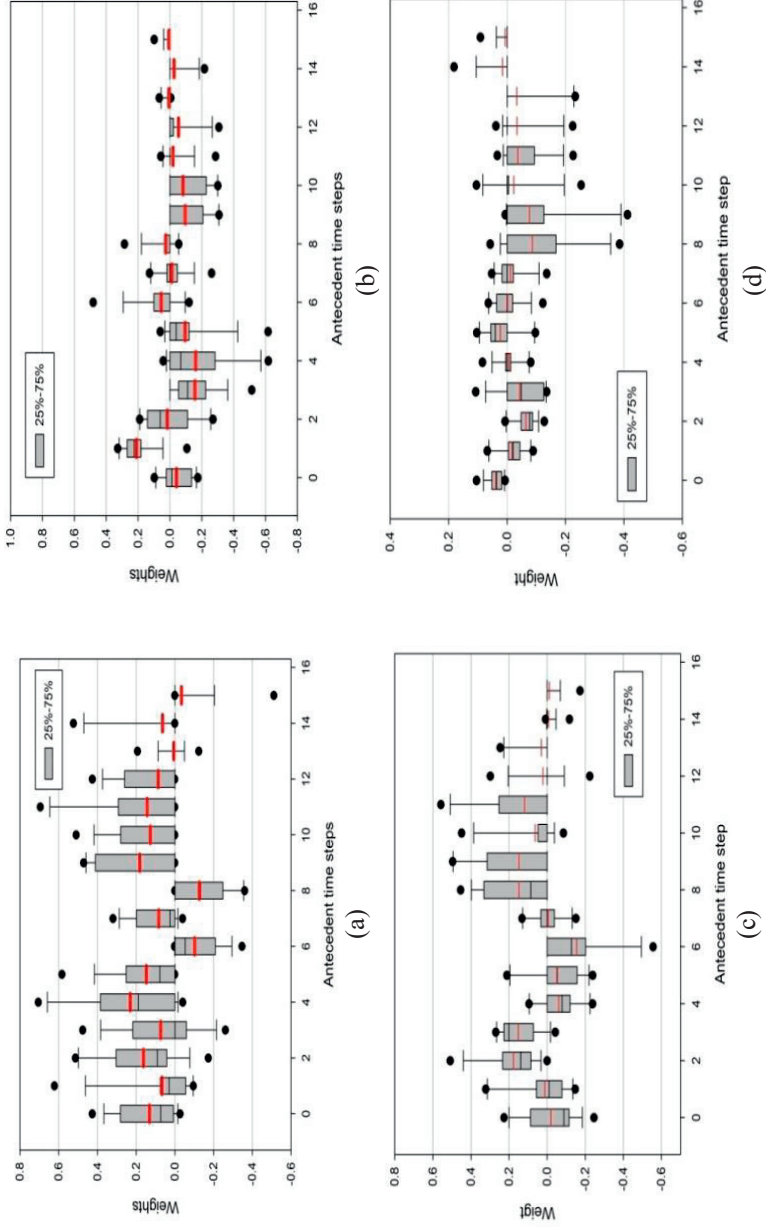
Figure 6.18: The box plot of weights of overland and infiltrated flow at each antecedent time step in the calibration of the second implementation of the discrete rainfall-runoff model. (a) the weights of overland flow in calibration for 2002; (b) the weights of infiltrated flow in calibration for 2002; (c) the weights of overland flow in calibration for 2005; (d) the weights of infiltrated flow in calibration of 2005. The duration of antecedent precipitation was increased step-wisely from 1 to 15 time steps in the calibration. The red dash line in each box is the mean value, the black line is the media value, and dot points are outliers.
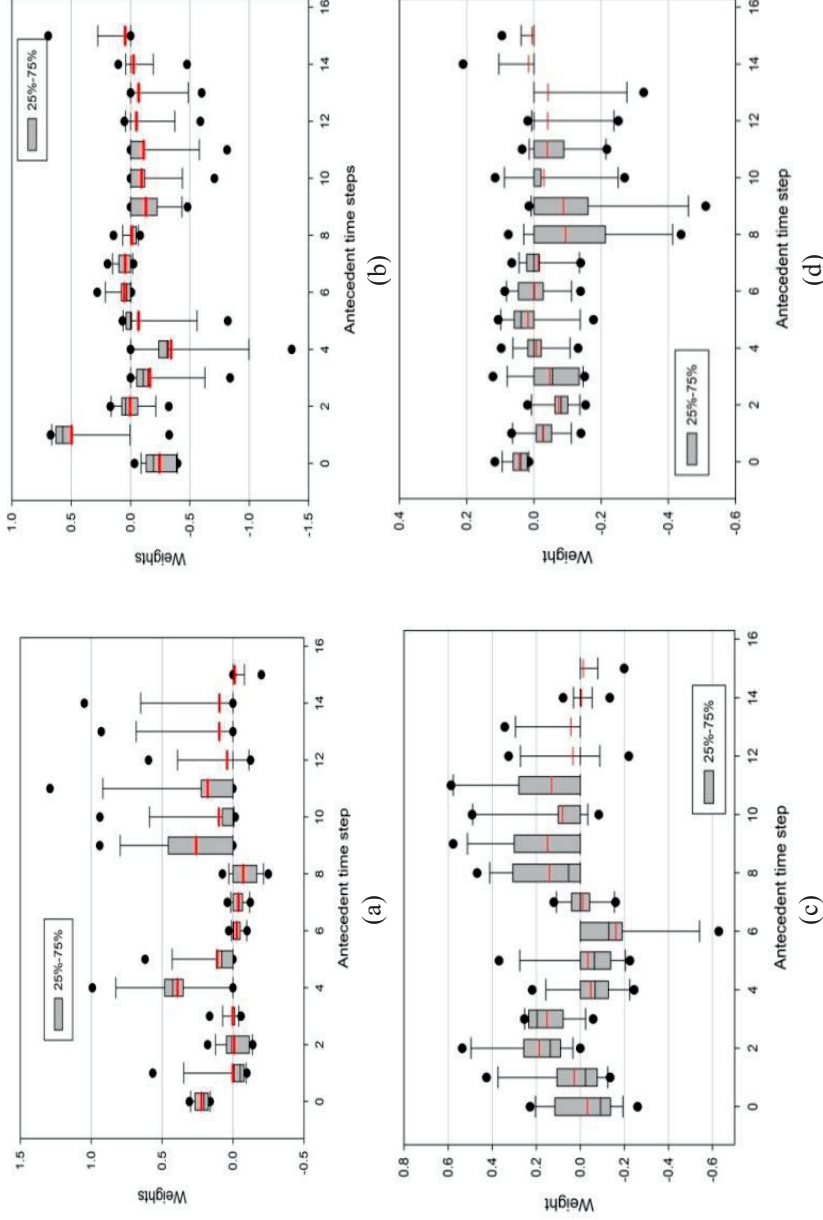
Figure 6.19: The box plot of weights of overland and potential subsurface flows at each antecedent time step in the calibration of the third implementation of the discrete rainfall-runoff model. (a)the weights of overland flow in calibration for 2002; (b) the weights of potential subsurface flow in calibration for 2002; (c) the weights of overland flow in calibration for 2005; (d) the weights of potential subsurface flow in calibration for 2005. The duration of antecedent precipitation was increased step-wisely from 1 to 15 time steps in the calibration. The red dash line in each box is the mean value, the black line is the media value, and dot points are outliers.

6.5.4 The recharge period of ground water

In the calibration period, there were some stages when the model performance was improved much more than in other cases (Fig. 6.5 and Fig. 6.6). This indicates that specific time steps have larger impacts on the model performance than others. In the validation experiments (Fig. 6.8), it was found that when the duration of antecedent precipitation was increased from 6 to 9, the model performance was improved in all three implementations. Thus, to analyze when these model performance improvements occur, the RRMSE was calculated in each season of both 2002 and 2005 for the three implementations with various durations (Fig. 6.20). When the duration was increased from 1 to 15 time steps, the reduction in RRMSE was significant in the autumn and winter for the first implementation (Fig. 6.20a). This indicates that the stream flow after June is influenced by longer antecedent precipitations, for example those in the spring. This is consistent with other studies on the floods in this river basin (Lin and Lu, 1991; Zhou, 1991; Zong and Chen, 2000), where the magnitude of floods after June was related to the rain in the spring. In the autumn and winter for the first implementation (Fig. 6.20a) and in all four seasons for the second and third implementations (Fig. 6.20b and 6.20c), when the longest duration < 8 or 9 time steps, RRMSE was much higher than those with the longest durations ≥ 8 or 9 time steps. When increasing the longest duration range from 8 or 9 time steps to 15 time steps, the RRMSE in each season improved slightly for all three implementations. This gives an estimate of time needed for precipitation to recharge ground water in our study area, i.e. 80 or 90 days, since all three implementation forms are based on the assumption that base flow is only from precipitations older than a certain time.
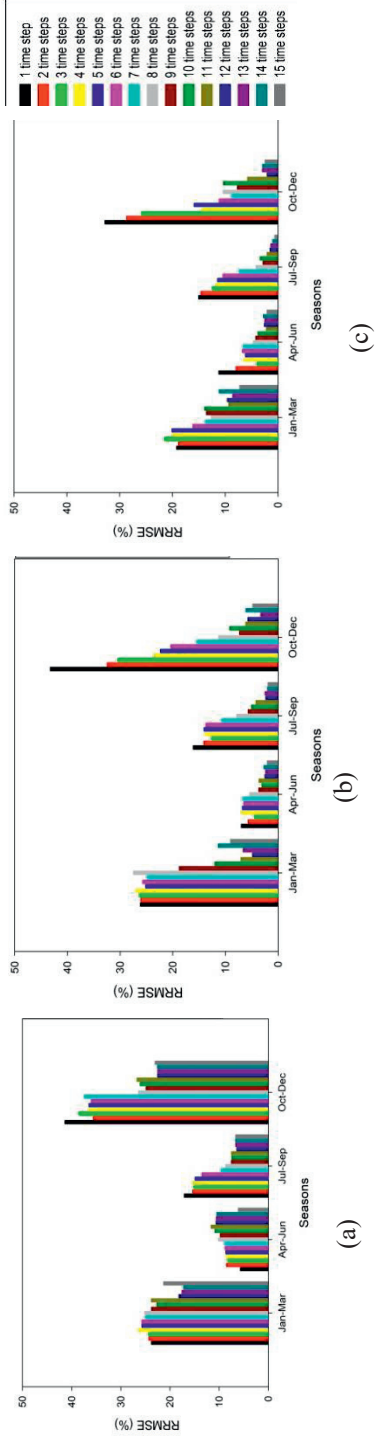
Figure 6.20: The Relative Root Mean Square Error (RRMSE) of modelled stream flow in each season during the calibration for both2002 and 2005. (a) the first implementation; (b) the second implementation; (c) the third implementation. The duration of antecedent precipitation was increased step-wisely from 1 to 15 time steps for each implementation

6.6 Conclusions

The retrievals of the Water Saturated Surface (WSS) area from 37 GHz microwave observation (Shang et al., 2015) supplies a straightforward and lagged relationship between precipitation and stream flow. To fully and effectively use this data, a discrete rainfall-runoff model and the three implementations had been developed in the previous chapter.

Through calibration and validation in this chapter, the three implementations were proved to be able to estimate stream flows in the Xiangjiang river basin, China. The longest duration of precipitation is an important factor to determine model performance. In the calibration experiments, 10-day mean stream flows at Changsha station in 2002 (wet) and 2005 (dry) are used to estimate the weights with various durations. Increasing the longest duration from 1 to 10 time steps, the NSE of the first implementation increased from 0.78 to 0.86 in 2002, from 0. 82 to 0.92 in 2005, and RRMSE decreased from 34 % to 27 % in 2002, from 28 % to 19 % in 2005. NSE for the second implementation increased from 0.78 to 0.94 in 2002, from 0. 83 to 0.96 in 2005, and RRMSE decreased from 34 % to 17 % in 2002, from 27 % to 12 % in 2005. NSE for the third implementation form increased from 0.86 to 0.97 in 2002, from 0. 83 to 0.96 in 2005, and RRMSE decreased from 27 % to 12 % in 2002, from 27 % to 12 % in 2005. Through cross-validation, it was proved that the increment in model performance is mainly due to the model structure, especially taking the WSS area and the ground water table depth into account, with the duration ≤ 10 time steps. In the validation experiments, the longest duration used in the second and third implementation should be less than 20 days, much less than for the first implementation, which used 90 days. The mean parameters over 2002 and 2005 gave a stable model performance with the first and second implementations. The complexity level of the second implementation was sufficient to simulate and predict stream flows in the study area.

The pattern of precipitation weights in the first implementation explains the interactions between catchment and stream flow. Clear differences in the catchment response were observed between the dry and wet years. The weights sets of component flows in the second and third implementation specify the path of precipitation towards stream flow. The range of weights in the first implementations was smaller than in the other two implementations, which probably explained why the first implementation was not so sensitive to the increasing duration of precipitation as the second and third implementations. The weights of overland and potential subsurface flows in the third implementation had a very similar pattern with those of overland and infiltrated flows in the second one, when the depth of water saturated soil was deeper and close to the depth of the groundwater table, e.g. in dry years.

The changes of the RRMSE in autumn for the first implementation indicate the influence of rain in the spring on stream flow in autumn (Lin and Lu, 1991; Zhou, 1991; Zong and Chen, 2000). The changes of RRMSE in each season for the three implementations lead to estimate the duration of ground-water recharged by precipitation as around 90 days. Overall, with the WSS as an essential parameter, the three implementations

of the discrete rainfall-runoff model not only simulated and predicted stream flow, but also characterized the catchment response to precipitation and the mechanisms determining stream flow. The application of the WSS area can make the discrete rainfall-runoff model to use fewer parameters.

Chapter 7

Conclusions and Perspectives

Surface water is one of the key resources for human life. The area of surface water body in a catchment has a close but lagged relationship with river discharge. Overland flow may lead to flooding that risks the properties and lives. Thus, the observations of surface water bodies and knowledge about inundation patterns are essentially important for water resource management and flood early warning. In large subtropical floodplains, it is attractive to observe surface water bodies using Polarization Difference Brightness Temperature (PDBT) at 37 GHz measured by radiometers onboard sun-synchronous satellites, due to its capability to penetrate clouds and vegetation, fast revisiting, and long-term and free data record. Due to the shallow detected depth at 37 GHz, the Water Saturated Surface (WSS), i.e. standing water and water saturated soil, can be retrieved from the PDBT. Seasonal changes in vegetation and various surface roughness conditions both complicate the retrieval of WSS in the subtropical floodplains. Atmospheric attenuation, observation gaps and errors in microwave observations, however, reduce the capability to observe daily or weekly changes of WSS with PDBT data. The role that WSS area plays in stream flow production has not been fully accounted for by current hydrological models. Accordingly, there are three research questions raised in this thesis: 1) Is there a possible method to retrieve Water Saturated Surface from PDBT at 37 GHz taking both the variable vegetation cover and surface roughness into account? 2) Is it possible to design a method to remove the atmosphere influence, observation gaps and errors in time series of microwave observations? 3) Is it possible to build up a new rainfall-runoff model that applies the retrieved WSS to mitigate the complication in model calibration and the difficulty in data accessibility?

7.1 Achievements

The two-step model was developed to retrieve fractional area of WSS from PDBT at 37 GHz in the subtropical floodplains with seasonal vegetation and various surface roughness conditions. In the first step, the zero-order radiative transfer model was simplified for PDBT at 37 GHz by eliminating the single scattering between vegetation and surface and introducing the fractional area of vegetation coverage. With this simplified model, the vegetation optical thickness was parameterized by regressing the PDBT and Normalized Difference Vegetation Index (NDVI) at flooded paddy fields. Large area of double-crop paddy fields in the study area, i.e. Poyang Lake and Dongting Lake floodplains, supplies a good experiment case, of which the surface temperature and water content can be assumed to be constant during their several flooding periods. The irrigation plan of paddy fields strictly follows the phenology of rice. Thus, only vegetation factor, i.e. vegetation fractional cover and vegetation optical thickness, influences the observed PDBT. After identifying these parameters, the Polarization Difference Effective Emissivity (PDEE) can be retrieved from the PDBT at 37 GHz with this simplified model.

In the second step, a linear model was developed to estimate the fractional area of WSS from the retrieved PDEE. This linear model was derived from the numerical analysis about the relationship between soil moisture and surface emissivity, which includes the soil-water mixtures models and the Qp surface roughness model. Both physical (e.g. Dobson model) and empirical (Wang-Schmugge model) soil-water mixtures models were applied to estimate the dielectric constant of soil-water mixture at 1.4 GHz, 19 GHz and 37 GHz, which were used to derive surface emissivity. This simulation clearly shows that the Polarization Difference Emissivity (PDE) at a smooth surface is quasi linearly related to soil moisture at 37 GHz, independent on the type of the applied soil-water mixture model. The polarization difference effective emissivity, i.e. PDEE, was derived from the PDE by estimating the attenuation of surface roughness with the Qp surface roughness model. Enlarging the surface roughness will smooth the linear relationship between PDEE and soil moisture at 37 GHz, thus it is necessary to take the surface roughness condition into account. Taking the spatial heterogeneity of soil moisture into account, the fractional area of WSS area can be expressed as the regional water saturation condition, which can be derived from PDEE with the linear model.

The two-step model can only be applied during clear days, since atmospheric attenuation at 37 GHz is very significant during cloudy and rainy days and has not been accounted for in the simplified radiative transfer model. Besides that, the observation gaps and errors are also introduced to PDBT observations by the configuration of swath path and the registration and resampling methods. Thus, the time series of PDBT consist of four components: the surface signal including surface emittance and vegetation attenuation, the atmospheric signal including atmosphere emittance and attenuation, the observation gaps and errors. According to the linear and multiplicative properties of Discrete Fourier Transform (DFT), the spectral features of each component signal can be revealed in the power spectrum of PDBT time series at a certain level. Based on that, the Time Series Analysis Procedure (TSAP) was developed and includes two stages: 1) to identify the

spectral range related to observation errors and gaps and filter them out with a boxcar filter; 2) to identify the spectral features of atmospheric signal by applying spectral analysis of precipitation time series and filter them out with the Harmonic ANalysis of Time Series (HANTS) algorithm. The spectral features of the observation gaps and periodic observation errors were all located in very high frequency domain, according to the numerical analysis of the power spectrum of these two components. The boxcar filter was modified to remove the spectral features of the observation gaps and errors, in order to deal with various gap sizes (that change when moving the filter over the time series step-wisely) and remove the possible periodic observation errors. The spectral features of the atmospheric signal were revealed by the power spectrum of rain-gauge time series, since the atmospheric influence at 37 GHz is mainly due to hydrometeors. Only short-term periodic components in precipitation time series were associated with the atmospheric signal, which can be identified by analyzing the increasing rate (i.e. slope) in the accumulated power spectrum of precipitation time series. We assumed that in the short period range, the spectral features of the precipitation time series are only associated with the atmospheric signal and the remaining spectral features in the PDBT time series are only associated with the surface signal, since Fourier analysis cannot separate the amplitude contribution of the overlapping frequencies of the two signals. Thus, the spectral features of the surface signal were the union of the spectral features in the short and long period range, The atmospheric signal was removed by reconstructing the surface signal by HANTS algorithm with the spectral features of the surface signal. The statistical evaluation proved that the noisy level of the PDBT time series had been significantly reduced by TSAP.

The overall method combined the TSAP and the two-step model. TSAP was first applied to PDBT time series to extract the surface signal and the WSS area was retrieved from the surface signal by the two-step model. This method was evaluated by comparing the retrieved WSS area of Poyang Lake with the lake area observed by MODIS and ASAR, with R^2 0.77 and RRMSE 22%. TSAP needs rain-gauge data to identify the spectral features of the surface signal, however, for a large floodplain, the limited number of rain gauges cannot cover each pixel. Thus, the uniform spectral features of the surface signal, which can be applied to all pixels, were derived from available rain-gauge data by choosing harmonic components with lower frequencies, since within the same floodplain, the long-term periodic components in the surface signal is dominated by the same atmospheric system, e.g. monsoon. The overall method using these uniform spectral features achieved a reasonable accuracy, and thus was applied to the Poyang Lake and Dongting Lake floodplains. In the Poyang Lake floodplain, the cross-correlation analysis between up- and down streams showed that Poyang lake extension is closely related to the fluctuations of upstream WSS area with a time lag 3 – 5 days. During the closure of the Three Gorge Dam, this relationship was more evident. The spatial and temporal pattern of the WSS area in the Poyang Lake and Dongting Lake floodplains demonstrated the flooding propagation, in a good agreement with the hydrological and meteorological records.

The straightforward and lagged relationship between the retrieved WSS area and stream flow leads to the development of the discrete rainfall-runoff model, so that to mitigate the complexity in model calibration and the required data set. The model simulated

stream flow as the integration of the contributions of precipitation or specific component flows within a certain period. Ground water table depth and the retrieved WSS area were applied to develop the three implementations with increasing complexity. According to the input parameters, the three implementations are: 1) precipitation and base flow; 2) overland flow, infiltrated flow and base flow; 3) overland flow, subsurface flow and the base flow. The second implementation was developed by partitioning precipitation in the first implementation into overland and infiltrated flows according to the retrieved WSS area. The third implementation wad developed by replacing the infiltrated flow in the second implementation with the potential subsurface flow that is the estimation of subsurface flow. The potential subsurface flow was estimated by scaling the infiltrated flow with the ground water table depth.

The three implementations of the discrete rainfall-runoff model were calibrated and validated in the Xiangjiang River basin, China, with the duration of involved antecedent precipitation increasing from 10 to 150 days. The second and third implementations had better performance than the first one, when the duration was increased step-wisely from 10 days to 100 days in the calibration period. In the validation period, the second and third implementations used the duration of 10 days to achieve the best performance of the first one using a duration of 90 days, with Nash-Sutcliffe Efficiency ≈0.83 and Relative Root Mean Square Error ≈ 34%. Cross validation proved that the better performance in the second and third implementations was due to applying the retrievals of WSS area. The set of model parameters is an indication of dominant hydrological processes in determining the catchment response to rainfall. The RRMSE of each season at the calibration stage indicates the possible ground water recharge period, i.e. 90 days, in the Xiangjiang River basin.

7.2   Perspectives

This thesis developed a two-step model to retrieve the fractional area of WSS from PDBT at 37 GHz, also quantifying the influence of vegetation attenuation and surface roughness. The accuracy of the retrievals depends on not only the developed model but also the quality of input PDBT data, of which the later one may be more important in the future works. A time series of daily PDBT observations is full of observation gaps and errors and is influenced by atmospheric water content, which all contaminate the surface signal (including surface emittance and vegetation attenuation) in the PDBT time series. TSAP was developed to remove these noisy components in the PDBT time series and to extract the surface signal as the qualified input data for the two-step model. Thus, the overall method combined the TSAP and the two-step model to retrieve daily fractional area of WSS from the PDBT time series. According to the evaluation in this thesis, the accuracy of the overall method was reasonable, however, through the comparison between SSM/I and AMSR-E data, it is clear that TSAP cannot remove the atmospheric influence due to clouds. To solve this problem, there might be two approaches.

The first approach may be to combine rain-gauge time series and the observations of clouds in a proper way, so that the full spectrum of the atmospheric signal (including atmosphere emittance and attenuation) in the PDBT time series can be identified. In TSAP, only rain-gauge time series was used to reveal the spectral features of the atmospheric signal, mainly due to that the atmospheric water content retrieved from microwave observations has low accuracy during cloudy and rainy days. Clouds can be clearly observed from optical and thermal images onboard stationary satellites, which can supply observations close to the passing time of microwave radiometers. The retrievals of atmospheric water content from microwave radiometers may be evaluated by comparison with the optical and thermal clouds observations, e.g. the area of clouds and its optical thickness. After this evaluation, atmospheric water content retrieved from microwave observations can be combined with rain-gauge data to identify the full spectrum of the atmospheric signal.

The second approach may be to combine the AMSR-E and SSM/I observations. Through the comparison between AMSR-E and SSM/I, it was found that in some periods, the PDBT time series acquired by AMSR-E showed a different trend from SSM/I, probably due to the different observation times and spatial resolution of these two radiometers. Combining two radiometer data sets intensifies the sampling frequency within a day and also reduces the number of observation gaps in the time series. More available samples might improve input data quality, i.e. with more samples that are less influenced by atmospheric water content. In fact, the two proposed approaches can be combined together to improve the performance of TSAP, by reducing the gap size and identifying the full spectrum of the atmospheric signal.

The development of the discrete rainfall-runoff model, from our point of view, has another important purpose, i.e. using only satellite observations to simulate and predict river discharge at any catchment. The second and third implementations had used the satellite observations of precipitation from TRMM and the retrievals of WSS area from SSM/I. Satellite observations of stream flow will be available in the future when SWOT mission is launched. The in-situ measurements of ground water table depth, however, are still needed. GRACE mission can supply the monthly changes of surface water mass, which is closely related to the changes of ground water table depth. It will be very interesting to improve the temporal resolution of the GRACE data and to replace the in-situ measurements in the discrete rainfall-runoff model with the GRACE data, so that all input data of the model can be derived from satellite observations. The major challenge in the application of GRACE data is the coarse spatial resolution, which would not cover the catchment exactly. How to merge the retrievals of WSS area at 37 GHz with GRACE data whose spatial resolution is even coarser would be the next step of the discrete rainfall-runoff model. In that case, the performance of the discrete rainfall-runoff model can be evaluated at many catchments, without asking for the permission to access hydrological data or implementing field measurements for each catchment.

References

Agrawal, R., Faloutsos, C., and Swami, A.: Efficient similarity search in sequence databases, Springer, 1993.

Aires, F., Prigent, C., Rossow, W., Rothstein, M., and Hansen, J. E.: A new neural network approach including first-guess for retrieval of atmospheric water vapor, cloud liquid water path, surface temperature and emissivities over land from satellite microwave observations, Journal of Geophysical Research, 2000. 2000.

Alsdorf, D. E.: Water storage of the central Amazon floodplain measured with GIS and remote sensing imagery, Annals of the Association of American Geographers, 93, 55-66, 2003.

Alsdorf, D. E., Rodríguez, E., and Lettenmaier, D. P.: Measuring surface water from space, Reviews of Geophysics, 45, 2007.

Alsdorf, D. E., Smith, L. C., and Melack, J. M.: Amazon floodplain water level changes measured with interferometric SIR-C radar, Geoscience and Remote Sensing, IEEE Transactions on, 39, 423-431, 2001.

Armstrong, R., Knowles, K., Brodzik, M., and Hardman, M. A.: DMSP SSM/I-SSMIS Pathfinder Daily EASE-Grid Brightness Temperatures. Version 2. Boulder, Colorado USA: NASA DAAC at the National Snow and Ice Data Center, 1998.

Babyak, M. A.: What you see may not be what you get: a brief, nontechnical introduction to overfitting in regression-type models, Psychosomatic medicine, 66, 411-421, 2004.

Barton, I. J. and Bathols, J. M.: Monitoring floods with AVHRR, Remote sensing of Environment, 30, 89-94, 1989.

Basist, A., Grody, N. C., Peterson, T. C., and Williams, C. N.: Using the Special Sensor Microwave/Imager to monitor land surface temperatures, wetness, and snow cover, Journal of Applied Meteorology, 37, 888-911, 1998.

Basist, A., Williams Jr, C., Ross, T. F., Menne, M. J., Grody, N., Ferraro, R., Shen, S., and Chang, A. T.: Using the Special Sensor Microwave Imager to monitor surface wetness, Journal of Hydrometeorology, 2, 297-308, 2001.

Bates, P. D., Neal, J. C., Alsdorf, D., and Schumann, G. J.-P.: Observing global surface water flood dynamics, Surveys in Geophysics, 35, 839-852, 2014.

Behrangi, A., Guan, B., Neiman, P. J., Schreier, M., and Lambrigtsen, B.: On the Quantification of Atmospheric Rivers Precipitation from Space: Composite Assessments

and Case Studies over the Eastern North Pacific Ocean and the Western United States, Journal of Hydrometeorology, 17, 369-382, 2016.

Beven, K. and Kirkby, M.: A physically based, variable contributing area model of basin hydrology/Un modèle à base physique de zone d'appel variable de l'hydrologie du bassin versant, Hydrological Sciences Journal, 24, 43-69, 1979.

Beven, K., Kirkby, M., Schofield, N., and Tagg, A.: Testing a physically-based flood forecasting model (TOPMODEL) for three UK catchments, Journal of Hydrology, 69, 119-143, 1984.

Biggin, D.: A comparison of ERS-1 satellite radar and aerial photography for river flood mapping, Water and Environment Journal, 10, 59-64, 1996.

Bjerklie, D. M., Dingman, S. L., Vorosmarty, C. J., Bolster, C. H., and Congalton, R. G.: Evaluating the potential for measuring river discharge from space, Journal of Hydrology, 278, 17-38, 2003.

Björck, A.: Numerical methods for least squares problems, Siam, 1996.

Boukabara, S.-A., Garrett, K., and Chen, W.: Global coverage of total precipitable water using a microwave variational algorithm, Ieee T Geosci Remote, 48, 3608-3621, 2010.

Brakenridge, G. R., Nghiem, S. V., Anderson, E., and Chien, S.: Space-based measurement of river runoff, EOS: Transactions of the American Geophysical Union, 86, 185-192, 2005.

Brakenridge, G. R., Nghiem, S. V., Anderson, E., and Mic, R.: Orbital microwave measurement of river discharge and ice status, Water Resources Research, 43, 2007.

Brodzik, M. and Knowles, K.: EASE-Grid: A Versatile Set of Equal-Area Prjoections and Grids, National Center for Geographic Information & Analysis, Santa Barbara, California USA, 2002.

Calvet, J. C., Wigneron, J. P., Chanzy, A., Raju, S., and Laguerre, L.: Microwave Dielectric-Properties of a Silt-Loam at High-Frequencies, Ieee T Geosci Remote, 33, 634-642, 1995.

Carlson, T. N. and Ripley, D. A.: On the relation between NDVI, fractional vegetation cover, and leaf area index, Remote sensing of Environment, 62, 241-252, 1997.

Chai, L., Wang, Z., Wang, Y., Yang, Z., Wang, H., and Wu, X.: Ingestion risks of metals in groundwater based on TIN model and dose-response assessment—A case study in the Xiangjiang watershed, central-south China, Science of the Total Environment, 408, 3118-3124, 2010.

Chappell, N. A., Jones, T. D., Tych, W., and Krishnaswamy, J.: Role of rainstorm intensity underestimated by data-derived flood models: emerging global evidence from subsurface-dominated watersheds, Environmental Modelling & Software, 88, 1-9, 2017.

Chen, Y., Huang, C., Ticehurst, C., Merrin, L., and Thew, P.: An evaluation of MODIS daily and 8-day composite products for floodplain and wetland inundation mapping, Wetlands, 33, 823-835, 2013.

Chen, Y., Yang, K., He, J., Qin, J., Shi, J., Du, J., and He, Q.: Improving land surface temperature modeling for dry land of China, Journal of Geophysical Research: Atmospheres (1984–2012), 116, 2011.

Choudhury, B. J.: Monitoring global land surface using Nimbus-7 37 GHz data. Theory and examples, International Journal of Remote Sensing, 10, 1579-1605, 1989.

Choudhury, B. J.: Passive microwave remote sensing contribution to hydrological variables. In: Land surface-atmosphere interactions for climate modeling, Springer, Dordrecht, The Netherlands, 1991.

Choudhury, B. J., Major, E. R., Smith, E. A., and Becker, F.: Atmospheric effects on SMMR and SSM/I 37 GHz polarization difference over the Sahel, International Journal of Remote Sensing, 13, 3443-3463, 1992.

Choudhury, B. J., Schmugge, T. J., Chang, A., and Newton, R. W.: Effect of surface roughness on the microwave emission from soils, Journal of Geophysical Research, 89, 5699-5706, 1979.

Choudhury, B. J. and Tucker, C. J.: Monitoring global vegetation using Nimbus-7 37 GHz data. Some empirical relations, International Journal of Remote Sensing, 8, 1085-1090, 1987.

Choudhury, B. J., Wang, J. R., Hsu, A. Y., and Chien, Y. L.: Simulated and observed 37GHz emission over Africa, International Journal of Remote Sensing, 11, 1837-1868, 1990.

Chunguo, C. and Zihui, L.: Chemical speciation and distribution of arsenic in water, suspended solids and sediment of Xiangjiang River, China, Science of the total environment, 77, 69-82, 1988.

Cooley, J. W., Lewis, P. A., and Welch, P. D.: Application of the fast Fourier transform to computation of Fourier integrals, Fourier series, and convolution integrals, Audio and Electroacoustics, IEEE Transactions on, 15, 79-84, 1967.

Cooley, J. W. and Tukey, J. W.: An algorithm for the machine calculation of complex Fourier series, Mathematics of computation, 19, 297-301, 1965.

Crow, W. and Ryu, D.: A new data assimilation approach for improving runoff prediction using remotely-sensed soil moisture retrievals, Hydrol Earth Syst Sc, 13, 1-16, 2009.

Czekala, H., Havemann, S., Schmidt, K., Rother, T., and Simmer, C.: Comparison of microwave radiative transfer calculations obtained with three different approximations of hydrometeor shape, Journal of Quantitative Spectroscopy and Radiative Transfer, 63, 545-558, 1999.

D'Odorico, P. and Rodríguez-Iturbe, I.: Space-time self-organization of mesoscale rainfall and soil moisture, Advances in water resources, 23, 349-357, 2000.

De Ridder, K.: Quantitative estimation of skin soil moisture with the special sensor microwave/imager, Boundary-Layer Meteorology, 96, 421-432, 2000.

Deshmukh, K. and Shinde, G.: An adaptive color image segmentation, ELCVIA Electronic Letters on Computer Vision and Image Analysis, 5, 12-23, 2005.

Dobson, M. C., Ulaby, F. T., Hallikainen, M. T., and Elrayes, M. A.: Microwave Dielectric Behavior of Wet Soil .2. Dielectric Mixing Models, Ieee T Geosci Remote, 23, 35-46, 1985.

Donohue, R., Roderick, M., and McVicar, T.: On the importance of including vegetation dynamics in Budyko's hydrological model, Hydrology and Earth System Sciences Discussions, 11, 983-995, 2007.

Dronova, I., Gong, P., and Wang, L.: Object-based analysis and change detection of major wetland cover types and their classification uncertainty during the low water period at Poyang Lake, China, Remote Sensing of Environment, 115, 3220-3236, 2011.

Eagleson, P. S.: Climate, soil, and vegetation: 1. Introduction to water balance dynamics, Water Resources Research, 14, 705-712, 1978.

Entin, J. K., Robock, A., Vinnikov, K. Y., Hollinger, S. E., Liu, S., and Namkhai, A.: Temporal and spatial scales of observed soil moisture variations in the extratropics, J Geophys Res, 105, 11865-11877, 2000.

Feng, L., Hu, C., Chen, X., Cai, X., Tian, L., and Gan, W.: Assessment of inundation changes of Poyang Lake using MODIS observations between 2000 and 2010, Remote Sensing of Environment, 121, 80-92, 2012a.

Feng, L., Hu, C., Chen, X., Tian, L., and Chen, L.: Human induced turbidity changes in Poyang Lake between 2000 and 2010: Observations from MODIS, Journal of Geophysical Research: Oceans, 117, 2012b.

Ferraro, R. R. and Marks, G. F.: The Development of SSM/I Rain-Rate Retrieval Algorithms Using Ground-Based Radar Measurements, Journal of Atmospheric and Oceanic Technology, 12, 755-770, 1995.

Fily, M., Royer, A., Goïta, K., and Prigent, C.: A simple retrieval method for land surface temperature and fraction of water surface determination from satellite microwave brightness temperatures in sub-arctic areas, Remote Sensing of Environment, 85, 328-338, 2003.

Frappart, F., Seyler, F., Martinez, J.-M., Leon, J. G., and Cazenave, A.: Floodplain water storage in the Negro River basin estimated from microwave remote sensing of inundation area and water levels, Remote Sensing of Environment, 99, 387-399, 2005.

Gao, H. L., Wood, E. F., Drusch, M., Crow, W., and Jackson, T. J.: Using a microwave emission model to estimate soil moisture from ESTAR observations during SGP99, Journal of Hydrometeorology, 5, 49-63, 2004.

Gerek, Ö. N. and Yardimci, Y.: Equiripple FIR filter design by the FFT algorithm, Signal Processing Magazine, IEEE, 14, 60-64, 1997.

Giddings, L. and Choudhury, B. J.: Observation of hydrological features with Nimbus-7 37 GHz data, applied to South America, International Journal of Remote Sensing, 10, 1673-1686, 1989.

Gleason, C. J. and Smith, L. C.: Toward global mapping of river discharge using satellite images and at-many-stations hydraulic geometry, Proceedings of the National Academy of Sciences, 111, 4788-4791, 2014.

Gleick, P. H.: The development and testing of a water balance model for climate impact assessment: modeling the Sacramento basin, Water Resources Research, 23, 1049-1061, 1987.

Goel, M., Jain, S. K., and Agarwal, P.: Assessment of sediment deposition rate in Bargi Reservoir using digital image processing, Hydrological sciences journal, 47, S81-S92, 2002.

Guerschman, J. P., Warren, G., Byrne, G., Lymburner, L., Mueller, N., and Van Dijk, A. I.: MODIS-based standing water detection for flood and large reservoir mapping: algorithm development and applications for the Australian continent, CSIRO Canberra, Australia, 2011.

Guo, H., Hu, Q., and Jiang, T.: Annual and seasonal streamflow responses to climate and land-cover changes in the Poyang Lake basin, China, Journal of Hydrology, 355, 106-122, 2008.

Guo, H., Hu, Q., and Zhang, Q.: Changes in hydrological interactions of the Yangtze River and the Poyang Lake in China during 1957–2008, Acta Geographica Sinica, 66, 609-618, 2011.

Guo, H., Hu, Q., Zhang, Q., and Feng, S.: Effects of the three gorges dam on Yangtze river flow and river interaction with Poyang Lake, China: 2003–2008, Journal of Hydrology, 416, 19-27, 2012.

Gupta, H. V., Sorooshian, S., and Yapo, P. O.: Status of automatic calibration for hydrologic models: Comparison with multilevel expert calibration, Journal of Hydrologic Engineering, 4, 135-143, 1999.

Gutman, G. and Ignatov, A.: The derivation of the green vegetation fraction from NOAA/AVHRR data for use in numerical weather prediction models, International Journal of remote sensing, 19, 1533-1543, 1998.

Hamilton, S. K., Sippel, S. J., and Melack, J. M.: Comparison of inundation patterns among major South American floodplains, Journal of Geophysical Research D: Atmospheres, 107, 1-14, 2002.

Hamilton, S. K., Sippel, S. J., and Melack, J. M.: Inundation patterns in the Pantanal wetland of South America determined from passive microwave remote sensing, Archiv fur Hydrobiologie, 137, 1-23, 1996.

Hamilton, S. K., Sippel, S. J., and Melack, J. M.: Seasonal inundation patterns in two large savanna floodplains of South America: The Llanos de Moxos (Bolivia) and the Llanos del Orinoco (Venezuela and Colombia), Hydrological Processes, 18, 2103-2116, 2004.

Harris, F. J.: On the use of windows for harmonic analysis with the discrete Fourier transform, Proceedings of the IEEE, 66, 51-83, 1978.

Hawkins, D. M.: The problem of overfitting, Journal of chemical information and computer sciences, 44, 1-12, 2004.

Hayashi, M., van der Kamp, G., and Rudolph, D. L.: Water and solute transfer between a prairie wetland and adjacent uplands, 1. Water balance, Journal of Hydrology, 207, 42-55, 1998.

Hess, L. L., Melack, J. M., Filoso, S., and Wang, Y.: Delineation of inundated area and vegetation along the Amazon floodplain with the SIR-C synthetic aperture radar, Geoscience and Remote Sensing, IEEE Transactions on, 33, 896-904, 1995.

Hess, L. L., Melack, J. M., Novo, E. M., Barbosa, C. C., and Gastil, M.: Dual-season mapping of wetland inundation and vegetation for the central Amazon basin, Remote Sensing of Environment, 87, 404-428, 2003.

Hollinger, J. P., Peirce, J. L., and Poe, G. A.: SSM/I instrument evaluation, Ieee T Geosci Remote, 28, 781-790, 1990.

Holmes, T. R. H., De Jeu, R. A. M., Owe, M., and Dolman, A. J.: Land surface temperature from Ka band (37 GHz) passive microwave observations, J Geophys Res-Atmos, 114, 2009.

Horritt, M., Mason, D., and Luckman, A.: Flood boundary delineation from synthetic aperture radar imagery using a statistical active contour model, International Journal of Remote Sensing, 22, 2489-2507, 2001.

Hostache, R., Matgen, P., Schumann, G., Puech, C., Hoffmann, L., and Pfister, L.: Water level estimation and reduction of hydraulic model calibration uncertainties using satellite SAR images of floods, Geoscience and Remote Sensing, IEEE Transactions on, 47, 431-441, 2009.

Houweling, S., Kaminski, T., Dentener, F., Lelieveld, J., and Heimann, M.: Inverse modeling of methane sources and sinks using the adjoint of a global transport model, Journal of Geophysical Research: Atmospheres, 104, 26137-26160, 1999.

Hu, Q., Feng, S., Guo, H., Chen, G., and Jiang, T.: Interactions of the Yangtze river flow and hydrologic processes of the Poyang Lake, China, Journal of Hydrology, 347, 90-100, 2007.

Huber, C., Li, J., Daillet, S., Chen, X., Xijun, L., Francois, C. J., Wei, Z., Carlos, U., Mathias, S., Shifeng, H., Stephane, A., Burnham, J., and Yesou, H.: Twelve year of water resource monitoring over Yangtze middle reaches exploiting DRAGON time series and field measurments, DRAGON II symposium, Beijing, 2012.

Huffman, G. J., Bolvin, D. T., Nelkin, E. J., Wolff, D. B., Adler, R. F., Gu, G., Hong, Y., Bowman, K. P., and Stocker, E. F.: The TRMM multisatellite precipitation analysis (TMPA): Quasi-global, multiyear, combined-sensor precipitation estimates at fine scales, Journal of Hydrometeorology, 8, 38-55, 2007.

Irons, J. R. and Petersen, G. W.: Texture transforms of remote sensing data, Remote Sensing of Environment, 11, 359-370, 1981.

Islam, A., Bala, S., and Haque, M.: Flood inundation map of Bangladesh using MODIS time-series images, Journal of Flood Risk Management, 3, 210-222, 2010.

Jain, S. K., Singh, P., and Seth, S.: Assessment of sedimentation in Bhakra Reservoir in the western Himalayan region using remotely sensed data, Hydrological sciences journal, 47, 203-212, 2002.

Jakeman, A. and Hornberger, G.: How much complexity is warranted in a rainfall-runoff model?, Water resources research, 29, 2637-2649, 1993.

Jakeman, A., Littlewood, I., and Whitehead, P.: Computation of the instantaneous unit hydrograph and identifiable component flows with application to two small upland catchments, Journal of hydrology, 117, 275-300, 1990.

Jia, L., Shang, H., Hu, G., and Menenti, M.: Phenological response of vegetation to upstream river flow in the Heihe Rive basin by time series analysis of MODIS data, Hydrol Earth Syst Sc, 15, 1047-1064, 2011.

Jin, Y.: A flooding index and its regional threshold value for monitoring floods in China from SSM/I data, International Journal of Remote Sensing, 20, 1025-1030, 1999.

Kawanishi, T., Sezai, T., Ito, Y., Imaoka, K., Takeshima, T., Ishido, Y., Shibata, A., Miura, M., Inahata, H., and Spencer, R. W.: The Advanced Microwave Scanning Radiometer for the Earth Observing System (AMSR-E), NASDA's contribution to the EOS for global energy and water cycle studies, Ieee T Geosci Remote, 41, 184-194, 2003.

Kazezyılmaz-Alhan, C. M., Medina, M. A., and Richardson, C. J.: A wetland hydrology and water quality model incorporating surface water/groundwater interactions, Water Resources Research, 43, 2007.

Keogh, E., Chakrabarti, K., Pazzani, M., and Mehrotra, S.: Dimensionality reduction for fast similarity search in large time series databases, Knowledge and information Systems, 3, 263-286, 2001.

Kerr, Y. H., Waldteufel, P., Wigneron, J.-P., Martinuzzi, J., Font, J., and Berger, M.: Soil moisture retrieval from space: The Soil Moisture and Ocean Salinity (SMOS) mission, Ieee T Geosci Remote, 39, 1729-1735, 2001.

Kirdiashev, K. P., Chucklantsev, A. A., and Shutko, A.: Microwave radiation of the earth's surface in the presence of vegetation cover, Radiotecknica, 24, 256-264, 1979.

Knowles, K., Savoie, M., Armstrong, R., and Brodzik, M.: AMSR-E/Aqua Daily EASE-Grid Brightness Temperatures, NASA DAAC at the National Snow and Ice Data Center, Boulder, Colorado USA, 2006.

Kummerow, C., Olson, W. S., and Giglio, L.: A simplified scheme for obtaining precipitation and vertical hydrometeor profiles from passive microwave sensors, Geoscience and Remote Sensing, IEEE Transactions on, 34, 1213-1232, 1996.

Lakshmi, V., Wood, E. F., and Choudhury, B. J.: Evaluation of Special Sensor Microwave/Imager satellite data for regional soil moisture estimation over the Red River basin, Journal of Applied Meteorology, 36, 1309-1328, 1997a.

Lakshmi, V., Wood, E. F., and Choudhury, B. J.: A soil-canopy-atmosphere model for use in satellite microwave remote sensing, Journal of Geophysical Research D: Atmospheres, 102, 6911-6927, 1997b.

Lane, J. and Saxton, J.: Dielectric dispersion in pure polar liquids at very high radio frequencies. III. The effect of electrolytes in solution, 1952, 531-545.

Lawson, C. L. and Hanson, R. J.: Solving least squares problems, SIAM, 1974.

Lee, J.-S., Papathanassiou, K. P., Ainsworth, T. L., Grunes, M. R., and Reigber, A.: A new technique for noise filtering of SAR interferometric phase images, Geoscience and Remote Sensing, IEEE Transactions on, 36, 1456-1465, 1998.

Li, F., Huang, J., Zeng, G., Yuan, X., Li, X., Liang, J., Wang, X., Tang, X., and Bai, B.: Spatial risk assessment and sources identification of heavy metals in surface sediments from the Dongting Lake, Middle China, Journal of Geochemical Exploration, 132, 75-83, 2013.

Li, P., Feng, Z., Jiang, L., Liu, Y., and Xiao, X.: Changes in rice cropping systems in the Poyang Lake Region, China during 2004–2010, Journal of Geographical Sciences, 22, 653-668, 2012.

Liang, X., Lettenmaier, D. P., Wood, E. F., and Burges, S. J.: A simple hydrologically based model of land surface water and energy fluxes for general circulation models, JOURNAL OF GEOPHYSICAL RESEARCH-ALL SERIES-, 99, 14,415-414,415, 1994.

Liebe, H. J., Hufford, G. A., and Manabe, T.: A model for the complex permittivity of water at frequencies below 1 THz, International Journal of Infrared and Millimeter Waves, 12, 659-675, 1991.

Lin, C. and Lu, J.: Studies on the anomaly of Plum Rain and flood disaster in the Yangtze River valley, J. Najing University, 1991. 76-83, 1991.

Lin, R., King-lp, A., and Shim, H. S. S. K.: Fast similarity search in the presence of noise, scaling, and translation in time-series databases, Zurich, Switzerland, 9 - 13 September 1995, 490-501.

Madsen, H.: Automatic calibration of a conceptual rainfall–runoff model using multiple objectives, Journal of hydrology, 235, 276-288, 2000.

Manabe, T., Liebe, H., and Hufford, G.: Complex permittivity of water between 0 and 30 THz, 1987, 229-230.

Matthews, E. and Fung, I.: Methane emission from natural wetlands: Global distribution, area, and environmental characteristics of sources, Global biogeochemical cycles, 1, 61-86, 1987.

Matthews, E., Fung, I., and Lerner, J.: Methane emission from rice cultivation: Geographic and seasonal distribution of cultivated areas and emissions, Global Biogeochemical Cycles, 5, 3-24, 1991.

Mätzler, C.: Thermal microwave radiation: applications for remote sensing, Iet, 2006.

McFeeters, S.: The use of the Normalized Difference Water Index (NDWI) in the delineation of open water features, International journal of remote sensing, 17, 1425-1432, 1996.

Menenti, M., Azzali, S., Verhoef, W., and van Swol, R.: Mapping agroecological zones and time lag in vegetation growth by means of fourier analysis of time series of NDVI images, Advances in Space Research, 13, 233-237, 1993.

Mertes, L. A.: Documentation and significance of the perirheic zone on inundated floodplains, Water Resources Research, 33, 1749-1762, 1997.

Mialon, A., Royer, A., and Fily, M.: Wetland seasonal dynamics and interannual variability over northern high latitudes, derived from microwave satellite data, Journal of Geophysical Research: Atmospheres, 110, 2005.

Miller, M. W. and Nudds, T. D.: Prairie landscape change and flooding in the Mississippi River Valley, Conservation Biology, 1996. 847-853, 1996.

Mo, T. and Schmugge, T. J.: A parameterization of the effect of surface roughness on microwave emission, Geoscience and Remote Sensing, IEEE Transactions on, 1987. 481-486, 1987.

Montandon, L. and Small, E.: The impact of soil reflectance on the quantification of the green vegetation fraction from NDVI, Remote Sensing of Environment, 112, 1835-1845, 2008.

Moore, R.: The PDM rainfall-runoff model, Hydrology and Earth System Sciences Discussions, 11, 483-499, 2007.

Moore, R.: The probability-distributed principle and runoff production at point and basin scales, Hydrological Sciences Journal, 30, 273-297, 1985.

Mörchen, F.: Time series feature extraction for data mining using DWT and DFT. Univ. of Marburg, Germany, 2003.

Nash, J. E. and Sutcliffe, J. V.: River flow forecasting through conceptual models part I — A discussion of principles, Journal of Hydrology, 10, 282-290, 1970.

Nerem, R., Chambers, D., Leuliette, E., Mitchum, G., and Giese, B.: Variations in global mean sea level associated with the 1997–1998 ENSO event: Implications for measuring long term sea level change, Geophys Res Lett, 26, 3005-3008, 1999.

Njoku, E. G., Jackson, T. J., Lakshmi, V., Chan, T. K., and Nghiem, S. V.: Soil moisture retrieval from AMSR-E, Ieee T Geosci Remote, 41, 215-229, 2003.

O'Neill, P. E., Jackson, T. J., Chauhan, N. S., and Seyfried, M. S.: Microwave soil moisture estimation in humid and semiarid watersheds, Advances in Space Research, 13, 115-118, 1993.

Oberstadler, R., Hönsch, H., and Huth, D.: Assessment of the mapping capabilities of ERS-1 SAR data for flood mapping: a case study in Germany, Hydrological processes, 11, 1415-1425, 1997.

Otsu, N.: A threshold selection method from gray-level histograms, Automatica, 11, 23-27, 1975.

Owe, M., de Jeu, R., and Walker, J.: A methodology for surface soil moisture and vegetation optical depth retrieval using the microwave polarization difference index, Geoscience and Remote Sensing, IEEE Transactions on, 39, 1643-1654, 2001.

Paiva, R. C., Durand, M. T., and Hossain, F.: Spatiotemporal interpolation of discharge across a river network by using synthetic SWOT satellite data, Water Resources Research, 51, 430-449, 2015.

Paloscia, S., Macelloni, G., Santi, E., and Koike, T.: A multifrequency algorithm for the retrieval of soil moisture on a large scale using microwave data from SMMR and SSM/I satellites, Ieee T Geosci Remote, 39, 1655-1661, 2001.

Pampaloni, P. and Paloscia, S.: Experimental relationships between microwave emission and vegetation features†, International Journal of Remote Sensing, 6, 315-323, 1985.

Pan, F., Liao, J., Li, X., and Guo, H.: Application of the inundation area—lake level rating curves constructed from the SRTM DEM to retrieving lake levels from satellite measured inundation areas, Computers & Geosciences, 52, 168-176, 2013.

Papa, F., Prigent, C., Durand, F., and Rossow, W. B.: Wetland dynamics using a suite of satellite observations: A case study of application and evaluation for the Indian Subcontinent, Geophys Res Lett, 33, 2006.

Peng, D., Guo, S., Liu, P., and Liu, T.: Reservoir storage curve estimation based on remote sensing data, Journal of hydrologic engineering, 11, 165-172, 2006.

Podest, E. and Saatchi, S.: Application of multiscale texture in classifying JERS-1 radar data over tropical vegetation, International Journal of Remote Sensing, 23, 1487-1506, 2002.

Poe, G. A.: Optimum Interpolation of Imaging Microwave Radiometer Data, Ieee T Geosci Remote, 28, 800-810, 1990.

Poe, G. A. and Conway, R. W.: A study of the geolocation errors of the Special Sensor Microwave/Imager (SSM/I), Ieee T Geosci Remote, 28, 791-799, 1990.

Prigent, C., Aires, F., Rossow, W., and Matthews, E.: Joint characterization of vegetation by satellite observations from visible to microwave wavelengths: A sensitivity analysis, Journal of Geophysical Research: Atmospheres, 106, 20665 - 20685, 2001a.

Prigent, C., Matthews, E., Aires, F., and Rossow, W. B.: Remote sensing of global wetland dynamics with multiple satellite data sets, Geophys Res Lett, 28, 4631-4634, 2001b.

Prigent, C., Papa, F., Aires, F., Rossow, W., and Matthews, E.: Global inundation dynamics inferred from multiple satellite observations, 1993–2000, Journal of Geophysical Research: Atmospheres, 112, 2007.

Prigent, C., Rossow, W. B., and Matthews, E.: Microwave land surface emissivities estimated from SSM/I observations, Journal of Geophysical Research: Atmospheres, 102, 21867-21890, 1997.

Project, B. M., Erdélyi, A., and Bateman, H.: Tables of Integral Transforms: Based in Part on Notes Left by Harry Bateman and Compiled by the Staff of the Bateman Manuscript Project, McGraw-Hill, New York, NY, USA, 1954.

Pulvirenti, L., Chini, M., Pierdicca, N., Guerriero, L., and Ferrazzoli, P.: Flood monitoring using multi-temporal COSMO-SkyMed data: Image segmentation and signature interpretation, Remote Sensing of Environment, 115, 990-1002, 2011.

Rasid, H. and Pramanik, M.: Visual interpretation of satellite imagery for monitoring floods in Bangladesh, Environmental Management, 14, 815-821, 1990.

Reale, A., Chalfant, M., Allegrino, A., Tiley, F., Gerguson, M., and Pettey, M.: Advanced-TOVS (ATOVS) sounding products from NOAA polar orbiting environmental satellites, 2003.

Richards, F. and Arkin, P.: On the relationship between satellite-observed cloud cover and precipitation, Monthly Weather Review, 109, 1081-1093, 1981.

Ritter, A. and Muñoz-Carpena, R.: Performance evaluation of hydrological models: Statistical significance for reducing subjectivity in goodness-of-fit assessments, Journal of Hydrology, 480, 33-45, 2013.

Roerink, G. J., Menenti, M., Soepboer, W., and Su, Z.: Assessment of climate impact on vegetation dynamics by using remote sensing, Physics and Chemistry of the Earth, Parts A/B/C, 28, 103-109, 2003.

Roerink, G. J., Menenti, M., and Verhoef, W.: Reconstructing cloudfree NDVI composites using Fourier analysis of time series, International Journal of Remote Sensing, 21, 1911-1917, 2000.

Rossow, W. B. and Schiffer, R. A.: Advances in understanding clouds from ISCCP, Bulletin of the American Meteorological Society, 80, 2261, 1999.

Sakamoto, T., Van Nguyen, N., Kotera, A., Ohno, H., Ishitsuka, N., and Yokozawa, M.: Detecting temporal changes in the extent of annual flooding within the Cambodia and the Vietnamese Mekong Delta from MODIS time-series imagery, Remote sensing of environment, 109, 295-313, 2007.

Schumann, G., Di Baldassarre, G., and Bates, P. D.: The utility of spaceborne radar to render flood inundation maps based on multialgorithm ensembles, Geoscience and Remote Sensing, IEEE Transactions on, 47, 2801-2807, 2009.

Schumann, G. J.-P. and Moller, D. K.: Microwave remote sensing of flood inundation, Physics and Chemistry of the Earth, Parts A/B/C, 83, 84-95, 2015.

Shang, H., Jia, J., and Menenti, M.: Analyzing the Inundation Pattern of the Poyang Lake floodplain by Passive Microwave Data, Journal of Hydrometeorology, 16, 652-667, 2015.

Shang, H., Jia, J., and Menenti, M.: Modeling and Reconstruction of Time Series of Passive Microwave Data by Discrete Fourier Transform Guided Filtering and Harmonic Analysis, Remote Sensing, 08, 970, 2016.

Shankman, D., Keim, B. D., and Song, J.: Flood frequency in China's Poyang Lake region: trends and teleconnections, International Journal of Climatology, 26, 1255-1266, 2006.

Sheng, Y., Gong, P., and Xiao, Q.: Quantitative dynamic flood monitoring with NOAA AVHRR, International Journal of Remote Sensing, 22, 1709-1724, 2001.

Sheng, Y., Su, Y., and Xiao, Q.: Challenging the cloud-contamination problem in flood monitoring with NOAA/AVHRR imagery, Photogrammetric Engineering and Remote Sensing, 64, 191-198, 1998.

Shi, J. C., Jackson, T., Tao, J., Du, J., Bindlish, R., Lu, L., and Chen, K. S.: Microwave vegetation indices for short vegetation covers from satellite passive microwave sensor AMSR-E, Remote Sensing of Environment, 112, 4285-4300, 2008.

Shi, J. C., Jiang, L. M., Zhang, L. X., Chen, K. S., Wigneron, J. P., and Chanzy, A.: A parameterized multifrequency-polarization surface emission model, Ieee T Geosci Remote, 43, 2831-2841, 2005.

Shjeflo, J. B.: Evapotranspiration and the water budget of prairie potholes in North Dakota, US Government Printing Office, 1968.

Singleton, R. C.: An algorithm for computing the mixed radix fast Fourier transform, Audio and Electroacoustics, IEEE Transactions on, 17, 93-103, 1969.

Sippel, S. J., Hamilton, S. K., Melack, J. M., and Choudhury, B. J.: Determination of inundation area in the Amazon River floodplain using the SMMR 37 GHz polarization difference, Remote Sensing of Environment, 48, 70-76, 1994.

Sippel, S. J., Hamilton, S. K., Melack, J. M., and Novo, E. M. M.: Passive microwave observations of inundation area and the area/stage relation in the Amazon River floodplain, International Journal of Remote Sensing, 19, 3055-3074, 1998.

Sivapalan, M., Beven, K., and Wood, E. F.: On hydrologic similarity: 2. A scaled model of storm runoff production, Water Resources Research, 23, 2266-2278, 1987.

Skøien, J. O., Blöschl, G., and Western, A.: Characteristic space scales and timescales in hydrology, Water Resources Research, 39, 2003.

Smith, L. C.: Satellite remote sensing of river inundation area, stage, and discharge: A review, Hydrological processes, 11, 1427-1439, 1997.

Smith, L. C., Alsdorf, D. E., Magilligan, F. J., Gomez, B., Mertes, L. A., Smith, N. D., and Garvin, J. B.: Estimation of erosion, deposition, and net volumetric change caused by the 1996 Skeiðarársandur jökulhlaup, Iceland, from synthetic aperture radar interferometry, Water Resources Research, 36, 1583-1594, 2000.

Smith, L. C., Isacks, B. L., Bloom, A. L., and Murray, A. B.: Estimation of discharge from three braided rivers using synthetic aperture radar satellite imagery: Potential application to ungaged basins, Water Resources Research, 32, 2021-2034, 1996.

Smith, L. C. and Pavelsky, T. M.: Estimation of river discharge, propagation speed, and hydraulic geometry from space: Lena River, Siberia, Water Resources Research, 44, 2008.

Sophocleous, M.: Interactions between groundwater and surface water: the state of the science, Hydrogeology journal, 10, 52-67, 2002.

Su, M., Stolte, W., and Van der Kamp, G.: Modelling Canadian prairie wetland hydrology using a semi-distributed streamflow model, Hydrological Processes, 14, 2405-2422, 2000.

Tanaka, M., Sugimura, T., and Tanaka, S.: Cover. Monitoring water surface ratio in the Chinese floods of summer 1998 by DMSP-SSM/I, 2000. 2000.

Tanaka, M., Sugimura, T., Tanaka, S., and Tamai, N.: Flood–drought cycle of Tonle Sap and Mekong Delta area observed by DMSP-SSM/I, International Journal of Remote Sensing, 24, 1487-1504, 2003.

Temimi, M., Leconte, R., Brissette, F., and Chaouch, N.: Flood and soil wetness monitoring over the Mackenzie River Basin using AMSR-E 37 GHz brightness temperature, 25-29 July 2005 2005, 4 pp.

Thompson, A. R., Moran, J. M., and Swenson Jr, G. W.: Interferometry and synthesis in radio astronomy, John Wiley & Sons, Weinheim, Germany, 2008.

Todini, E.: The ARNO rainfall—runoff model, Journal of Hydrology, 175, 339-382, 1996.

Torbick, N., Salas, W., Xiao, X., Ingraham, P., Fearon, M., Biradar, C., Zhao, D., Liu, Y., Li, P., and Zhao, Y.: Integrating SAR and optical imagery for regional mapping of paddy rice attributes in the Poyang Lake Watershed, China, Canadian Journal of Remote Sensing, 37, 17-26, 2011.

Townsend, P. A.: Mapping seasonal flooding in forested wetlands using multi-temporal Radarsat SAR, Photogrammetric engineering and remote sensing, 67, 857-864, 2001.

Tsang, L., Blanchard, A. J., Newton, R. W., and Kong, J. A.: A simple relation between active and passive microwave remote sensing measurements of earth terrain, Geoscience and Remote Sensing, IEEE Transactions on, 1982. 482-485, 1982.

Ulaby, F. T., Moore, R. K., and Fung, A. K.: Microwave remote sensing : active and passive, Addison-Wesley Pub. Co., Advanced Book Program/World Science Division, Reading, Mass., 1981.

Usachev, V.: Evaluation of flood plain inundations by remote sensing methods, Hydrological Applications of Remote Sensing and Remote Data Transmission, 1983. 475-482, 1983.

Vachaud, G., Passerat de Silans, A., Balabanis, P., and Vauclin, M.: Temporal stability of spatially measured soil water probability density function, Soil Science Society of America Journal, 49, 822-828, 1985.

Vandegriend, A. A. and Owe, M.: Determination of Microwave Vegetation Optical Depth and Single Scattering Albedo from Large-Scale Soil-Moisture and Nimbus Smmr Satellite-Observations, International Journal of Remote Sensing, 14, 1875-1886, 1993.

Verdin, J.: Remote sensing of ephemeral water bodies in western Niger, International Journal of Remote Sensing, 17, 733-748, 1996.

Verhoef, W.: Application of Harmonic Analysis of NDVI Time Series (HANTS), In Fourier Analysis of Temporal NDVI in the Souther African and American Continents Wageningen, The Netherlands, 19-24, 1996.

Vinnikov, K. Y., Robock, A., Qiu, S., Entin, J. K., Owe, M., Choudhury, B. J., Hollinger, S. E., and Njoku, E. G.: Satellite remote sensing of soil moisture in Illinois, United States, Journal of Geophysical Research D: Atmospheres, 104, 4145-4168, 1999.

Vinnikov, K. Y., Robock, A., Speranskaya, N. A., and Schlosser, C. A.: Scales of temporal and spatial variability of midlatitude soil moisture, Journal of Geophysical Research: Atmospheres, 101, 7163-7174, 1996.

Vörösmarty, C. J., Moore, B., Grace, A. L., Gildea, M. P., Melillo, J. M., Peterson, B. J., Rastetter, E. B., and Steudler, P. A.: Continental scale models of water balance and fluvial transport: an application to South America, Global biogeochemical cycles, 3, 241-265, 1989.

Vörösmarty, C. J., Willmott, C. J., Choudhury, B. J., Schloss, A. L., Stearns, T. K., Robeson, S. M., and Dorman, T. J.: Analyzing the discharge regime of a large tropical river through remote sensing, ground-based climatic data, and modeling, Water Resources Research, 32, 3137-3150, 1996.

Walter, B. P., Heimann, M., and Matthews, E.: Modeling modern methane emissions from natural wetlands: 1. Model description and results, Journal of Geophysical Research: Atmospheres, 106, 34189-34206, 2001.

Wang, J. R. and Choudhury, B. J.: Remote sensing of soil moisture content over bare field at 1.4 GHz frequency, Journal of Geophysical Research, 86, 5277-5282, 1981.

Wang, J. R. and Schmugge, T. J.: An Empirical-Model for the Complex Dielectric Permittivity of Soils as a Function of Water-Content, Ieee T Geosci Remote, 18, 288-295, 1980.

Wang, Y., Hess, L. L., Filoso, S., and Melack, J. M.: Understanding the radar backscattering from flooded and nonflooded Amazonian forests: Results from canopy backscatter modeling, Remote Sensing of Environment, 54, 324-332, 1995.

Wang, Z., Chai, L., Wang, Y., Yang, Z., Wang, H., and Wu, X.: Potential health risk of arsenic and cadmium in groundwater near Xiangjiang River, China: a case study for risk assessment and management of toxic substances, Environmental monitoring and assessment, 175, 167-173, 2011.

Wen, J., Su, Z. B., and Ma, Y. M.: Determination of land surface temperature and soil moisture from Tropical Rainfall Measuring Mission/Microwave Imager remote sensing data, J Geophys Res-Atmos, 108, 2003.

Wentz, F. J.: Measurement of oceanic wind vector using satellite microwave radiometers, Ieee T Geosci Remote, 30, 960-972, 1992.

Wentz, F. J.: SSM/I Version-7 Calibration Report, Remote Sensing Systems, Santa Rosa, CA, 46pp pp., 2013.

Westerhoff, R., Kleuskens, M., Winsemius, H., Huizinga, H., Brakenridge, G., and Bishop, C.: Automated global water mapping based on wide-swath orbital synthetic-aperture radar, Hydrol. Earth Syst. Sci, 17, 651-663, 2013.

Wiesmann, A. and Mätzler, C.: Microwave emission model of layered snowpacks, Remote Sensing of Environment, 70, 307-316, 1999.

Wigneron, J.-P., Chanzy, A., Calvet, J.-C., and Bruguier, N.: A simple algorithm to retrieve soil moisture and vegetation biomass using passive microwave measurements over crop fields, Remote Sensing of Environment, 51, 331-341, 1995.

Wigneron, J. P., Kerr, Y., Chanzy, A., and Jin, Y. Q.: Inversion of surface parameters from passive microwave measurements over a soybean field, Remote Sensing of Environment, 46, 61-72, 1993.

Wilson, D. J., Western, A. W., and Grayson, R. B.: Identifying and quantifying sources of variability in temporal and spatial soil moisture observations, Water Resources Research, 40, 2004.

Winter, T. C. and Rosenberry, D. O.: The interaction of ground water with prairie pothole wetlands in the Cottonwood Lake area, east-central North Dakota, 1979–1990, Wetlands, 15, 193-211, 1995.

Winter, T. C. and Valk, A.: Hydrologic studies of wetlands in the northern prairie, Northern prairie wetlands., 1989. 16-54, 1989.

Woo, M.-K. and Rowsell, R. D.: Hydrology of a prairie slough, Journal of Hydrology, 146, 175-207, 1993.

Wood, E. F., Lettenmaier, D. P., and Zartarian, V. G.: A land-surface hydrology parameterization with subgrid variability for general circulation models, Journal of Geophysical Research: Atmospheres (1984–2012), 97, 2717-2728, 1992.

Wu, Y.-L., Agrawal, D., and El Abbadi, A.: A comparison of DFT and DWT based similarity search in time-series databases, McLean, VA, USA, 6 - 11 November 2000, 488-495.

Xiao, Q. and Chen, W.: Songhua River flood monitoring with meteorological satellite imagery, Remote Sensing Information, 4, 37-41, 1987.

Xu, C.-Y. and Singh, V. P.: Review on regional water resources assessment models under stationary and changing climate, Water Resources Management, 18, 591-612, 2004.

Xu, H.: Modification of normalised difference water index (NDWI) to enhance open water features in remotely sensed imagery, International Journal of Remote Sensing, 27, 3025-3033, 2006.

Yang, K., He, J., Tang, W., Qin, J., and Cheng, C. C.: On downward shortwave and longwave radiations over high altitude regions: Observation and modeling in the Tibetan Plateau, Agricultural and Forest Meteorology, 150, 38-46, 2010.

Ye, X., Zhang, Q., Bai, L., and Hu, Q.: A modeling study of catchment discharge to Poyang Lake under future climate in China, Quaternary International, 244, 221-229, 2011.

Ye, X., Zhang, Q., Liu, J., Li, X., and Xu, C.-y.: Distinguishing the relative impacts of climate change and human activities on variation of streamflow in the Poyang Lake catchment, China, Journal of Hydrology, 494, 83-95, 2013.

Yésou, H., Claire, H., Xijun, L., Stéphane, A., Jiren, L., Sylviane, D., Muriel, B.-N., Xiaoling, C., Shifeng, H., Burnham, J., Jean-François, C., Tiphanie, M., Jinggang, L., Rémi, A., and Carlos, U.: Nine years of water resources monitoring over the middle reaches of the Yangtze River, with ENVISAT, MODIS, Beijing-1 time series, Altimetric data and field measurements, Lakes & Reservoirs: Research & Management, 16, 231-247, 2011.

Yesou, H., Huber, C., Shifeng, H., Xijun, L., and Sylviane, D.-R.: Chinese lakes behaviours in the framework of the meteorology and water management practices: EO based monitoring lessons, the ESA Living Planet symposium, Edinburg, 2013.

Young, P.: Recursive estimation and time-series analysis: an introduction, 1984. 1984.

Zhang, L., Li, D., Tong, Q., and Zheng, L.: Study of the spectral mixture model of soil and vegetation in PoYang Lake area, China, International Journal of Remote Sensing, 19, 2077-2084, 1998.

Zhang, L., Yin, J., Jiang, Y., and Wang, H.: Relationship between the hydrological conditions and the distribution of vegetation communities within the Poyang Lake National Nature Reserve, China, Ecological Informatics, 11, 65-75, 2012.

Zhang, Q., Liu, C., Xu, C.-y., Xu, Y., and Jiang, T.: Observed trends of annual maximum water level and streamflow during past 130 years in the Yangtze River basin, China, Journal of Hydrology, 324, 255-265, 2006.

Zhang, Q., Liu, Y., Yang, G., and Zhang, Z.: Precipitation and hydrological variations and related associations with large-scale circulation in the Poyang Lake basin, China, Hydrological Processes, 25, 740-751, 2011.

Zhao, G., Hörmann, G., Fohrer, N., Zhang, Z., and Zhai, J.: Streamflow trends and climate variability impacts in Poyang Lake Basin, China, Water resources management, 24, 689-706, 2010.

Zhao, R.: Flood forecasting method for humid regions of China, East China College of Hydraulic Engineering, Nanjing, 1977. 19-51, 1977.

Zhao, R.: Watershed hydrological modelling, Water Resources and Electric Power Press, Beijing, 1984. 1984.

Zhou, Z.: Synoptic characteristics of atmoshperic cirulation during abnormal Plum Rain period in 1991, J. Nanjing University, 1991. 84-93, 1991.

Zong, Y. and Chen, X.: The 1998 flood on the Yangtze, China, Natural Hazards, 22, 165-184, 2000.

Agrawal, R., Faloutsos, C., and Swami, A.: Efficient similarity search in sequence databases, Springer, 1993.

Aires, F., Prigent, C., Rossow, W., Rothstein, M., and Hansen, J. E.: A new neural network approach including first-guess for retrieval of atmospheric water vapor, cloud liquid water path, surface temperature and emissivities over land from satellite microwave observations, Journal of Geophysical Research, 2000. 2000.

Alsdorf, D. E.: Water storage of the central Amazon floodplain measured with GIS and remote sensing imagery, Annals of the Association of American Geographers, 93, 55-66, 2003.

Alsdorf, D. E., Rodríguez, E., and Lettenmaier, D. P.: Measuring surface water from space, Reviews of Geophysics, 45, 2007.

Alsdorf, D. E., Smith, L. C., and Melack, J. M.: Amazon floodplain water level changes measured with interferometric SIR-C radar, Geoscience and Remote Sensing, IEEE Transactions on, 39, 423-431, 2001.

Armstrong, R., Knowles, K., Brodzik, M., and Hardman, M. A.: DMSP SSM/I-SSMIS Pathfinder Daily EASE-Grid Brightness Temperatures. Version 2. Boulder, Colorado USA: NASA DAAC at the National Snow and Ice Data Center, 1998.

Babyak, M. A.: What you see may not be what you get: a brief, nontechnical introduction to overfitting in regression-type models, Psychosomatic medicine, 66, 411-421, 2004.

Barton, I. J. and Bathols, J. M.: Monitoring floods with AVHRR, Remote sensing of Environment, 30, 89-94, 1989.

Basist, A., Grody, N. C., Peterson, T. C., and Williams, C. N.: Using the Special Sensor Microwave/Imager to monitor land surface temperatures, wetness, and snow cover, Journal of Applied Meteorology, 37, 888-911, 1998.

Basist, A., Williams Jr, C., Ross, T. F., Menne, M. J., Grody, N., Ferraro, R., Shen, S., and Chang, A. T.: Using the Special Sensor Microwave Imager to monitor surface wetness, Journal of Hydrometeorology, 2, 297-308, 2001.

Bates, P. D., Neal, J. C., Alsdorf, D., and Schumann, G. J.-P.: Observing global surface water flood dynamics, Surveys in Geophysics, 35, 839-852, 2014.

Behrangi, A., Guan, B., Neiman, P. J., Schreier, M., and Lambrigtsen, B.: On the Quantification of Atmospheric Rivers Precipitation from Space: Composite Assessments and Case Studies over the Eastern North Pacific Ocean and the Western United States, Journal of Hydrometeorology, 17, 369-382, 2016.

Beven, K. and Kirkby, M.: A physically based, variable contributing area model of basin hydrology/Un modèle à base physique de zone d'appel variable de l'hydrologie du bassin versant, Hydrological Sciences Journal, 24, 43-69, 1979.

Beven, K., Kirkby, M., Schofield, N., and Tagg, A.: Testing a physically-based flood forecasting model (TOPMODEL) for three UK catchments, Journal of Hydrology, 69, 119-143, 1984.

Biggin, D.: A comparison of ERS-1 satellite radar and aerial photography for river flood mapping, Water and Environment Journal, 10, 59-64, 1996.

Bjerklie, D. M., Dingman, S. L., Vorosmarty, C. J., Bolster, C. H., and Congalton, R. G.: Evaluating the potential for measuring river discharge from space, Journal of Hydrology, 278, 17-38, 2003.

Björck, A.: Numerical methods for least squares problems, Siam, 1996.

Boukabara, S.-A., Garrett, K., and Chen, W.: Global coverage of total precipitable water using a microwave variational algorithm, Ieee T Geosci Remote, 48, 3608-3621, 2010.

Brakenridge, G. R., Nghiem, S. V., Anderson, E., and Chien, S.: Space-based measurement of river runoff, EOS: Transactions of the American Geophysical Union, 86, 185-192, 2005.

Brakenridge, G. R., Nghiem, S. V., Anderson, E., and Mic, R.: Orbital microwave measurement of river discharge and ice status, Water Resources Research, 43, 2007.

Brodzik, M. and Knowles, K.: EASE-Grid: A Versatile Set of Equal-Area Prjoections and Grids, National Center for Geographic Information & Analysis, Santa Barbara, California USA, 2002.

Calvet, J. C., Wigneron, J. P., Chanzy, A., Raju, S., and Laguerre, L.: Microwave Dielectric-Properties of a Silt-Loam at High-Frequencies, Ieee T Geosci Remote, 33, 634-642, 1995.

Carlson, T. N. and Ripley, D. A.: On the relation between NDVI, fractional vegetation cover, and leaf area index, Remote sensing of Environment, 62, 241-252, 1997.

Chai, L., Wang, Z., Wang, Y., Yang, Z., Wang, H., and Wu, X.: Ingestion risks of metals in groundwater based on TIN model and dose-response assessment—A case study in the Xiangjiang watershed, central-south China, Science of the Total Environment, 408, 3118-3124, 2010.

Chappell, N. A., Jones, T. D., Tych, W., and Krishnaswamy, J.: Role of rainstorm intensity underestimated by data-derived flood models: emerging global evidence from subsurface-dominated watersheds, Environmental Modelling & Software, 88, 1-9, 2017.

Chen, Y., Huang, C., Ticehurst, C., Merrin, L., and Thew, P.: An evaluation of MODIS daily and 8-day composite products for floodplain and wetland inundation mapping, Wetlands, 33, 823-835, 2013.

Chen, Y., Yang, K., He, J., Qin, J., Shi, J., Du, J., and He, Q.: Improving land surface temperature modeling for dry land of China, Journal of Geophysical Research: Atmospheres (1984–2012), 116, 2011.

Choudhury, B. J.: Monitoring global land surface using Nimbus-7 37 GHz data. Theory and examples, International Journal of Remote Sensing, 10, 1579-1605, 1989.

Choudhury, B. J.: Passive microwave remote sensing contribution to hydrological variables. In: Land surface-atmosphere interactions for climate modeling, Springer, Dordrecht, The Netherlands, 1991.

Choudhury, B. J., Major, E. R., Smith, E. A., and Becker, F.: Atmospheric effects on SMMR and SSM/I 37 GHz polarization difference over the Sahel, International Journal of Remote Sensing, 13, 3443-3463, 1992.

Choudhury, B. J., Schmugge, T. J., Chang, A., and Newton, R. W.: Effect of surface roughness on the microwave emission from soils, Journal of Geophysical Research, 89, 5699-5706, 1979.

Choudhury, B. J. and Tucker, C. J.: Monitoring global vegetation using Nimbus-7 37 GHz data. Some empirical relations, International Journal of Remote Sensing, 8, 1085-1090, 1987.

Choudhury, B. J., Wang, J. R., Hsu, A. Y., and Chien, Y. L.: Simulated and observed 37GHz emission over Africa, International Journal of Remote Sensing, 11, 1837-1868, 1990.

Chunguo, C. and Zihui, L.: Chemical speciation and distribution of arsenic in water, suspended solids and sediment of Xiangjiang River, China, Science of the total environment, 77, 69-82, 1988.

Cooley, J. W., Lewis, P. A., and Welch, P. D.: Application of the fast Fourier transform to computation of Fourier integrals, Fourier series, and convolution integrals, Audio and Electroacoustics, IEEE Transactions on, 15, 79-84, 1967.

Cooley, J. W. and Tukey, J. W.: An algorithm for the machine calculation of complex Fourier series, Mathematics of computation, 19, 297-301, 1965.

Crow, W. and Ryu, D.: A new data assimilation approach for improving runoff prediction using remotely-sensed soil moisture retrievals, Hydrol Earth Syst Sc, 13, 1-16, 2009.

Czekala, H., Havemann, S., Schmidt, K., Rother, T., and Simmer, C.: Comparison of microwave radiative transfer calculations obtained with three different approximations of hydrometeor shape, Journal of Quantitative Spectroscopy and Radiative Transfer, 63, 545-558, 1999.

D'Odorico, P. and Rodríguez-Iturbe, I.: Space-time self-organization of mesoscale rainfall and soil moisture, Advances in water resources, 23, 349-357, 2000.

De Ridder, K.: Quantitative estimation of skin soil moisture with the special sensor microwave/imager, Boundary-Layer Meteorology, 96, 421-432, 2000.

Deshmukh, K. and Shinde, G.: An adaptive color image segmentation, ELCVIA Electronic Letters on Computer Vision and Image Analysis, 5, 12-23, 2005.

Dobson, M. C., Ulaby, F. T., Hallikainen, M. T., and Elrayes, M. A.: Microwave Dielectric Behavior of Wet Soil .2. Dielectric Mixing Models, Ieee T Geosci Remote, 23, 35-46, 1985.

Donohue, R., Roderick, M., and McVicar, T.: On the importance of including vegetation dynamics in Budyko's hydrological model, Hydrology and Earth System Sciences Discussions, 11, 983-995, 2007.

Dronova, I., Gong, P., and Wang, L.: Object-based analysis and change detection of major wetland cover types and their classification uncertainty during the low water period at Poyang Lake, China, Remote Sensing of Environment, 115, 3220-3236, 2011.

Eagleson, P. S.: Climate, soil, and vegetation: 1. Introduction to water balance dynamics, Water Resources Research, 14, 705-712, 1978.

Entin, J. K., Robock, A., Vinnikov, K. Y., Hollinger, S. E., Liu, S., and Namkhai, A.: Temporal and spatial scales of observed soil moisture variations in the extratropics, J Geophys Res, 105, 11865-11877, 2000.

Feng, L., Hu, C., Chen, X., Cai, X., Tian, L., and Gan, W.: Assessment of inundation changes of Poyang Lake using MODIS observations between 2000 and 2010, Remote Sensing of Environment, 121, 80-92, 2012a.

Feng, L., Hu, C., Chen, X., Tian, L., and Chen, L.: Human induced turbidity changes in Poyang Lake between 2000 and 2010: Observations from MODIS, Journal of Geophysical Research: Oceans, 117, 2012b.

Ferraro, R. R. and Marks, G. F.: The Development of SSM/I Rain-Rate Retrieval Algorithms Using Ground-Based Radar Measurements, Journal of Atmospheric and Oceanic Technology, 12, 755-770, 1995.

Fily, M., Royer, A., Goïta, K., and Prigent, C.: A simple retrieval method for land surface temperature and fraction of water surface determination from satellite microwave brightness temperatures in sub-arctic areas, Remote Sensing of Environment, 85, 328-338, 2003.

Frappart, F., Seyler, F., Martinez, J.-M., Leon, J. G., and Cazenave, A.: Floodplain water storage in the Negro River basin estimated from microwave remote sensing of inundation area and water levels, Remote Sensing of Environment, 99, 387-399, 2005.

Gao, H. L., Wood, E. F., Drusch, M., Crow, W., and Jackson, T. J.: Using a microwave emission model to estimate soil moisture from ESTAR observations during SGP99, Journal of Hydrometeorology, 5, 49-63, 2004.

Gerek, Ö. N. and Yardimci, Y.: Equiripple FIR filter design by the FFT algorithm, Signal Processing Magazine, IEEE, 14, 60-64, 1997.

Giddings, L. and Choudhury, B. J.: Observation of hydrological features with Nimbus-7 37 GHz data, applied to South America, International Journal of Remote Sensing, 10, 1673-1686, 1989.

Gleason, C. J. and Smith, L. C.: Toward global mapping of river discharge using satellite images and at-many-stations hydraulic geometry, Proceedings of the National Academy of Sciences, 111, 4788-4791, 2014.

Gleick, P. H.: The development and testing of a water balance model for climate impact assessment: modeling the Sacramento basin, Water Resources Research, 23, 1049-1061, 1987.

Goel, M., Jain, S. K., and Agarwal, P.: Assessment of sediment deposition rate in Bargi Reservoir using digital image processing, Hydrological sciences journal, 47, S81-S92, 2002.

Guerschman, J. P., Warren, G., Byrne, G., Lymburner, L., Mueller, N., and Van Dijk, A. I.: MODIS-based standing water detection for flood and large reservoir mapping: algorithm development and applications for the Australian continent, CSIRO Canberra, Australia, 2011.

Guo, H., Hu, Q., and Jiang, T.: Annual and seasonal streamflow responses to climate and land-cover changes in the Poyang Lake basin, China, Journal of Hydrology, 355, 106-122, 2008.

Guo, H., Hu, Q., and Zhang, Q.: Changes in hydrological interactions of the Yangtze River and the Poyang Lake in China during 1957–2008, Acta Geographica Sinica, 66, 609-618, 2011.

Guo, H., Hu, Q., Zhang, Q., and Feng, S.: Effects of the three gorges dam on Yangtze river flow and river interaction with Poyang Lake, China: 2003–2008, Journal of Hydrology, 416, 19-27, 2012.

Gupta, H. V., Sorooshian, S., and Yapo, P. O.: Status of automatic calibration for hydrologic models: Comparison with multilevel expert calibration, Journal of Hydrologic Engineering, 4, 135-143, 1999.

Gutman, G. and Ignatov, A.: The derivation of the green vegetation fraction from NOAA/AVHRR data for use in numerical weather prediction models, International Journal of remote sensing, 19, 1533-1543, 1998.

Hamilton, S. K., Sippel, S. J., and Melack, J. M.: Comparison of inundation patterns among major South American floodplains, Journal of Geophysical Research D: Atmospheres, 107, 1-14, 2002.

Hamilton, S. K., Sippel, S. J., and Melack, J. M.: Inundation patterns in the Pantanal wetland of South America determined from passive microwave remote sensing, Archiv fur Hydrobiologie, 137, 1-23, 1996.

Hamilton, S. K., Sippel, S. J., and Melack, J. M.: Seasonal inundation patterns in two large savanna floodplains of South America: The Llanos de Moxos (Bolivia) and the Llanos del Orinoco (Venezuela and Colombia), Hydrological Processes, 18, 2103-2116, 2004.

Harris, F. J.: On the use of windows for harmonic analysis with the discrete Fourier transform, Proceedings of the IEEE, 66, 51-83, 1978.

Hawkins, D. M.: The problem of overfitting, Journal of chemical information and computer sciences, 44, 1-12, 2004.

Hayashi, M., van der Kamp, G., and Rudolph, D. L.: Water and solute transfer between a prairie wetland and adjacent uplands, 1. Water balance, Journal of Hydrology, 207, 42-55, 1998.

Hess, L. L., Melack, J. M., Filoso, S., and Wang, Y.: Delineation of inundated area and vegetation along the Amazon floodplain with the SIR-C synthetic aperture radar, Geoscience and Remote Sensing, IEEE Transactions on, 33, 896-904, 1995.

Hess, L. L., Melack, J. M., Novo, E. M., Barbosa, C. C., and Gastil, M.: Dual-season mapping of wetland inundation and vegetation for the central Amazon basin, Remote Sensing of Environment, 87, 404-428, 2003.

Hollinger, J. P., Peirce, J. L., and Poe, G. A.: SSM/I instrument evaluation, Ieee T Geosci Remote, 28, 781-790, 1990.

Holmes, T. R. H., De Jeu, R. A. M., Owe, M., and Dolman, A. J.: Land surface temperature from Ka band (37 GHz) passive microwave observations, J Geophys Res-Atmos, 114, 2009.

Horritt, M., Mason, D., and Luckman, A.: Flood boundary delineation from synthetic aperture radar imagery using a statistical active contour model, International Journal of Remote Sensing, 22, 2489-2507, 2001.

Hostache, R., Matgen, P., Schumann, G., Puech, C., Hoffmann, L., and Pfister, L.: Water level estimation and reduction of hydraulic model calibration uncertainties using satellite SAR images of floods, Geoscience and Remote Sensing, IEEE Transactions on, 47, 431-441, 2009.

Houweling, S., Kaminski, T., Dentener, F., Lelieveld, J., and Heimann, M.: Inverse modeling of methane sources and sinks using the adjoint of a global transport model, Journal of Geophysical Research: Atmospheres, 104, 26137-26160, 1999.

Hu, Q., Feng, S., Guo, H., Chen, G., and Jiang, T.: Interactions of the Yangtze river flow and hydrologic processes of the Poyang Lake, China, Journal of Hydrology, 347, 90-100, 2007.

Huber, C., Li, J., Daillet, S., Chen, X., Xijun, L., Francois, C. J., Wei, Z., Carlos, U., Mathias, S., Shifeng, H., Stephane, A., Burnham, J., and Yesou, H.: Twelve year of water resource monitoring over Yangtze middle reaches exploiting DRAGON time series and field measurments, DRAGON II symposium, Beijing, 2012.

Huffman, G. J., Bolvin, D. T., Nelkin, E. J., Wolff, D. B., Adler, R. F., Gu, G., Hong, Y., Bowman, K. P., and Stocker, E. F.: The TRMM multisatellite precipitation analysis (TMPA): Quasi-global, multiyear, combined-sensor precipitation estimates at fine scales, Journal of Hydrometeorology, 8, 38-55, 2007.

Irons, J. R. and Petersen, G. W.: Texture transforms of remote sensing data, Remote Sensing of Environment, 11, 359-370, 1981.

Islam, A., Bala, S., and Haque, M.: Flood inundation map of Bangladesh using MODIS time-series images, Journal of Flood Risk Management, 3, 210-222, 2010.

Jain, S. K., Singh, P., and Seth, S.: Assessment of sedimentation in Bhakra Reservoir in the western Himalayan region using remotely sensed data, Hydrological sciences journal, 47, 203-212, 2002.

Jakeman, A. and Hornberger, G.: How much complexity is warranted in a rainfall-runoff model?, Water resources research, 29, 2637-2649, 1993.

Jakeman, A., Littlewood, I., and Whitehead, P.: Computation of the instantaneous unit hydrograph and identifiable component flows with application to two small upland catchments, Journal of hydrology, 117, 275-300, 1990.

Jia, L., Shang, H., Hu, G., and Menenti, M.: Phenological response of vegetation to upstream river flow in the Heihe Rive basin by time series analysis of MODIS data, Hydrol Earth Syst Sc, 15, 1047-1064, 2011.

Jin, Y.: A flooding index and its regional threshold value for monitoring floods in China from SSM/I data, International Journal of Remote Sensing, 20, 1025-1030, 1999.

Kawanishi, T., Sezai, T., Ito, Y., Imaoka, K., Takeshima, T., Ishido, Y., Shibata, A., Miura, M., Inahata, H., and Spencer, R. W.: The Advanced Microwave Scanning Radiometer for

the Earth Observing System (AMSR-E), NASDA's contribution to the EOS for global energy and water cycle studies, Ieee T Geosci Remote, 41, 184-194, 2003.

Kazezyılmaz-Alhan, C. M., Medina, M. A., and Richardson, C. J.: A wetland hydrology and water quality model incorporating surface water/groundwater interactions, Water Resources Research, 43, 2007.

Keogh, E., Chakrabarti, K., Pazzani, M., and Mehrotra, S.: Dimensionality reduction for fast similarity search in large time series databases, Knowledge and information Systems, 3, 263-286, 2001.

Kerr, Y. H., Waldteufel, P., Wigneron, J.-P., Martinuzzi, J., Font, J., and Berger, M.: Soil moisture retrieval from space: The Soil Moisture and Ocean Salinity (SMOS) mission, Ieee T Geosci Remote, 39, 1729-1735, 2001.

Kirdiashev, K. P., Chucklantsev, A. A., and Shutko, A.: Microwave radiation of the earth's surface in the presence of vegetation cover, Radiotecknica, 24, 256-264, 1979.

Knowles, K., Savoie, M., Armstrong, R., and Brodzik, M.: AMSR-E/Aqua Daily EASE-Grid Brightness Temperatures, NASA DAAC at the National Snow and Ice Data Center, Boulder, Colorado USA, 2006.

Kummerow, C., Olson, W. S., and Giglio, L.: A simplified scheme for obtaining precipitation and vertical hydrometeor profiles from passive microwave sensors, Geoscience and Remote Sensing, IEEE Transactions on, 34, 1213-1232, 1996.

Lakshmi, V., Wood, E. F., and Choudhury, B. J.: Evaluation of Special Sensor Microwave/Imager satellite data for regional soil moisture estimation over the Red River basin, Journal of Applied Meteorology, 36, 1309-1328, 1997a.

Lakshmi, V., Wood, E. F., and Choudhury, B. J.: A soil-canopy-atmosphere model for use in satellite microwave remote sensing, Journal of Geophysical Research D: Atmospheres, 102, 6911-6927, 1997b.

Lane, J. and Saxton, J.: Dielectric dispersion in pure polar liquids at very high radio frequencies. III. The effect of electrolytes in solution, 1952, 531-545.

Lawson, C. L. and Hanson, R. J.: Solving least squares problems, SIAM, 1974.

Lee, J.-S., Papathanassiou, K. P., Ainsworth, T. L., Grunes, M. R., and Reigber, A.: A new technique for noise filtering of SAR interferometric phase images, Geoscience and Remote Sensing, IEEE Transactions on, 36, 1456-1465, 1998.

Li, F., Huang, J., Zeng, G., Yuan, X., Li, X., Liang, J., Wang, X., Tang, X., and Bai, B.: Spatial risk assessment and sources identification of heavy metals in surface sediments from the Dongting Lake, Middle China, Journal of Geochemical Exploration, 132, 75-83, 2013.

Li, P., Feng, Z., Jiang, L., Liu, Y., and Xiao, X.: Changes in rice cropping systems in the Poyang Lake Region, China during 2004–2010, Journal of Geographical Sciences, 22, 653-668, 2012.

Liang, X., Lettenmaier, D. P., Wood, E. F., and Burges, S. J.: A simple hydrologically based model of land surface water and energy fluxes for general circulation models, JOURNAL OF GEOPHYSICAL RESEARCH-ALL SERIES-, 99, 14,415-414,415, 1994.

Liebe, H. J., Hufford, G. A., and Manabe, T.: A model for the complex permittivity of water at frequencies below 1 THz, International Journal of Infrared and Millimeter Waves, 12, 659-675, 1991.

Lin, C. and Lu, J.: Studies on the anomaly of Plum Rain and flood disaster in the Yangtze River valley, J. Najing University, 1991. 76-83, 1991.

Lin, R., King-lp, A., and Shim, H. S. S. K.: Fast similarity search in the presence of noise, scaling, and translation in time-series databases, Zurich, Switzerland, 9 - 13 September 1995, 490-501.

Madsen, H.: Automatic calibration of a conceptual rainfall–runoff model using multiple objectives, Journal of hydrology, 235, 276-288, 2000.

Manabe, T., Liebe, H., and Hufford, G.: Complex permittivity of water between 0 and 30 THz, 1987, 229-230.

Matthews, E. and Fung, I.: Methane emission from natural wetlands: Global distribution, area, and environmental characteristics of sources, Global biogeochemical cycles, 1, 61-86, 1987.

Matthews, E., Fung, I., and Lerner, J.: Methane emission from rice cultivation: Geographic and seasonal distribution of cultivated areas and emissions, Global Biogeochemical Cycles, 5, 3-24, 1991.

Mätzler, C.: Thermal microwave radiation: applications for remote sensing, Iet, 2006.

McFeeters, S.: The use of the Normalized Difference Water Index (NDWI) in the delineation of open water features, International journal of remote sensing, 17, 1425-1432, 1996.

Menenti, M., Azzali, S., Verhoef, W., and van Swol, R.: Mapping agroecological zones and time lag in vegetation growth by means of fourier analysis of time series of NDVI images, Advances in Space Research, 13, 233-237, 1993.

Mertes, L. A.: Documentation and significance of the perirheic zone on inundated floodplains, Water Resources Research, 33, 1749-1762, 1997.

Mialon, A., Royer, A., and Fily, M.: Wetland seasonal dynamics and interannual variability over northern high latitudes, derived from microwave satellite data, Journal of Geophysical Research: Atmospheres, 110, 2005.

Miller, M. W. and Nudds, T. D.: Prairie landscape change and flooding in the Mississippi River Valley, Conservation Biology, 1996. 847-853, 1996.

Mo, T. and Schmugge, T. J.: A parameterization of the effect of surface roughness on microwave emission, Geoscience and Remote Sensing, IEEE Transactions on, 1987. 481-486, 1987.

Montandon, L. and Small, E.: The impact of soil reflectance on the quantification of the green vegetation fraction from NDVI, Remote Sensing of Environment, 112, 1835-1845, 2008.

Moore, R.: The PDM rainfall-runoff model, Hydrology and Earth System Sciences Discussions, 11, 483-499, 2007.

Moore, R.: The probability-distributed principle and runoff production at point and basin scales, Hydrological Sciences Journal, 30, 273-297, 1985.

Mörchen, F.: Time series feature extraction for data mining using DWT and DFT. Univ. of Marburg, Germany, 2003.

Nash, J. E. and Sutcliffe, J. V.: River flow forecasting through conceptual models part I — A discussion of principles, Journal of Hydrology, 10, 282-290, 1970.

Nerem, R., Chambers, D., Leuliette, E., Mitchum, G., and Giese, B.: Variations in global mean sea level associated with the 1997–1998 ENSO event: Implications for measuring long term sea level change, Geophys Res Lett, 26, 3005-3008, 1999.

Njoku, E. G., Jackson, T. J., Lakshmi, V., Chan, T. K., and Nghiem, S. V.: Soil moisture retrieval from AMSR-E, Ieee T Geosci Remote, 41, 215-229, 2003.

O'Neill, P. E., Jackson, T. J., Chauhan, N. S., and Seyfried, M. S.: Microwave soil moisture estimation in humid and semiarid watersheds, Advances in Space Research, 13, 115-118, 1993.

Oberstadler, R., Hönsch, H., and Huth, D.: Assessment of the mapping capabilities of ERS-1 SAR data for flood mapping: a case study in Germany, Hydrological processes, 11, 1415-1425, 1997.

Otsu, N.: A threshold selection method from gray-level histograms, Automatica, 11, 23-27, 1975.

Owe, M., de Jeu, R., and Walker, J.: A methodology for surface soil moisture and vegetation optical depth retrieval using the microwave polarization difference index, Geoscience and Remote Sensing, IEEE Transactions on, 39, 1643-1654, 2001.

Paiva, R. C., Durand, M. T., and Hossain, F.: Spatiotemporal interpolation of discharge across a river network by using synthetic SWOT satellite data, Water Resources Research, 51, 430-449, 2015.

Paloscia, S., Macelloni, G., Santi, E., and Koike, T.: A multifrequency algorithm for the retrieval of soil moisture on a large scale using microwave data from SMMR and SSM/I satellites, Ieee T Geosci Remote, 39, 1655-1661, 2001.

Pampaloni, P. and Paloscia, S.: Experimental relationships between microwave emission and vegetation features†, International Journal of Remote Sensing, 6, 315-323, 1985.

Pan, F., Liao, J., Li, X., and Guo, H.: Application of the inundation area—lake level rating curves constructed from the SRTM DEM to retrieving lake levels from satellite measured inundation areas, Computers & Geosciences, 52, 168-176, 2013.

Papa, F., Prigent, C., Durand, F., and Rossow, W. B.: Wetland dynamics using a suite of satellite observations: A case study of application and evaluation for the Indian Subcontinent, Geophys Res Lett, 33, 2006.

Peng, D., Guo, S., Liu, P., and Liu, T.: Reservoir storage curve estimation based on remote sensing data, Journal of hydrologic engineering, 11, 165-172, 2006.

Podest, E. and Saatchi, S.: Application of multiscale texture in classifying JERS-1 radar data over tropical vegetation, International Journal of Remote Sensing, 23, 1487-1506, 2002.

Poe, G. A.: Optimum Interpolation of Imaging Microwave Radiometer Data, Ieee T Geosci Remote, 28, 800-810, 1990.

Poe, G. A. and Conway, R. W.: A study of the geolocation errors of the Special Sensor Microwave/Imager (SSM/I), Ieee T Geosci Remote, 28, 791-799, 1990.

Prigent, C., Aires, F., Rossow, W., and Matthews, E.: Joint characterization of vegetation by satellite observations from visible to microwave wavelengths: A sensitivity analysis, Journal of Geophysical Research: Atmospheres, 106, 20665 - 20685, 2001a.

Prigent, C., Matthews, E., Aires, F., and Rossow, W. B.: Remote sensing of global wetland dynamics with multiple satellite data sets, Geophys Res Lett, 28, 4631-4634, 2001b.

Prigent, C., Papa, F., Aires, F., Rossow, W., and Matthews, E.: Global inundation dynamics inferred from multiple satellite observations, 1993–2000, Journal of Geophysical Research: Atmospheres, 112, 2007.

Prigent, C., Rossow, W. B., and Matthews, E.: Microwave land surface emissivities estimated from SSM/I observations, Journal of Geophysical Research: Atmospheres, 102, 21867-21890, 1997.

Project, B. M., Erdélyi, A., and Bateman, H.: Tables of Integral Transforms: Based in Part on Notes Left by Harry Bateman and Compiled by the Staff of the Bateman Manuscript Project, McGraw-Hill, New York, NY, USA, 1954.

Pulvirenti, L., Chini, M., Pierdicca, N., Guerriero, L., and Ferrazzoli, P.: Flood monitoring using multi-temporal COSMO-SkyMed data: Image segmentation and signature interpretation, Remote Sensing of Environment, 115, 990-1002, 2011.

Rasid, H. and Pramanik, M.: Visual interpretation of satellite imagery for monitoring floods in Bangladesh, Environmental Management, 14, 815-821, 1990.

Reale, A., Chalfant, M., Allegrino, A., Tiley, F., Gerguson, M., and Pettey, M.: Advanced-TOVS (ATOVS) sounding products from NOAA polar orbiting environmental satellites, 2003.

Richards, F. and Arkin, P.: On the relationship between satellite-observed cloud cover and precipitation, Monthly Weather Review, 109, 1081-1093, 1981.

Ritter, A. and Muñoz-Carpena, R.: Performance evaluation of hydrological models: Statistical significance for reducing subjectivity in goodness-of-fit assessments, Journal of Hydrology, 480, 33-45, 2013.

Roerink, G. J., Menenti, M., Soepboer, W., and Su, Z.: Assessment of climate impact on vegetation dynamics by using remote sensing, Physics and Chemistry of the Earth, Parts A/B/C, 28, 103-109, 2003.

Roerink, G. J., Menenti, M., and Verhoef, W.: Reconstructing cloudfree NDVI composites using Fourier analysis of time series, International Journal of Remote Sensing, 21, 1911-1917, 2000.

Rossow, W. B. and Schiffer, R. A.: Advances in understanding clouds from ISCCP, Bulletin of the American Meteorological Society, 80, 2261, 1999.

Sakamoto, T., Van Nguyen, N., Kotera, A., Ohno, H., Ishitsuka, N., and Yokozawa, M.: Detecting temporal changes in the extent of annual flooding within the Cambodia and the Vietnamese Mekong Delta from MODIS time-series imagery, Remote sensing of environment, 109, 295-313, 2007.

Schumann, G., Di Baldassarre, G., and Bates, P. D.: The utility of spaceborne radar to render flood inundation maps based on multialgorithm ensembles, Geoscience and Remote Sensing, IEEE Transactions on, 47, 2801-2807, 2009.

Schumann, G. J.-P. and Moller, D. K.: Microwave remote sensing of flood inundation, Physics and Chemistry of the Earth, Parts A/B/C, 83, 84-95, 2015.

Shang, H., Jia, J., and Menenti, M.: Analyzing the Inundation Pattern of the Poyang Lake floodplain by Passive Microwave Data, Journal of Hydrometeorology, 16, 652-667, 2015.

Shang, H., Jia, J., and Menenti, M.: Modeling and Reconstruction of Time Series of Passive Microwave Data by Discrete Fourier Transform Guided Filtering and Harmonic Analysis, Remote Sensing, 08, 970, 2016.

Shankman, D., Keim, B. D., and Song, J.: Flood frequency in China's Poyang Lake region: trends and teleconnections, International Journal of Climatology, 26, 1255-1266, 2006.

Sheng, Y., Gong, P., and Xiao, Q.: Quantitative dynamic flood monitoring with NOAA AVHRR, International Journal of Remote Sensing, 22, 1709-1724, 2001.

Sheng, Y., Su, Y., and Xiao, Q.: Challenging the cloud-contamination problem in flood monitoring with NOAA/AVHRR imagery, Photogrammetric Engineering and Remote Sensing, 64, 191-198, 1998.

Shi, J. C., Jackson, T., Tao, J., Du, J., Bindlish, R., Lu, L., and Chen, K. S.: Microwave vegetation indices for short vegetation covers from satellite passive microwave sensor AMSR-E, Remote Sensing of Environment, 112, 4285-4300, 2008.

Shi, J. C., Jiang, L. M., Zhang, L. X., Chen, K. S., Wigneron, J. P., and Chanzy, A.: A parameterized multifrequency-polarization surface emission model, Ieee T Geosci Remote, 43, 2831-2841, 2005.

Shjeflo, J. B.: Evapotranspiration and the water budget of prairie potholes in North Dakota, US Government Printing Office, 1968.

Singleton, R. C.: An algorithm for computing the mixed radix fast Fourier transform, Audio and Electroacoustics, IEEE Transactions on, 17, 93-103, 1969.

Sippel, S. J., Hamilton, S. K., Melack, J. M., and Choudhury, B. J.: Determination of inundation area in the Amazon River floodplain using the SMMR 37 GHz polarization difference, Remote Sensing of Environment, 48, 70-76, 1994.

Sippel, S. J., Hamilton, S. K., Melack, J. M., and Novo, E. M. M.: Passive microwave observations of inundation area and the area/stage relation in the Amazon River floodplain, International Journal of Remote Sensing, 19, 3055-3074, 1998.

Sivapalan, M., Beven, K., and Wood, E. F.: On hydrologic similarity: 2. A scaled model of storm runoff production, Water Resources Research, 23, 2266-2278, 1987.

Skøien, J. O., Blöschl, G., and Western, A.: Characteristic space scales and timescales in hydrology, Water Resources Research, 39, 2003.

Smith, L. C.: Satellite remote sensing of river inundation area, stage, and discharge: A review, Hydrological processes, 11, 1427-1439, 1997.

Smith, L. C., Alsdorf, D. E., Magilligan, F. J., Gomez, B., Mertes, L. A., Smith, N. D., and Garvin, J. B.: Estimation of erosion, deposition, and net volumetric change caused by the 1996 Skeiðarársandur jökulhlaup, Iceland, from synthetic aperture radar interferometry, Water Resources Research, 36, 1583-1594, 2000.

Smith, L. C., Isacks, B. L., Bloom, A. L., and Murray, A. B.: Estimation of discharge from three braided rivers using synthetic aperture radar satellite imagery: Potential application to ungaged basins, Water Resources Research, 32, 2021-2034, 1996.

Smith, L. C. and Pavelsky, T. M.: Estimation of river discharge, propagation speed, and hydraulic geometry from space: Lena River, Siberia, Water Resources Research, 44, 2008.

Sophocleous, M.: Interactions between groundwater and surface water: the state of the science, Hydrogeology journal, 10, 52-67, 2002.

Su, M., Stolte, W., and Van der Kamp, G.: Modelling Canadian prairie wetland hydrology using a semi-distributed streamflow model, Hydrological Processes, 14, 2405-2422, 2000.

Tanaka, M., Sugimura, T., and Tanaka, S.: Cover. Monitoring water surface ratio in the Chinese floods of summer 1998 by DMSP-SSM/I, 2000. 2000.

Tanaka, M., Sugimura, T., Tanaka, S., and Tamai, N.: Flood–drought cycle of Tonle Sap and Mekong Delta area observed by DMSP-SSM/I, International Journal of Remote Sensing, 24, 1487-1504, 2003.

Temimi, M., Leconte, R., Brissette, F., and Chaouch, N.: Flood and soil wetness monitoring over the Mackenzie River Basin using AMSR-E 37 GHz brightness temperature, 25-29 July 2005 2005, 4 pp.

Thompson, A. R., Moran, J. M., and Swenson Jr, G. W.: Interferometry and synthesis in radio astronomy, John Wiley & Sons, Weinheim, Germany, 2008.

Todini, E.: The ARNO rainfall—runoff model, Journal of Hydrology, 175, 339-382, 1996.

Torbick, N., Salas, W., Xiao, X., Ingraham, P., Fearon, M., Biradar, C., Zhao, D., Liu, Y., Li, P., and Zhao, Y.: Integrating SAR and optical imagery for regional mapping of paddy rice attributes in the Poyang Lake Watershed, China, Canadian Journal of Remote Sensing, 37, 17-26, 2011.

Townsend, P. A.: Mapping seasonal flooding in forested wetlands using multi-temporal Radarsat SAR, Photogrammetric engineering and remote sensing, 67, 857-864, 2001.

Tsang, L., Blanchard, A. J., Newton, R. W., and Kong, J. A.: A simple relation between active and passive microwave remote sensing measurements of earth terrain, Geoscience and Remote Sensing, IEEE Transactions on, 1982. 482-485, 1982.

Ulaby, F. T., Moore, R. K., and Fung, A. K.: Microwave remote sensing : active and passive, Addison-Wesley Pub. Co., Advanced Book Program/World Science Division, Reading, Mass., 1981.

Usachev, V.: Evaluation of flood plain inundations by remote sensing methods, Hydrological Applications of Remote Sensing and Remote Data Transmission, 1983. 475-482, 1983.

Vachaud, G., Passerat de Silans, A., Balabanis, P., and Vauclin, M.: Temporal stability of spatially measured soil water probability density function, Soil Science Society of America Journal, 49, 822-828, 1985.

Vandegriend, A. A. and Owe, M.: Determination of Microwave Vegetation Optical Depth and Single Scattering Albedo from Large-Scale Soil-Moisture and Nimbus Smmr Satellite-Observations, International Journal of Remote Sensing, 14, 1875-1886, 1993.

Verdin, J.: Remote sensing of ephemeral water bodies in western Niger, International Journal of Remote Sensing, 17, 733-748, 1996.

Verhoef, W.: Application of Harmonic Analysis of NDVI Time Series (HANTS), In Fourier Analysis of Temporal NDVI in the Souther African and American Continents Wageningen, The Netherlands, 19-24, 1996.

Vinnikov, K. Y., Robock, A., Qiu, S., Entin, J. K., Owe, M., Choudhury, B. J., Hollinger, S. E., and Njoku, E. G.: Satellite remote sensing of soil moisture in Illinois, United States, Journal of Geophysical Research D: Atmospheres, 104, 4145-4168, 1999.

Vinnikov, K. Y., Robock, A., Speranskaya, N. A., and Schlosser, C. A.: Scales of temporal and spatial variability of midlatitude soil moisture, Journal of Geophysical Research: Atmospheres, 101, 7163-7174, 1996.

Vörösmarty, C. J., Moore, B., Grace, A. L., Gildea, M. P., Melillo, J. M., Peterson, B. J., Rastetter, E. B., and Steudler, P. A.: Continental scale models of water balance and fluvial transport: an application to South America, Global biogeochemical cycles, 3, 241-265, 1989.

Vörösmarty, C. J., Willmott, C. J., Choudhury, B. J., Schloss, A. L., Stearns, T. K., Robeson, S. M., and Dorman, T. J.: Analyzing the discharge regime of a large tropical river through remote sensing, ground-based climatic data, and modeling, Water Resources Research, 32, 3137-3150, 1996.

Walter, B. P., Heimann, M., and Matthews, E.: Modeling modern methane emissions from natural wetlands: 1. Model description and results, Journal of Geophysical Research: Atmospheres, 106, 34189-34206, 2001.

Wang, J. R. and Choudhury, B. J.: Remote sensing of soil moisture content over bare field at 1.4 GHz frequency, Journal of Geophysical Research, 86, 5277-5282, 1981.

Wang, J. R. and Schmugge, T. J.: An Empirical-Model for the Complex Dielectric Permittivity of Soils as a Function of Water-Content, Ieee T Geosci Remote, 18, 288-295, 1980.

Wang, Y., Hess, L. L., Filoso, S., and Melack, J. M.: Understanding the radar backscattering from flooded and nonflooded Amazonian forests: Results from canopy backscatter modeling, Remote Sensing of Environment, 54, 324-332, 1995.

Wang, Z., Chai, L., Wang, Y., Yang, Z., Wang, H., and Wu, X.: Potential health risk of arsenic and cadmium in groundwater near Xiangjiang River, China: a case study for risk assessment and management of toxic substances, Environmental monitoring and assessment, 175, 167-173, 2011.

Wen, J., Su, Z. B., and Ma, Y. M.: Determination of land surface temperature and soil moisture from Tropical Rainfall Measuring Mission/Microwave Imager remote sensing data, J Geophys Res-Atmos, 108, 2003.

Wentz, F. J.: Measurement of oceanic wind vector using satellite microwave radiometers, Ieee T Geosci Remote, 30, 960-972, 1992.

Wentz, F. J.: SSM/I Version-7 Calibration Report, Remote Sensing Systems, Santa Rosa, CA, 46pp pp., 2013.

Westerhoff, R., Kleuskens, M., Winsemius, H., Huizinga, H., Brakenridge, G., and Bishop, C.: Automated global water mapping based on wide-swath orbital synthetic-aperture radar, Hydrol. Earth Syst. Sci, 17, 651-663, 2013.

Wiesmann, A. and Mätzler, C.: Microwave emission model of layered snowpacks, Remote Sensing of Environment, 70, 307-316, 1999.

Wigneron, J.-P., Chanzy, A., Calvet, J.-C., and Bruguier, N.: A simple algorithm to retrieve soil moisture and vegetation biomass using passive microwave measurements over crop fields, Remote Sensing of Environment, 51, 331-341, 1995.

Wigneron, J. P., Kerr, Y., Chanzy, A., and Jin, Y. Q.: Inversion of surface parameters from passive microwave measurements over a soybean field, Remote Sensing of Environment, 46, 61-72, 1993.

Wilson, D. J., Western, A. W., and Grayson, R. B.: Identifying and quantifying sources of variability in temporal and spatial soil moisture observations, Water Resources Research, 40, 2004.

Winter, T. C. and Rosenberry, D. O.: The interaction of ground water with prairie pothole wetlands in the Cottonwood Lake area, east-central North Dakota, 1979–1990, Wetlands, 15, 193-211, 1995.

Winter, T. C. and Valk, A.: Hydrologic studies of wetlands in the northern prairie, Northern prairie wetlands., 1989. 16-54, 1989.

Woo, M.-K. and Rowsell, R. D.: Hydrology of a prairie slough, Journal of Hydrology, 146, 175-207, 1993.

Wood, E. F., Lettenmaier, D. P., and Zartarian, V. G.: A land-surface hydrology parameterization with subgrid variability for general circulation models, Journal of Geophysical Research: Atmospheres (1984–2012), 97, 2717-2728, 1992.

Wu, Y.-L., Agrawal, D., and El Abbadi, A.: A comparison of DFT and DWT based similarity search in time-series databases, McLean, VA, USA, 6 - 11 November 2000, 488-495.

Xiao, Q. and Chen, W.: Songhua River flood monitoring with meteorological satellite imagery, Remote Sensing Information, 4, 37-41, 1987.

Xu, C.-Y. and Singh, V. P.: Review on regional water resources assessment models under stationary and changing climate, Water Resources Management, 18, 591-612, 2004.

Xu, H.: Modification of normalised difference water index (NDWI) to enhance open water features in remotely sensed imagery, International Journal of Remote Sensing, 27, 3025-3033, 2006.

Yang, K., He, J., Tang, W., Qin, J., and Cheng, C. C.: On downward shortwave and longwave radiations over high altitude regions: Observation and modeling in the Tibetan Plateau, Agricultural and Forest Meteorology, 150, 38-46, 2010.

Ye, X., Zhang, Q., Bai, L., and Hu, Q.: A modeling study of catchment discharge to Poyang Lake under future climate in China, Quaternary International, 244, 221-229, 2011.

Ye, X., Zhang, Q., Liu, J., Li, X., and Xu, C.-y.: Distinguishing the relative impacts of climate change and human activities on variation of streamflow in the Poyang Lake catchment, China, Journal of Hydrology, 494, 83-95, 2013.

Yésou, H., Claire, H., Xijun, L., Stéphane, A., Jiren, L., Sylviane, D., Muriel, B.-N., Xiaoling, C., Shifeng, H., Burnham, J., Jean-François, C., Tiphanie, M., Jinggang, L., Rémi, A., and Carlos, U.: Nine years of water resources monitoring over the middle reaches of the Yangtze River, with ENVISAT, MODIS, Beijing-1 time series, Altimetric data and field measurements, Lakes & Reservoirs: Research & Management, 16, 231-247, 2011.

Yesou, H., Huber, C., Shifeng, H., Xijun, L., and Sylviane, D.-R.: Chinese lakes behaviours in the framework of the meteorology and water management practices: EO based monitoring lessons, the ESA Living Planet symposium, Edinburg, 2013.

Young, P.: Recursive estimation and time-series analysis: an introduction, 1984. 1984.

Zhang, L., Li, D., Tong, Q., and Zheng, L.: Study of the spectral mixture model of soil and vegetation in PoYang Lake area, China, International Journal of Remote Sensing, 19, 2077-2084, 1998.

Zhang, L., Yin, J., Jiang, Y., and Wang, H.: Relationship between the hydrological conditions and the distribution of vegetation communities within the Poyang Lake National Nature Reserve, China, Ecological Informatics, 11, 65-75, 2012.

Zhang, Q., Liu, C., Xu, C.-y., Xu, Y., and Jiang, T.: Observed trends of annual maximum water level and streamflow during past 130 years in the Yangtze River basin, China, Journal of Hydrology, 324, 255-265, 2006.

Zhang, Q., Liu, Y., Yang, G., and Zhang, Z.: Precipitation and hydrological variations and related associations with large-scale circulation in the Poyang Lake basin, China, Hydrological Processes, 25, 740-751, 2011.

Zhao, G., Hörmann, G., Fohrer, N., Zhang, Z., and Zhai, J.: Streamflow trends and climate variability impacts in Poyang Lake Basin, China, Water resources management, 24, 689-706, 2010.

Zhao, R.: Flood forecasting method for humid regions of China, East China College of Hydraulic Engineering, Nanjing, 1977. 19-51, 1977.

Zhao, R.: Watershed hydrological modelling, Water Resources and Electric Power Press, Beijing, 1984. 1984.

Zhou, Z.: Synoptic characteristics of atmoshperic cirulation during abnormal Plum Rain period in 1991, J. Nanjing University, 1991. 84-93, 1991.

Zong, Y. and Chen, X.: The 1998 flood on the Yangtze, China, Natural Hazards, 22, 165-184, 2000.

Agrawal, R., Faloutsos, C., and Swami, A.: Efficient similarity search in sequence databases, Springer, 1993.

Aires, F., Prigent, C., Rossow, W., Rothstein, M., and Hansen, J. E.: A new neural network approach including first-guess for retrieval of atmospheric water vapor, cloud liquid water path, surface temperature and emissivities over land from satellite microwave observations, Journal of Geophysical Research, 2000. 2000.

Alsdorf, D. E.: Water storage of the central Amazon floodplain measured with GIS and remote sensing imagery, Annals of the Association of American Geographers, 93, 55-66, 2003.

Alsdorf, D. E., Rodríguez, E., and Lettenmaier, D. P.: Measuring surface water from space, Reviews of Geophysics, 45, 2007.

Alsdorf, D. E., Smith, L. C., and Melack, J. M.: Amazon floodplain water level changes measured with interferometric SIR-C radar, Geoscience and Remote Sensing, IEEE Transactions on, 39, 423-431, 2001.

Armstrong, R., Knowles, K., Brodzik, M., and Hardman, M. A.: DMSP SSM/I-SSMIS Pathfinder Daily EASE-Grid Brightness Temperatures. Version 2. Boulder, Colorado USA: NASA DAAC at the National Snow and Ice Data Center, 1998.

Babyak, M. A.: What you see may not be what you get: a brief, nontechnical introduction to overfitting in regression-type models, Psychosomatic medicine, 66, 411-421, 2004.

Barton, I. J. and Bathols, J. M.: Monitoring floods with AVHRR, Remote sensing of Environment, 30, 89-94, 1989.

Basist, A., Grody, N. C., Peterson, T. C., and Williams, C. N.: Using the Special Sensor Microwave/Imager to monitor land surface temperatures, wetness, and snow cover, Journal of Applied Meteorology, 37, 888-911, 1998.

Basist, A., Williams Jr, C., Ross, T. F., Menne, M. J., Grody, N., Ferraro, R., Shen, S., and Chang, A. T.: Using the Special Sensor Microwave Imager to monitor surface wetness, Journal of Hydrometeorology, 2, 297-308, 2001.

Bates, P. D., Neal, J. C., Alsdorf, D., and Schumann, G. J.-P.: Observing global surface water flood dynamics, Surveys in Geophysics, 35, 839-852, 2014.

Behrangi, A., Guan, B., Neiman, P. J., Schreier, M., and Lambrigtsen, B.: On the Quantification of Atmospheric Rivers Precipitation from Space: Composite Assessments and Case Studies over the Eastern North Pacific Ocean and the Western United States, Journal of Hydrometeorology, 17, 369-382, 2016.

Beven, K. and Kirkby, M.: A physically based, variable contributing area model of basin hydrology/Un modèle à base physique de zone d'appel variable de l'hydrologie du bassin versant, Hydrological Sciences Journal, 24, 43-69, 1979.

Beven, K., Kirkby, M., Schofield, N., and Tagg, A.: Testing a physically-based flood forecasting model (TOPMODEL) for three UK catchments, Journal of Hydrology, 69, 119-143, 1984.

Biggin, D.: A comparison of ERS-1 satellite radar and aerial photography for river flood mapping, Water and Environment Journal, 10, 59-64, 1996.

Bjerklie, D. M., Dingman, S. L., Vorosmarty, C. J., Bolster, C. H., and Congalton, R. G.: Evaluating the potential for measuring river discharge from space, Journal of Hydrology, 278, 17-38, 2003.

Björck, A.: Numerical methods for least squares problems, Siam, 1996.

Boukabara, S.-A., Garrett, K., and Chen, W.: Global coverage of total precipitable water using a microwave variational algorithm, Ieee T Geosci Remote, 48, 3608-3621, 2010.

Brakenridge, G. R., Nghiem, S. V., Anderson, E., and Chien, S.: Space-based measurement of river runoff, EOS: Transactions of the American Geophysical Union, 86, 185-192, 2005.

Brakenridge, G. R., Nghiem, S. V., Anderson, E., and Mic, R.: Orbital microwave measurement of river discharge and ice status, Water Resources Research, 43, 2007.

Brodzik, M. and Knowles, K.: EASE-Grid: A Versatile Set of Equal-Area Prjoections and Grids, National Center for Geographic Information & Analysis, Santa Barbara, California USA, 2002.

Calvet, J. C., Wigneron, J. P., Chanzy, A., Raju, S., and Laguerre, L.: Microwave Dielectric-Properties of a Silt-Loam at High-Frequencies, Ieee T Geosci Remote, 33, 634-642, 1995.

Carlson, T. N. and Ripley, D. A.: On the relation between NDVI, fractional vegetation cover, and leaf area index, Remote sensing of Environment, 62, 241-252, 1997.

Chai, L., Wang, Z., Wang, Y., Yang, Z., Wang, H., and Wu, X.: Ingestion risks of metals in groundwater based on TIN model and dose-response assessment—A case study in the Xiangjiang watershed, central-south China, Science of the Total Environment, 408, 3118-3124, 2010.

Chappell, N. A., Jones, T. D., Tych, W., and Krishnaswamy, J.: Role of rainstorm intensity underestimated by data-derived flood models: emerging global evidence from subsurface-dominated watersheds, Environmental Modelling & Software, 88, 1-9, 2017.

Chen, Y., Huang, C., Ticehurst, C., Merrin, L., and Thew, P.: An evaluation of MODIS daily and 8-day composite products for floodplain and wetland inundation mapping, Wetlands, 33, 823-835, 2013.

Chen, Y., Yang, K., He, J., Qin, J., Shi, J., Du, J., and He, Q.: Improving land surface temperature modeling for dry land of China, Journal of Geophysical Research: Atmospheres (1984–2012), 116, 2011.

Choudhury, B. J.: Monitoring global land surface using Nimbus-7 37 GHz data. Theory and examples, International Journal of Remote Sensing, 10, 1579-1605, 1989.

Choudhury, B. J.: Passive microwave remote sensing contribution to hydrological variables. In: Land surface-atmosphere interactions for climate modeling, Springer, Dordrecht, The Netherlands, 1991.

Choudhury, B. J., Major, E. R., Smith, E. A., and Becker, F.: Atmospheric effects on SMMR and SSM/I 37 GHz polarization difference over the Sahel, International Journal of Remote Sensing, 13, 3443-3463, 1992.

Choudhury, B. J., Schmugge, T. J., Chang, A., and Newton, R. W.: Effect of surface roughness on the microwave emission from soils, Journal of Geophysical Research, 89, 5699-5706, 1979.

Choudhury, B. J. and Tucker, C. J.: Monitoring global vegetation using Nimbus-7 37 GHz data. Some empirical relations, International Journal of Remote Sensing, 8, 1085-1090, 1987.

Choudhury, B. J., Wang, J. R., Hsu, A. Y., and Chien, Y. L.: Simulated and observed 37GHz emission over Africa, International Journal of Remote Sensing, 11, 1837-1868, 1990.

Chunguo, C. and Zihui, L.: Chemical speciation and distribution of arsenic in water, suspended solids and sediment of Xiangjiang River, China, Science of the total environment, 77, 69-82, 1988.

Cooley, J. W., Lewis, P. A., and Welch, P. D.: Application of the fast Fourier transform to computation of Fourier integrals, Fourier series, and convolution integrals, Audio and Electroacoustics, IEEE Transactions on, 15, 79-84, 1967.

Cooley, J. W. and Tukey, J. W.: An algorithm for the machine calculation of complex Fourier series, Mathematics of computation, 19, 297-301, 1965.

Crow, W. and Ryu, D.: A new data assimilation approach for improving runoff prediction using remotely-sensed soil moisture retrievals, Hydrol Earth Syst Sc, 13, 1-16, 2009.

Czekala, H., Havemann, S., Schmidt, K., Rother, T., and Simmer, C.: Comparison of microwave radiative transfer calculations obtained with three different approximations of hydrometeor shape, Journal of Quantitative Spectroscopy and Radiative Transfer, 63, 545-558, 1999.

D'Odorico, P. and Rodríguez-Iturbe, I.: Space-time self-organization of mesoscale rainfall and soil moisture, Advances in water resources, 23, 349-357, 2000.

De Ridder, K.: Quantitative estimation of skin soil moisture with the special sensor microwave/imager, Boundary-Layer Meteorology, 96, 421-432, 2000.

Deshmukh, K. and Shinde, G.: An adaptive color image segmentation, ELCVIA Electronic Letters on Computer Vision and Image Analysis, 5, 12-23, 2005.

Dobson, M. C., Ulaby, F. T., Hallikainen, M. T., and Elrayes, M. A.: Microwave Dielectric Behavior of Wet Soil .2. Dielectric Mixing Models, Ieee T Geosci Remote, 23, 35-46, 1985.

Donohue, R., Roderick, M., and McVicar, T.: On the importance of including vegetation dynamics in Budyko's hydrological model, Hydrology and Earth System Sciences Discussions, 11, 983-995, 2007.

Dronova, I., Gong, P., and Wang, L.: Object-based analysis and change detection of major wetland cover types and their classification uncertainty during the low water period at Poyang Lake, China, Remote Sensing of Environment, 115, 3220-3236, 2011.

Eagleson, P. S.: Climate, soil, and vegetation: 1. Introduction to water balance dynamics, Water Resources Research, 14, 705-712, 1978.

Entin, J. K., Robock, A., Vinnikov, K. Y., Hollinger, S. E., Liu, S., and Namkhai, A.: Temporal and spatial scales of observed soil moisture variations in the extratropics, J Geophys Res, 105, 11865-11877, 2000.

Feng, L., Hu, C., Chen, X., Cai, X., Tian, L., and Gan, W.: Assessment of inundation changes of Poyang Lake using MODIS observations between 2000 and 2010, Remote Sensing of Environment, 121, 80-92, 2012a.

Feng, L., Hu, C., Chen, X., Tian, L., and Chen, L.: Human induced turbidity changes in Poyang Lake between 2000 and 2010: Observations from MODIS, Journal of Geophysical Research: Oceans, 117, 2012b.

Ferraro, R. R. and Marks, G. F.: The Development of SSM/I Rain-Rate Retrieval Algorithms Using Ground-Based Radar Measurements, Journal of Atmospheric and Oceanic Technology, 12, 755-770, 1995.

Fily, M., Royer, A., Goïta, K., and Prigent, C.: A simple retrieval method for land surface temperature and fraction of water surface determination from satellite microwave brightness temperatures in sub-arctic areas, Remote Sensing of Environment, 85, 328-338, 2003.

Frappart, F., Seyler, F., Martinez, J.-M., Leon, J. G., and Cazenave, A.: Floodplain water storage in the Negro River basin estimated from microwave remote sensing of inundation area and water levels, Remote Sensing of Environment, 99, 387-399, 2005.

Gao, H. L., Wood, E. F., Drusch, M., Crow, W., and Jackson, T. J.: Using a microwave emission model to estimate soil moisture from ESTAR observations during SGP99, Journal of Hydrometeorology, 5, 49-63, 2004.

Gerek, Ö. N. and Yardimci, Y.: Equiripple FIR filter design by the FFT algorithm, Signal Processing Magazine, IEEE, 14, 60-64, 1997.

Giddings, L. and Choudhury, B. J.: Observation of hydrological features with Nimbus-7 37 GHz data, applied to South America, International Journal of Remote Sensing, 10, 1673-1686, 1989.

Gleason, C. J. and Smith, L. C.: Toward global mapping of river discharge using satellite images and at-many-stations hydraulic geometry, Proceedings of the National Academy of Sciences, 111, 4788-4791, 2014.

Gleick, P. H.: The development and testing of a water balance model for climate impact assessment: modeling the Sacramento basin, Water Resources Research, 23, 1049-1061, 1987.

Goel, M., Jain, S. K., and Agarwal, P.: Assessment of sediment deposition rate in Bargi Reservoir using digital image processing, Hydrological sciences journal, 47, S81-S92, 2002.

Guerschman, J. P., Warren, G., Byrne, G., Lymburner, L., Mueller, N., and Van Dijk, A. I.: MODIS-based standing water detection for flood and large reservoir mapping: algorithm development and applications for the Australian continent, CSIRO Canberra, Australia, 2011.

Guo, H., Hu, Q., and Jiang, T.: Annual and seasonal streamflow responses to climate and land-cover changes in the Poyang Lake basin, China, Journal of Hydrology, 355, 106-122, 2008.

Guo, H., Hu, Q., and Zhang, Q.: Changes in hydrological interactions of the Yangtze River and the Poyang Lake in China during 1957–2008, Acta Geographica Sinica, 66, 609-618, 2011.

Guo, H., Hu, Q., Zhang, Q., and Feng, S.: Effects of the three gorges dam on Yangtze river flow and river interaction with Poyang Lake, China: 2003–2008, Journal of Hydrology, 416, 19-27, 2012.

Gupta, H. V., Sorooshian, S., and Yapo, P. O.: Status of automatic calibration for hydrologic models: Comparison with multilevel expert calibration, Journal of Hydrologic Engineering, 4, 135-143, 1999.

Gutman, G. and Ignatov, A.: The derivation of the green vegetation fraction from NOAA/AVHRR data for use in numerical weather prediction models, International Journal of remote sensing, 19, 1533-1543, 1998.

Hamilton, S. K., Sippel, S. J., and Melack, J. M.: Comparison of inundation patterns among major South American floodplains, Journal of Geophysical Research D: Atmospheres, 107, 1-14, 2002.

Hamilton, S. K., Sippel, S. J., and Melack, J. M.: Inundation patterns in the Pantanal wetland of South America determined from passive microwave remote sensing, Archiv fur Hydrobiologie, 137, 1-23, 1996.

Hamilton, S. K., Sippel, S. J., and Melack, J. M.: Seasonal inundation patterns in two large savanna floodplains of South America: The Llanos de Moxos (Bolivia) and the Llanos del Orinoco (Venezuela and Colombia), Hydrological Processes, 18, 2103-2116, 2004.

Harris, F. J.: On the use of windows for harmonic analysis with the discrete Fourier transform, Proceedings of the IEEE, 66, 51-83, 1978.

Hawkins, D. M.: The problem of overfitting, Journal of chemical information and computer sciences, 44, 1-12, 2004.

Hayashi, M., van der Kamp, G., and Rudolph, D. L.: Water and solute transfer between a prairie wetland and adjacent uplands, 1. Water balance, Journal of Hydrology, 207, 42-55, 1998.

Hess, L. L., Melack, J. M., Filoso, S., and Wang, Y.: Delineation of inundated area and vegetation along the Amazon floodplain with the SIR-C synthetic aperture radar, Geoscience and Remote Sensing, IEEE Transactions on, 33, 896-904, 1995.

Hess, L. L., Melack, J. M., Novo, E. M., Barbosa, C. C., and Gastil, M.: Dual-season mapping of wetland inundation and vegetation for the central Amazon basin, Remote Sensing of Environment, 87, 404-428, 2003.

Hollinger, J. P., Peirce, J. L., and Poe, G. A.: SSM/I instrument evaluation, Ieee T Geosci Remote, 28, 781-790, 1990.

Holmes, T. R. H., De Jeu, R. A. M., Owe, M., and Dolman, A. J.: Land surface temperature from Ka band (37 GHz) passive microwave observations, J Geophys Res-Atmos, 114, 2009.

Horritt, M., Mason, D., and Luckman, A.: Flood boundary delineation from synthetic aperture radar imagery using a statistical active contour model, International Journal of Remote Sensing, 22, 2489-2507, 2001.

Hostache, R., Matgen, P., Schumann, G., Puech, C., Hoffmann, L., and Pfister, L.: Water level estimation and reduction of hydraulic model calibration uncertainties using satellite SAR images of floods, Geoscience and Remote Sensing, IEEE Transactions on, 47, 431-441, 2009.

Houweling, S., Kaminski, T., Dentener, F., Lelieveld, J., and Heimann, M.: Inverse modeling of methane sources and sinks using the adjoint of a global transport model, Journal of Geophysical Research: Atmospheres, 104, 26137-26160, 1999.

Hu, Q., Feng, S., Guo, H., Chen, G., and Jiang, T.: Interactions of the Yangtze river flow and hydrologic processes of the Poyang Lake, China, Journal of Hydrology, 347, 90-100, 2007.

Huber, C., Li, J., Daillet, S., Chen, X., Xijun, L., Francois, C. J., Wei, Z., Carlos, U., Mathias, S., Shifeng, H., Stephane, A., Burnham, J., and Yesou, H.: Twelve year of water resource monitoring over Yangtze middle reaches exploiting DRAGON time series and field measurments, DRAGON II symposium, Beijing, 2012.

Huffman, G. J., Bolvin, D. T., Nelkin, E. J., Wolff, D. B., Adler, R. F., Gu, G., Hong, Y., Bowman, K. P., and Stocker, E. F.: The TRMM multisatellite precipitation analysis (TMPA): Quasi-global, multiyear, combined-sensor precipitation estimates at fine scales, Journal of Hydrometeorology, 8, 38-55, 2007.

Irons, J. R. and Petersen, G. W.: Texture transforms of remote sensing data, Remote Sensing of Environment, 11, 359-370, 1981.

Islam, A., Bala, S., and Haque, M.: Flood inundation map of Bangladesh using MODIS time-series images, Journal of Flood Risk Management, 3, 210-222, 2010.

Jain, S. K., Singh, P., and Seth, S.: Assessment of sedimentation in Bhakra Reservoir in the western Himalayan region using remotely sensed data, Hydrological sciences journal, 47, 203-212, 2002.

Jakeman, A. and Hornberger, G.: How much complexity is warranted in a rainfall-runoff model?, Water resources research, 29, 2637-2649, 1993.

Jakeman, A., Littlewood, I., and Whitehead, P.: Computation of the instantaneous unit hydrograph and identifiable component flows with application to two small upland catchments, Journal of hydrology, 117, 275-300, 1990.

Jia, L., Shang, H., Hu, G., and Menenti, M.: Phenological response of vegetation to upstream river flow in the Heihe Rive basin by time series analysis of MODIS data, Hydrol Earth Syst Sc, 15, 1047-1064, 2011.

Jin, Y.: A flooding index and its regional threshold value for monitoring floods in China from SSM/I data, International Journal of Remote Sensing, 20, 1025-1030, 1999.

Kawanishi, T., Sezai, T., Ito, Y., Imaoka, K., Takeshima, T., Ishido, Y., Shibata, A., Miura, M., Inahata, H., and Spencer, R. W.: The Advanced Microwave Scanning Radiometer for the Earth Observing System (AMSR-E), NASDA's contribution to the EOS for global energy and water cycle studies, Ieee T Geosci Remote, 41, 184-194, 2003.

Kazezyılmaz-Alhan, C. M., Medina, M. A., and Richardson, C. J.: A wetland hydrology and water quality model incorporating surface water/groundwater interactions, Water Resources Research, 43, 2007.

Keogh, E., Chakrabarti, K., Pazzani, M., and Mehrotra, S.: Dimensionality reduction for fast similarity search in large time series databases, Knowledge and information Systems, 3, 263-286, 2001.

Kerr, Y. H., Waldteufel, P., Wigneron, J.-P., Martinuzzi, J., Font, J., and Berger, M.: Soil moisture retrieval from space: The Soil Moisture and Ocean Salinity (SMOS) mission, Ieee T Geosci Remote, 39, 1729-1735, 2001.

Kirdiashev, K. P., Chucklantsev, A. A., and Shutko, A.: Microwave radiation of the earth's surface in the presence of vegetation cover, Radiotecknica, 24, 256-264, 1979.

Knowles, K., Savoie, M., Armstrong, R., and Brodzik, M.: AMSR-E/Aqua Daily EASE-Grid Brightness Temperatures, NASA DAAC at the National Snow and Ice Data Center, Boulder, Colorado USA, 2006.

Kummerow, C., Olson, W. S., and Giglio, L.: A simplified scheme for obtaining precipitation and vertical hydrometeor profiles from passive microwave sensors, Geoscience and Remote Sensing, IEEE Transactions on, 34, 1213-1232, 1996.

Lakshmi, V., Wood, E. F., and Choudhury, B. J.: Evaluation of Special Sensor Microwave/Imager satellite data for regional soil moisture estimation over the Red River basin, Journal of Applied Meteorology, 36, 1309-1328, 1997a.

Lakshmi, V., Wood, E. F., and Choudhury, B. J.: A soil-canopy-atmosphere model for use in satellite microwave remote sensing, Journal of Geophysical Research D: Atmospheres, 102, 6911-6927, 1997b.

Lane, J. and Saxton, J.: Dielectric dispersion in pure polar liquids at very high radio frequencies. III. The effect of electrolytes in solution, 1952, 531-545.

Lawson, C. L. and Hanson, R. J.: Solving least squares problems, SIAM, 1974.

Lee, J.-S., Papathanassiou, K. P., Ainsworth, T. L., Grunes, M. R., and Reigber, A.: A new technique for noise filtering of SAR interferometric phase images, Geoscience and Remote Sensing, IEEE Transactions on, 36, 1456-1465, 1998.

Li, F., Huang, J., Zeng, G., Yuan, X., Li, X., Liang, J., Wang, X., Tang, X., and Bai, B.: Spatial risk assessment and sources identification of heavy metals in surface sediments from the Dongting Lake, Middle China, Journal of Geochemical Exploration, 132, 75-83, 2013.

Li, P., Feng, Z., Jiang, L., Liu, Y., and Xiao, X.: Changes in rice cropping systems in the Poyang Lake Region, China during 2004–2010, Journal of Geographical Sciences, 22, 653-668, 2012.

Liang, X., Lettenmaier, D. P., Wood, E. F., and Burges, S. J.: A simple hydrologically based model of land surface water and energy fluxes for general circulation models, JOURNAL OF GEOPHYSICAL RESEARCH-ALL SERIES-, 99, 14,415-414,415, 1994.

Liebe, H. J., Hufford, G. A., and Manabe, T.: A model for the complex permittivity of water at frequencies below 1 THz, International Journal of Infrared and Millimeter Waves, 12, 659-675, 1991.

Lin, C. and Lu, J.: Studies on the anomaly of Plum Rain and flood disaster in the Yangtze River valley, J. Najing University, 1991. 76-83, 1991.

Lin, R., King-lp, A., and Shim, H. S. S. K.: Fast similarity search in the presence of noise, scaling, and translation in time-series databases, Zurich, Switzerland, 9 - 13 September 1995, 490-501.

Madsen, H.: Automatic calibration of a conceptual rainfall–runoff model using multiple objectives, Journal of hydrology, 235, 276-288, 2000.

Manabe, T., Liebe, H., and Hufford, G.: Complex permittivity of water between 0 and 30 THz, 1987, 229-230.

Matthews, E. and Fung, I.: Methane emission from natural wetlands: Global distribution, area, and environmental characteristics of sources, Global biogeochemical cycles, 1, 61-86, 1987.

Matthews, E., Fung, I., and Lerner, J.: Methane emission from rice cultivation: Geographic and seasonal distribution of cultivated areas and emissions, Global Biogeochemical Cycles, 5, 3-24, 1991.

Mätzler, C.: Thermal microwave radiation: applications for remote sensing, Iet, 2006.

McFeeters, S.: The use of the Normalized Difference Water Index (NDWI) in the delineation of open water features, International journal of remote sensing, 17, 1425-1432, 1996.

Menenti, M., Azzali, S., Verhoef, W., and van Swol, R.: Mapping agroecological zones and time lag in vegetation growth by means of fourier analysis of time series of NDVI images, Advances in Space Research, 13, 233-237, 1993.

Mertes, L. A.: Documentation and significance of the perirheic zone on inundated floodplains, Water Resources Research, 33, 1749-1762, 1997.

Mialon, A., Royer, A., and Fily, M.: Wetland seasonal dynamics and interannual variability over northern high latitudes, derived from microwave satellite data, Journal of Geophysical Research: Atmospheres, 110, 2005.

Miller, M. W. and Nudds, T. D.: Prairie landscape change and flooding in the Mississippi River Valley, Conservation Biology, 1996. 847-853, 1996.

Mo, T. and Schmugge, T. J.: A parameterization of the effect of surface roughness on microwave emission, Geoscience and Remote Sensing, IEEE Transactions on, 1987. 481-486, 1987.

Montandon, L. and Small, E.: The impact of soil reflectance on the quantification of the green vegetation fraction from NDVI, Remote Sensing of Environment, 112, 1835-1845, 2008.

Moore, R.: The PDM rainfall-runoff model, Hydrology and Earth System Sciences Discussions, 11, 483-499, 2007.

Moore, R.: The probability-distributed principle and runoff production at point and basin scales, Hydrological Sciences Journal, 30, 273-297, 1985.

Mörchen, F.: Time series feature extraction for data mining using DWT and DFT. Univ. of Marburg, Germany, 2003.

Nash, J. E. and Sutcliffe, J. V.: River flow forecasting through conceptual models part I — A discussion of principles, Journal of Hydrology, 10, 282-290, 1970.

Nerem, R., Chambers, D., Leuliette, E., Mitchum, G., and Giese, B.: Variations in global mean sea level associated with the 1997–1998 ENSO event: Implications for measuring long term sea level change, Geophys Res Lett, 26, 3005-3008, 1999.

Njoku, E. G., Jackson, T. J., Lakshmi, V., Chan, T. K., and Nghiem, S. V.: Soil moisture retrieval from AMSR-E, Ieee T Geosci Remote, 41, 215-229, 2003.

O'Neill, P. E., Jackson, T. J., Chauhan, N. S., and Seyfried, M. S.: Microwave soil moisture estimation in humid and semiarid watersheds, Advances in Space Research, 13, 115-118, 1993.

Oberstadler, R., Hönsch, H., and Huth, D.: Assessment of the mapping capabilities of ERS-1 SAR data for flood mapping: a case study in Germany, Hydrological processes, 11, 1415-1425, 1997.

Otsu, N.: A threshold selection method from gray-level histograms, Automatica, 11, 23-27, 1975.

Owe, M., de Jeu, R., and Walker, J.: A methodology for surface soil moisture and vegetation optical depth retrieval using the microwave polarization difference index, Geoscience and Remote Sensing, IEEE Transactions on, 39, 1643-1654, 2001.

Paiva, R. C., Durand, M. T., and Hossain, F.: Spatiotemporal interpolation of discharge across a river network by using synthetic SWOT satellite data, Water Resources Research, 51, 430-449, 2015.

Paloscia, S., Macelloni, G., Santi, E., and Koike, T.: A multifrequency algorithm for the retrieval of soil moisture on a large scale using microwave data from SMMR and SSM/I satellites, Ieee T Geosci Remote, 39, 1655-1661, 2001.

Pampaloni, P. and Paloscia, S.: Experimental relationships between microwave emission and vegetation features†, International Journal of Remote Sensing, 6, 315-323, 1985.

Pan, F., Liao, J., Li, X., and Guo, H.: Application of the inundation area—lake level rating curves constructed from the SRTM DEM to retrieving lake levels from satellite measured inundation areas, Computers & Geosciences, 52, 168-176, 2013.

Papa, F., Prigent, C., Durand, F., and Rossow, W. B.: Wetland dynamics using a suite of satellite observations: A case study of application and evaluation for the Indian Subcontinent, Geophys Res Lett, 33, 2006.

Peng, D., Guo, S., Liu, P., and Liu, T.: Reservoir storage curve estimation based on remote sensing data, Journal of hydrologic engineering, 11, 165-172, 2006.

Podest, E. and Saatchi, S.: Application of multiscale texture in classifying JERS-1 radar data over tropical vegetation, International Journal of Remote Sensing, 23, 1487-1506, 2002.

Poe, G. A.: Optimum Interpolation of Imaging Microwave Radiometer Data, Ieee T Geosci Remote, 28, 800-810, 1990.

Poe, G. A. and Conway, R. W.: A study of the geolocation errors of the Special Sensor Microwave/Imager (SSM/I), Ieee T Geosci Remote, 28, 791-799, 1990.

Prigent, C., Aires, F., Rossow, W., and Matthews, E.: Joint characterization of vegetation by satellite observations from visible to microwave wavelengths: A sensitivity analysis, Journal of Geophysical Research: Atmospheres, 106, 20665 - 20685, 2001a.

Prigent, C., Matthews, E., Aires, F., and Rossow, W. B.: Remote sensing of global wetland dynamics with multiple satellite data sets, Geophys Res Lett, 28, 4631-4634, 2001b.

Prigent, C., Papa, F., Aires, F., Rossow, W., and Matthews, E.: Global inundation dynamics inferred from multiple satellite observations, 1993–2000, Journal of Geophysical Research: Atmospheres, 112, 2007.

Prigent, C., Rossow, W. B., and Matthews, E.: Microwave land surface emissivities estimated from SSM/I observations, Journal of Geophysical Research: Atmospheres, 102, 21867-21890, 1997.

Project, B. M., Erdélyi, A., and Bateman, H.: Tables of Integral Transforms: Based in Part on Notes Left by Harry Bateman and Compiled by the Staff of the Bateman Manuscript Project, McGraw-Hill, New York, NY, USA, 1954.

Pulvirenti, L., Chini, M., Pierdicca, N., Guerriero, L., and Ferrazzoli, P.: Flood monitoring using multi-temporal COSMO-SkyMed data: Image segmentation and signature interpretation, Remote Sensing of Environment, 115, 990-1002, 2011.

Rasid, H. and Pramanik, M.: Visual interpretation of satellite imagery for monitoring floods in Bangladesh, Environmental Management, 14, 815-821, 1990.

Reale, A., Chalfant, M., Allegrino, A., Tiley, F., Gerguson, M., and Pettey, M.: Advanced-TOVS (ATOVS) sounding products from NOAA polar orbiting environmental satellites, 2003.

Richards, F. and Arkin, P.: On the relationship between satellite-observed cloud cover and precipitation, Monthly Weather Review, 109, 1081-1093, 1981.

Ritter, A. and Muñoz-Carpena, R.: Performance evaluation of hydrological models: Statistical significance for reducing subjectivity in goodness-of-fit assessments, Journal of Hydrology, 480, 33-45, 2013.

Roerink, G. J., Menenti, M., Soepboer, W., and Su, Z.: Assessment of climate impact on vegetation dynamics by using remote sensing, Physics and Chemistry of the Earth, Parts A/B/C, 28, 103-109, 2003.

Roerink, G. J., Menenti, M., and Verhoef, W.: Reconstructing cloudfree NDVI composites using Fourier analysis of time series, International Journal of Remote Sensing, 21, 1911-1917, 2000.

Rossow, W. B. and Schiffer, R. A.: Advances in understanding clouds from ISCCP, Bulletin of the American Meteorological Society, 80, 2261, 1999.

Sakamoto, T., Van Nguyen, N., Kotera, A., Ohno, H., Ishitsuka, N., and Yokozawa, M.: Detecting temporal changes in the extent of annual flooding within the Cambodia and the Vietnamese Mekong Delta from MODIS time-series imagery, Remote sensing of environment, 109, 295-313, 2007.

Schumann, G., Di Baldassarre, G., and Bates, P. D.: The utility of spaceborne radar to render flood inundation maps based on multialgorithm ensembles, Geoscience and Remote Sensing, IEEE Transactions on, 47, 2801-2807, 2009.

Schumann, G. J.-P. and Moller, D. K.: Microwave remote sensing of flood inundation, Physics and Chemistry of the Earth, Parts A/B/C, 83, 84-95, 2015.

Shang, H., Jia, J., and Menenti, M.: Analyzing the Inundation Pattern of the Poyang Lake floodplain by Passive Microwave Data, Journal of Hydrometeorology, 16, 652-667, 2015.

Shang, H., Jia, J., and Menenti, M.: Modeling and Reconstruction of Time Series of Passive Microwave Data by Discrete Fourier Transform Guided Filtering and Harmonic Analysis, Remote Sensing, 08, 970, 2016.

Shankman, D., Keim, B. D., and Song, J.: Flood frequency in China's Poyang Lake region: trends and teleconnections, International Journal of Climatology, 26, 1255-1266, 2006.

Sheng, Y., Gong, P., and Xiao, Q.: Quantitative dynamic flood monitoring with NOAA AVHRR, International Journal of Remote Sensing, 22, 1709-1724, 2001.

Sheng, Y., Su, Y., and Xiao, Q.: Challenging the cloud-contamination problem in flood monitoring with NOAA/AVHRR imagery, Photogrammetric Engineering and Remote Sensing, 64, 191-198, 1998.

Shi, J. C., Jackson, T., Tao, J., Du, J., Bindlish, R., Lu, L., and Chen, K. S.: Microwave vegetation indices for short vegetation covers from satellite passive microwave sensor AMSR-E, Remote Sensing of Environment, 112, 4285-4300, 2008.

Shi, J. C., Jiang, L. M., Zhang, L. X., Chen, K. S., Wigneron, J. P., and Chanzy, A.: A parameterized multifrequency-polarization surface emission model, Ieee T Geosci Remote, 43, 2831-2841, 2005.

Shjeflo, J. B.: Evapotranspiration and the water budget of prairie potholes in North Dakota, US Government Printing Office, 1968.

Singleton, R. C.: An algorithm for computing the mixed radix fast Fourier transform, Audio and Electroacoustics, IEEE Transactions on, 17, 93-103, 1969.

Sippel, S. J., Hamilton, S. K., Melack, J. M., and Choudhury, B. J.: Determination of inundation area in the Amazon River floodplain using the SMMR 37 GHz polarization difference, Remote Sensing of Environment, 48, 70-76, 1994.

Sippel, S. J., Hamilton, S. K., Melack, J. M., and Novo, E. M. M.: Passive microwave observations of inundation area and the area/stage relation in the Amazon River floodplain, International Journal of Remote Sensing, 19, 3055-3074, 1998.

Sivapalan, M., Beven, K., and Wood, E. F.: On hydrologic similarity: 2. A scaled model of storm runoff production, Water Resources Research, 23, 2266-2278, 1987.

Skøien, J. O., Blöschl, G., and Western, A.: Characteristic space scales and timescales in hydrology, Water Resources Research, 39, 2003.

Smith, L. C.: Satellite remote sensing of river inundation area, stage, and discharge: A review, Hydrological processes, 11, 1427-1439, 1997.

Smith, L. C., Alsdorf, D. E., Magilligan, F. J., Gomez, B., Mertes, L. A., Smith, N. D., and Garvin, J. B.: Estimation of erosion, deposition, and net volumetric change caused by the 1996 Skeiðarársandur jökulhlaup, Iceland, from synthetic aperture radar interferometry, Water Resources Research, 36, 1583-1594, 2000.

Smith, L. C., Isacks, B. L., Bloom, A. L., and Murray, A. B.: Estimation of discharge from three braided rivers using synthetic aperture radar satellite imagery: Potential application to ungaged basins, Water Resources Research, 32, 2021-2034, 1996.

Smith, L. C. and Pavelsky, T. M.: Estimation of river discharge, propagation speed, and hydraulic geometry from space: Lena River, Siberia, Water Resources Research, 44, 2008.

Sophocleous, M.: Interactions between groundwater and surface water: the state of the science, Hydrogeology journal, 10, 52-67, 2002.

Su, M., Stolte, W., and Van der Kamp, G.: Modelling Canadian prairie wetland hydrology using a semi-distributed streamflow model, Hydrological Processes, 14, 2405-2422, 2000.

Tanaka, M., Sugimura, T., and Tanaka, S.: Cover. Monitoring water surface ratio in the Chinese floods of summer 1998 by DMSP-SSM/I, 2000. 2000.

Tanaka, M., Sugimura, T., Tanaka, S., and Tamai, N.: Flood–drought cycle of Tonle Sap and Mekong Delta area observed by DMSP-SSM/I, International Journal of Remote Sensing, 24, 1487-1504, 2003.

Temimi, M., Leconte, R., Brissette, F., and Chaouch, N.: Flood and soil wetness monitoring over the Mackenzie River Basin using AMSR-E 37 GHz brightness temperature, 25-29 July 2005 2005, 4 pp.

Thompson, A. R., Moran, J. M., and Swenson Jr, G. W.: Interferometry and synthesis in radio astronomy, John Wiley & Sons, Weinheim, Germany, 2008.

Todini, E.: The ARNO rainfall—runoff model, Journal of Hydrology, 175, 339-382, 1996.

Torbick, N., Salas, W., Xiao, X., Ingraham, P., Fearon, M., Biradar, C., Zhao, D., Liu, Y., Li, P., and Zhao, Y.: Integrating SAR and optical imagery for regional mapping of paddy rice attributes in the Poyang Lake Watershed, China, Canadian Journal of Remote Sensing, 37, 17-26, 2011.

Townsend, P. A.: Mapping seasonal flooding in forested wetlands using multi-temporal Radarsat SAR, Photogrammetric engineering and remote sensing, 67, 857-864, 2001.

Tsang, L., Blanchard, A. J., Newton, R. W., and Kong, J. A.: A simple relation between active and passive microwave remote sensing measurements of earth terrain, Geoscience and Remote Sensing, IEEE Transactions on, 1982. 482-485, 1982.

Ulaby, F. T., Moore, R. K., and Fung, A. K.: Microwave remote sensing : active and passive, Addison-Wesley Pub. Co., Advanced Book Program/World Science Division, Reading, Mass., 1981.

Usachev, V.: Evaluation of flood plain inundations by remote sensing methods, Hydrological Applications of Remote Sensing and Remote Data Transmission, 1983. 475-482, 1983.

Vachaud, G., Passerat de Silans, A., Balabanis, P., and Vauclin, M.: Temporal stability of spatially measured soil water probability density function, Soil Science Society of America Journal, 49, 822-828, 1985.

Vandegriend, A. A. and Owe, M.: Determination of Microwave Vegetation Optical Depth and Single Scattering Albedo from Large-Scale Soil-Moisture and Nimbus Smmr Satellite-Observations, International Journal of Remote Sensing, 14, 1875-1886, 1993.

Verdin, J.: Remote sensing of ephemeral water bodies in western Niger, International Journal of Remote Sensing, 17, 733-748, 1996.

Verhoef, W.: Application of Harmonic Analysis of NDVI Time Series (HANTS), In Fourier Analysis of Temporal NDVI in the Souther African and American Continents Wageningen, The Netherlands, 19-24, 1996.

Vinnikov, K. Y., Robock, A., Qiu, S., Entin, J. K., Owe, M., Choudhury, B. J., Hollinger, S. E., and Njoku, E. G.: Satellite remote sensing of soil moisture in Illinois, United States, Journal of Geophysical Research D: Atmospheres, 104, 4145-4168, 1999.

Vinnikov, K. Y., Robock, A., Speranskaya, N. A., and Schlosser, C. A.: Scales of temporal and spatial variability of midlatitude soil moisture, Journal of Geophysical Research: Atmospheres, 101, 7163-7174, 1996.

Vörösmarty, C. J., Moore, B., Grace, A. L., Gildea, M. P., Melillo, J. M., Peterson, B. J., Rastetter, E. B., and Steudler, P. A.: Continental scale models of water balance and fluvial transport: an application to South America, Global biogeochemical cycles, 3, 241-265, 1989.

Vörösmarty, C. J., Willmott, C. J., Choudhury, B. J., Schloss, A. L., Stearns, T. K., Robeson, S. M., and Dorman, T. J.: Analyzing the discharge regime of a large tropical river through remote sensing, ground-based climatic data, and modeling, Water Resources Research, 32, 3137-3150, 1996.

Walter, B. P., Heimann, M., and Matthews, E.: Modeling modern methane emissions from natural wetlands: 1. Model description and results, Journal of Geophysical Research: Atmospheres, 106, 34189-34206, 2001.

Wang, J. R. and Choudhury, B. J.: Remote sensing of soil moisture content over bare field at 1.4 GHz frequency, Journal of Geophysical Research, 86, 5277-5282, 1981.

Wang, J. R. and Schmugge, T. J.: An Empirical-Model for the Complex Dielectric Permittivity of Soils as a Function of Water-Content, Ieee T Geosci Remote, 18, 288-295, 1980.

Wang, Y., Hess, L. L., Filoso, S., and Melack, J. M.: Understanding the radar backscattering from flooded and nonflooded Amazonian forests: Results from canopy backscatter modeling, Remote Sensing of Environment, 54, 324-332, 1995.

Wang, Z., Chai, L., Wang, Y., Yang, Z., Wang, H., and Wu, X.: Potential health risk of arsenic and cadmium in groundwater near Xiangjiang River, China: a case study for risk assessment and management of toxic substances, Environmental monitoring and assessment, 175, 167-173, 2011.

Wen, J., Su, Z. B., and Ma, Y. M.: Determination of land surface temperature and soil moisture from Tropical Rainfall Measuring Mission/Microwave Imager remote sensing data, J Geophys Res-Atmos, 108, 2003.

Wentz, F. J.: Measurement of oceanic wind vector using satellite microwave radiometers, Ieee T Geosci Remote, 30, 960-972, 1992.

Wentz, F. J.: SSM/I Version-7 Calibration Report, Remote Sensing Systems, Santa Rosa, CA, 46pp pp., 2013.

Westerhoff, R., Kleuskens, M., Winsemius, H., Huizinga, H., Brakenridge, G., and Bishop, C.: Automated global water mapping based on wide-swath orbital synthetic-aperture radar, Hydrol. Earth Syst. Sci, 17, 651-663, 2013.

Wiesmann, A. and Mätzler, C.: Microwave emission model of layered snowpacks, Remote Sensing of Environment, 70, 307-316, 1999.

Wigneron, J.-P., Chanzy, A., Calvet, J.-C., and Bruguier, N.: A simple algorithm to retrieve soil moisture and vegetation biomass using passive microwave measurements over crop fields, Remote Sensing of Environment, 51, 331-341, 1995.

Wigneron, J. P., Kerr, Y., Chanzy, A., and Jin, Y. Q.: Inversion of surface parameters from passive microwave measurements over a soybean field, Remote Sensing of Environment, 46, 61-72, 1993.

Wilson, D. J., Western, A. W., and Grayson, R. B.: Identifying and quantifying sources of variability in temporal and spatial soil moisture observations, Water Resources Research, 40, 2004.

Winter, T. C. and Rosenberry, D. O.: The interaction of ground water with prairie pothole wetlands in the Cottonwood Lake area, east-central North Dakota, 1979–1990, Wetlands, 15, 193-211, 1995.

Winter, T. C. and Valk, A.: Hydrologic studies of wetlands in the northern prairie, Northern prairie wetlands., 1989. 16-54, 1989.

Woo, M.-K. and Rowsell, R. D.: Hydrology of a prairie slough, Journal of Hydrology, 146, 175-207, 1993.

Wood, E. F., Lettenmaier, D. P., and Zartarian, V. G.: A land-surface hydrology parameterization with subgrid variability for general circulation models, Journal of Geophysical Research: Atmospheres (1984–2012), 97, 2717-2728, 1992.

Wu, Y.-L., Agrawal, D., and El Abbadi, A.: A comparison of DFT and DWT based similarity search in time-series databases, McLean, VA, USA, 6 - 11 November 2000, 488-495.

Xiao, Q. and Chen, W.: Songhua River flood monitoring with meteorological satellite imagery, Remote Sensing Information, 4, 37-41, 1987.

Xu, C.-Y. and Singh, V. P.: Review on regional water resources assessment models under stationary and changing climate, Water Resources Management, 18, 591-612, 2004.

Xu, H.: Modification of normalised difference water index (NDWI) to enhance open water features in remotely sensed imagery, International Journal of Remote Sensing, 27, 3025-3033, 2006.

Yang, K., He, J., Tang, W., Qin, J., and Cheng, C. C.: On downward shortwave and longwave radiations over high altitude regions: Observation and modeling in the Tibetan Plateau, Agricultural and Forest Meteorology, 150, 38-46, 2010.

Ye, X., Zhang, Q., Bai, L., and Hu, Q.: A modeling study of catchment discharge to Poyang Lake under future climate in China, Quaternary International, 244, 221-229, 2011.

Ye, X., Zhang, Q., Liu, J., Li, X., and Xu, C.-y.: Distinguishing the relative impacts of climate change and human activities on variation of streamflow in the Poyang Lake catchment, China, Journal of Hydrology, 494, 83-95, 2013.

Yésou, H., Claire, H., Xijun, L., Stéphane, A., Jiren, L., Sylviane, D., Muriel, B.-N., Xiaoling, C., Shifeng, H., Burnham, J., Jean-François, C., Tiphanie, M., Jinggang, L., Rémi, A., and Carlos, U.: Nine years of water resources monitoring over the middle reaches of the Yangtze River, with ENVISAT, MODIS, Beijing-1 time series, Altimetric data and field measurements, Lakes & Reservoirs: Research & Management, 16, 231-247, 2011.

Yesou, H., Huber, C., Shifeng, H., Xijun, L., and Sylviane, D.-R.: Chinese lakes behaviours in the framework of the meteorology and water management practices: EO based monitoring lessons, the ESA Living Planet symposium, Edinburg, 2013.

Young, P.: Recursive estimation and time-series analysis: an introduction, 1984. 1984.

Zhang, L., Li, D., Tong, Q., and Zheng, L.: Study of the spectral mixture model of soil and vegetation in PoYang Lake area, China, International Journal of Remote Sensing, 19, 2077-2084, 1998.

Zhang, L., Yin, J., Jiang, Y., and Wang, H.: Relationship between the hydrological conditions and the distribution of vegetation communities within the Poyang Lake National Nature Reserve, China, Ecological Informatics, 11, 65-75, 2012.

Zhang, Q., Liu, C., Xu, C.-y., Xu, Y., and Jiang, T.: Observed trends of annual maximum water level and streamflow during past 130 years in the Yangtze River basin, China, Journal of Hydrology, 324, 255-265, 2006.

Zhang, Q., Liu, Y., Yang, G., and Zhang, Z.: Precipitation and hydrological variations and related associations with large-scale circulation in the Poyang Lake basin, China, Hydrological Processes, 25, 740-751, 2011.

Zhao, G., Hörmann, G., Fohrer, N., Zhang, Z., and Zhai, J.: Streamflow trends and climate variability impacts in Poyang Lake Basin, China, Water resources management, 24, 689-706, 2010.

Zhao, R.: Flood forecasting method for humid regions of China, East China College of Hydraulic Engineering, Nanjing, 1977. 19-51, 1977.

Zhao, R.: Watershed hydrological modelling, Water Resources and Electric Power Press, Beijing, 1984. 1984.

Zhou, Z.: Synoptic characteristics of atmoshperic cirulation during abnormal Plum Rain period in 1991, J. Nanjing University, 1991. 84-93, 1991.

Zong, Y. and Chen, X.: The 1998 flood on the Yangtze, China, Natural Hazards, 22, 165-184, 2000.

Agrawal, R., Faloutsos, C., and Swami, A.: Efficient similarity search in sequence databases, Springer, 1993.

Aires, F., Prigent, C., Rossow, W., Rothstein, M., and Hansen, J. E.: A new neural network approach including first-guess for retrieval of atmospheric water vapor, cloud liquid water path, surface temperature and emissivities over land from satellite microwave observations, Journal of Geophysical Research, 2000. 2000.

Alsdorf, D. E.: Water storage of the central Amazon floodplain measured with GIS and remote sensing imagery, Annals of the Association of American Geographers, 93, 55-66, 2003.

Alsdorf, D. E., Rodríguez, E., and Lettenmaier, D. P.: Measuring surface water from space, Reviews of Geophysics, 45, 2007.

Alsdorf, D. E., Smith, L. C., and Melack, J. M.: Amazon floodplain water level changes measured with interferometric SIR-C radar, Geoscience and Remote Sensing, IEEE Transactions on, 39, 423-431, 2001.

Armstrong, R., Knowles, K., Brodzik, M., and Hardman, M. A.: DMSP SSM/I-SSMIS Pathfinder Daily EASE-Grid Brightness Temperatures. Version 2. Boulder, Colorado USA: NASA DAAC at the National Snow and Ice Data Center, 1998.

Babyak, M. A.: What you see may not be what you get: a brief, nontechnical introduction to overfitting in regression-type models, Psychosomatic medicine, 66, 411-421, 2004.

Barton, I. J. and Bathols, J. M.: Monitoring floods with AVHRR, Remote sensing of Environment, 30, 89-94, 1989.

Basist, A., Grody, N. C., Peterson, T. C., and Williams, C. N.: Using the Special Sensor Microwave/Imager to monitor land surface temperatures, wetness, and snow cover, Journal of Applied Meteorology, 37, 888-911, 1998.

Basist, A., Williams Jr, C., Ross, T. F., Menne, M. J., Grody, N., Ferraro, R., Shen, S., and Chang, A. T.: Using the Special Sensor Microwave Imager to monitor surface wetness, Journal of Hydrometeorology, 2, 297-308, 2001.

Bates, P. D., Neal, J. C., Alsdorf, D., and Schumann, G. J.-P.: Observing global surface water flood dynamics, Surveys in Geophysics, 35, 839-852, 2014.

Behrangi, A., Guan, B., Neiman, P. J., Schreier, M., and Lambrigtsen, B.: On the Quantification of Atmospheric Rivers Precipitation from Space: Composite Assessments

and Case Studies over the Eastern North Pacific Ocean and the Western United States, Journal of Hydrometeorology, 17, 369-382, 2016.

Beven, K. and Kirkby, M.: A physically based, variable contributing area model of basin hydrology/Un modèle à base physique de zone d'appel variable de l'hydrologie du bassin versant, Hydrological Sciences Journal, 24, 43-69, 1979.

Beven, K., Kirkby, M., Schofield, N., and Tagg, A.: Testing a physically-based flood forecasting model (TOPMODEL) for three UK catchments, Journal of Hydrology, 69, 119-143, 1984.

Biggin, D.: A comparison of ERS-1 satellite radar and aerial photography for river flood mapping, Water and Environment Journal, 10, 59-64, 1996.

Bjerklie, D. M., Dingman, S. L., Vorosmarty, C. J., Bolster, C. H., and Congalton, R. G.: Evaluating the potential for measuring river discharge from space, Journal of Hydrology, 278, 17-38, 2003.

Björck, A.: Numerical methods for least squares problems, Siam, 1996.

Boukabara, S.-A., Garrett, K., and Chen, W.: Global coverage of total precipitable water using a microwave variational algorithm, Ieee T Geosci Remote, 48, 3608-3621, 2010.

Brakenridge, G. R., Nghiem, S. V., Anderson, E., and Chien, S.: Space-based measurement of river runoff, EOS: Transactions of the American Geophysical Union, 86, 185-192, 2005.

Brakenridge, G. R., Nghiem, S. V., Anderson, E., and Mic, R.: Orbital microwave measurement of river discharge and ice status, Water Resources Research, 43, 2007.

Brodzik, M. and Knowles, K.: EASE-Grid: A Versatile Set of Equal-Area Prjoections and Grids, National Center for Geographic Information & Analysis, Santa Barbara, California USA, 2002.

Calvet, J. C., Wigneron, J. P., Chanzy, A., Raju, S., and Laguerre, L.: Microwave Dielectric-Properties of a Silt-Loam at High-Frequencies, Ieee T Geosci Remote, 33, 634-642, 1995.

Carlson, T. N. and Ripley, D. A.: On the relation between NDVI, fractional vegetation cover, and leaf area index, Remote sensing of Environment, 62, 241-252, 1997.

Chai, L., Wang, Z., Wang, Y., Yang, Z., Wang, H., and Wu, X.: Ingestion risks of metals in groundwater based on TIN model and dose-response assessment—A case study in the Xiangjiang watershed, central-south China, Science of the Total Environment, 408, 3118-3124, 2010.

Chappell, N. A., Jones, T. D., Tych, W., and Krishnaswamy, J.: Role of rainstorm intensity underestimated by data-derived flood models: emerging global evidence from subsurface-dominated watersheds, Environmental Modelling & Software, 88, 1-9, 2017.

Chen, Y., Huang, C., Ticehurst, C., Merrin, L., and Thew, P.: An evaluation of MODIS daily and 8-day composite products for floodplain and wetland inundation mapping, Wetlands, 33, 823-835, 2013.

Chen, Y., Yang, K., He, J., Qin, J., Shi, J., Du, J., and He, Q.: Improving land surface temperature modeling for dry land of China, Journal of Geophysical Research: Atmospheres (1984–2012), 116, 2011.

Choudhury, B. J.: Monitoring global land surface using Nimbus-7 37 GHz data. Theory and examples, International Journal of Remote Sensing, 10, 1579-1605, 1989.

Choudhury, B. J.: Passive microwave remote sensing contribution to hydrological variables. In: Land surface-atmosphere interactions for climate modeling, Springer, Dordrecht, The Netherlands, 1991.

Choudhury, B. J., Major, E. R., Smith, E. A., and Becker, F.: Atmospheric effects on SMMR and SSM/I 37 GHz polarization difference over the Sahel, International Journal of Remote Sensing, 13, 3443-3463, 1992.

Choudhury, B. J., Schmugge, T. J., Chang, A., and Newton, R. W.: Effect of surface roughness on the microwave emission from soils, Journal of Geophysical Research, 89, 5699-5706, 1979.

Choudhury, B. J. and Tucker, C. J.: Monitoring global vegetation using Nimbus-7 37 GHz data. Some empirical relations, International Journal of Remote Sensing, 8, 1085-1090, 1987.

Choudhury, B. J., Wang, J. R., Hsu, A. Y., and Chien, Y. L.: Simulated and observed 37GHz emission over Africa, International Journal of Remote Sensing, 11, 1837-1868, 1990.

Chunguo, C. and Zihui, L.: Chemical speciation and distribution of arsenic in water, suspended solids and sediment of Xiangjiang River, China, Science of the total environment, 77, 69-82, 1988.

Cooley, J. W., Lewis, P. A., and Welch, P. D.: Application of the fast Fourier transform to computation of Fourier integrals, Fourier series, and convolution integrals, Audio and Electroacoustics, IEEE Transactions on, 15, 79-84, 1967.

Cooley, J. W. and Tukey, J. W.: An algorithm for the machine calculation of complex Fourier series, Mathematics of computation, 19, 297-301, 1965.

Crow, W. and Ryu, D.: A new data assimilation approach for improving runoff prediction using remotely-sensed soil moisture retrievals, Hydrol Earth Syst Sc, 13, 1-16, 2009.

D'Odorico, P. and Rodríguez-Iturbe, I.: Space-time self-organization of mesoscale rainfall and soil moisture, Advances in water resources, 23, 349-357, 2000.

De Ridder, K.: Quantitative estimation of skin soil moisture with the special sensor microwave/imager, Boundary-Layer Meteorology, 96, 421-432, 2000.

Deshmukh, K. and Shinde, G.: An adaptive color image segmentation, ELCVIA Electronic Letters on Computer Vision and Image Analysis, 5, 12-23, 2005.

Dobson, M. C., Ulaby, F. T., Hallikainen, M. T., and Elrayes, M. A.: Microwave Dielectric Behavior of Wet Soil .2. Dielectric Mixing Models, Ieee T Geosci Remote, 23, 35-46, 1985.

Donohue, R., Roderick, M., and McVicar, T.: On the importance of including vegetation dynamics in Budyko's hydrological model, Hydrology and Earth System Sciences Discussions, 11, 983-995, 2007.

Dronova, I., Gong, P., and Wang, L.: Object-based analysis and change detection of major wetland cover types and their classification uncertainty during the low water period at Poyang Lake, China, Remote Sensing of Environment, 115, 3220-3236, 2011.

Eagleson, P. S.: Climate, soil, and vegetation: 1. Introduction to water balance dynamics, Water Resources Research, 14, 705-712, 1978.

Entin, J. K., Robock, A., Vinnikov, K. Y., Hollinger, S. E., Liu, S., and Namkhai, A.: Temporal and spatial scales of observed soil moisture variations in the extratropics, J Geophys Res, 105, 11865-11877, 2000.

Feng, L., Hu, C., Chen, X., Cai, X., Tian, L., and Gan, W.: Assessment of inundation changes of Poyang Lake using MODIS observations between 2000 and 2010, Remote Sensing of Environment, 121, 80-92, 2012a.

Feng, L., Hu, C., Chen, X., Tian, L., and Chen, L.: Human induced turbidity changes in Poyang Lake between 2000 and 2010: Observations from MODIS, Journal of Geophysical Research: Oceans, 117, 2012b.

Ferraro, R. R. and Marks, G. F.: The Development of SSM/I Rain-Rate Retrieval Algorithms Using Ground-Based Radar Measurements, Journal of Atmospheric and Oceanic Technology, 12, 755-770, 1995.

Fily, M., Royer, A., Goıta, K., and Prigent, C.: A simple retrieval method for land surface temperature and fraction of water surface determination from satellite microwave brightness temperatures in sub-arctic areas, Remote Sensing of Environment, 85, 328-338, 2003.

Frappart, F., Seyler, F., Martinez, J.-M., Leon, J. G., and Cazenave, A.: Floodplain water storage in the Negro River basin estimated from microwave remote sensing of inundation area and water levels, Remote Sensing of Environment, 99, 387-399, 2005.

Gao, H. L., Wood, E. F., Drusch, M., Crow, W., and Jackson, T. J.: Using a microwave emission model to estimate soil moisture from ESTAR observations during SGP99, Journal of Hydrometeorology, 5, 49-63, 2004.

Gerek, Ö. N. and Yardimci, Y.: Equiripple FIR filter design by the FFT algorithm, Signal Processing Magazine, IEEE, 14, 60-64, 1997.

Giddings, L. and Choudhury, B. J.: Observation of hydrological features with Nimbus-7 37 GHz data, applied to South America, International Journal of Remote Sensing, 10, 1673-1686, 1989.

Gleason, C. J. and Smith, L. C.: Toward global mapping of river discharge using satellite images and at-many-stations hydraulic geometry, Proceedings of the National Academy of Sciences, 111, 4788-4791, 2014.

Gleick, P. H.: The development and testing of a water balance model for climate impact assessment: modeling the Sacramento basin, Water Resources Research, 23, 1049-1061, 1987.

Goel, M., Jain, S. K., and Agarwal, P.: Assessment of sediment deposition rate in Bargi Reservoir using digital image processing, Hydrological sciences journal, 47, S81-S92, 2002.

Guerschman, J. P., Warren, G., Byrne, G., Lymburner, L., Mueller, N., and Van Dijk, A. I.: MODIS-based standing water detection for flood and large reservoir mapping: algorithm development and applications for the Australian continent, CSIRO Canberra, Australia, 2011.

Guo, H., Hu, Q., and Jiang, T.: Annual and seasonal streamflow responses to climate and land-cover changes in the Poyang Lake basin, China, Journal of Hydrology, 355, 106-122, 2008.

Guo, H., Hu, Q., and Zhang, Q.: Changes in hydrological interactions of the Yangtze River and the Poyang Lake in China during 1957–2008, Acta Geographica Sinica, 66, 609-618, 2011.

Guo, H., Hu, Q., Zhang, Q., and Feng, S.: Effects of the three gorges dam on Yangtze river flow and river interaction with Poyang Lake, China: 2003–2008, Journal of Hydrology, 416, 19-27, 2012.

Gupta, H. V., Sorooshian, S., and Yapo, P. O.: Status of automatic calibration for hydrologic models: Comparison with multilevel expert calibration, Journal of Hydrologic Engineering, 4, 135-143, 1999.

Gutman, G. and Ignatov, A.: The derivation of the green vegetation fraction from NOAA/AVHRR data for use in numerical weather prediction models, International Journal of remote sensing, 19, 1533-1543, 1998.

Hamilton, S. K., Sippel, S. J., and Melack, J. M.: Comparison of inundation patterns among major South American floodplains, Journal of Geophysical Research D: Atmospheres, 107, 1-14, 2002.

Hamilton, S. K., Sippel, S. J., and Melack, J. M.: Inundation patterns in the Pantanal wetland of South America determined from passive microwave remote sensing, Archiv fur Hydrobiologie, 137, 1-23, 1996.

Hamilton, S. K., Sippel, S. J., and Melack, J. M.: Seasonal inundation patterns in two large savanna floodplains of South America: The Llanos de Moxos (Bolivia) and the Llanos del Orinoco (Venezuela and Colombia), Hydrological Processes, 18, 2103-2116, 2004.

Harris, F. J.: On the use of windows for harmonic analysis with the discrete Fourier transform, Proceedings of the IEEE, 66, 51-83, 1978.

Hawkins, D. M.: The problem of overfitting, Journal of chemical information and computer sciences, 44, 1-12, 2004.

Hayashi, M., van der Kamp, G., and Rudolph, D. L.: Water and solute transfer between a prairie wetland and adjacent uplands, 1. Water balance, Journal of Hydrology, 207, 42-55, 1998.

Hess, L. L., Melack, J. M., Filoso, S., and Wang, Y.: Delineation of inundated area and vegetation along the Amazon floodplain with the SIR-C synthetic aperture radar, Geoscience and Remote Sensing, IEEE Transactions on, 33, 896-904, 1995.

Hess, L. L., Melack, J. M., Novo, E. M., Barbosa, C. C., and Gastil, M.: Dual-season mapping of wetland inundation and vegetation for the central Amazon basin, Remote Sensing of Environment, 87, 404-428, 2003.

Hollinger, J. P., Peirce, J. L., and Poe, G. A.: SSM/I instrument evaluation, Ieee T Geosci Remote, 28, 781-790, 1990.

Holmes, T. R. H., De Jeu, R. A. M., Owe, M., and Dolman, A. J.: Land surface temperature from Ka band (37 GHz) passive microwave observations, J Geophys Res-Atmos, 114, 2009.

Horritt, M., Mason, D., and Luckman, A.: Flood boundary delineation from synthetic aperture radar imagery using a statistical active contour model, International Journal of Remote Sensing, 22, 2489-2507, 2001.

Hostache, R., Matgen, P., Schumann, G., Puech, C., Hoffmann, L., and Pfister, L.: Water level estimation and reduction of hydraulic model calibration uncertainties using satellite SAR images of floods, Geoscience and Remote Sensing, IEEE Transactions on, 47, 431-441, 2009.

Houweling, S., Kaminski, T., Dentener, F., Lelieveld, J., and Heimann, M.: Inverse modeling of methane sources and sinks using the adjoint of a global transport model, Journal of Geophysical Research: Atmospheres, 104, 26137-26160, 1999.

Hu, Q., Feng, S., Guo, H., Chen, G., and Jiang, T.: Interactions of the Yangtze river flow and hydrologic processes of the Poyang Lake, China, Journal of Hydrology, 347, 90-100, 2007.

Huber, C., Li, J., Daillet, S., Chen, X., Xijun, L., Francois, C. J., Wei, Z., Carlos, U., Mathias, S., Shifeng, H., Stephane, A., Burnham, J., and Yesou, H.: Twelve year of water resource monitoring over Yangtze middle reaches exploiting DRAGON time series and field measurments, DRAGON II symposium, Beijing, 2012.

Huffman, G. J., Bolvin, D. T., Nelkin, E. J., Wolff, D. B., Adler, R. F., Gu, G., Hong, Y., Bowman, K. P., and Stocker, E. F.: The TRMM multisatellite precipitation analysis (TMPA): Quasi-global, multiyear, combined-sensor precipitation estimates at fine scales, Journal of Hydrometeorology, 8, 38-55, 2007.

Irons, J. R. and Petersen, G. W.: Texture transforms of remote sensing data, Remote Sensing of Environment, 11, 359-370, 1981.

Islam, A., Bala, S., and Haque, M.: Flood inundation map of Bangladesh using MODIS time-series images, Journal of Flood Risk Management, 3, 210-222, 2010.

Jain, S. K., Singh, P., and Seth, S.: Assessment of sedimentation in Bhakra Reservoir in the western Himalayan region using remotely sensed data, Hydrological sciences journal, 47, 203-212, 2002.

Jakeman, A. and Hornberger, G.: How much complexity is warranted in a rainfall-runoff model?, Water resources research, 29, 2637-2649, 1993.

Jakeman, A., Littlewood, I., and Whitehead, P.: Computation of the instantaneous unit hydrograph and identifiable component flows with application to two small upland catchments, Journal of hydrology, 117, 275-300, 1990.

Jia, L., Shang, H., Hu, G., and Menenti, M.: Phenological response of vegetation to upstream river flow in the Heihe Rive basin by time series analysis of MODIS data, Hydrol Earth Syst Sc, 15, 1047-1064, 2011.

Jin, Y.: A flooding index and its regional threshold value for monitoring floods in China from SSM/I data, International Journal of Remote Sensing, 20, 1025-1030, 1999.

Kawanishi, T., Sezai, T., Ito, Y., Imaoka, K., Takeshima, T., Ishido, Y., Shibata, A., Miura, M., Inahata, H., and Spencer, R. W.: The Advanced Microwave Scanning Radiometer for the Earth Observing System (AMSR-E), NASDA's contribution to the EOS for global energy and water cycle studies, Ieee T Geosci Remote, 41, 184-194, 2003.

Kazezyılmaz-Alhan, C. M., Medina, M. A., and Richardson, C. J.: A wetland hydrology and water quality model incorporating surface water/groundwater interactions, Water Resources Research, 43, 2007.

Keogh, E., Chakrabarti, K., Pazzani, M., and Mehrotra, S.: Dimensionality reduction for fast similarity search in large time series databases, Knowledge and information Systems, 3, 263-286, 2001.

Kerr, Y. H., Waldteufel, P., Wigneron, J.-P., Martinuzzi, J., Font, J., and Berger, M.: Soil moisture retrieval from space: The Soil Moisture and Ocean Salinity (SMOS) mission, Ieee T Geosci Remote, 39, 1729-1735, 2001.

Kirdiashev, K. P., Chucklantsev, A. A., and Shutko, A.: Microwave radiation of the earth's surface in the presence of vegetation cover, Radiotecknica, 24, 256-264, 1979.

Knowles, K., Savoie, M., Armstrong, R., and Brodzik, M.: AMSR-E/Aqua Daily EASE-Grid Brightness Temperatures, NASA DAAC at the National Snow and Ice Data Center, Boulder, Colorado USA, 2006.

Kummerow, C., Olson, W. S., and Giglio, L.: A simplified scheme for obtaining precipitation and vertical hydrometeor profiles from passive microwave sensors, Geoscience and Remote Sensing, IEEE Transactions on, 34, 1213-1232, 1996.

Lakshmi, V., Wood, E. F., and Choudhury, B. J.: Evaluation of Special Sensor Microwave/Imager satellite data for regional soil moisture estimation over the Red River basin, Journal of Applied Meteorology, 36, 1309-1328, 1997a.

Lakshmi, V., Wood, E. F., and Choudhury, B. J.: A soil-canopy-atmosphere model for use in satellite microwave remote sensing, Journal of Geophysical Research D: Atmospheres, 102, 6911-6927, 1997b.

Lane, J. and Saxton, J.: Dielectric dispersion in pure polar liquids at very high radio frequencies. III. The effect of electrolytes in solution, 1952, 531-545.

Lawson, C. L. and Hanson, R. J.: Solving least squares problems, SIAM, 1974.

Lee, J.-S., Papathanassiou, K. P., Ainsworth, T. L., Grunes, M. R., and Reigber, A.: A new technique for noise filtering of SAR interferometric phase images, Geoscience and Remote Sensing, IEEE Transactions on, 36, 1456-1465, 1998.

Li, F., Huang, J., Zeng, G., Yuan, X., Li, X., Liang, J., Wang, X., Tang, X., and Bai, B.: Spatial risk assessment and sources identification of heavy metals in surface sediments from the Dongting Lake, Middle China, Journal of Geochemical Exploration, 132, 75-83, 2013.

Li, P., Feng, Z., Jiang, L., Liu, Y., and Xiao, X.: Changes in rice cropping systems in the Poyang Lake Region, China during 2004–2010, Journal of Geographical Sciences, 22, 653-668, 2012.

Liang, X., Lettenmaier, D. P., Wood, E. F., and Burges, S. J.: A simple hydrologically based model of land surface water and energy fluxes for general circulation models, JOURNAL OF GEOPHYSICAL RESEARCH-ALL SERIES-, 99, 14,415-414,415, 1994.

Liebe, H. J., Hufford, G. A., and Manabe, T.: A model for the complex permittivity of water at frequencies below 1 THz, International Journal of Infrared and Millimeter Waves, 12, 659-675, 1991.

Lin, C. and Lu, J.: Studies on the anomaly of Plum Rain and flood disaster in the Yangtze River valley, J. Najing University, 1991. 76-83, 1991.

Lin, R., King-lp, A., and Shim, H. S. S. K.: Fast similarity search in the presence of noise, scaling, and translation in time-series databases, Zurich, Switzerland, 9 - 13 September 1995, 490-501.

Madsen, H.: Automatic calibration of a conceptual rainfall–runoff model using multiple objectives, Journal of hydrology, 235, 276-288, 2000.

Manabe, T., Liebe, H., and Hufford, G.: Complex permittivity of water between 0 and 30 THz, 1987, 229-230.

Matthews, E. and Fung, I.: Methane emission from natural wetlands: Global distribution, area, and environmental characteristics of sources, Global biogeochemical cycles, 1, 61-86, 1987.

Matthews, E., Fung, I., and Lerner, J.: Methane emission from rice cultivation: Geographic and seasonal distribution of cultivated areas and emissions, Global Biogeochemical Cycles, 5, 3-24, 1991.

Mätzler, C.: Thermal microwave radiation: applications for remote sensing, Iet, 2006.

McFeeters, S.: The use of the Normalized Difference Water Index (NDWI) in the delineation of open water features, International journal of remote sensing, 17, 1425-1432, 1996.

Menenti, M., Azzali, S., Verhoef, W., and van Swol, R.: Mapping agroecological zones and time lag in vegetation growth by means of fourier analysis of time series of NDVI images, Advances in Space Research, 13, 233-237, 1993.

Mertes, L. A.: Documentation and significance of the perirheic zone on inundated floodplains, Water Resources Research, 33, 1749-1762, 1997.

Mialon, A., Royer, A., and Fily, M.: Wetland seasonal dynamics and interannual variability over northern high latitudes, derived from microwave satellite data, Journal of Geophysical Research: Atmospheres, 110, 2005.

Miller, M. W. and Nudds, T. D.: Prairie landscape change and flooding in the Mississippi River Valley, Conservation Biology, 1996. 847-853, 1996.

Mo, T. and Schmugge, T. J.: A parameterization of the effect of surface roughness on microwave emission, Geoscience and Remote Sensing, IEEE Transactions on, 1987. 481-486, 1987.

Montandon, L. and Small, E.: The impact of soil reflectance on the quantification of the green vegetation fraction from NDVI, Remote Sensing of Environment, 112, 1835-1845, 2008.

Moore, R.: The PDM rainfall-runoff model, Hydrology and Earth System Sciences Discussions, 11, 483-499, 2007.

Moore, R.: The probability-distributed principle and runoff production at point and basin scales, Hydrological Sciences Journal, 30, 273-297, 1985.

Mörchen, F.: Time series feature extraction for data mining using DWT and DFT. Univ. of Marburg, Germany, 2003.

Nash, J. E. and Sutcliffe, J. V.: River flow forecasting through conceptual models part I — A discussion of principles, Journal of Hydrology, 10, 282-290, 1970.

Nerem, R., Chambers, D., Leuliette, E., Mitchum, G., and Giese, B.: Variations in global mean sea level associated with the 1997–1998 ENSO event: Implications for measuring long term sea level change, Geophys Res Lett, 26, 3005-3008, 1999.

Njoku, E. G., Jackson, T. J., Lakshmi, V., Chan, T. K., and Nghiem, S. V.: Soil moisture retrieval from AMSR-E, Ieee T Geosci Remote, 41, 215-229, 2003.

O'Neill, P. E., Jackson, T. J., Chauhan, N. S., and Seyfried, M. S.: Microwave soil moisture estimation in humid and semiarid watersheds, Advances in Space Research, 13, 115-118, 1993.

Oberstadler, R., Hönsch, H., and Huth, D.: Assessment of the mapping capabilities of ERS-1 SAR data for flood mapping: a case study in Germany, Hydrological processes, 11, 1415-1425, 1997.

Otsu, N.: A threshold selection method from gray-level histograms, Automatica, 11, 23-27, 1975.

Owe, M., de Jeu, R., and Walker, J.: A methodology for surface soil moisture and vegetation optical depth retrieval using the microwave polarization difference index, Geoscience and Remote Sensing, IEEE Transactions on, 39, 1643-1654, 2001.

Paiva, R. C., Durand, M. T., and Hossain, F.: Spatiotemporal interpolation of discharge across a river network by using synthetic SWOT satellite data, Water Resources Research, 51, 430-449, 2015.

Paloscia, S., Macelloni, G., Santi, E., and Koike, T.: A multifrequency algorithm for the retrieval of soil moisture on a large scale using microwave data from SMMR and SSM/I satellites, Ieee T Geosci Remote, 39, 1655-1661, 2001.

Pampaloni, P. and Paloscia, S.: Experimental relationships between microwave emission and vegetation features†, International Journal of Remote Sensing, 6, 315-323, 1985.

Pan, F., Liao, J., Li, X., and Guo, H.: Application of the inundation area—lake level rating curves constructed from the SRTM DEM to retrieving lake levels from satellite measured inundation areas, Computers & Geosciences, 52, 168-176, 2013.

Papa, F., Prigent, C., Durand, F., and Rossow, W. B.: Wetland dynamics using a suite of satellite observations: A case study of application and evaluation for the Indian Subcontinent, Geophys Res Lett, 33, 2006.

Peng, D., Guo, S., Liu, P., and Liu, T.: Reservoir storage curve estimation based on remote sensing data, Journal of hydrologic engineering, 11, 165-172, 2006.

Podest, E. and Saatchi, S.: Application of multiscale texture in classifying JERS-1 radar data over tropical vegetation, International Journal of Remote Sensing, 23, 1487-1506, 2002.

Poe, G. A.: Optimum Interpolation of Imaging Microwave Radiometer Data, Ieee T Geosci Remote, 28, 800-810, 1990.

Poe, G. A. and Conway, R. W.: A study of the geolocation errors of the Special Sensor Microwave/Imager (SSM/I), Ieee T Geosci Remote, 28, 791-799, 1990.

Prigent, C., Aires, F., Rossow, W., and Matthews, E.: Joint characterization of vegetation by satellite observations from visible to microwave wavelengths: A sensitivity analysis, Journal of Geophysical Research: Atmospheres, 106, 20665 - 20685, 2001a.

Prigent, C., Matthews, E., Aires, F., and Rossow, W. B.: Remote sensing of global wetland dynamics with multiple satellite data sets, Geophys Res Lett, 28, 4631-4634, 2001b.

Prigent, C., Papa, F., Aires, F., Rossow, W., and Matthews, E.: Global inundation dynamics inferred from multiple satellite observations, 1993–2000, Journal of Geophysical Research: Atmospheres, 112, 2007.

Prigent, C., Rossow, W. B., and Matthews, E.: Microwave land surface emissivities estimated from SSM/I observations, Journal of Geophysical Research: Atmospheres, 102, 21867-21890, 1997.

Project, B. M., Erdélyi, A., and Bateman, H.: Tables of Integral Transforms: Based in Part on Notes Left by Harry Bateman and Compiled by the Staff of the Bateman Manuscript Project, McGraw-Hill, New York, NY, USA, 1954.

Pulvirenti, L., Chini, M., Pierdicca, N., Guerriero, L., and Ferrazzoli, P.: Flood monitoring using multi-temporal COSMO-SkyMed data: Image segmentation and signature interpretation, Remote Sensing of Environment, 115, 990-1002, 2011.

Rasid, H. and Pramanik, M.: Visual interpretation of satellite imagery for monitoring floods in Bangladesh, Environmental Management, 14, 815-821, 1990.

Reale, A., Chalfant, M., Allegrino, A., Tiley, F., Gerguson, M., and Pettey, M.: Advanced-TOVS (ATOVS) sounding products from NOAA polar orbiting environmental satellites, 2003.

Richards, F. and Arkin, P.: On the relationship between satellite-observed cloud cover and precipitation, Monthly Weather Review, 109, 1081-1093, 1981.

Ritter, A. and Muñoz-Carpena, R.: Performance evaluation of hydrological models: Statistical significance for reducing subjectivity in goodness-of-fit assessments, Journal of Hydrology, 480, 33-45, 2013.

Roerink, G. J., Menenti, M., Soepboer, W., and Su, Z.: Assessment of climate impact on vegetation dynamics by using remote sensing, Physics and Chemistry of the Earth, Parts A/B/C, 28, 103-109, 2003.

Roerink, G. J., Menenti, M., and Verhoef, W.: Reconstructing cloudfree NDVI composites using Fourier analysis of time series, International Journal of Remote Sensing, 21, 1911-1917, 2000.

Rossow, W. B. and Schiffer, R. A.: Advances in understanding clouds from ISCCP, Bulletin of the American Meteorological Society, 80, 2261, 1999.

Sakamoto, T., Van Nguyen, N., Kotera, A., Ohno, H., Ishitsuka, N., and Yokozawa, M.: Detecting temporal changes in the extent of annual flooding within the Cambodia and the Vietnamese Mekong Delta from MODIS time-series imagery, Remote sensing of environment, 109, 295-313, 2007.

Schumann, G., Di Baldassarre, G., and Bates, P. D.: The utility of spaceborne radar to render flood inundation maps based on multialgorithm ensembles, Geoscience and Remote Sensing, IEEE Transactions on, 47, 2801-2807, 2009.

Schumann, G. J.-P. and Moller, D. K.: Microwave remote sensing of flood inundation, Physics and Chemistry of the Earth, Parts A/B/C, 83, 84-95, 2015.

Shang, H., Jia, J., and Menenti, M.: Analyzing the Inundation Pattern of the Poyang Lake floodplain by Passive Microwave Data, Journal of Hydrometeorology, 16, 652-667, 2015.

Shang, H., Jia, J., and Menenti, M.: Modeling and Reconstruction of Time Series of Passive Microwave Data by Discrete Fourier Transform Guided Filtering and Harmonic Analysis, Remote Sensing, 08, 970, 2016.

Shankman, D., Keim, B. D., and Song, J.: Flood frequency in China's Poyang Lake region: trends and teleconnections, International Journal of Climatology, 26, 1255-1266, 2006.

Sheng, Y., Gong, P., and Xiao, Q.: Quantitative dynamic flood monitoring with NOAA AVHRR, International Journal of Remote Sensing, 22, 1709-1724, 2001.

Sheng, Y., Su, Y., and Xiao, Q.: Challenging the cloud-contamination problem in flood monitoring with NOAA/AVHRR imagery, Photogrammetric Engineering and Remote Sensing, 64, 191-198, 1998.

Shi, J. C., Jackson, T., Tao, J., Du, J., Bindlish, R., Lu, L., and Chen, K. S.: Microwave vegetation indices for short vegetation covers from satellite passive microwave sensor AMSR-E, Remote Sensing of Environment, 112, 4285-4300, 2008.

Shi, J. C., Jiang, L. M., Zhang, L. X., Chen, K. S., Wigneron, J. P., and Chanzy, A.: A parameterized multifrequency-polarization surface emission model, Ieee T Geosci Remote, 43, 2831-2841, 2005.

Shjeflo, J. B.: Evapotranspiration and the water budget of prairie potholes in North Dakota, US Government Printing Office, 1968.

Singleton, R. C.: An algorithm for computing the mixed radix fast Fourier transform, Audio and Electroacoustics, IEEE Transactions on, 17, 93-103, 1969.

Sippel, S. J., Hamilton, S. K., Melack, J. M., and Choudhury, B. J.: Determination of inundation area in the Amazon River floodplain using the SMMR 37 GHz polarization difference, Remote Sensing of Environment, 48, 70-76, 1994.

Sippel, S. J., Hamilton, S. K., Melack, J. M., and Novo, E. M. M.: Passive microwave observations of inundation area and the area/stage relation in the Amazon River floodplain, International Journal of Remote Sensing, 19, 3055-3074, 1998.

Sivapalan, M., Beven, K., and Wood, E. F.: On hydrologic similarity: 2. A scaled model of storm runoff production, Water Resources Research, 23, 2266-2278, 1987.

Skøien, J. O., Blöschl, G., and Western, A.: Characteristic space scales and timescales in hydrology, Water Resources Research, 39, 2003.

Smith, L. C.: Satellite remote sensing of river inundation area, stage, and discharge: A review, Hydrological processes, 11, 1427-1439, 1997.

Smith, L. C., Alsdorf, D. E., Magilligan, F. J., Gomez, B., Mertes, L. A., Smith, N. D., and Garvin, J. B.: Estimation of erosion, deposition, and net volumetric change caused by the 1996 Skeiðarársandur jökulhlaup, Iceland, from synthetic aperture radar interferometry, Water Resources Research, 36, 1583-1594, 2000.

Smith, L. C., Isacks, B. L., Bloom, A. L., and Murray, A. B.: Estimation of discharge from three braided rivers using synthetic aperture radar satellite imagery: Potential application to ungaged basins, Water Resources Research, 32, 2021-2034, 1996.

Smith, L. C. and Pavelsky, T. M.: Estimation of river discharge, propagation speed, and hydraulic geometry from space: Lena River, Siberia, Water Resources Research, 44, 2008.

Sophocleous, M.: Interactions between groundwater and surface water: the state of the science, Hydrogeology journal, 10, 52-67, 2002.

Su, M., Stolte, W., and Van der Kamp, G.: Modelling Canadian prairie wetland hydrology using a semi-distributed streamflow model, Hydrological Processes, 14, 2405-2422, 2000.

Tanaka, M., Sugimura, T., and Tanaka, S.: Cover. Monitoring water surface ratio in the Chinese floods of summer 1998 by DMSP-SSM/I, 2000. 2000.

Tanaka, M., Sugimura, T., Tanaka, S., and Tamai, N.: Flood–drought cycle of Tonle Sap and Mekong Delta area observed by DMSP-SSM/I, International Journal of Remote Sensing, 24, 1487-1504, 2003.

Temimi, M., Leconte, R., Brissette, F., and Chaouch, N.: Flood and soil wetness monitoring over the Mackenzie River Basin using AMSR-E 37 GHz brightness temperature, 25-29 July 2005 2005, 4 pp.

Thompson, A. R., Moran, J. M., and Swenson Jr, G. W.: Interferometry and synthesis in radio astronomy, John Wiley & Sons, Weinheim, Germany, 2008.

Todini, E.: The ARNO rainfall—runoff model, Journal of Hydrology, 175, 339-382, 1996.

Torbick, N., Salas, W., Xiao, X., Ingraham, P., Fearon, M., Biradar, C., Zhao, D., Liu, Y., Li, P., and Zhao, Y.: Integrating SAR and optical imagery for regional mapping of paddy rice attributes in the Poyang Lake Watershed, China, Canadian Journal of Remote Sensing, 37, 17-26, 2011.

Townsend, P. A.: Mapping seasonal flooding in forested wetlands using multi-temporal Radarsat SAR, Photogrammetric engineering and remote sensing, 67, 857-864, 2001.

Tsang, L., Blanchard, A. J., Newton, R. W., and Kong, J. A.: A simple relation between active and passive microwave remote sensing measurements of earth terrain, Geoscience and Remote Sensing, IEEE Transactions on, 1982. 482-485, 1982.

Ulaby, F. T., Moore, R. K., and Fung, A. K.: Microwave remote sensing : active and passive, Addison-Wesley Pub. Co., Advanced Book Program/World Science Division, Reading, Mass., 1981.

Usachev, V.: Evaluation of flood plain inundations by remote sensing methods, Hydrological Applications of Remote Sensing and Remote Data Transmission, 1983. 475-482, 1983.

Vachaud, G., Passerat de Silans, A., Balabanis, P., and Vauclin, M.: Temporal stability of spatially measured soil water probability density function, Soil Science Society of America Journal, 49, 822-828, 1985.

Vandegriend, A. A. and Owe, M.: Determination of Microwave Vegetation Optical Depth and Single Scattering Albedo from Large-Scale Soil-Moisture and Nimbus Smmr Satellite-Observations, International Journal of Remote Sensing, 14, 1875-1886, 1993.

Verdin, J.: Remote sensing of ephemeral water bodies in western Niger, International Journal of Remote Sensing, 17, 733-748, 1996.

Verhoef, W.: Application of Harmonic Analysis of NDVI Time Series (HANTS), In Fourier Analysis of Temporal NDVI in the Souther African and American Continents Wageningen, The Netherlands, 19-24, 1996.

Vinnikov, K. Y., Robock, A., Qiu, S., Entin, J. K., Owe, M., Choudhury, B. J., Hollinger, S. E., and Njoku, E. G.: Satellite remote sensing of soil moisture in Illinois, United States, Journal of Geophysical Research D: Atmospheres, 104, 4145-4168, 1999.

Vinnikov, K. Y., Robock, A., Speranskaya, N. A., and Schlosser, C. A.: Scales of temporal and spatial variability of midlatitude soil moisture, Journal of Geophysical Research: Atmospheres, 101, 7163-7174, 1996.

Vörösmarty, C. J., Moore, B., Grace, A. L., Gildea, M. P., Melillo, J. M., Peterson, B. J., Rastetter, E. B., and Steudler, P. A.: Continental scale models of water balance and fluvial transport: an application to South America, Global biogeochemical cycles, 3, 241-265, 1989.

Vörösmarty, C. J., Willmott, C. J., Choudhury, B. J., Schloss, A. L., Stearns, T. K., Robeson, S. M., and Dorman, T. J.: Analyzing the discharge regime of a large tropical river through remote sensing, ground-based climatic data, and modeling, Water Resources Research, 32, 3137-3150, 1996.

Walter, B. P., Heimann, M., and Matthews, E.: Modeling modern methane emissions from natural wetlands: 1. Model description and results, Journal of Geophysical Research: Atmospheres, 106, 34189-34206, 2001.

Wang, J. R. and Choudhury, B. J.: Remote sensing of soil moisture content over bare field at 1.4 GHz frequency, Journal of Geophysical Research, 86, 5277-5282, 1981.

Wang, J. R. and Schmugge, T. J.: An Empirical-Model for the Complex Dielectric Permittivity of Soils as a Function of Water-Content, Ieee T Geosci Remote, 18, 288-295, 1980.

Wang, Y., Hess, L. L., Filoso, S., and Melack, J. M.: Understanding the radar backscattering from flooded and nonflooded Amazonian forests: Results from canopy backscatter modeling, Remote Sensing of Environment, 54, 324-332, 1995.

Wang, Z., Chai, L., Wang, Y., Yang, Z., Wang, H., and Wu, X.: Potential health risk of arsenic and cadmium in groundwater near Xiangjiang River, China: a case study for risk assessment and management of toxic substances, Environmental monitoring and assessment, 175, 167-173, 2011.

Wen, J., Su, Z. B., and Ma, Y. M.: Determination of land surface temperature and soil moisture from Tropical Rainfall Measuring Mission/Microwave Imager remote sensing data, J Geophys Res-Atmos, 108, 2003.

Wentz, F. J.: Measurement of oceanic wind vector using satellite microwave radiometers, Ieee T Geosci Remote, 30, 960-972, 1992.

Wentz, F. J.: SSM/I Version-7 Calibration Report, Remote Sensing Systems, Santa Rosa, CA, 46pp pp., 2013.

Westerhoff, R., Kleuskens, M., Winsemius, H., Huizinga, H., Brakenridge, G., and Bishop, C.: Automated global water mapping based on wide-swath orbital synthetic-aperture radar, Hydrol. Earth Syst. Sci, 17, 651-663, 2013.

Wiesmann, A. and Mätzler, C.: Microwave emission model of layered snowpacks, Remote Sensing of Environment, 70, 307-316, 1999.

Wigneron, J.-P., Chanzy, A., Calvet, J.-C., and Bruguier, N.: A simple algorithm to retrieve soil moisture and vegetation biomass using passive microwave measurements over crop fields, Remote Sensing of Environment, 51, 331-341, 1995.

Wigneron, J. P., Kerr, Y., Chanzy, A., and Jin, Y. Q.: Inversion of surface parameters from passive microwave measurements over a soybean field, Remote Sensing of Environment, 46, 61-72, 1993.

Wilson, D. J., Western, A. W., and Grayson, R. B.: Identifying and quantifying sources of variability in temporal and spatial soil moisture observations, Water Resources Research, 40, 2004.

Winter, T. C. and Rosenberry, D. O.: The interaction of ground water with prairie pothole wetlands in the Cottonwood Lake area, east-central North Dakota, 1979–1990, Wetlands, 15, 193-211, 1995.

Winter, T. C. and Valk, A.: Hydrologic studies of wetlands in the northern prairie, Northern prairie wetlands., 1989. 16-54, 1989.

Woo, M.-K. and Rowsell, R. D.: Hydrology of a prairie slough, Journal of Hydrology, 146, 175-207, 1993.

Wood, E. F., Lettenmaier, D. P., and Zartarian, V. G.: A land-surface hydrology parameterization with subgrid variability for general circulation models, Journal of Geophysical Research: Atmospheres (1984–2012), 97, 2717-2728, 1992.

Wu, Y.-L., Agrawal, D., and El Abbadi, A.: A comparison of DFT and DWT based similarity search in time-series databases, McLean, VA, USA, 6 - 11 November 2000, 488-495.

Xiao, Q. and Chen, W.: Songhua River flood monitoring with meteorological satellite imagery, Remote Sensing Information, 4, 37-41, 1987.

Xu, C.-Y. and Singh, V. P.: Review on regional water resources assessment models under stationary and changing climate, Water Resources Management, 18, 591-612, 2004.

Xu, H.: Modification of normalised difference water index (NDWI) to enhance open water features in remotely sensed imagery, International Journal of Remote Sensing, 27, 3025-3033, 2006.

Yang, K., He, J., Tang, W., Qin, J., and Cheng, C. C.: On downward shortwave and longwave radiations over high altitude regions: Observation and modeling in the Tibetan Plateau, Agricultural and Forest Meteorology, 150, 38-46, 2010.

Ye, X., Zhang, Q., Bai, L., and Hu, Q.: A modeling study of catchment discharge to Poyang Lake under future climate in China, Quaternary International, 244, 221-229, 2011.

Ye, X., Zhang, Q., Liu, J., Li, X., and Xu, C.-y.: Distinguishing the relative impacts of climate change and human activities on variation of streamflow in the Poyang Lake catchment, China, Journal of Hydrology, 494, 83-95, 2013.

Yésou, H., Claire, H., Xijun, L., Stéphane, A., Jiren, L., Sylviane, D., Muriel, B.-N., Xiaoling, C., Shifeng, H., Burnham, J., Jean-François, C., Tiphanie, M., Jinggang, L., Rémi, A., and Carlos, U.: Nine years of water resources monitoring over the middle reaches of the Yangtze River, with ENVISAT, MODIS, Beijing-1 time series, Altimetric data and field measurements, Lakes & Reservoirs: Research & Management, 16, 231-247, 2011.

Yesou, H., Huber, C., Shifeng, H., Xijun, L., and Sylviane, D.-R.: Chinese lakes behaviours in the framework of the meteorology and water management practices: EO based monitoring lessons, the ESA Living Planet symposium, Edinburg, 2013.

Young, P.: Recursive estimation and time-series analysis: an introduction, 1984. 1984.

Zhang, L., Li, D., Tong, Q., and Zheng, L.: Study of the spectral mixture model of soil and vegetation in PoYang Lake area, China, International Journal of Remote Sensing, 19, 2077-2084, 1998.

Zhang, L., Yin, J., Jiang, Y., and Wang, H.: Relationship between the hydrological conditions and the distribution of vegetation communities within the Poyang Lake National Nature Reserve, China, Ecological Informatics, 11, 65-75, 2012.

Zhang, Q., Liu, C., Xu, C.-y., Xu, Y., and Jiang, T.: Observed trends of annual maximum water level and streamflow during past 130 years in the Yangtze River basin, China, Journal of Hydrology, 324, 255-265, 2006.

Zhang, Q., Liu, Y., Yang, G., and Zhang, Z.: Precipitation and hydrological variations and related associations with large-scale circulation in the Poyang Lake basin, China, Hydrological Processes, 25, 740-751, 2011.

Zhao, G., Hörmann, G., Fohrer, N., Zhang, Z., and Zhai, J.: Streamflow trends and climate variability impacts in Poyang Lake Basin, China, Water resources management, 24, 689-706, 2010.

Zhao, R.: Flood forecasting method for humid regions of China, East China College of Hydraulic Engineering, Nanjing, 1977. 19-51, 1977.

Zhao, R.: Watershed hydrological modelling, Water Resources and Electric Power Press, Beijing, 1984. 1984.

Zhou, Z.: Synoptic characteristics of atmoshperic cirulation during abnormal Plum Rain period in 1991, J. Nanjing University, 1991. 84-93, 1991.

Zong, Y. and Chen, X.: The 1998 flood on the Yangtze, China, Natural Hazards, 22, 165-184, 2000.

Agrawal, R., Faloutsos, C., and Swami, A.: Efficient similarity search in sequence databases, Springer, 1993.

Aires, F., Prigent, C., Rossow, W., Rothstein, M., and Hansen, J. E.: A new neural network approach including first-guess for retrieval of atmospheric water vapor, cloud liquid water path, surface temperature and emissivities over land from satellite microwave observations, Journal of Geophysical Research, 2000. 2000.

Alsdorf, D. E.: Water storage of the central Amazon floodplain measured with GIS and remote sensing imagery, Annals of the Association of American Geographers, 93, 55-66, 2003.

Alsdorf, D. E., Rodríguez, E., and Lettenmaier, D. P.: Measuring surface water from space, Reviews of Geophysics, 45, 2007.

Alsdorf, D. E., Smith, L. C., and Melack, J. M.: Amazon floodplain water level changes measured with interferometric SIR-C radar, Geoscience and Remote Sensing, IEEE Transactions on, 39, 423-431, 2001.

Armstrong, R., Knowles, K., Brodzik, M., and Hardman, M. A.: DMSP SSM/I-SSMIS Pathfinder Daily EASE-Grid Brightness Temperatures. Version 2. Boulder, Colorado USA: NASA DAAC at the National Snow and Ice Data Center, 1998.

Babyak, M. A.: What you see may not be what you get: a brief, nontechnical introduction to overfitting in regression-type models, Psychosomatic medicine, 66, 411-421, 2004.

Barton, I. J. and Bathols, J. M.: Monitoring floods with AVHRR, Remote sensing of Environment, 30, 89-94, 1989.

Basist, A., Grody, N. C., Peterson, T. C., and Williams, C. N.: Using the Special Sensor Microwave/Imager to monitor land surface temperatures, wetness, and snow cover, Journal of Applied Meteorology, 37, 888-911, 1998.

Basist, A., Williams Jr, C., Ross, T. F., Menne, M. J., Grody, N., Ferraro, R., Shen, S., and Chang, A. T.: Using the Special Sensor Microwave Imager to monitor surface wetness, Journal of Hydrometeorology, 2, 297-308, 2001.

Bates, P. D., Neal, J. C., Alsdorf, D., and Schumann, G. J.-P.: Observing global surface water flood dynamics, Surveys in Geophysics, 35, 839-852, 2014.

Behrangi, A., Guan, B., Neiman, P. J., Schreier, M., and Lambrigtsen, B.: On the Quantification of Atmospheric Rivers Precipitation from Space: Composite Assessments and Case Studies over the Eastern North Pacific Ocean and the Western United States, Journal of Hydrometeorology, 17, 369-382, 2016.

Beven, K. and Kirkby, M.: A physically based, variable contributing area model of basin hydrology/Un modèle à base physique de zone d'appel variable de l'hydrologie du bassin versant, Hydrological Sciences Journal, 24, 43-69, 1979.

Beven, K., Kirkby, M., Schofield, N., and Tagg, A.: Testing a physically-based flood forecasting model (TOPMODEL) for three UK catchments, Journal of Hydrology, 69, 119-143, 1984.

Biggin, D.: A comparison of ERS-1 satellite radar and aerial photography for river flood mapping, Water and Environment Journal, 10, 59-64, 1996.

Bjerklie, D. M., Dingman, S. L., Vorosmarty, C. J., Bolster, C. H., and Congalton, R. G.: Evaluating the potential for measuring river discharge from space, Journal of Hydrology, 278, 17-38, 2003.

Björck, A.: Numerical methods for least squares problems, Siam, 1996.

Boukabara, S.-A., Garrett, K., and Chen, W.: Global coverage of total precipitable water using a microwave variational algorithm, Ieee T Geosci Remote, 48, 3608-3621, 2010.

Brakenridge, G. R., Nghiem, S. V., Anderson, E., and Chien, S.: Space-based measurement of river runoff, EOS: Transactions of the American Geophysical Union, 86, 185-192, 2005.

Brakenridge, G. R., Nghiem, S. V., Anderson, E., and Mic, R.: Orbital microwave measurement of river discharge and ice status, Water Resources Research, 43, 2007.

Brodzik, M. and Knowles, K.: EASE-Grid: A Versatile Set of Equal-Area Prjoections and Grids, National Center for Geographic Information & Analysis, Santa Barbara, California USA, 2002.

Calvet, J. C., Wigneron, J. P., Chanzy, A., Raju, S., and Laguerre, L.: Microwave Dielectric-Properties of a Silt-Loam at High-Frequencies, Ieee T Geosci Remote, 33, 634-642, 1995.

Carlson, T. N. and Ripley, D. A.: On the relation between NDVI, fractional vegetation cover, and leaf area index, Remote sensing of Environment, 62, 241-252, 1997.

Chai, L., Wang, Z., Wang, Y., Yang, Z., Wang, H., and Wu, X.: Ingestion risks of metals in groundwater based on TIN model and dose-response assessment—A case study in the Xiangjiang watershed, central-south China, Science of the Total Environment, 408, 3118-3124, 2010.

Chappell, N. A., Jones, T. D., Tych, W., and Krishnaswamy, J.: Role of rainstorm intensity underestimated by data-derived flood models: emerging global evidence from subsurface-dominated watersheds, Environmental Modelling & Software, 88, 1-9, 2017.

Chen, Y., Huang, C., Ticehurst, C., Merrin, L., and Thew, P.: An evaluation of MODIS daily and 8-day composite products for floodplain and wetland inundation mapping, Wetlands, 33, 823-835, 2013.

Chen, Y., Yang, K., He, J., Qin, J., Shi, J., Du, J., and He, Q.: Improving land surface temperature modeling for dry land of China, Journal of Geophysical Research: Atmospheres (1984–2012), 116, 2011.

Choudhury, B. J.: Monitoring global land surface using Nimbus-7 37 GHz data. Theory and examples, International Journal of Remote Sensing, 10, 1579-1605, 1989.

Choudhury, B. J.: Passive microwave remote sensing contribution to hydrological variables. In: Land surface-atmosphere interactions for climate modeling, Springer, Dordrecht, The Netherlands, 1991.

Choudhury, B. J., Major, E. R., Smith, E. A., and Becker, F.: Atmospheric effects on SMMR and SSM/I 37 GHz polarization difference over the Sahel, International Journal of Remote Sensing, 13, 3443-3463, 1992.

Choudhury, B. J., Schmugge, T. J., Chang, A., and Newton, R. W.: Effect of surface roughness on the microwave emission from soils, Journal of Geophysical Research, 89, 5699-5706, 1979.

Choudhury, B. J. and Tucker, C. J.: Monitoring global vegetation using Nimbus-7 37 GHz data. Some empirical relations, International Journal of Remote Sensing, 8, 1085-1090, 1987.

Choudhury, B. J., Wang, J. R., Hsu, A. Y., and Chien, Y. L.: Simulated and observed 37GHz emission over Africa, International Journal of Remote Sensing, 11, 1837-1868, 1990.

Chunguo, C. and Zihui, L.: Chemical speciation and distribution of arsenic in water, suspended solids and sediment of Xiangjiang River, China, Science of the total environment, 77, 69-82, 1988.

Cooley, J. W., Lewis, P. A., and Welch, P. D.: Application of the fast Fourier transform to computation of Fourier integrals, Fourier series, and convolution integrals, Audio and Electroacoustics, IEEE Transactions on, 15, 79-84, 1967.

Cooley, J. W. and Tukey, J. W.: An algorithm for the machine calculation of complex Fourier series, Mathematics of computation, 19, 297-301, 1965.

Crow, W. and Ryu, D.: A new data assimilation approach for improving runoff prediction using remotely-sensed soil moisture retrievals, Hydrol Earth Syst Sc, 13, 1-16, 2009.

Czekala, H., Havemann, S., Schmidt, K., Rother, T., and Simmer, C.: Comparison of microwave radiative transfer calculations obtained with three different approximations of hydrometeor shape, Journal of Quantitative Spectroscopy and Radiative Transfer, 63, 545-558, 1999.

D'Odorico, P. and Rodríguez-Iturbe, I.: Space-time self-organization of mesoscale rainfall and soil moisture, Advances in water resources, 23, 349-357, 2000.

De Ridder, K.: Quantitative estimation of skin soil moisture with the special sensor microwave/imager, Boundary-Layer Meteorology, 96, 421-432, 2000.

Deshmukh, K. and Shinde, G.: An adaptive color image segmentation, ELCVIA Electronic Letters on Computer Vision and Image Analysis, 5, 12-23, 2005.

Dobson, M. C., Ulaby, F. T., Hallikainen, M. T., and Elrayes, M. A.: Microwave Dielectric Behavior of Wet Soil .2. Dielectric Mixing Models, Ieee T Geosci Remote, 23, 35-46, 1985.

Donohue, R., Roderick, M., and McVicar, T.: On the importance of including vegetation dynamics in Budyko's hydrological model, Hydrology and Earth System Sciences Discussions, 11, 983-995, 2007.

Dronova, I., Gong, P., and Wang, L.: Object-based analysis and change detection of major wetland cover types and their classification uncertainty during the low water period at Poyang Lake, China, Remote Sensing of Environment, 115, 3220-3236, 2011.

Eagleson, P. S.: Climate, soil, and vegetation: 1. Introduction to water balance dynamics, Water Resources Research, 14, 705-712, 1978.

Entin, J. K., Robock, A., Vinnikov, K. Y., Hollinger, S. E., Liu, S., and Namkhai, A.: Temporal and spatial scales of observed soil moisture variations in the extratropics, J Geophys Res, 105, 11865-11877, 2000.

Feng, L., Hu, C., Chen, X., Cai, X., Tian, L., and Gan, W.: Assessment of inundation changes of Poyang Lake using MODIS observations between 2000 and 2010, Remote Sensing of Environment, 121, 80-92, 2012a.

Feng, L., Hu, C., Chen, X., Tian, L., and Chen, L.: Human induced turbidity changes in Poyang Lake between 2000 and 2010: Observations from MODIS, Journal of Geophysical Research: Oceans, 117, 2012b.

Ferraro, R. R. and Marks, G. F.: The Development of SSM/I Rain-Rate Retrieval Algorithms Using Ground-Based Radar Measurements, Journal of Atmospheric and Oceanic Technology, 12, 755-770, 1995.

Fily, M., Royer, A., Goïta, K., and Prigent, C.: A simple retrieval method for land surface temperature and fraction of water surface determination from satellite microwave brightness temperatures in sub-arctic areas, Remote Sensing of Environment, 85, 328-338, 2003.

Frappart, F., Seyler, F., Martinez, J.-M., Leon, J. G., and Cazenave, A.: Floodplain water storage in the Negro River basin estimated from microwave remote sensing of inundation area and water levels, Remote Sensing of Environment, 99, 387-399, 2005.

Gao, H. L., Wood, E. F., Drusch, M., Crow, W., and Jackson, T. J.: Using a microwave emission model to estimate soil moisture from ESTAR observations during SGP99, Journal of Hydrometeorology, 5, 49-63, 2004.

Gerek, Ö. N. and Yardimci, Y.: Equiripple FIR filter design by the FFT algorithm, Signal Processing Magazine, IEEE, 14, 60-64, 1997.

Giddings, L. and Choudhury, B. J.: Observation of hydrological features with Nimbus-7 37 GHz data, applied to South America, International Journal of Remote Sensing, 10, 1673-1686, 1989.

Gleason, C. J. and Smith, L. C.: Toward global mapping of river discharge using satellite images and at-many-stations hydraulic geometry, Proceedings of the National Academy of Sciences, 111, 4788-4791, 2014.

Gleick, P. H.: The development and testing of a water balance model for climate impact assessment: modeling the Sacramento basin, Water Resources Research, 23, 1049-1061, 1987.

Goel, M., Jain, S. K., and Agarwal, P.: Assessment of sediment deposition rate in Bargi Reservoir using digital image processing, Hydrological sciences journal, 47, S81-S92, 2002.

Guerschman, J. P., Warren, G., Byrne, G., Lymburner, L., Mueller, N., and Van Dijk, A. I.: MODIS-based standing water detection for flood and large reservoir mapping: algorithm development and applications for the Australian continent, CSIRO Canberra, Australia, 2011.

Guo, H., Hu, Q., and Jiang, T.: Annual and seasonal streamflow responses to climate and land-cover changes in the Poyang Lake basin, China, Journal of Hydrology, 355, 106-122, 2008.

Guo, H., Hu, Q., and Zhang, Q.: Changes in hydrological interactions of the Yangtze River and the Poyang Lake in China during 1957–2008, Acta Geographica Sinica, 66, 609-618, 2011.

Guo, H., Hu, Q., Zhang, Q., and Feng, S.: Effects of the three gorges dam on Yangtze river flow and river interaction with Poyang Lake, China: 2003–2008, Journal of Hydrology, 416, 19-27, 2012.

Gupta, H. V., Sorooshian, S., and Yapo, P. O.: Status of automatic calibration for hydrologic models: Comparison with multilevel expert calibration, Journal of Hydrologic Engineering, 4, 135-143, 1999.

Gutman, G. and Ignatov, A.: The derivation of the green vegetation fraction from NOAA/AVHRR data for use in numerical weather prediction models, International Journal of remote sensing, 19, 1533-1543, 1998.

Hamilton, S. K., Sippel, S. J., and Melack, J. M.: Comparison of inundation patterns among major South American floodplains, Journal of Geophysical Research D: Atmospheres, 107, 1-14, 2002.

Hamilton, S. K., Sippel, S. J., and Melack, J. M.: Inundation patterns in the Pantanal wetland of South America determined from passive microwave remote sensing, Archiv fur Hydrobiologie, 137, 1-23, 1996.

Hamilton, S. K., Sippel, S. J., and Melack, J. M.: Seasonal inundation patterns in two large savanna floodplains of South America: The Llanos de Moxos (Bolivia) and the Llanos del Orinoco (Venezuela and Colombia), Hydrological Processes, 18, 2103-2116, 2004.

Harris, F. J.: On the use of windows for harmonic analysis with the discrete Fourier transform, Proceedings of the IEEE, 66, 51-83, 1978.

Hawkins, D. M.: The problem of overfitting, Journal of chemical information and computer sciences, 44, 1-12, 2004.

Hayashi, M., van der Kamp, G., and Rudolph, D. L.: Water and solute transfer between a prairie wetland and adjacent uplands, 1. Water balance, Journal of Hydrology, 207, 42-55, 1998.

Hess, L. L., Melack, J. M., Filoso, S., and Wang, Y.: Delineation of inundated area and vegetation along the Amazon floodplain with the SIR-C synthetic aperture radar, Geoscience and Remote Sensing, IEEE Transactions on, 33, 896-904, 1995.

Hess, L. L., Melack, J. M., Novo, E. M., Barbosa, C. C., and Gastil, M.: Dual-season mapping of wetland inundation and vegetation for the central Amazon basin, Remote Sensing of Environment, 87, 404-428, 2003.

Hollinger, J. P., Peirce, J. L., and Poe, G. A.: SSM/I instrument evaluation, Ieee T Geosci Remote, 28, 781-790, 1990.

Holmes, T. R. H., De Jeu, R. A. M., Owe, M., and Dolman, A. J.: Land surface temperature from Ka band (37 GHz) passive microwave observations, J Geophys Res-Atmos, 114, 2009.

Horritt, M., Mason, D., and Luckman, A.: Flood boundary delineation from synthetic aperture radar imagery using a statistical active contour model, International Journal of Remote Sensing, 22, 2489-2507, 2001.

Hostache, R., Matgen, P., Schumann, G., Puech, C., Hoffmann, L., and Pfister, L.: Water level estimation and reduction of hydraulic model calibration uncertainties using satellite SAR images of floods, Geoscience and Remote Sensing, IEEE Transactions on, 47, 431-441, 2009.

Houweling, S., Kaminski, T., Dentener, F., Lelieveld, J., and Heimann, M.: Inverse modeling of methane sources and sinks using the adjoint of a global transport model, Journal of Geophysical Research: Atmospheres, 104, 26137-26160, 1999.

Hu, Q., Feng, S., Guo, H., Chen, G., and Jiang, T.: Interactions of the Yangtze river flow and hydrologic processes of the Poyang Lake, China, Journal of Hydrology, 347, 90-100, 2007.

Huber, C., Li, J., Daillet, S., Chen, X., Xijun, L., Francois, C. J., Wei, Z., Carlos, U., Mathias, S., Shifeng, H., Stephane, A., Burnham, J., and Yesou, H.: Twelve year of water resource monitoring over Yangtze middle reaches exploiting DRAGON time series and field measurments, DRAGON II symposium, Beijing, 2012.

Huffman, G. J., Bolvin, D. T., Nelkin, E. J., Wolff, D. B., Adler, R. F., Gu, G., Hong, Y., Bowman, K. P., and Stocker, E. F.: The TRMM multisatellite precipitation analysis (TMPA): Quasi-global, multiyear, combined-sensor precipitation estimates at fine scales, Journal of Hydrometeorology, 8, 38-55, 2007.

Irons, J. R. and Petersen, G. W.: Texture transforms of remote sensing data, Remote Sensing of Environment, 11, 359-370, 1981.

Islam, A., Bala, S., and Haque, M.: Flood inundation map of Bangladesh using MODIS time-series images, Journal of Flood Risk Management, 3, 210-222, 2010.

Jain, S. K., Singh, P., and Seth, S.: Assessment of sedimentation in Bhakra Reservoir in the western Himalayan region using remotely sensed data, Hydrological sciences journal, 47, 203-212, 2002.

Jakeman, A. and Hornberger, G.: How much complexity is warranted in a rainfall-runoff model?, Water resources research, 29, 2637-2649, 1993.

Jakeman, A., Littlewood, I., and Whitehead, P.: Computation of the instantaneous unit hydrograph and identifiable component flows with application to two small upland catchments, Journal of hydrology, 117, 275-300, 1990.

Jia, L., Shang, H., Hu, G., and Menenti, M.: Phenological response of vegetation to upstream river flow in the Heihe Rive basin by time series analysis of MODIS data, Hydrol Earth Syst Sc, 15, 1047-1064, 2011.

Jin, Y.: A flooding index and its regional threshold value for monitoring floods in China from SSM/I data, International Journal of Remote Sensing, 20, 1025-1030, 1999.

Kawanishi, T., Sezai, T., Ito, Y., Imaoka, K., Takeshima, T., Ishido, Y., Shibata, A., Miura, M., Inahata, H., and Spencer, R. W.: The Advanced Microwave Scanning Radiometer for

the Earth Observing System (AMSR-E), NASDA's contribution to the EOS for global energy and water cycle studies, Ieee T Geosci Remote, 41, 184-194, 2003.

Kazezyılmaz-Alhan, C. M., Medina, M. A., and Richardson, C. J.: A wetland hydrology and water quality model incorporating surface water/groundwater interactions, Water Resources Research, 43, 2007.

Keogh, E., Chakrabarti, K., Pazzani, M., and Mehrotra, S.: Dimensionality reduction for fast similarity search in large time series databases, Knowledge and information Systems, 3, 263-286, 2001.

Kerr, Y. H., Waldteufel, P., Wigneron, J.-P., Martinuzzi, J., Font, J., and Berger, M.: Soil moisture retrieval from space: The Soil Moisture and Ocean Salinity (SMOS) mission, Ieee T Geosci Remote, 39, 1729-1735, 2001.

Kirdiashev, K. P., Chucklantsev, A. A., and Shutko, A.: Microwave radiation of the earth's surface in the presence of vegetation cover, Radiotecknica, 24, 256-264, 1979.

Knowles, K., Savoie, M., Armstrong, R., and Brodzik, M.: AMSR-E/Aqua Daily EASE-Grid Brightness Temperatures, NASA DAAC at the National Snow and Ice Data Center, Boulder, Colorado USA, 2006.

Kummerow, C., Olson, W. S., and Giglio, L.: A simplified scheme for obtaining precipitation and vertical hydrometeor profiles from passive microwave sensors, Geoscience and Remote Sensing, IEEE Transactions on, 34, 1213-1232, 1996.

Lakshmi, V., Wood, E. F., and Choudhury, B. J.: Evaluation of Special Sensor Microwave/Imager satellite data for regional soil moisture estimation over the Red River basin, Journal of Applied Meteorology, 36, 1309-1328, 1997a.

Lakshmi, V., Wood, E. F., and Choudhury, B. J.: A soil-canopy-atmosphere model for use in satellite microwave remote sensing, Journal of Geophysical Research D: Atmospheres, 102, 6911-6927, 1997b.

Lane, J. and Saxton, J.: Dielectric dispersion in pure polar liquids at very high radio frequencies. III. The effect of electrolytes in solution, 1952, 531-545.

Lawson, C. L. and Hanson, R. J.: Solving least squares problems, SIAM, 1974.

Lee, J.-S., Papathanassiou, K. P., Ainsworth, T. L., Grunes, M. R., and Reigber, A.: A new technique for noise filtering of SAR interferometric phase images, Geoscience and Remote Sensing, IEEE Transactions on, 36, 1456-1465, 1998.

Li, F., Huang, J., Zeng, G., Yuan, X., Li, X., Liang, J., Wang, X., Tang, X., and Bai, B.: Spatial risk assessment and sources identification of heavy metals in surface sediments from the Dongting Lake, Middle China, Journal of Geochemical Exploration, 132, 75-83, 2013.

Li, P., Feng, Z., Jiang, L., Liu, Y., and Xiao, X.: Changes in rice cropping systems in the Poyang Lake Region, China during 2004–2010, Journal of Geographical Sciences, 22, 653-668, 2012.

Liang, X., Lettenmaier, D. P., Wood, E. F., and Burges, S. J.: A simple hydrologically based model of land surface water and energy fluxes for general circulation models, JOURNAL OF GEOPHYSICAL RESEARCH-ALL SERIES-, 99, 14,415-414,415, 1994.

Liebe, H. J., Hufford, G. A., and Manabe, T.: A model for the complex permittivity of water at frequencies below 1 THz, International Journal of Infrared and Millimeter Waves, 12, 659-675, 1991.

Lin, C. and Lu, J.: Studies on the anomaly of Plum Rain and flood disaster in the Yangtze River valley, J. Najing University, 1991. 76-83, 1991.

Lin, R., King-lp, A., and Shim, H. S. S. K.: Fast similarity search in the presence of noise, scaling, and translation in time-series databases, Zurich, Switzerland, 9 - 13 September 1995, 490-501.

Madsen, H.: Automatic calibration of a conceptual rainfall–runoff model using multiple objectives, Journal of hydrology, 235, 276-288, 2000.

Manabe, T., Liebe, H., and Hufford, G.: Complex permittivity of water between 0 and 30 THz, 1987, 229-230.

Matthews, E. and Fung, I.: Methane emission from natural wetlands: Global distribution, area, and environmental characteristics of sources, Global biogeochemical cycles, 1, 61-86, 1987.

Matthews, E., Fung, I., and Lerner, J.: Methane emission from rice cultivation: Geographic and seasonal distribution of cultivated areas and emissions, Global Biogeochemical Cycles, 5, 3-24, 1991.

Mätzler, C.: Thermal microwave radiation: applications for remote sensing, Iet, 2006.

McFeeters, S.: The use of the Normalized Difference Water Index (NDWI) in the delineation of open water features, International journal of remote sensing, 17, 1425-1432, 1996.

Menenti, M., Azzali, S., Verhoef, W., and van Swol, R.: Mapping agroecological zones and time lag in vegetation growth by means of fourier analysis of time series of NDVI images, Advances in Space Research, 13, 233-237, 1993.

Mertes, L. A.: Documentation and significance of the perirheic zone on inundated floodplains, Water Resources Research, 33, 1749-1762, 1997.

Mialon, A., Royer, A., and Fily, M.: Wetland seasonal dynamics and interannual variability over northern high latitudes, derived from microwave satellite data, Journal of Geophysical Research: Atmospheres, 110, 2005.

Miller, M. W. and Nudds, T. D.: Prairie landscape change and flooding in the Mississippi River Valley, Conservation Biology, 1996. 847-853, 1996.

Mo, T. and Schmugge, T. J.: A parameterization of the effect of surface roughness on microwave emission, Geoscience and Remote Sensing, IEEE Transactions on, 1987. 481-486, 1987.

Montandon, L. and Small, E.: The impact of soil reflectance on the quantification of the green vegetation fraction from NDVI, Remote Sensing of Environment, 112, 1835-1845, 2008.

Moore, R.: The PDM rainfall-runoff model, Hydrology and Earth System Sciences Discussions, 11, 483-499, 2007.

Moore, R.: The probability-distributed principle and runoff production at point and basin scales, Hydrological Sciences Journal, 30, 273-297, 1985.

Mörchen, F.: Time series feature extraction for data mining using DWT and DFT. Univ. of Marburg, Germany, 2003.

Nash, J. E. and Sutcliffe, J. V.: River flow forecasting through conceptual models part I — A discussion of principles, Journal of Hydrology, 10, 282-290, 1970.

Nerem, R., Chambers, D., Leuliette, E., Mitchum, G., and Giese, B.: Variations in global mean sea level associated with the 1997–1998 ENSO event: Implications for measuring long term sea level change, Geophys Res Lett, 26, 3005-3008, 1999.

Njoku, E. G., Jackson, T. J., Lakshmi, V., Chan, T. K., and Nghiem, S. V.: Soil moisture retrieval from AMSR-E, Ieee T Geosci Remote, 41, 215-229, 2003.

O'Neill, P. E., Jackson, T. J., Chauhan, N. S., and Seyfried, M. S.: Microwave soil moisture estimation in humid and semiarid watersheds, Advances in Space Research, 13, 115-118, 1993.

Oberstadler, R., Hönsch, H., and Huth, D.: Assessment of the mapping capabilities of ERS-1 SAR data for flood mapping: a case study in Germany, Hydrological processes, 11, 1415-1425, 1997.

Otsu, N.: A threshold selection method from gray-level histograms, Automatica, 11, 23-27, 1975.

Owe, M., de Jeu, R., and Walker, J.: A methodology for surface soil moisture and vegetation optical depth retrieval using the microwave polarization difference index, Geoscience and Remote Sensing, IEEE Transactions on, 39, 1643-1654, 2001.

Paiva, R. C., Durand, M. T., and Hossain, F.: Spatiotemporal interpolation of discharge across a river network by using synthetic SWOT satellite data, Water Resources Research, 51, 430-449, 2015.

Paloscia, S., Macelloni, G., Santi, E., and Koike, T.: A multifrequency algorithm for the retrieval of soil moisture on a large scale using microwave data from SMMR and SSM/I satellites, Ieee T Geosci Remote, 39, 1655-1661, 2001.

Pampaloni, P. and Paloscia, S.: Experimental relationships between microwave emission and vegetation features†, International Journal of Remote Sensing, 6, 315-323, 1985.

Pan, F., Liao, J., Li, X., and Guo, H.: Application of the inundation area—lake level rating curves constructed from the SRTM DEM to retrieving lake levels from satellite measured inundation areas, Computers & Geosciences, 52, 168-176, 2013.

Papa, F., Prigent, C., Durand, F., and Rossow, W. B.: Wetland dynamics using a suite of satellite observations: A case study of application and evaluation for the Indian Subcontinent, Geophys Res Lett, 33, 2006.

Peng, D., Guo, S., Liu, P., and Liu, T.: Reservoir storage curve estimation based on remote sensing data, Journal of hydrologic engineering, 11, 165-172, 2006.

Podest, E. and Saatchi, S.: Application of multiscale texture in classifying JERS-1 radar data over tropical vegetation, International Journal of Remote Sensing, 23, 1487-1506, 2002.

Poe, G. A.: Optimum Interpolation of Imaging Microwave Radiometer Data, Ieee T Geosci Remote, 28, 800-810, 1990.

Poe, G. A. and Conway, R. W.: A study of the geolocation errors of the Special Sensor Microwave/Imager (SSM/I), Ieee T Geosci Remote, 28, 791-799, 1990.

Prigent, C., Aires, F., Rossow, W., and Matthews, E.: Joint characterization of vegetation by satellite observations from visible to microwave wavelengths: A sensitivity analysis, Journal of Geophysical Research: Atmospheres, 106, 20665 - 20685, 2001a.

Prigent, C., Matthews, E., Aires, F., and Rossow, W. B.: Remote sensing of global wetland dynamics with multiple satellite data sets, Geophys Res Lett, 28, 4631-4634, 2001b.

Prigent, C., Papa, F., Aires, F., Rossow, W., and Matthews, E.: Global inundation dynamics inferred from multiple satellite observations, 1993–2000, Journal of Geophysical Research: Atmospheres, 112, 2007.

Prigent, C., Rossow, W. B., and Matthews, E.: Microwave land surface emissivities estimated from SSM/I observations, Journal of Geophysical Research: Atmospheres, 102, 21867-21890, 1997.

Project, B. M., Erdélyi, A., and Bateman, H.: Tables of Integral Transforms: Based in Part on Notes Left by Harry Bateman and Compiled by the Staff of the Bateman Manuscript Project, McGraw-Hill, New York, NY, USA, 1954.

Pulvirenti, L., Chini, M., Pierdicca, N., Guerriero, L., and Ferrazzoli, P.: Flood monitoring using multi-temporal COSMO-SkyMed data: Image segmentation and signature interpretation, Remote Sensing of Environment, 115, 990-1002, 2011.

Rasid, H. and Pramanik, M.: Visual interpretation of satellite imagery for monitoring floods in Bangladesh, Environmental Management, 14, 815-821, 1990.

Reale, A., Chalfant, M., Allegrino, A., Tiley, F., Gerguson, M., and Pettey, M.: Advanced-TOVS (ATOVS) sounding products from NOAA polar orbiting environmental satellites, 2003.

Richards, F. and Arkin, P.: On the relationship between satellite-observed cloud cover and precipitation, Monthly Weather Review, 109, 1081-1093, 1981.

Ritter, A. and Muñoz-Carpena, R.: Performance evaluation of hydrological models: Statistical significance for reducing subjectivity in goodness-of-fit assessments, Journal of Hydrology, 480, 33-45, 2013.

Roerink, G. J., Menenti, M., Soepboer, W., and Su, Z.: Assessment of climate impact on vegetation dynamics by using remote sensing, Physics and Chemistry of the Earth, Parts A/B/C, 28, 103-109, 2003.

Roerink, G. J., Menenti, M., and Verhoef, W.: Reconstructing cloudfree NDVI composites using Fourier analysis of time series, International Journal of Remote Sensing, 21, 1911-1917, 2000.

Rossow, W. B. and Schiffer, R. A.: Advances in understanding clouds from ISCCP, Bulletin of the American Meteorological Society, 80, 2261, 1999.

Sakamoto, T., Van Nguyen, N., Kotera, A., Ohno, H., Ishitsuka, N., and Yokozawa, M.: Detecting temporal changes in the extent of annual flooding within the Cambodia and the Vietnamese Mekong Delta from MODIS time-series imagery, Remote sensing of environment, 109, 295-313, 2007.

Schumann, G., Di Baldassarre, G., and Bates, P. D.: The utility of spaceborne radar to render flood inundation maps based on multialgorithm ensembles, Geoscience and Remote Sensing, IEEE Transactions on, 47, 2801-2807, 2009.

Schumann, G. J.-P. and Moller, D. K.: Microwave remote sensing of flood inundation, Physics and Chemistry of the Earth, Parts A/B/C, 83, 84-95, 2015.

Shang, H., Jia, J., and Menenti, M.: Analyzing the Inundation Pattern of the Poyang Lake floodplain by Passive Microwave Data, Journal of Hydrometeorology, 16, 652-667, 2015.

Shang, H., Jia, J., and Menenti, M.: Modeling and Reconstruction of Time Series of Passive Microwave Data by Discrete Fourier Transform Guided Filtering and Harmonic Analysis, Remote Sensing, 08, 970, 2016.

Shankman, D., Keim, B. D., and Song, J.: Flood frequency in China's Poyang Lake region: trends and teleconnections, International Journal of Climatology, 26, 1255-1266, 2006.

Sheng, Y., Gong, P., and Xiao, Q.: Quantitative dynamic flood monitoring with NOAA AVHRR, International Journal of Remote Sensing, 22, 1709-1724, 2001.

Sheng, Y., Su, Y., and Xiao, Q.: Challenging the cloud-contamination problem in flood monitoring with NOAA/AVHRR imagery, Photogrammetric Engineering and Remote Sensing, 64, 191-198, 1998.

Shi, J. C., Jackson, T., Tao, J., Du, J., Bindlish, R., Lu, L., and Chen, K. S.: Microwave vegetation indices for short vegetation covers from satellite passive microwave sensor AMSR-E, Remote Sensing of Environment, 112, 4285-4300, 2008.

Shi, J. C., Jiang, L. M., Zhang, L. X., Chen, K. S., Wigneron, J. P., and Chanzy, A.: A parameterized multifrequency-polarization surface emission model, Ieee T Geosci Remote, 43, 2831-2841, 2005.

Shjeflo, J. B.: Evapotranspiration and the water budget of prairie potholes in North Dakota, US Government Printing Office, 1968.

Singleton, R. C.: An algorithm for computing the mixed radix fast Fourier transform, Audio and Electroacoustics, IEEE Transactions on, 17, 93-103, 1969.

Sippel, S. J., Hamilton, S. K., Melack, J. M., and Choudhury, B. J.: Determination of inundation area in the Amazon River floodplain using the SMMR 37 GHz polarization difference, Remote Sensing of Environment, 48, 70-76, 1994.

Sippel, S. J., Hamilton, S. K., Melack, J. M., and Novo, E. M. M.: Passive microwave observations of inundation area and the area/stage relation in the Amazon River floodplain, International Journal of Remote Sensing, 19, 3055-3074, 1998.

Sivapalan, M., Beven, K., and Wood, E. F.: On hydrologic similarity: 2. A scaled model of storm runoff production, Water Resources Research, 23, 2266-2278, 1987.

Skøien, J. O., Blöschl, G., and Western, A.: Characteristic space scales and timescales in hydrology, Water Resources Research, 39, 2003.

Smith, L. C.: Satellite remote sensing of river inundation area, stage, and discharge: A review, Hydrological processes, 11, 1427-1439, 1997.

Smith, L. C., Alsdorf, D. E., Magilligan, F. J., Gomez, B., Mertes, L. A., Smith, N. D., and Garvin, J. B.: Estimation of erosion, deposition, and net volumetric change caused by the 1996 Skeiðarársandur jökulhlaup, Iceland, from synthetic aperture radar interferometry, Water Resources Research, 36, 1583-1594, 2000.

Smith, L. C., Isacks, B. L., Bloom, A. L., and Murray, A. B.: Estimation of discharge from three braided rivers using synthetic aperture radar satellite imagery: Potential application to ungaged basins, Water Resources Research, 32, 2021-2034, 1996.

Smith, L. C. and Pavelsky, T. M.: Estimation of river discharge, propagation speed, and hydraulic geometry from space: Lena River, Siberia, Water Resources Research, 44, 2008.

Sophocleous, M.: Interactions between groundwater and surface water: the state of the science, Hydrogeology journal, 10, 52-67, 2002.

Su, M., Stolte, W., and Van der Kamp, G.: Modelling Canadian prairie wetland hydrology using a semi-distributed streamflow model, Hydrological Processes, 14, 2405-2422, 2000.

Tanaka, M., Sugimura, T., and Tanaka, S.: Cover. Monitoring water surface ratio in the Chinese floods of summer 1998 by DMSP-SSM/I, 2000. 2000.

Tanaka, M., Sugimura, T., Tanaka, S., and Tamai, N.: Flood–drought cycle of Tonle Sap and Mekong Delta area observed by DMSP-SSM/I, International Journal of Remote Sensing, 24, 1487-1504, 2003.

Temimi, M., Leconte, R., Brissette, F., and Chaouch, N.: Flood and soil wetness monitoring over the Mackenzie River Basin using AMSR-E 37 GHz brightness temperature, 25-29 July 2005 2005, 4 pp.

Thompson, A. R., Moran, J. M., and Swenson Jr, G. W.: Interferometry and synthesis in radio astronomy, John Wiley & Sons, Weinheim, Germany, 2008.

Todini, E.: The ARNO rainfall—runoff model, Journal of Hydrology, 175, 339-382, 1996.

Torbick, N., Salas, W., Xiao, X., Ingraham, P., Fearon, M., Biradar, C., Zhao, D., Liu, Y., Li, P., and Zhao, Y.: Integrating SAR and optical imagery for regional mapping of paddy rice attributes in the Poyang Lake Watershed, China, Canadian Journal of Remote Sensing, 37, 17-26, 2011.

Townsend, P. A.: Mapping seasonal flooding in forested wetlands using multi-temporal Radarsat SAR, Photogrammetric engineering and remote sensing, 67, 857-864, 2001.

Tsang, L., Blanchard, A. J., Newton, R. W., and Kong, J. A.: A simple relation between active and passive microwave remote sensing measurements of earth terrain, Geoscience and Remote Sensing, IEEE Transactions on, 1982. 482-485, 1982.

Ulaby, F. T., Moore, R. K., and Fung, A. K.: Microwave remote sensing : active and passive, Addison-Wesley Pub. Co., Advanced Book Program/World Science Division, Reading, Mass., 1981.

Usachev, V.: Evaluation of flood plain inundations by remote sensing methods, Hydrological Applications of Remote Sensing and Remote Data Transmission, 1983. 475-482, 1983.

Vachaud, G., Passerat de Silans, A., Balabanis, P., and Vauclin, M.: Temporal stability of spatially measured soil water probability density function, Soil Science Society of America Journal, 49, 822-828, 1985.

Vandegriend, A. A. and Owe, M.: Determination of Microwave Vegetation Optical Depth and Single Scattering Albedo from Large-Scale Soil-Moisture and Nimbus Smmr Satellite-Observations, International Journal of Remote Sensing, 14, 1875-1886, 1993.

Verdin, J.: Remote sensing of ephemeral water bodies in western Niger, International Journal of Remote Sensing, 17, 733-748, 1996.

Verhoef, W.: Application of Harmonic Analysis of NDVI Time Series (HANTS), In Fourier Analysis of Temporal NDVI in the Souther African and American Continents Wageningen, The Netherlands, 19-24, 1996.

Vinnikov, K. Y., Robock, A., Qiu, S., Entin, J. K., Owe, M., Choudhury, B. J., Hollinger, S. E., and Njoku, E. G.: Satellite remote sensing of soil moisture in Illinois, United States, Journal of Geophysical Research D: Atmospheres, 104, 4145-4168, 1999.

Vinnikov, K. Y., Robock, A., Speranskaya, N. A., and Schlosser, C. A.: Scales of temporal and spatial variability of midlatitude soil moisture, Journal of Geophysical Research: Atmospheres, 101, 7163-7174, 1996.

Vörösmarty, C. J., Moore, B., Grace, A. L., Gildea, M. P., Melillo, J. M., Peterson, B. J., Rastetter, E. B., and Steudler, P. A.: Continental scale models of water balance and fluvial transport: an application to South America, Global biogeochemical cycles, 3, 241-265, 1989.

Vörösmarty, C. J., Willmott, C. J., Choudhury, B. J., Schloss, A. L., Stearns, T. K., Robeson, S. M., and Dorman, T. J.: Analyzing the discharge regime of a large tropical river through remote sensing, ground-based climatic data, and modeling, Water Resources Research, 32, 3137-3150, 1996.

Walter, B. P., Heimann, M., and Matthews, E.: Modeling modern methane emissions from natural wetlands: 1. Model description and results, Journal of Geophysical Research: Atmospheres, 106, 34189-34206, 2001.

Wang, J. R. and Choudhury, B. J.: Remote sensing of soil moisture content over bare field at 1.4 GHz frequency, Journal of Geophysical Research, 86, 5277-5282, 1981.

Wang, J. R. and Schmugge, T. J.: An Empirical-Model for the Complex Dielectric Permittivity of Soils as a Function of Water-Content, Ieee T Geosci Remote, 18, 288-295, 1980.

Wang, Y., Hess, L. L., Filoso, S., and Melack, J. M.: Understanding the radar backscattering from flooded and nonflooded Amazonian forests: Results from canopy backscatter modeling, Remote Sensing of Environment, 54, 324-332, 1995.

Wang, Z., Chai, L., Wang, Y., Yang, Z., Wang, H., and Wu, X.: Potential health risk of arsenic and cadmium in groundwater near Xiangjiang River, China: a case study for risk assessment and management of toxic substances, Environmental monitoring and assessment, 175, 167-173, 2011.

Wen, J., Su, Z. B., and Ma, Y. M.: Determination of land surface temperature and soil moisture from Tropical Rainfall Measuring Mission/Microwave Imager remote sensing data, J Geophys Res-Atmos, 108, 2003.

Wentz, F. J.: Measurement of oceanic wind vector using satellite microwave radiometers, Ieee T Geosci Remote, 30, 960-972, 1992.

Wentz, F. J.: SSM/I Version-7 Calibration Report, Remote Sensing Systems, Santa Rosa, CA, 46pp pp., 2013.

Westerhoff, R., Kleuskens, M., Winsemius, H., Huizinga, H., Brakenridge, G., and Bishop, C.: Automated global water mapping based on wide-swath orbital synthetic-aperture radar, Hydrol. Earth Syst. Sci, 17, 651-663, 2013.

Wiesmann, A. and Mätzler, C.: Microwave emission model of layered snowpacks, Remote Sensing of Environment, 70, 307-316, 1999.

Wigneron, J.-P., Chanzy, A., Calvet, J.-C., and Bruguier, N.: A simple algorithm to retrieve soil moisture and vegetation biomass using passive microwave measurements over crop fields, Remote Sensing of Environment, 51, 331-341, 1995.

Wigneron, J. P., Kerr, Y., Chanzy, A., and Jin, Y. Q.: Inversion of surface parameters from passive microwave measurements over a soybean field, Remote Sensing of Environment, 46, 61-72, 1993.

Wilson, D. J., Western, A. W., and Grayson, R. B.: Identifying and quantifying sources of variability in temporal and spatial soil moisture observations, Water Resources Research, 40, 2004.

Winter, T. C. and Rosenberry, D. O.: The interaction of ground water with prairie pothole wetlands in the Cottonwood Lake area, east-central North Dakota, 1979–1990, Wetlands, 15, 193-211, 1995.

Winter, T. C. and Valk, A.: Hydrologic studies of wetlands in the northern prairie, Northern prairie wetlands., 1989. 16-54, 1989.

Woo, M.-K. and Rowsell, R. D.: Hydrology of a prairie slough, Journal of Hydrology, 146, 175-207, 1993.

Wood, E. F., Lettenmaier, D. P., and Zartarian, V. G.: A land-surface hydrology parameterization with subgrid variability for general circulation models, Journal of Geophysical Research: Atmospheres (1984–2012), 97, 2717-2728, 1992.

Wu, Y.-L., Agrawal, D., and El Abbadi, A.: A comparison of DFT and DWT based similarity search in time-series databases, McLean, VA, USA, 6 - 11 November 2000, 488-495.

Xiao, Q. and Chen, W.: Songhua River flood monitoring with meteorological satellite imagery, Remote Sensing Information, 4, 37-41, 1987.

Xu, C.-Y. and Singh, V. P.: Review on regional water resources assessment models under stationary and changing climate, Water Resources Management, 18, 591-612, 2004.

Xu, H.: Modification of normalised difference water index (NDWI) to enhance open water features in remotely sensed imagery, International Journal of Remote Sensing, 27, 3025-3033, 2006.

Yang, K., He, J., Tang, W., Qin, J., and Cheng, C. C.: On downward shortwave and longwave radiations over high altitude regions: Observation and modeling in the Tibetan Plateau, Agricultural and Forest Meteorology, 150, 38-46, 2010.

Ye, X., Zhang, Q., Bai, L., and Hu, Q.: A modeling study of catchment discharge to Poyang Lake under future climate in China, Quaternary International, 244, 221-229, 2011.

Ye, X., Zhang, Q., Liu, J., Li, X., and Xu, C.-y.: Distinguishing the relative impacts of climate change and human activities on variation of streamflow in the Poyang Lake catchment, China, Journal of Hydrology, 494, 83-95, 2013.

Yésou, H., Claire, H., Xijun, L., Stéphane, A., Jiren, L., Sylviane, D., Muriel, B.-N., Xiaoling, C., Shifeng, H., Burnham, J., Jean-François, C., Tiphanie, M., Jinggang, L., Rémi, A., and Carlos, U.: Nine years of water resources monitoring over the middle reaches of the Yangtze River, with ENVISAT, MODIS, Beijing-1 time series, Altimetric data and field measurements, Lakes & Reservoirs: Research & Management, 16, 231-247, 2011.

Yesou, H., Huber, C., Shifeng, H., Xijun, L., and Sylviane, D.-R.: Chinese lakes behaviours in the framework of the meteorology and water management practices: EO based monitoring lessons, the ESA Living Planet symposium, Edinburg, 2013.

Young, P.: Recursive estimation and time-series analysis: an introduction, 1984. 1984.

Zhang, L., Li, D., Tong, Q., and Zheng, L.: Study of the spectral mixture model of soil and vegetation in PoYang Lake area, China, International Journal of Remote Sensing, 19, 2077-2084, 1998.

Zhang, L., Yin, J., Jiang, Y., and Wang, H.: Relationship between the hydrological conditions and the distribution of vegetation communities within the Poyang Lake National Nature Reserve, China, Ecological Informatics, 11, 65-75, 2012.

Zhang, Q., Liu, C., Xu, C.-y., Xu, Y., and Jiang, T.: Observed trends of annual maximum water level and streamflow during past 130 years in the Yangtze River basin, China, Journal of Hydrology, 324, 255-265, 2006.

Zhang, Q., Liu, Y., Yang, G., and Zhang, Z.: Precipitation and hydrological variations and related associations with large-scale circulation in the Poyang Lake basin, China, Hydrological Processes, 25, 740-751, 2011.

Zhao, G., Hörmann, G., Fohrer, N., Zhang, Z., and Zhai, J.: Streamflow trends and climate variability impacts in Poyang Lake Basin, China, Water resources management, 24, 689-706, 2010.

Zhao, R.: Flood forecasting method for humid regions of China, East China College of Hydraulic Engineering, Nanjing, 1977. 19-51, 1977.

Zhao, R.: Watershed hydrological modelling, Water Resources and Electric Power Press, Beijing, 1984. 1984.

Zhou, Z.: Synoptic characteristics of atmoshperic cirulation during abnormal Plum Rain period in 1991, J. Nanjing University, 1991. 84-93, 1991.

Zong, Y. and Chen, X.: The 1998 flood on the Yangtze, China, Natural Hazards, 22, 165-184, 2000.

Acknowledge

It is a so long journey to do my PhD in Delft University of Technology and Chinese Academy of Science, that I may not be able to list everyone who has impressed and encouraged me to reach the final destination. I would, however, never have courage and patience to go through my weakness, depression and unimaged stress to finish the PhD, without the support of following people.

First, I would like to thank Pro. Massimo Menenti and Pro. Li Jia to give me the opportunity to do my PhD in TU Delft. Special thanks to Pro. Li Jia, since she was also the supervisor of my minor Master thesis in Wageningen University and introduced me to Pro. Massimo Menenti, which is the start of my journey. I was really appreciated to have Pro. Massimo Menenti to be my supervisor, for his great patience and meticulous teaching. He is more than the promotor and daily supervisor of my thesis, but the navigator who leads me to sail in science. I had never imaged that Dr. Susan Steele-Dunne would be my copromotor many years ago, when we discussed my proposal at her office. Many thanks to her, for being my copromotor and so many valuable and constructive suggestions on my dissertation.

Secondly, I would like to thank all my friends who shared their data with me. I am very grateful to Pro. Herve Yesou and Dr. Hube Claire from University of Strasbourg, who shared their observations on Poyang Lake with me. My special thanks to Pro. Zhenghui Xie from the Institute of Atmospheric Physics, Dr. Weiguo Jiang and Dr. Zhigang Liu of Beijing Normal University, and Ming Yin from the Institute of Geo-Environmental Monitoring, China, for sharing the data with me according to the data policy of Chinese government. I would like to thank my friends who had helped me to obtain data, i.e. Jiawen Dai and Liuyi Tao.

I would like to express my appreciations to my colleagues and friends in TU Delft. I am grateful to Dr. Roderik Lindenbergh, a nice person who helped me translate the summary in Dutch. I am appreciated to Pro. Roman Hanssen for discussing about my PhD thesis. Many thanks to Junchao Shi, my closest friend in TU Delft, for studying together for so long time. I was so appreciated that Marcel Kleinherenbrink, my dear friend, helped me pass the most difficult time in my life, even though he had never realized that. I feel so luck to meet Laure Roupioz. We are classmates from master to PhD and saw the growth of each other during so many years. We did the experiment together in Tibet, which is an unforgettable experience for me. I would like to thank Arjan Tabak for promising me translate the thesis. Many thanks to Alexander Bucksch, who introduced me around TU delft when I just arrived. I am grateful to Yerong Wu and Yu Sun for sharing the office with me and helping me prepare the final version of the dissertation. Many thanks to these active new PhD students to welcome me back, e.g. Han Dun, Kaixuan Zhou, Jiapeng Yin, Seyed Anayat Hosseini Aria and so on, especially for Seyed's helps on the printing format of the

dissertation. Special thanks to the secretaries of Geo-science and Remote Sensing, Lidwien de Jong, Debbie Rietdijk, Irma Zomerdijk, Rebeca Domingo and Suzanne de Hoog, for their helps in extending my hospitality every year and arranging everything during my stay in Delft.

I am also grateful to my colleagues and friends in Chinese Academy of Science (CAS). Without them, I could not complete my researches. I am really appreciated to Pro. Li Jia and her group members in the institute of Remote Sensing and Digital Earth (RADI), e.g. Chengyun Song, Bo Gao, Jie Zhou, Guangchen Hu, Kun Wang, Zhaojie Ruan, Qiting Chen, Zhansheng Li, Ning Wang, Baojian Wu, Yaokui Cui, Yibo Sun, and so on. I spent five years with these smart and hardworking peoples to work on different projects. In Zhangye, we have very busy and funny field measurements and I met many nice people, like Wenping Yu. The experience with Wang Kun, Qiting Chen, Ning Wang and Baojian Wu in Ejin Oasis is also amazing. Many thanks to Pro. Jiancheng Shi and his group members in RADI, e.g. Yonghui Lei, Tianxing Wang, Anqi Wang, Zhiyu Zhang, Tianjie Zhao, Qian Cui, Dabin Ji, Ting Mei, Peng Guo, Chenzhou Liu, Qiang Liu, Yunqing Li, Bin Peng, Haokui Xu and so on. They helped me a lot in the radiative transfer model of passive wave. Special thanks to Bin Peng, who gave me a lot of suggestions on the hydrological models. I enjoy the discussion with Haokui Xu, a smart boy thinking deeply, and many thanks to him for sharing his book list with me. Very special thanks to Anqi Wang. I am also grateful to Pro. Peng Gong, Dr. Wei Fu and Shuang Liu, who shared their knowledge about the Poyang Lake floodplain with me. I am really appreciated to Jinbo Xie and Binghao Jia, who I met in Zhangye and introduced me to the football team. I want to play soccer with my team members as long as I can. There are so many other people in CAS, who had helped me a lot, e.g. Xiangzhi Huang, Yi Cen, Shuhan Liu, Xiaojun Yin, Bo Zhong, Jing Zhao, Zhikun Zhu, Guoshuai Zhang and so on.

I would also like to thank all my friends in Wageningen University, where I started my studying in the Netherlands and met so many nice people: Willy ten Haaf, my study adviser, Dr. Gerard Heuvelink and Dr. Sytze de Bruin, the supervisors of my major master thesis, Pro. Arnold Bregt, the reason I came to Wageningen University, and so on. I also miss Hanneke, Sam, Lorena, Lily, Paul, Azlim, Marleen, Marian and so many other classmates in this group whose names are always difficult to remember for me. But, I remember the time we had spent together, forever.

I am very grateful to my Chinese classmates in Wageningen, also my friends forever, Yuan Zeng, Jing Li, Jie Bai, Shixuan Deng, Jixing Liu, Jiabo Di, Zhuyan Shi, Bingzhen Du, An An, Yuehan Dou, Zhuobiao Ni, and Yafei Wang. Very special thanks to Bingzhen Du, Yuehan Dou, Yuan Zeng and Jing Li for helping me study in China for so many years. I would also like to thank my friends in Beijing, i.e. Junhui Qi, Yuanping Zhang, Yecheng Yuan and Chao Xie.

Finally, I need to give my greatest appreciations to my families, my parents, my parents in law, my wife and my little boy. I realized the dream that my parents wanted to give me, though I may do not like it at all. But without their support, I could not study abroad and finish my PhD. After my little baby was born, I suddenly understood them. The

dream will continue for my children, since the way to acquire knowledge and the way to extend our understanding are lying deeply in human's gene, which we may call curiosity. Many thanks to my parents in law and their families, e.g. the sister in law, for taking care my wife, my baby and me for so long time.

It was the best thing in my life to meet my wife, Xiaoyu Liu. She lightens my life and gives me so many happiness. Her supporting and understanding are the most important things for me. Even more, she gave the best gift in my life, my little boy – Boyuan Shang, to me. I hope we can take care of him together and give him the chance to realize his dreams.

Life will be continued, with or without anyone. But the meaning of life is the people we have met, understood and loved and the views in each journey together with my lovers, friends and families. This is the end of my long journey in TU Delft, but also the start of another chapter in my life. Thanks again to all the people I have met in the last 7 years.

List of Publications

Journal publications

H. Shang, L. Jia, and M. Menenti, 2016: Modeling and reconstruction of time series of passive microwave data by FFT guided filtering and harmonic analysis. Remote Sensing, 2016, 08, 970.

H. Shang, Li Jia, and M. Menenti, 2016: Application of 37GHz PDBT microwave observation to simulate stream flow in the downstream of Xiangjiang river basin with a discrete rainfall-runoff model. HESS discussion, 2016.

H. Shang, L. Jia, and M. Menenti, 2015: Analyzing the Inundation Pattern of the Poyang Lake Floodplain by Passive Microwave Data. J. Hydrometeor., 16, 652–667.

L. Jia, **H. Shang**, G. Hu, and M. Menenti, 2011: Phenological response of vegetation to upstream river flow in the Heihe Rive basin by time series analysis of MODIS data, Hydrol Earth Syst Sc, 15, 1047-1064, 2011.

Conference contributions

H. Shang, L.Jia and M.Menenti, 2012: Analyzing the inundation patterns in Asia floodplains by passive microwave data. SPIE conference in Kyoto Japan.

Book chapter

Chapter of "Observing the response of terrestrial vegetation to climate variability across a range of time scales by time series analysis of land surface temperature" In book: Multitemporal Remote Sensing, Chapter: 14, Publisher: Springer International Publishing, Editors: Yifang Ban,

M. Menenti, H.R. Ghafarian Malamiri, **H. Shang**, S.M. Alfieri, C. Maffei and L. Jia.

About the Author

Haolyu Shang was born in Shengzhou, Zhejiang Province, P.R. China, on March 11 1985. Since 2003, he did his bachelor in Geographical Information System in Zhejiang University, P.R. China, where he started to know GIS, remote sensing, data management on geo-data, and spatial statistics. Wageningen University opened the door for him in 2007 and educated him as a pre-researcher. He finished his master thesis "Accuracy of Mean Annual N2O Emission Estimates from Agricultural and Natural Area in the EU27 using Stratified Random Sampling" supervised by dr. ir. Gerard Heuvelink and dr. ir. Sytze De Bruin. During his minor thesis, dr. Li Jia supervised him with great patient and suggested him as a PhD candidate of Delft University of Technology to Pro. Dr. Massimo Menenti in 2010. He final finished his PhD on "Applications of passive microwave data to monitor inundated areas and model stream flow" in Delft University of Technology, in 2017.